

Dissertation zur Erlangung des Doktorgrades der Fakultät für  
Chemie und Pharmazie der Ludwig-Maximilians-Universität  
München

# **Engineering DNA origami NanoAntennas for DNA detection at the point-of-care**



Renukka Yaadav

aus

Shahjahanpur, India

2024

## Erklärung

Diese Dissertation wurde im Sinne von § 7 der Promotionsordnung vom 28. November 2011 von Herrn Prof. Dr. Philip Tinnefeld betreut.

## Eidesstattliche Versicherung

Diese Dissertation wurde eigenständig und ohne unerlaubte Hilfe erarbeitet.

München, 16.10.2024

Renukka Yaadav

Dissertation eingereicht am 17.10.2024

1. Gutachter: Prof. Dr. Philip Tinnefeld

2. Gutachterin: Prof. Dr. Alena Khmelinskaia

Mündliche Prüfung am 25.11.2024



## ABSTRACT

The convergence of biosensing and nanotechnology heralds a new era in diagnostics, enabling unprecedented molecular-level sensitivity and specificity. Central to this advancement is DNA origami—a technique utilizing the self-assembly of DNA strands to create nanostructures with precise geometries. By employing DNA origami, we can arrange plasmonic nanoparticles (NPs) at defined distances to form hotspots, significantly enhancing the fluorescence signals of nearby fluorophores. Combining this with single-molecule imaging offers ultimate detection sensitivity, allowing direct observation and counting of individual molecules. This capability is crucial for detecting clinically relevant analyte concentrations below picomolar levels, as even single binding events can be observed. However, efficiently capturing and detecting all target molecules within a given volume in a reasonable timeframe remains a critical challenge, especially when molecules are sparsely distributed at low concentrations. This thesis explores how manipulating matter at the nanoscale through DNA origami-based NanoAntennas can address these challenges.

We aimed to determine whether DNA origami NanoAntennas can be used to develop a point-of-care (POC)-compatible, molecular amplification-free DNA detection method, and how sensitive such a system can be. To address these questions, we utilized the plasmonic enhancement capabilities of NanoAntennas to amplify the signal from a single fluorophore by 100-fold, making it detectable with low-tech devices. We incorporated a nucleic acid capture assay within the hotspot of the NanoAntenna, targeting a 151-nucleotide (nt) sequence specific to carbapenem-resistant *Klebsiella pneumoniae*. Recognizing that at ultra-low target concentrations (sub-femtomolar), the main hurdle is efficiently finding and capturing the scarce molecules within a reasonable timeframe, we implemented strategies to maximize the probability that a target molecule encounters a NanoAntenna quickly. We increased the number of capturing strands per NanoAntenna to enhance binding efficiency while minimizing sources of nonspecific binding. We arranged NanoAntennas in a hexagonal array with 400 nm spacing, effectively packing the surface with potential capturing sites. We incorporated a microfluidic chip to create repetitive flow, enhancing mass transport. Together with collaborators, we built a simple fluorescence reader with a larger field-of-view, allowing us to visualize most of the captured molecules in one frame and count them with built-in analysis software. This integrated approach resulted in a detection limit of 5 attomolar (aM) in

optimized buffer solutions. To test the assay in a more clinically relevant fluid like human blood plasma, we coated the NanoAntennas with silica to protect them against degradation by enzymes present in biological fluids. The assay maintained similar functionality, resulting in a 10 aM detection limit in untreated, target-spiked human blood plasma. Additionally, we designed a strand-displacement strategy that allowed the chip to be reused, addressing cost and practicality for POC applications.

In the second part of the thesis, we explored the capture of alternative nanoemitters, such as quantum dots (QDs), within the hotspot of NanoAntennas. QDs are semiconducting nanoparticles, typically ranging from 2 to 8 nm in size, which offer broad absorption spectra, narrow emission spectra, and improved photostability compared to traditional fluorophores. Additionally, the emission wavelengths of QDs can be tuned based on their size, making them attractive candidates for multiplexing assays. We used DNA-tagged QDs of three different sizes (2–4 nm) and captured them within the hotspots of NanoAntennas. We observed a maximum fluorescence enhancement of 200-fold for the smallest QDs, comparable to the enhancement observed with common dyes. However, we identified several challenges related to QD surface passivation and their extreme sensitivity to the immediate environment, providing insights for future development. With optimizations to improve their robustness, QDs have the potential to be used in advanced photonic devices and biosensing applications.

In conclusion, this work advances the application of DNA origami NanoAntennas in biosensing, particularly for point-of-care diagnostics. By developing a highly sensitive assay for detecting DNA targets and demonstrating the effective use of QDs as alternative fluorophores, we contribute to the development of rapid, accessible diagnostic tools. Future directions include integrating NanoAntennas with spotting technologies to create multiplexed infectious disease panels and exploring further improvements in assay sensitivity and device integration.

# PUBLICATIONS

PEER-REVIEWED AND SUBMITTED PUBLICATIONS THAT ARE A PART OF THIS THESIS

1. Kateryna Trofymchuk, Viktorija Glembockyte, Lennart Grabenhorst, Florian Steiner, Carolin Vietz, Cindy Close, Martina Pfeiffer, Lars Richter, Max L Schütte, Florian Selbach, **Renukka Yaadav**, Jonas Zähringer, Qingshan Wei, Aydogan Ozcan, Birka Lalkens, Guillermo P Acuna, Philip Tinnefeld  
“Addressable nanoantennas with cleared hotspots for single-molecule detection on a portable smartphone microscope”  
*Nature Communication* 2021 12, 950. [10.1038/s41467-021-21238-9](https://doi.org/10.1038/s41467-021-21238-9)
2. **Renukka Yaadav**, Kateryna Trofymchuk, Mihir Dass, Vivien Behrendt, Benedikt Hauer, Jan Schütz, Cindy Close, Michael Scheckenbach, Giovanni Ferrari, Leoni Maeurer, Sophia Sebina, Viktorija Glembockyte, Tim Liedl, Philip Tinnefeld  
“Bringing Attomolar Detection to the Point-of-Care with Nanopatterned DNA Origami Nanoantennas”  
*bioRxiv* 2024.10.14.618183. [10.1101/2024.10.14.618183](https://doi.org/10.1101/2024.10.14.618183)
3. **Renukka Yaadav**, Kateryna Trofymchuk, Feng Gong, Xinghu Ji, Florian Steiner, Philip Tinnefeld, Zhike He  
“Broad-Band Fluorescence Enhancement of QDs Captured in the Hotspot of DNA Origami Nanonantennas”  
*The Journal of Physical Chemistry C* 2024. [10.1021/acs.jpcc.4c01797](https://doi.org/10.1021/acs.jpcc.4c01797)

OTHER PEER-REVIEWED PUBLICATIONS

1. Stefan Krause, Evelyn Ploetz, Johann Bohlen, Patrick Schüler, **Renukka Yaadav**, Florian Selbach, Florian Steiner, Izabela Kamińska, and Philip Tinnefeld  
“Graphene-on-Glass Preparation and Cleaning Methods Characterized by Single-Molecule DNA Origami Fluorescent Probes and Raman Spectroscopy”  
*ACS Nano* 2021, 15, 4, 6430–6438. [10.1021/acsnano.0c08383](https://doi.org/10.1021/acsnano.0c08383)

2. Izabela Kamińska, Johann Bohlen, **Renukka Yaadav**, Patrick Schüler, Mario Raab, Tim Schröder, Jonas Zähringer, Karolina Zielonka, Stefan Krause, Philip Tinnefeld  
 “Graphene Energy Transfer for Single-Molecule Biophysics, Biosensing, and Super-Resolution Microscopy”  
*Advanced Materials* 2021, 33, 2101099. [10.1002/adma.202101099](https://doi.org/10.1002/adma.202101099)
  
3. Alena Khmelinskaia, Henri G. Franquelim, **Renukka Yaadav**, Eugene P. Petrov, Petra Schwille  
 “Membrane-Mediated Self-Organization of Rod-Like DNA Origami on Supported Lipid Bilayers”  
*Advanced Materials Interfaces* 2021, 8, 2101094. [10.1002/admi.202101094](https://doi.org/10.1002/admi.202101094)
  
4. Julian Bauer, Fiona Cole, **Renukka Yaadav**, Jonas Zähringer, Tim Schröder, and Philip Tinnefeld "Ultra-specific detection of nucleic acids by intramolecular referencing"  
*Proc. SPIE 12849*, Single Molecule Spectroscopy and Superresolution Imaging XVII, 1284905 (12 March 2024). [10.1117/12.3010119](https://doi.org/10.1117/12.3010119)
  
5. Ece Büber, **Renukka Yaadav**, Tim Schröder, Henri G. Franquelim, Philip Tinnefeld  
 “DNA Origami Vesicle Sensors with Triggered Cargo Transfer”  
*Angew. Chem. Int. Ed.* 2024, e202408295. [10.1002/anie.202408295](https://doi.org/10.1002/anie.202408295)

## PRESENTATIONS

1. **Renukka Yaadav**, Cindy Mara Close, Viktorija Glembockyte, Kateryna Trofymchuk, Martina Pfeiffer, Lennart Grabenhorst, Florian Selbach, Birka Lalkens, Philip Tinnefeld. **Single-molecule diagnostics using self-assembled DNA nanoantennas**. March 2019, CeNS Retreat-Kleinwalsertal, Austria
  
2. **Renukka Yaadav**, Izabela Kaminska, Johann Bohlen, Sara Rocchetti, Florian Selbach, G. P. Acuna, Philip Tinnefeld. **DNA origami-based nanopositioners for distance dependent energy transfer to graphene**. July 2019, International Physics of Living Systems Network (iPoLS)- Munich, Germany

3. **Renukka Yaadav**, Johann Bohlen, Karolina Zielonka, Stefan Krause, Izabela Kamińska, Philip Tinnefeld. **Like to fluoresce? Don't get too close to graphene DNA origami nanopositioners for biosensing on graphene.** October 2020, 4<sup>th</sup> Functional DNA Nanotechnology Workshop- Rome, Italy
4. **Renukka Yaadav**, Izabela Kaminska, Karolina Zielonka, Philip Tinnefeld. **Introducing graphene-on-glass coverslips for single-molecule biosensing.** April 2021, 18<sup>th</sup> Annual Conference on FOUNDATIONS OF NANOSCIENCE - Held virtually. **Award:** *'Excellent poster presentation by a student'*
5. **Renukka Yaadav**, Kateryna Trofymchuk, Mihir Dass, Benedikt Hauer, Vivien Behrendt, Jan Schütz, Cindy Close, Viktorija Glembockyte, Leoni Mäurer, Tim Liedl, Albrecht Brandenburg, Philip Tinnefeld. **Towards a point of care system based on fluorescence signal enhancement.** May 2022, CeNS Retreat-Kleinwalsertal, Austria
6. **Renukka Yaadav**, Kateryna Trofymchuk, Mihir Dass, Benedikt Hauer, Vivien Behrendt, Jan Schütz, Cindy Close, Viktorija Glembockyte, Leoni Mäurer, Tim Liedl, Albrecht Brandenburg, Philip Tinnefeld. **A point of care system using fluorescence signal enhancement.** September 2022, 17<sup>th</sup> Conference on Methods and Applications in Fluorescence- Gothenburg, Sweden
7. **Renukka Yaadav**, Kateryna Trofymchuk, Mihir Dass, Vivien Behrendt, Benedikt Hauer, Jan Schuetz, Cindy Close, Viktorija Glembockyte, Tim Liedl, Albrecht Brandenburg and Philip Tinnefeld. **Bringing Attomolar Detection to the Point-of-care with DNA Origami Nanoantennas.** April 2023, 20th Annual Conference on FOUNDATIONS OF NANOSCIENCE- Utah, USA. **Award:** *'Best student talk'*
8. **Renukka Yaadav**, Kateryna Trofymchuk, Mihir Dass, Vivien Behrendt, Benedikt Hauer, Jan Schuetz, Cindy Close, Viktorija Glembockyte, Tim Liedl, Albrecht Brandenburg and Philip Tinnefeld. **DNA Origami Nanoantennas for digital attomolar nucleic acid detection.** March 2024, IGLD 2024 Leipzig, Germany- Presented virtually

## **ACKNOWLEDGEMENTS**

"Science and everyday life cannot and should not be separated."

-Rosalind Franklin

I've always been fond of the sound of the word 'scientist.' There's something about it that appealed to me and made me wonder if I could become one. My father, who holds a PhD in Botany and transitioned from a scientist to a businessman, often with rather alternate methods, managed to ignite my interest in science and research at a fairly young age. My dearest mother always encouraged me to be independent, firmly believing that pursuing a PhD would grant me that independence. Science felt familiar to me, and education was fundamental. My brother, as a good sibling does, made sure to keep me grounded while celebrating the smallest successes that came my way. Thank you, mummy, papa, and bhai. None of this would have been possible without you.

My time at the university in India, provided me with some of my most cherished lifelong friendships with Mihir, Isha, Aashish, and Emmanuel. I am deeply grateful for your love and support throughout this journey.

Moving to a new country to pursue a PhD is easier said than done. It was undoubtedly one of the most exciting yet extremely challenging feats to achieve. However, I was fortunate to have you around. Mihir, thank you for the unconditional support, the delicious food, love and laughter. Even when I didn't believe in myself, you did. Thank you for that.

I want to thank Philip, my PhD supervisor, for giving me this opportunity in the first place. I am thankful for the flexibility in choosing projects, for the motivational words, for the weird sense of humour, for trusting me with the project, for the honest criticism, and for reminding me that 'only the people who try make mistakes.'

Doing my PhD in an international setup allowed me to meet and connect with some of the most incredible people. The most special among them is Ece. What started as a bond over the struggle to adjust to an unknown country and work environment turned into a relationship that is closest to my heart. We travelled to different countries together, the most memorable trips being to Turkey and India. I couldn't believe you were coming to India with me until I saw you walk out of immigration at the Delhi airport. Ece's role in this journey has been that of a

friend, a sister, a therapist, and a guardian. Words don't do justice to my feelings for you. Thank you, my friend—Seni seviyorum!

Thank you, Lorena. With our endless conversations, passing time was never an issue around you. Your deep interest in my project helped me understand it more deeply. I learned so much from you. We were almost partners in a potential start-up -I bet not many people can say that!

Thank you, Michi. From office mates to buddies, you became a friend at a time when I did not know anyone. You are my favourite German. I love how passionate you get in conversations.

Thank you, Alan. I got to learn so much from you and thoroughly enjoyed both bullying you and being bullied by you. I am still waiting for you to say 'Tim' and 'Team' differently.

Thank you, Luciano. Nobody cheered harder than you for the smallest of achievements. You are a gem! And thank you, Giovanni, for your infectious laughter. It is pure fun to be around you. Thank you to both Lucho and Gio for making me a part of the Guardini household, the Friday dinners, the sofa and overcooked sessions.

Thank you, Julian. I will cherish the dark humour and your keen interest in solving scientific questions. Together with Lore and Gio, we form the perfect 'cone of ignorance'. I am eternally grateful to the 'cone' for the longest coffee breaks and the spontaneous Rasmalai visits.

Thank you, Cem for introducing me to your beautiful family, especially your mother. Thank you for making Ece happy which allowed her to make everyone around her happy.

Thank you, Luna, for getting me to try Hip-hop and Latin fusion classes. I can never forget how a simple question- 'how was your vacation?' -be turned into the funniest answer I ever heard. I am still laughing about it.

Thank you, Kateryna and Viktorija, for being my first teachers in the lab. Thank you, Izabela, for your support in the graphene projects. Thank you, Cindy for the conversations, yummy cakes and support. Thank you, Angelika, for the lab support and conversations about art, India, and life in general. Thank you, Tim, Bosong (you are too funny), Lennart, Jacob, Merve, Karina, Melanie and Priyanshi for great conversations.

Thank you, Andreas, Leoni, Dominik, and Sophia, for trusting me to supervise your internships and teaching me how to teach.

Thank you, Herr Ehrl for the support. Thank you, Uta and Kalys. Thank you, to all the past and present members of the Tinnefeld lab who spent time to share a conversation and maybe even a laugh.

I am thankful to my PhD defence committee for taking out the time to evaluate this thesis and mark the end of this beautiful journey. I especially want to thank Alena, under whose supervision I started my Munich scientific journey at the MPI Biochemistry in Martinsried, before I started the PhD. I am very happy that you were an evaluator for my PhD thesis.

I also want to thank, Sangya, Rishabh, Amma, Mama ji, Ginni Maasi, Hema di, Yashvi, Harsh, and Yuwan.

I want to acknowledge Kleinwalsertal retreat and the invaluable workshops, which provided a great opportunity to meet others and connect in a relaxed setting, all while exchanging the latest research. These events organized by the Centre for NanoScience (CeNS) were very helpful, and I extend a special thank you to Susanne Hennig for her planning and effort in making these gatherings enjoyable.



# TABLE OF CONTENTS

<b>PUBLICATIONS</b> .....	5
<b>PRESENTATIONS</b> .....	6
<b>ACKNOWLEDGEMENTS</b> .....	8
<b>LIST OF FIGURES</b> .....	13
<b>ACRONYMS</b> .....	14
<b>AIM AND OUTLINE</b> .....	15
<b>INTRODUCTION</b> .....	17
1.1 BIOSENSING THROUGH THE AGES .....	17
1.1.1 ELEMENTS OF A BIOSENSOR.....	21
1.2 NANOTECHNOLOGY .....	22
1.2.1 BUILDING AT THE NANOSCALE .....	23
1.2.2 SEEING AT THE NANOSCALE .....	23
1.3 SINGLE-MOLECULE DETECTION: THE ULTIMATE SENSITIVITY .....	26
1.3.1 SINGLE-MOLECULE IMAGING AT ULTRA-LOW CONCENTRATIONS .....	29
1.4 PLASMONIC NANOPARTICLES AS OPTICAL ANTENNAS.....	33
1.5 DNA ORIGAMI FOR CONTROLLED ASSEMBLY .....	35
<b>THEORETICAL CONCEPTS</b> .....	38
2.1 FLUORESCENCE .....	38
2.1.1 SINGLE MOLECULE FLUORESCENCE: HOW FAR HAVE WE COME? .....	38
2.1.2 FUNDAMENTALS OF FLUORESCENCE .....	41
2.2 PLASMONICS FOR FLUORESCENCE ENHANCEMENT .....	46
2.2.1 COUPLING BETWEEN TWO NANOSPHERES .....	47
2.2.2 FLUOROPHORE IN A PLASMONIC HOTSPOT .....	48
2.3 DNA.....	49
2.3.1 STRUCTURE OF DNA.....	50
2.3.2 CONSTRUCTING WITH DNA.....	52
2.4 MICROSCOPY SETUPS .....	56
2.4.1. CONFOCAL MICROSCOPY .....	56
2.4.2. TIRF MICROSCOPE .....	58
<b>INTRODUCING DNA ORIGAMI NANOANTENNAS</b> .....	61
3.1 A SHORT REVIEW .....	61
3.2 APPLICATION IN BIOSENSING .....	63
3.2.1 CAN WE USE A LOW-TECH DEVICE TO SEE SINGLE MOLECULES?.....	65
<b>BRINGING ATTOMOLAR DETECTION TO POC DIAGNOSTICS</b> .....	68
4.1 OVERVIEW .....	68
4.2 ASSOCIATED PUBLICATION. 1 .....	71
<b>QUANTUM DOTS: AN ALTERNATE EMITTER</b> .....	93

5.1 OVERVIEW.....	93
5.2 ASSOCIATED PUBLICATION. 2.....	96
<b>SUMMARY AND OUTLOOK .....</b>	<b>112</b>
<b>REFERENCES .....</b>	<b>115</b>
<b>APPENDIX .....</b>	<b>133</b>
7.1. SUPPORTING INFORMATION FOR P1.....	133
7.2. SUPPORTING INFORMATION FOR P2 .....	188

# LIST OF FIGURES

Figure 1	Detect and respond- examples and evolution	17
Figure 2	Illustrations showing Zika virus and coronavirus	18
Figure 3	Size of different objects at the nanoscale	21
Figure 4	Young neurons labelled for actin and microtubules	24
Figure 5	Role of signal-to-noise ratio in single-molecule detection	25
Figure 6	Commonly used fluorescence microscopy techniques	26
Figure 7	Concentration barrier	27
Figure 8	Enzyme-based amplification	28
Figure 9	PCR workflow	29
Figure 10	Plasmonic nanoparticles interact with light	30
Figure 11	Transmitting antenna and receiving antenna	30
Figure 12	Common morphologies of AuNPs	31
Figure 13	Examples of optical antennas fabricated using lithography-based methods	32
Figure 14	DNA origami technique	32
Figure 15	Examples of use of DNA origami for controlled assembly of nanoparticles	33
Figure 16	Evolution of single-molecule fluorescence methods	35
Figure 17	Jablonski diagram and Frank-Condon principle energy diagram	36
Figure 18	Fluorophores	37
Figure 19	Representation of fluorescence lifetime decay	39
Figure 20	Localized surface plasmon resonance	40
Figure 21	Plasmon hybridisation in a nanosphere-dimer system	42
Figure 22	Photo 51 and the first model of the double helical structure of DNA	44
Figure 23	Structure of DNA	45
Figure 24	Constructing with DNA	46
Figure 25	Twists, curvatures and multimeric DNA origami structures	48
Figure 26	Dynamic DNA origami structures	49
Figure 27	Schematic of confocal microscope	50
Figure 28	Working of TIRFM	52
Figure 29	3D DNA origami pillar capturing two AuNPs forming a dimer nanoantenna	53
Figure 30	Evolution of the 3D nanoantenna design in our lab	54
Figure 31	FQH assay	55
Figure 32	Schematic of an automated POC system based on DNA origami nanoantennas	57
Figure 33	NanoAntennas with Cleared HOtSpots	57
Figure 34	Sandwich binding assay incorporated in the hotspot of NACHOS	58

## ACRONYMS

DNA	deoxyribonucleic acid	CRISPR	clustered regularly interspaced short palindromic repeat
RNA	ribonucleic acid	TIRFM	total internal reflection fluorescence microscope
ssDNA	single stranded DNA	NACHOS	nanoantennas with cleared hotspots
dsDNA	double stranded DNA	LAMP	loop-mediated isothermal amplification
FOV	field of view	PALM	photo activated localization microscopy
POC	point of care	STORM	stochastic optical reconstruction microscopy
DON	DNA origami nanoantenna	ATP	adenosine triphosphate
2D	two-dimensional	GFP	green fluorescent protein
3D	three-dimensional	sm	single molecule
bp	base pair	STED	stimulated-emission depletion
nt	nucleotide	FPALM	fluorescence photoactivated localization microscopy
NP	nanoparticle	RESOLFT	reversible saturable optical fluorescence transitions
NS	nanosphere	PAINT	points accumulation for imaging in nanoscale topography RESI resolution Enhancement by sequential Imaging
TEM	transmission electron microscope	NADH	nicotinamide adenine dinucleotide
AFM	atomic force microscope	FRET	förster resonance energy transfer
SEM	scanning electron microscope	RET	resonance energy transfer
Au	gold	TCSPC	time-correlated single-photon counting
Ag	silver	PMT	photomultiplier tube
LSPR	localized surface plasmon resonance	IRF	instrument response function
FQH	fluorescence quenching hairpin	LDOS	local density of optical states
DOP	DNA origami placement	NA	numerical aperture
PS	polystyrene	LED	light emitting diode
nm	nanometre	BBQ	blackberry quencher
STM	scanning tunnelling microscope	FE	fluorescence enhancement
CVD	chemical vapor deposition	NIR	near-infrared
CGM	continuous glucose monitoring	zL	zeptoliter
SNR	signal-to-noise ratio	NR	nanorod
ZMW	zero-mode waveguides		
fL	femtolitre		
QD	quantum Dot		
PCR	polymerase chain reaction		
LFA	lateral flow assays		
DAN	DNA assembles nanoantenna		

## AIM AND OUTLINE

Advancements in biosensing technologies are critical for addressing modern health challenges, such as increasing antimicrobial resistance and the need for early detection of cancer biomarkers<sup>1,2</sup>. The ability to detect ultra-low concentrations of biomarkers quickly and accurately can significantly improve patient outcomes by enabling timely diagnosis and treatment. However, current diagnostic methods often face limitations in sensitivity, speed, affordability, and portability, hindering their effectiveness in point-of-care (POC) settings. This thesis strives to bridge this research gap by developing innovative solutions that enhance biosensing capabilities in accessible formats.

**The aim of this thesis is to develop a highly sensitive, POC-compatible biosensing platform capable of detecting target DNA without the need for molecular amplification, leveraging single-molecule detection enabled by DNA origami-based NanoAntennas.**

Sensitive detection methods, such as single-molecule fluorescence techniques, are crucial in biological applications to understand heterogeneity within samples that is often masked in ensemble measurements<sup>3</sup>. However, single-molecule detection mostly requires sophisticated equipment, limiting its accessibility and applicability outside specialized laboratory settings. Simplifying these methods is essential to unlock the full potential of single-molecule detection for biosensing applications, especially in resource-limited settings. This thesis addresses the following questions:

- Can we detect single molecules with a low-tech device?
- If so, how can we apply this capability to practical biosensing applications?

This thesis is structured as follows:

**Chapter 1** introduces the concept of biosensing and the need for high-sensitivity biosensors in current healthcare scenarios. It delves into nanotechnology and its role in advancing biosensor technology. It discusses fluorescence microscopy and single-molecule detection, highlighting the challenges involved in single molecule detection, especially at low-concentrations. It explores the role of plasmonic nanoparticles as optical antennas and DNA origami to precisely position plasmonic nanoparticles. **Chapter 2** covers theoretical concepts associated with this

thesis and the microscopy methods used. **Chapter 3** introduces DNA origami nanoantennas covering their design evolution, application in diagnostics and how they enable single-molecule detection on a low-tech device. **Chapter 4** covers the development of a POC-compatible single-molecule diagnostic platform capable of detecting attomolar concentrations in untreated human blood plasma. **Chapter 5** explores QDs as an alternative emitter to traditional fluorophores and studies broadband enhancement of three different sizes of QDs enabled by DNA origami nanoantennas. **Chapter 6** concludes the key findings, discusses limitations, and suggests future research directions to further enhance the biosensing platform. Throughout this thesis, the pronoun "we" reflects the collaborative nature of the projects and the PhD. **Chapter 7** includes the supporting information for chapter 4 and 5, discussing experimental protocols in detail.

## INTRODUCTION

### 1.1 BIOSENSING THROUGH THE AGES

Life is characterized by its capacity for homeostasis<sup>A</sup>, organization, metabolism, growth, adaptation, reproduction, and, importantly, the **ability to sense and respond to changes in the environment**<sup>1</sup>.

Unicellular organisms developed the capability to sense chemical gradients, a process known as chemotaxis (Figure 1). This basic sensing enabled early life forms to navigate their aqueous environments, seeking nutrients and avoiding hazards. As epochs passed, life evolved into more complex forms, with the emergence of multicellular organisms.

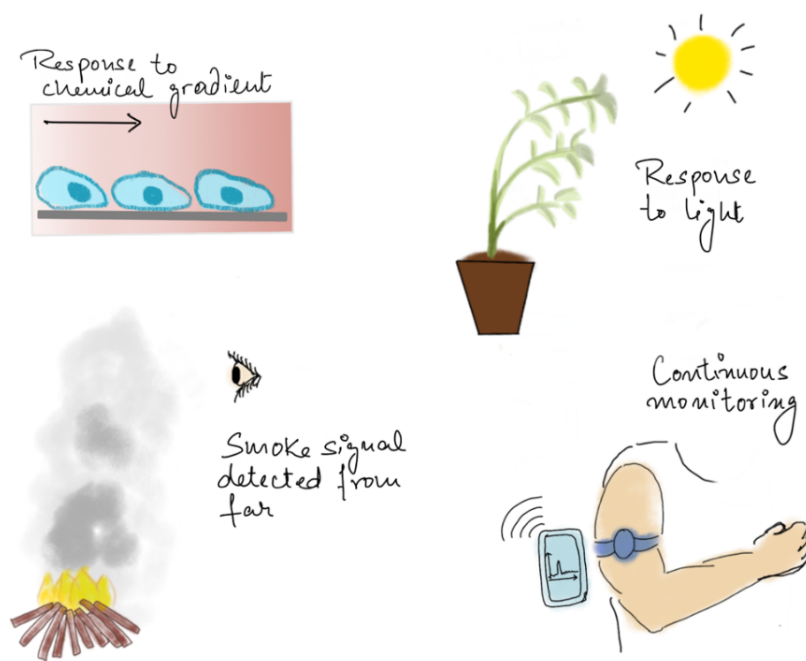


Figure 1. Examples showing 'detect and respond' as an inherent part of life and its evolution starting from chemotaxis in unicellular organisms on the top left, phototropism by plants, use of smoke signal as a warning sign by early humans, to continuous blood glucose monitoring in the present.

<sup>A</sup> *Homeostasis* is the process organisms use to maintain stable internal conditions, such as temperature and pH balance, despite external changes.

These developed elaborate systems, including endocrine and nervous systems, enabling organisms to maintain homeostasis and interact with their surroundings in increasingly nuanced ways. For example, plants demonstrate similar abilities by adjusting their growth towards light (phototropism) (Figure 1) and closing their leaves in response to touch (thigmotropism). Early humans employed the same fundamental principles of biosensing to master their environment. The creation of early warning systems, like smoke signals (Figure 1), marked the beginning of human ingenuity in augmenting natural biosensing abilities—such as sight and smell—with technology, setting the stage for a future where detection and interpretation of signals would become central to humanity's progress.

In the modern age, the need to monitor physiological conditions has driven the development of biosensors. Chronic diseases, such as diabetes, have necessitated continuous monitoring of biological parameters to manage health effectively. The enzyme electrode<sup>12</sup>, developed in the mid-20th century for glucose monitoring, exemplifies this shift towards medical biosensing. And the recent COVID-19 pandemic highlights the importance of monitoring infectious diseases, as globalization has accelerated the spread of pathogens.

Biosensors today must combine sensitivity, selectivity, speed, affordability, portability, and ease of use. This interdisciplinary effort requires biologists, chemists, physicists, and engineers to work together. An example of progress in the field of biosensing is the development of wearable continuous glucose monitoring (CGM) devices (Figure 1) that connect to smartphones, providing real-time glucose data and personalized diabetes management. Thus, as we confront new health challenges in the modern era, the field of biosensing continues to evolve, necessitating advancements in sensitivity and technology to meet these demands.

### **1.1.1 MODERN BIOSENSING AND THE NEED FOR HIGH SENSITIVITY**

As humanity advances, public health challenges have evolved in complexity and scale, necessitating the development of more sophisticated biosensing technologies. Emerging infectious diseases, such as those caused by the Zika virus (Figure 2) and COVID-19 pandemic (Coronavirus, Figure 2), have highlighted the critical need for rapid and sensitive detection methods to prevent widespread transmission<sup>13,14</sup>. Antimicrobial resistance (AMR) has become a global threat, with an increasing number of infections becoming difficult or impossible to treat due to resistant pathogens<sup>2</sup>. In cases of sepsis, a life-threatening response to infection, every hour of delay in appropriate treatment increases mortality rates significantly<sup>15</sup>. Early and accurate detection is thus paramount. In another example of cancer diagnosis, detecting biomarkers at ultra-low concentrations can improve patient outcomes<sup>1</sup>. For example,



circulating tumor DNA (ctDNA) and microRNAs are present at very low levels in the blood, especially in early-stage cancers. Sensitive detection of these biomarkers can facilitate early diagnosis, monitoring of treatment efficacy, and detection of relapse.



Figure 2. Paintings depicting the complex nature of biological processes. On the left is the cross section of Zika virus. The viruses (in red) are shown interacting with receptors on the cell surface (green) and are surrounded by blood plasma molecules at the top. The painting on the right shows a coronavirus entering the lungs, surrounded by mucus secreted by respiratory cells, secreted antibodies, and several small immune systems proteins. Illustrations by David S. Goodsell, RCSB Protein Data Bank<sup>16,17</sup>. Licensed under CC-BY-4.0.

### **Conventional and emerging diagnostic methods**

Conventional diagnostic methods typically involve culturing bacteria—a process that can take several days to produce results. Additionally, serological tests used to detect antibodies or antigens may not be effective in the early stages of infection and can cross-react with other pathogens, resulting in false positives or negatives. A typical workflow for molecular methods used for diagnosing antibiotic resistance would involve starting with a bacterial culture to grow any bacteria present in the bodily fluids, from which a bacterial colony is isolated. The isolated colony undergoes DNA extraction, where genetic material is harvested from the bacteria. The extracted DNA is then subjected to Polymerase Chain Reaction (PCR)<sup>8</sup>, where specific segments of DNA, especially those associated with antibiotic resistance genes, are

---

<sup>8</sup> The *polymerase chain reaction* is a method used to amplify a specific nucleic acid sequence to generate more copies, making it easier to detect the amplified product.

selectively amplified and analysed, before obtaining final results. The time taken from sample collection to final results can span several days, during which effective treatment may be delayed. Due to the delay in obtaining precise diagnostics, physicians often resort to using broad-spectrum antibiotics as an initial treatment<sup>18,19</sup>. Empirical use of broad-spectrum antibiotics contributes to the larger global issue of antibiotic resistance<sup>20</sup>.

In recent years, innovative diagnostic technologies have emerged, aiming to enhance sensitivity and speed in detecting low-abundance biomarkers. Recent developments based on PCR like droplet-digital PCR (ddPCR) partition a DNA sample into thousands of small droplets, each acting as an individual PCR reaction chamber. Droplets containing the target DNA emit fluorescence, allowing counting of positive droplets and achieving high sensitivities. However, ddPCR suffers from limitations such as a time-consuming and cumbersome workflow, need for trained personnel, and higher costs.

CRISPR<sup>C</sup>-based diagnostics, such as SHERLOCK (Specific High-sensitivity Enzymatic Reporter unLOCKing)<sup>21</sup> and DETECTR (DNA Endonuclease Targeted CRISPR Trans Reporter)<sup>22</sup>, leverage the precise targeting ability of the CRISPR-Cas system to detect specific genetic sequences. These methods involve designing a guide RNA (gRNA) that directs the Cas enzyme to the target DNA or RNA sequence. Upon binding, the Cas enzyme's collateral cleavage activity is activated, cutting nearby reporter molecules and generating a detectable signal. While CRISPR-based diagnostics offer high specificity and the potential for rapid, point-of-care testing, they often require pre-amplification steps such as Recombinase Polymerase Amplification (RPA) or Loop-mediated Isothermal Amplification (LAMP) to reach attomolar sensitivity<sup>23</sup>. This adds complexity, increases the risk of contamination, and necessitates precise temperature control.

Nanopore sequencing technologies, provide another cutting-edge approach. They allow for direct, real-time sequencing of nucleic acids by measuring changes in ionic current as single DNA or RNA molecules pass through a nanopore<sup>24</sup>. Nanopore devices are portable and capable of sequencing long reads, making them valuable for rapid pathogen identification and genomic surveillance. However, limitations include relatively high error rates compared to other sequencing methods, the need for high concentrations of purified nucleic acids, and the requirement for specialized equipment and trained personnel. Additionally, the cost per sample can be prohibitive for widespread clinical adoption.

---

<sup>C</sup> *CRISPR*-clustered regularly interspaced short palindromic repeats

Despite these advancements, significant challenges remain. Many of these state-of-the-art diagnostics face issues such as the need for complex sample preparation, reliance on amplification steps that can introduce errors or contamination, dependency on sophisticated instrumentation, and limitations in detecting small, structurally diverse targets like microRNAs<sup>25,26</sup>. Moreover, detecting ultra-short nucleic acids or proteins at attomolar concentrations without amplification remains a formidable task. Therefore, there is a pressing need to explore alternative biosensing approaches that can overcome these limitations. Ideal solutions would combine ultra-high sensitivity without the need for amplification, simplicity of use, rapid response times, and affordability.

### **1.1.2 ELEMENTS OF A BIOSENSOR**

To bridge this research gap, we must first understand what a biosensor is and what makes up an ideal biosensor. A *biosensor* refers to an analytical device or system integrating biological elements with a transducer to detect and measure specific biological analytes or processes. An effective biosensor comprises several key components. The first is the biorecognition element, such as enzymes, antibodies, nucleic acids, or aptamers, which specifically interacts with the target analyte. This component provides the necessary selectivity by ensuring that only the intended molecule induces a response, reducing false positives and enhancing the reliability of the biosensor. The second component is the transducer, which converts the biorecognition event into a measurable signal, often electrical, optical, or electrochemical. The efficiency of this conversion directly affects the sensitivity and accuracy of the biosensor, as it translates the physical or chemical changes resulting from the analyte interaction into quantifiable data. Another crucial aspect is the signal amplification mechanism, which enhances the detectable signal without compromising specificity, especially when the intrinsic signal is weak. Additionally, a biosensor includes a data processing system, comprising hardware and software that process the transduced signal and present the results in a user-friendly format. This system enables real-time analysis and easy interpretation, which is important for point-of-care applications where rapid decision-making is necessary.

Understanding these components highlights the complexity and interdisciplinary nature of designing biosensors capable of meeting modern diagnostic demands. In this regard, nanotechnology has been playing a transformative role in enhancing the capabilities of biosensors. Nanotechnology enables us to access and manipulate the very scale at which biological interactions occur. By employing nanotechnology, we can design and fabricate

nanomaterials with unique optical, electrical, and mechanical properties that enhance biosensor functionality. For example, nanostructured surfaces can increase the surface area for biorecognition events, improving the probability of target-analyte interactions. Furthermore, nanotechnology facilitates the miniaturization of biosensor components, leading to portable and implantable devices suitable for point-of-care and real-time monitoring applications<sup>27</sup>.

## 1.2 NANOTECHNOLOGY

You might have heard the term 'nanotechnology' mentioned in popular films like *'Terminator'*, where machines reconstruct themselves at a microscopic level, harnessing the power of small, individual components. Much like science fiction in movies, nanotechnology in the real world focuses on the smallest units of matter- atoms and molecules -that assemble everything we know, from a single cell to the entire human body. Now, to diagnose or rectify an issue within the human body, one must start at the cellular level, understanding how cells combine to form tissues, organs, and ultimately, organ systems. This principle of starting at the fundamental level to understand complex systems is mirrored in the fields of manufacturing and engineering. The scale of these fundamental units, with atoms ranging from 0.1 to 0.5 nanometres (nm) and biological molecules like deoxyribonucleic acid (DNA) measuring a diameter around 2 nm (Figure 3), falls well below the threshold of human visibility (0.1 mm), necessitating a method to bridge this observational gap. This is where *nanotechnology* comes into play, serving as an interdisciplinary science that empowers us to access, manipulate, and innovate within the 1 to 100 nm range.

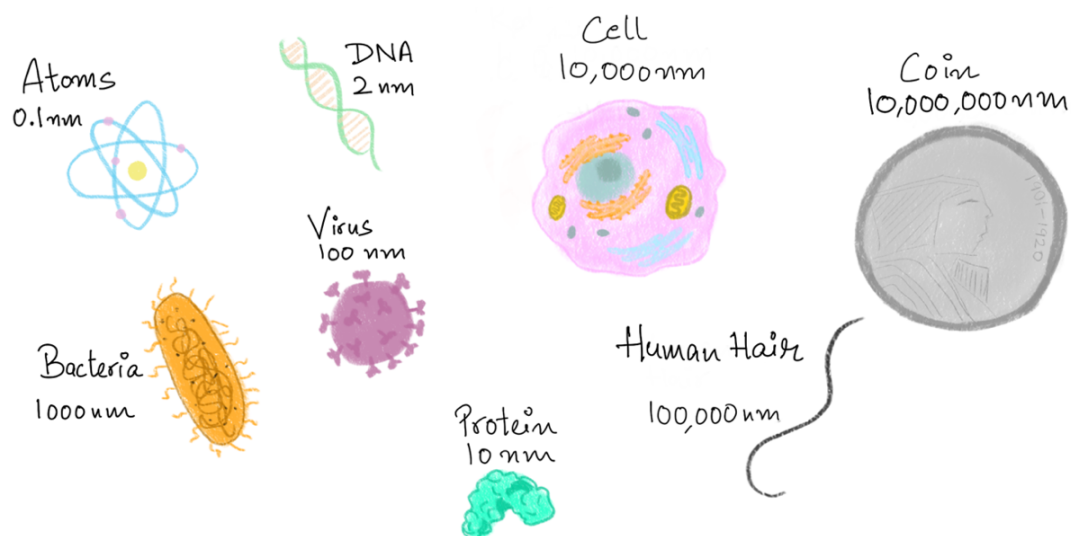


Figure 3. The size of different objects in nm. Objects not to scale.

## 1.2.1 BUILDING AT THE NANOSCALE

And now we arise at the main question; how do we manipulate atoms or molecules at the nanoscale? The answer to this challenge includes two strategies, namely top-down and bottom-up, aka the yin and yang of nanotechnology. The **top-down** approach starts at the macro scale, sculpting down bulk materials to nanoscale dimensions, similar to chiselling a marble block into a sculpture. Techniques like lithography<sup>D</sup> etch nano-sized features on silicon chips, creating nanostructures from larger materials. Despite its directness, this method can lead to imperfections and material waste, yet its precision makes it essential in fields like microelectronics manufacturing. In contrast, the **bottom-up** approach mirrors nature's assembly of complex structures from individual atoms and molecules, similar to seeds growing into trees. Techniques like chemical vapour deposition<sup>E</sup> and molecular self-assembly facilitate this process, allowing for the creation of innovative materials and devices, from nanoparticles for targeted drug delivery to advanced materials for electronics.

## 1.2.2 SEEING AT THE NANOSCALE

So, now we know how to build at the nanoscale, the next question is how do we see what we build, or how do we characterize the behaviour of our construct? In addressing this question, the field of nanotechnology truly gained momentum in 1981 with the invention of scanning tunnelling microscope (STM) by Gerd Binnig and Heinrich Rohrer. They went on to receive the Nobel Prize in Physics in 1986<sup>28</sup>. STM is a microscope that allows us to see and manipulate atoms by scanning the sample with a sharp conducting tip, capable of distinguishing features smaller than 0.1 nm. That same year, Atomic Force Microscope (AFM) was also invented, which similarly to STM, scans the sample surface with nm resolution. Although these are very powerful tools to study nanomaterials, they come with certain limitations. STM can only be used to image conducting materials, and requires special treatment for non-conductive samples. Both STM and AFM are surface-scanning methods meaning they provide only topological information. Both techniques require significant time for sample preparation and expertise to get high resolution data. Another family of

---

<sup>D</sup> In semiconductor manufacturing, *lithography* refers to a technique used to create intricate patterns on silicon wafers, which are then developed into electronic circuits. It involves coating the wafer with a light-sensitive material, exposing it to a pattern of light, and then etching away the exposed or unexposed regions to create the desired pattern.

<sup>E</sup> *Chemical Vapour Deposition (CVD)* is a process that deposits thin solid material layers on a substrate through a chemical reaction of gas-phase precursors.

microscopes include Scanning Electron Microscope (SEM) which uses an electron beam to scan across the sample and requires a conductive coating, and Transmission Electron Microscope (TEM) that can achieve atomic-scale resolution but requires thin, electron-transparent samples. Most of these either don't allow inspection of real-time processes and interactions, or fail to be completely non-invasive. As an alternative, we can look at the most traditional member of the microscopy family- an optical microscope.

Optical microscopes, based on the use of visible light and a system of lenses to magnify small objects, were the earliest man-made microscopes and have been around for more than 400 years. However, optical microscopes are limited to resolutions of ~200 nm laterally and ~500 nm axially, due to the diffraction limit of light<sup>F</sup>, as described by Ernst Abbe in 1873<sup>29</sup>. So we cannot employ them for direct visualization of nanostructures. Although, if we label a part of the nanostructure with a fluorescent molecule (or a fluorophore) which emits light under special conditions, and track this light (called fluorescence), we access another branch of optical microscopy called *Fluorescence microscopy*. In the next sections, we will explore how this technique has expanded our visual capacity to observe biological phenomena previously beyond the realm of imagination.

### **1.2.2.1 FLUORESCENCE MICROSCOPY**

Fluorescence, the emission of light within nanoseconds after absorbing light of a shorter wavelength, is particularly prized for its sensitivity<sup>30</sup>. This is because the emitted light is detected against a dark background, unlike absorbance measurements, which can be influenced by the intensity of the light source and other absorbing species in the path of light. Also, each fluorophore that gets excited gives thousands to millions of photons before photobleaching<sup>G</sup>, resulting in an intrinsically amplified signal<sup>31</sup>. Fluorescence is thus widely utilized in the life sciences as a non-destructive method for tracking and analysing biological molecules (See Figure 4). The technique relies on detecting fluorescent emissions at specific frequencies that are distinct from the excitation light, minimizing background interference since only a few cellular components exhibit natural fluorescence (known as intrinsic or autofluorescence). Proteins or other biological components can be labelled with extrinsic

---

<sup>F</sup> The *diffraction limit of light* is the minimum distance between two points at which they can still be distinguished as separate entities in an image. It's typically about half the wavelength of the light used, setting a lateral resolution limit for conventional optical microscopes to around 200 nm.

<sup>G</sup> *Photobleaching* is the irreversible destruction of a fluorophore, rendering it incapable of fluorescence

fluorophores, which are fluorescent dyes that may be small molecules, proteins, or quantum dots<sup>32</sup>.

One of the earlier examples of the use of fluorescence was documented in 1845, when Sir John Fredrich William Herschel observed the blue emission of quinine (a common fluorophore) in tonic water under ultraviolet light from the sun<sup>33</sup>. Another remarkable example occurred in 1877 when fluorescein was added to the river Danube; its characteristic green fluorescence was detected sixty hours later in the river Rhine, confirming an underground connection between the two rivers<sup>34</sup>.

But fluorescence does more than just provide visual cues; it offers deep insights into the molecular environment. The intensity of fluorescence can increase (enhancement) or decrease (quenching) based on the surrounding conditions. Some fluorophores are non-fluorescent in solution but become fluorescent upon binding to a biomolecule. Conversely, small molecules or ions like iodide, oxygen, and acrylamide can quench fluorescence, revealing probe locations on macromolecules or the porosity of proteins and membranes<sup>32</sup>. Furthermore, it can be used to measure fluctuations in intensity, indicating how freely molecules diffuse, which can signal the formation of larger complexes. We can study protein association or folding by measuring energy transfer between a donor and an acceptor fluorophore within 2-10 nm distances, where changes in acceptor fluorescence reflect the distance between the two fluorophores.



Figure 4. Young neurons labelled for actin (orange) and microtubules (cyan). Image captured by Christophe Leterrier, [NeuroCyto](#) INP, CNRS-AMU, Marseille. An example of using fluorescence to target different regions of neurons to dive deeper into their structural components.



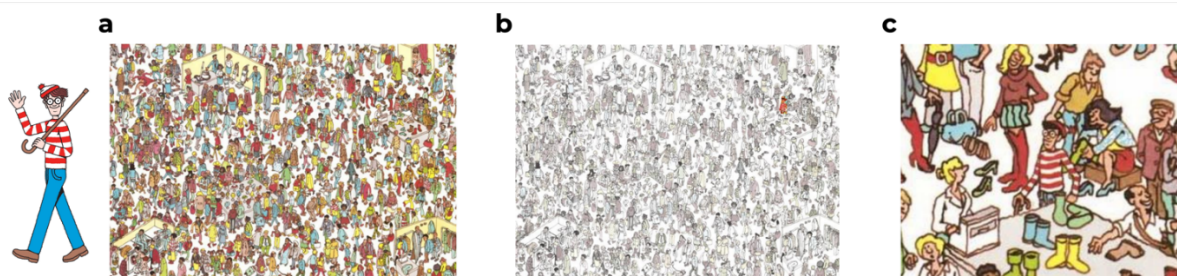
While these techniques provide valuable information, they often represent averaged behaviour, known as ensemble<sup>H</sup> measurements. Imagine looking at a jar filled with Lego pieces—you see many pieces in different colours, which is an ensemble measurement. However, if you take the pieces out and examine them individually, you notice specific sizes, patterns, and dominant colours or shapes. This is an example of single- “molecule” detection.

### 1.3 SINGLE-MOLECULE DETECTION: THE ULTIMATE SENSITIVITY

*“As analytical chemists, the highest resolution measurement one can make is at the single molecule level; it just does not get any better than that.”*

David R. Walt<sup>31</sup>

At the single molecule level, one can directly count individual molecules within a given volume, providing the most accurate measurement of concentration possible<sup>31</sup>. However, to detect a single molecule is like looking for a needle in a haystack, making it crucial to detect the emission from a single molecule above the signal from the background. Consider the ‘Where’s Waldo?’ children’s puzzle illustrated by Martin Handford as an analogy. In a busy scene, Waldo (representing the single molecule) is challenging to spot due to the multitude of surrounding characters (the background), illustrating the issue of a low signal-to-noise ratio (SNR) (Figure 5a). However, if Waldo is made to stand out against the background, he becomes quickly identifiable (Figure 5b). Similarly, enhancing the brightness and photostability of fluorophores increases the SNR, aiding single-molecule detection. Additionally, just as zooming into Waldo’s location can make finding him easier (Figure 5c), reducing the observation volume in molecular detection significantly enhances our ability to identify single molecules.



<sup>H</sup> *Ensemble* refers to a collection or group of entities, such as particles, systems, or events, considered together for analysis.



Figure 5. The puzzle Where's Waldo as an example for understanding the role of signal-to-noise ratio in single-molecule detection. This example was introduced to me by Lennart Grabenhorst and Viktorija Glembockyte. Image of Waldo on the left, **a** crowded image where it is difficult to spot Waldo, **b** Waldo shown in colour against a black and white background **c** zoomed-in image where it is easier to spot Waldo.

Despite the sensitivity offered by single-molecule imaging, several challenges hinder its practical application in biosensing, especially when dealing with low concentrations of analytes:

**I. BACKGROUND FLUORESCENCE.** Background noise comes from scattering (Raman and Rayleigh) and from fluorescence due to impurities in solvents, glass coverslips, etc. To effectively detect single molecules, one needs to: (1) minimise background fluorescence and (2) maximize the signal brightness from a single-molecule.

To optimize signal-to-noise ratio (SNR) and photon collection in single-molecule imaging, various optical setups are employed, primarily using inverted microscopes with widefield or confocal configurations (Figure 6). Epifluorescence microscopy uses a focused beam to excite the sample and collects fluorescence with cameras, but it suffers from significant background noise due to out-of-focus light from the large excitation volume. Total Internal Reflection Fluorescence Microscopy (TIRFM) addresses this issue by directing the excitation beam at an angle to create an evanescent field at the glass-water interface, exciting only a thin layer (~100 nm) of the sample, thereby reducing background noise and improving SNR. However, TIRFM requires samples to be close to or on the glass surface. Confocal microscopy further enhances SNR by focusing the excitation light to a very small volume (~1 fL) and using a pinhole to block out-of-focus light, providing lower background and higher SNR than TIRFM, though it requires scanning the beam across the sample, preventing simultaneous imaging of multiple areas. Both TIRFM and confocal microscopy rely on high-quality optical components and sensitive detectors, such as filters and mirrors with optimal transmittance, high numerical aperture objectives, and detectors with low noise and high efficiency, to maximize fluorescence collection and minimize noise in single-molecule experiments<sup>35</sup>.

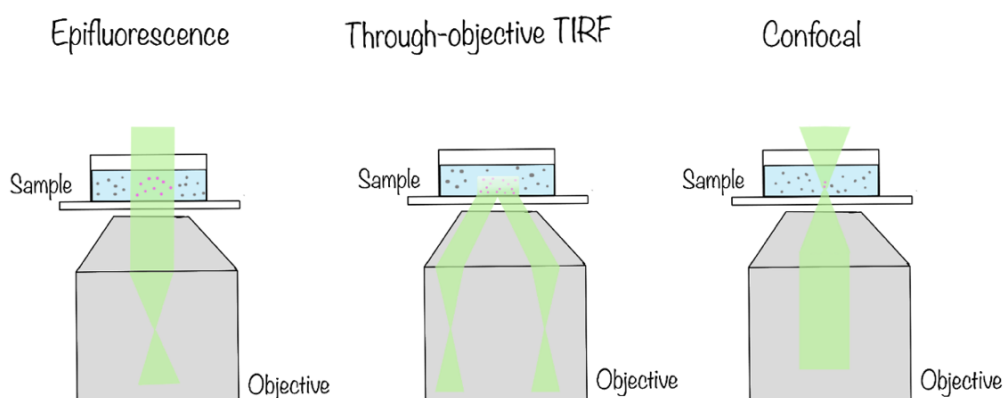


Figure 6. Schematic comparing the excitation volume for three commonly used fluorescence microscopy techniques—Epifluorescence, Objective-based TIRF and Confocal microscopy. Pink spots represent the excited molecules whereas the grey spots represent non-excited molecules.

**II. CONCENTRATION BARRIER.** Single-molecule detection methods face challenges with biological samples due to their narrow dynamic concentration range (Figure 7). Detecting a single molecule ideally requires only one fluorescent molecule in the diffraction-limited observation volume (about 1 fL), corresponding to an optimal concentration of around 2 nM. In biological settings, where concentrations often range from micromolar to millimolar, multiple molecules occupy the observation volume, masking individual molecule behaviour and complicating dynamic process detection. Protein-protein and DNA-protein interactions occur at micromolar concentrations, exceed this optimal range and preventing accurate monitoring due to multiple molecule overlap<sup>36</sup>.

Moreover, at extremely low concentrations—necessary for detecting rare disease biomarkers—the probability of target molecules being present in the observation volume becomes negligible. For example, at 1 aM, there are only ~60 molecules in a sample volume of 100  $\mu$ l. Detecting such rare targets requires methods that can process large volumes to capture sufficient molecules for analysis. This situation is common when attempting to detect low-abundance biomarkers for early disease diagnosis or environmental contaminants at trace levels.

This concentration limit creates both chemical and temporal barriers. High-affinity interactions stable at higher concentrations rarely form at such low concentrations, hindering significant biological event detection<sup>36</sup>. Additionally, the time required to observe a single molecule increases dramatically, making real-time detection impractical.

To address the upper concentration limit, techniques like Zero-mode waveguides (ZMWs)<sup>1</sup> have been employed to create locally defined sub-wavelength volumes<sup>36</sup>. ZMWs confine light to an extremely small volume at the waveguide's bottom, allowing single-molecule detection even in high-concentration backgrounds. Eid et al.<sup>37</sup> demonstrated this by immobilizing DNA polymerase bound to a DNA template in ZMWs and tracking its activity at the single-molecule level with micromolar concentrations of fluorescently labelled nucleotides (Figure 7).

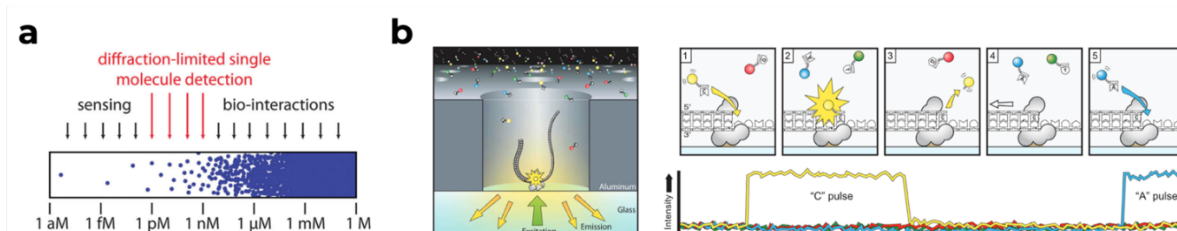


Figure 7. **a** Single-molecule experiments are effective between picomolar and low nanomolar concentrations. Below picomolar levels, molecule detection becomes time-consuming. At concentrations above micromolar, diffraction-limited optics cannot observe individual molecules, complicating studies of protein interactions and enzymatic activities. Reproduced with permission by Royal Society of Chemistry<sup>36</sup>. **b** A single DNA with a DNA polymerase is fixed inside a ZMW and illuminated from beneath<sup>37</sup>. (1) A nucleotide binds the polymerase's active site, (2) increasing fluorescence in the specific colour channel, (3) followed by phosphodiester bond formation which releases a dye-linked product that exits the ZMW, ending the fluorescence pulse. (4) The polymerase moves to the next site, and (5) a new nucleotide binds, initiating another pulse. From [Eid, J. et. al. Science 323, 133-138 (2009)<sup>37</sup>]/Reprinted with permission from AAAS.

### 1.3.1 SINGLE-MOLECULE IMAGING AT ULTRA-LOW CONCENTRATIONS

Detecting or counting molecules at low concentrations may involve solutions such as reducing detection time by enhancing diffusion speed, parallelizing detection, concentrating molecules before measurement, or using signal amplification mechanisms<sup>36</sup>. The idea is to maximise the probability of interaction between the biorecognition unit and the analyte by increasing the effective local concentration of the analyte and then amplifying the signal generated by that interaction for a more effective detection.

<sup>1</sup>Zero-mode waveguides (ZMWs) are nanoscale optical structures that enable the observation of biochemical reactions at the single-molecule level with high temporal resolution. These small cylindrical holes are etched into a metal film and are small enough that they don't support propagating light modes at the wavelengths used for illumination.

**SIGNAL AMPLIFICATION. Choosing the right fluorophore:** Ideally, a fluorophore with high quantum yield, high extinction coefficient, high photostability and low fluorescence lifetime would provide the most optimal scenario for maximizing the fluorescence signal. A high quantum yield<sup>J</sup> ensures more absorbed light is converted to fluorescence, enhancing signal brightness. A higher extinction coefficient<sup>K</sup> allows more light absorption, and when combined with high quantum yield, results in stronger fluorescence emission. High photostability<sup>L</sup> is essential for long-term imaging and for experiments requiring repeated excitation and emission cycles. A low fluorescence lifetime<sup>M</sup> implies rapid emission of light after excitation, which can potentially enhance the photostability.

**Multi-fluorophore labelling:** The second obvious solution could be to label a single molecule with many fluorophores to amplify the signal. However, this may not be practical in every case<sup>38</sup> as- steric hindrance introduced by multiple fluorophores can block interaction sites or alter the molecule's conformation; when fluorophores are too close to each other, they can undergo self-quenching; multiple fluorophores can complicate the quantification of molecular interactions and concentrations; and synthesizing and conjugating multiple fluorophores to a target molecule can increase the complexity and cost of experiment preparation<sup>39</sup>.

**Enzyme-based amplification:** An alternate method uses enzymes like  $\beta$ -galactosidase to amplify the signal, that convert non-fluorescent substrates into hundreds of highly fluorescent resorufin molecules per second<sup>31,40</sup>. In the Simoa<sup>41</sup> platform (single-molecule arrays) by the Walt group (Figure 8), magnetic beads coated with a capture antibody are mixed into a sample where they outnumber the target analytes. These beads are then isolated magnetically and treated with a biotinylated antibody and a streptavidin- $\beta$ -galactosidase conjugate (Figure 8a). Most beads remain unlabelled, with only a few capturing an enzyme molecule. The beads are placed into a femtoliter array, introduced to a fluorogenic substrate, and sealed with a gasket or oil (Figure 8b). Fluorescence builds up exclusively in wells with a bead that has captured an

---

<sup>J</sup> *Quantum yield* ( $\phi$ ) is the measure of the efficiency with which absorbed light is converted into emitted light.

<sup>K</sup> The *extinction coefficient* ( $\epsilon$ ) represents the ability of a fluorophore to absorb light at a specific wavelength.

<sup>L</sup> *Photostability* refers to the resistance of a fluorophore to photobleaching, which is the permanent loss of fluorescence due to the breakdown of the fluorophore when it is exposed to light.

<sup>M</sup> *Fluorescence lifetime* ( $\tau$ ) is the average time a fluorophore remains in its excited state before returning to the ground state by emitting a photon.

analyte, allowing for digital quantification of the analyte based on the count of fluorescent wells (Figure 8c, d).

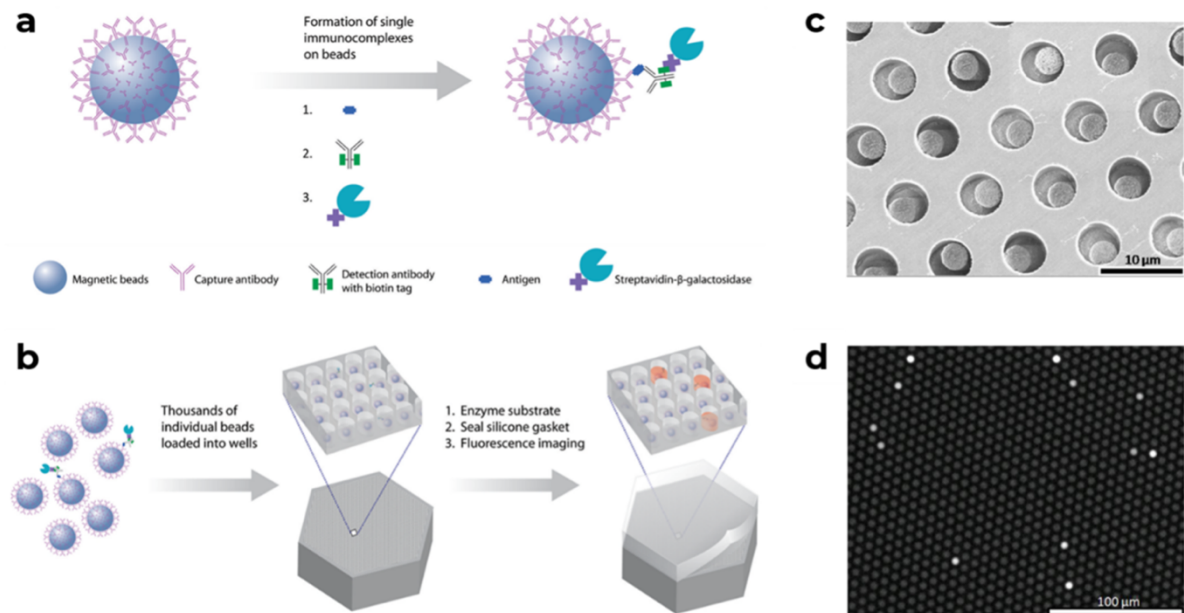


Figure 8. **a** Capturing and labelling single protein molecules on beads with standard ELISA reagents. **b** Loading beads into femtoliter well arrays to isolate and detect single molecules. **c** An SEM image shows a section of the array post-loading. **d** A fluorescence image of the array reveals signal from single enzymes. Reproduced from Rissin, D. M. et. al. *Nat Biotechnol* 28, 595-599 (2010) with permission from Springer Nature<sup>41</sup>.

**PCR:** Another interesting approach is to replicate the molecule of interest multiple times to amplify the fluorescence signal. This is the basis of PCR based nucleic acid detection (Figure 9).

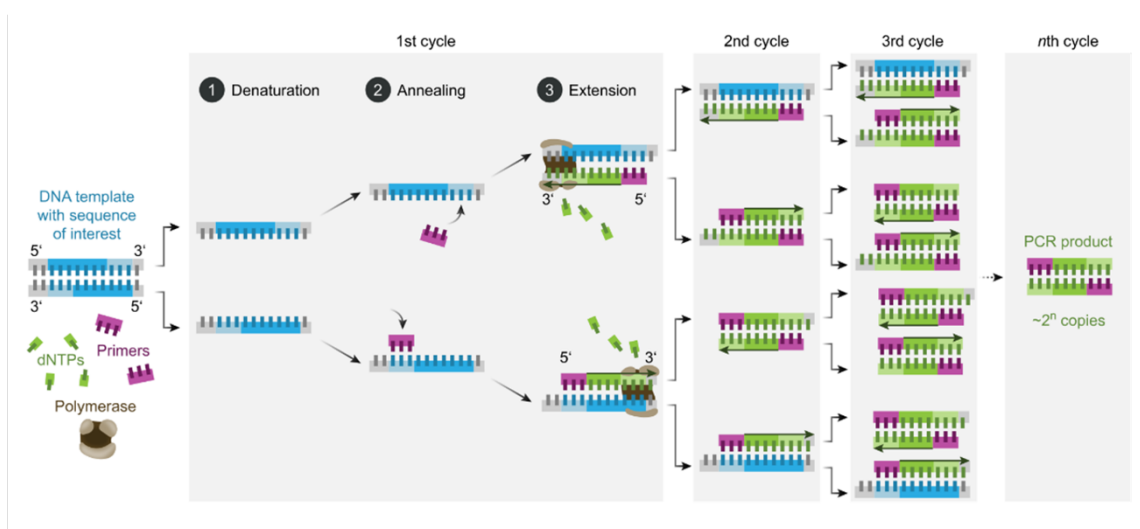


Figure 9. Schematic for PCR workflow with steps involved in each cycle- Denaturation, Annealing, Extension. Image by Enzoklop, licensed under CC BY-SA 4.0.

The process begins with the denaturation step, where the DNA sample is heated to separate its two strands. Next, the temperature is lowered to allow primers to bind to specific target sequences on the single-stranded DNA, during the annealing step. Following this, in the extension step, a DNA polymerase enzyme synthesizes new DNA strands by extending from the primers. This sequence of steps: denaturation, annealing, and extension, is repeated over multiple cycles, typically 25-35 times, doubling the amount of target DNA with each cycle. This exponential amplification results in millions of copies of the specific DNA segment, making it much easier to study in detail.

**Plasmonic nanoparticles:** Plasmonic nanoparticles (NPs), especially gold nanoparticles, are routinely used for sensitive optical readout in Lateral Flow Assays (LFAs)<sup>40</sup>. Their strong absorption and scattering properties create visible bands on test strips, exemplified by rapid antigen tests for SARS-CoV-2. These nanoparticles interact with light, exhibiting interesting scattering, absorbance and coupling properties (Figure 10).

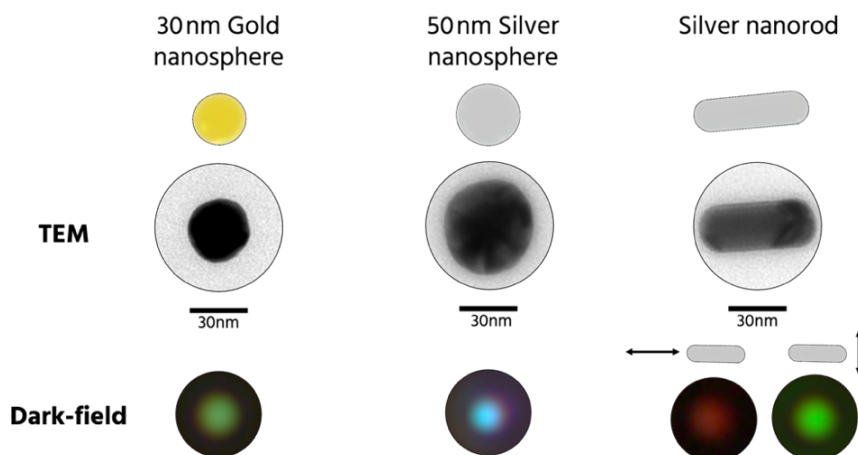


Figure 10. Plasmonic nanoparticles interact with light and this interaction is dependent on the shape, size and material composition of the NPs. Image by Mihir Dass from the lab of Prof. Tim Liedl at the Department of Physics at LMU Munich.

One of the most relevant effects for this thesis exhibited by plasmonic NPs is localized surface plasmon resonance (LSPR). When a small spherical metallic nanoparticle is irradiated by light, the oscillating electric field causes the conduction electrons to oscillate. This effect causes subwavelength localization, enhancing the electric field close to the nanoparticle surface. Coupling between nearby particles creates stronger fields or plasmonic hotspots. The field decays rapidly away from the surface and is also dependent on the size, shape and material composition of the nanoparticles<sup>42</sup>. The electric field enhancement allows nanoparticles to act as optical nanoantennas, much like regular radio antennas<sup>43-45</sup>, boosting the fluorescence

signal of nearby emitters. Optical antennas have since been used to enhance the fluorescence signal of an emitter<sup>43,46,47</sup>, with recent reports focussing on detecting single molecules with low-cost optics and a smartphone<sup>5,48-52</sup>. Such low-tech devices have the potential to bring the sensitivity of single-molecule detection to a resource-limited setting of point-of-care devices<sup>5</sup>.

## 1.4 PLASMONIC NANOPARTICLES AS OPTICAL ANTENNAS

Optical antennas, counterparts to microwave and radio wave antennas, enable the manipulation and control of optical radiation at subwavelength scales<sup>43,53</sup>, by converting freely propagating optical radiation into localized energy and vice versa<sup>44</sup>. This control and manipulation allows them to enhance the performance and efficiency of photodetection<sup>54,55</sup>, light emission<sup>56,57</sup>, and sensing<sup>58</sup>.

Antennas are integral to modern technology, used in everything from satellite communications, television and radio, navigation systems to baby monitors. While radio wave and microwave antennas are commonplace, their optical counterparts need fabrication accuracies down to a few nanometres, matching the order of the wavelength they handle, which is a very demanding size requirement<sup>44</sup>. Advances in nanotechnology have made these scales more accessible. Using techniques like focused ion-beam milling<sup>53,59</sup> and electron-beam lithography<sup>60,61</sup>, along with bottom-up self-assembly<sup>62,63</sup> methods, prototypes of optical antennas have been created. The goal of designing optical antennas mirrors that of traditional antennas: to optimize energy transfer between localized sources or receivers and the free-radiation field<sup>44</sup>. In applications like spectroscopy and microscopy, optical antennas function both as receivers and transmitters, guided by the principle of reciprocity<sup>44</sup> (Figure 11). Essentially, if a pathway exists for energy to travel from point A to point B, the same pathway can conduct energy from point B back to point A with equal efficiency. This principle is fundamental in designing and understanding antennas, ensuring that an antenna's performance as a transmitter will directly correlate with its performance as a receiver.

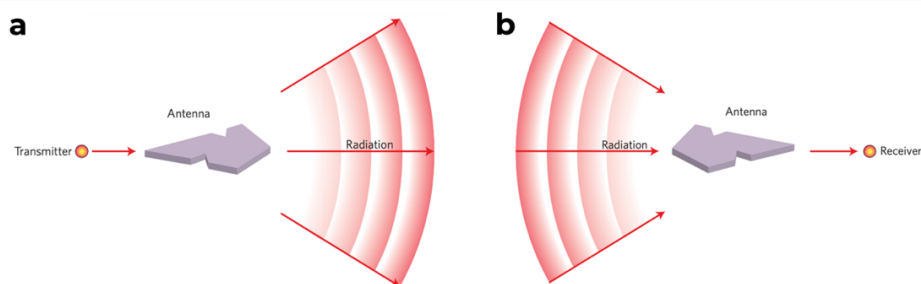


Figure 11. **a** Transmitting antenna and **b** receiving antenna, with arrows showing the direction of energy flow. Reproduced from Novotny, L. & Van Hulst, N. *Nat Photonics* 5, 83-90 (2011) with permission from Springer Nature<sup>23</sup>.

## Optical antenna fabrication

Plasmonic NPs are the simplest example of an optical nanoantenna. But how do we make them? The easiest way to synthesize nanoparticles of different sizes and shapes is through wet-chemical synthesis. Wet-chemical synthesis of metal particles involves reducing metal ions in solution. When specific shapes of metal particles are desired, chemicals that serve as shape-directing agents are often added<sup>64</sup> (Figure 12). Nanospheres<sup>65</sup>, nanorods<sup>66,67</sup> and nanobipyramids<sup>68</sup> are some of the common shapes synthesized by wet-chemistry. These methods allow a fairly good yield of nanoparticles to be synthesized with homogeneous size and shape distribution, and due to their crystalline<sup>68</sup> nature a high electric field enhancement is achieved. However, the highest possible enhancements occur between the gaps of two or more nanoparticles<sup>69</sup>. Creating these precise gaps or placing two nanoparticles at a certain distance to each other is not a trivial task.

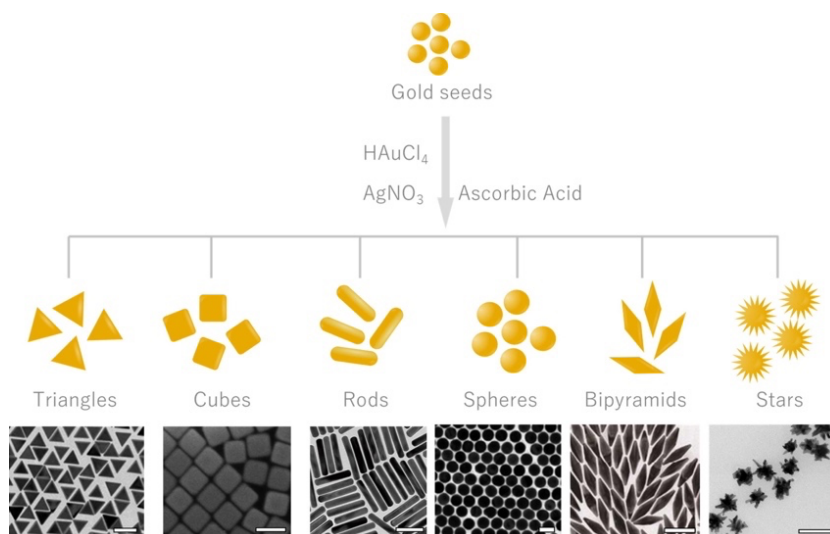


Figure 12. Examples of some of the common morphologies of AuNPs synthesized by the seed-mediated approach. Scale bar represents 100 nm. Reprinted with permission<sup>70-75</sup>. Copyright 2010, 2014, 2016, 2017, 2019 American Chemical Society. Reused with permission by Elsevier (2022)<sup>76</sup>.

The most common method for creating controlled and reproducible assemblies is lithography. This technique uses particle beams, such as electrons or ions, to directly etch nanostructures onto surfaces<sup>77</sup>. Examples include Yagi-Uda antennas<sup>53</sup> (Figure 13a), bow-tie<sup>61,78</sup> (Figure 13b) and dimers of gold disks<sup>79,80</sup> (Figure 13c), and arrays of gold nanorods<sup>78,81</sup> (Figure 13d). Lithography allows precise control over the size, spacing, and orientation of these structures. However, the



resolution of lithographic methods depends on the quality of the particle beam and the resist used, with gaps smaller than 10 nm typically challenging to achieve. Also, the amorphous structure and the presence of adhesion layers cause broadened plasmon resonances and reduced near-field enhancements in lithographic structures<sup>78</sup>.

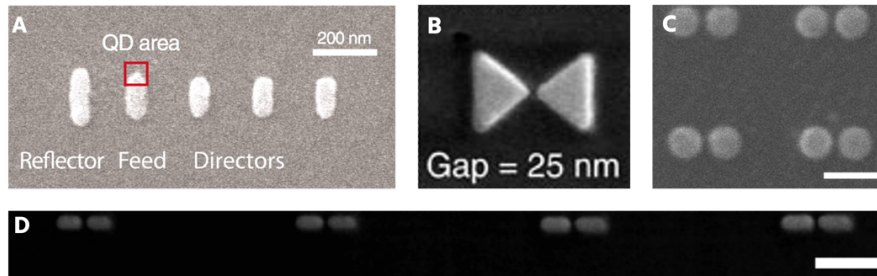


Figure 13. Examples of optical antennas fabricated using lithography-based methods. **a** Yagi-Uda optical antenna driven by quantum dots. From [Curto, A. G. et. al. *Science* (1979) 329, 930-933 (2010)<sup>26</sup>]/Reprinted with permission from AAAS. **b** Bow-tie antenna with a gap of 25 nm. Reproduced from Huang, J.-S. et. al. *Nat Commun* 1, 150 (2010) with permission by Springer Nature<sup>78</sup>. **c** nanopatterned array of dimer gold disks. Scale bar represents 200 nm. Reproduced from Aćimović, S. S., Kreuzer, M. P., González, M. U. & Quidant, R. *ACS Nano* 3, 1231–1237 (2009) with permission<sup>80</sup>. Copyright 2009 American Chemical Society. **d** arrays of fold nanorods. Scale bar is at 300 nm. Reproduced with permission by Springer Nature<sup>78</sup>

## 1.5 DNA ORIGAMI FOR CONTROLLED ASSEMBLY

Among the emerging techniques in nanofabrication, DNA Origami<sup>82,83</sup> is an excellent candidate to create controlled gaps between NPs with precision down to a few nm. It is a bottom-up self-assembly technique that involves a long single-stranded (ss) scaffold DNA which is pulled into the desired two- or three-dimensional shape by addition of many short staple strands (Figure 14). The technique thus allows the marriage of unique plasmonic crystalline properties of colloidal nanoparticles with controlled spacing and orientation<sup>84</sup>. The gap in these cases can be determined by the thickness of the DNA spacer involved.



Figure 14. Schematic for DNA Origami folding technique to create two- or three-dimensional nanostructures. Copyright 2021<sup>45</sup>. Published by American Chemical Society, licensed under CC-BY-NC-ND 4.0

A DNA Origami nanostructure is often seen as a molecular breadboard as there is an option to modify or add any desired functionality with a resolution theoretically equal to the distance from one base pair to another, or 0.34 nm<sup>85</sup>. This has allowed many applications from a DNA “box” that can release a drug on trigger<sup>86</sup> to a controllable nanoscale robotic arm<sup>87</sup>. Furthermore, unlike lithography techniques, it does not require the elaborate machinery and a clean room as it is a self-assembly method, and can be adapted in labs more democratically. Now, we know how to assemble a DNA origami nanostructure and we have colloidal nanoparticles. To create DNA origami-based nanoparticle assemblies, we first have to create an interaction between the two. One of the most common strategies is to use thiol-modified DNA to functionalize the nanoparticles<sup>88,89</sup>. The gold-thiol bond is known for its strong binding due to its pseudo-covalent nature, yet achieving high-density DNA loading on colloidal particles is challenging due to the negatively charged phosphate backbone of DNA<sup>85</sup>. Salt-aging, which involves slow salt addition, helps by neutralizing these charges, allowing tighter DNA packing on nanoparticle surfaces<sup>90-92</sup>. Alternatively, the freeze-thaw method developed by Liu and Liu accelerates this process<sup>93,94</sup>. By freezing a mixture of gold nanoparticles (AuNPs), DNA, and salt, ice crystals form, pushing non-water components into concentrated areas and enhancing the binding of thiolated DNA ends to gold. This method is robust, simple, and fast, making it appealing for broader adoption in both research and industry. Following this we can extend the staples in the origami bearing a complementary sequence which can hybridize with the thiolated DNA and define where and how the NPs will be positioned on the origami structure. In line with this, many different assemblies like spatially ordered assembly of NPs<sup>95</sup> (Figure 15a), dimers of gold nanospheres<sup>96</sup> (Figure 15b), chiral<sup>97</sup> (Figure 15c) and linear chains<sup>98</sup> (Figure 15d) of NPs, controlled spacing and relative orientation of gold nanorods<sup>99</sup> (Figure 15e), have been enabled by DNA origami nanostructures.

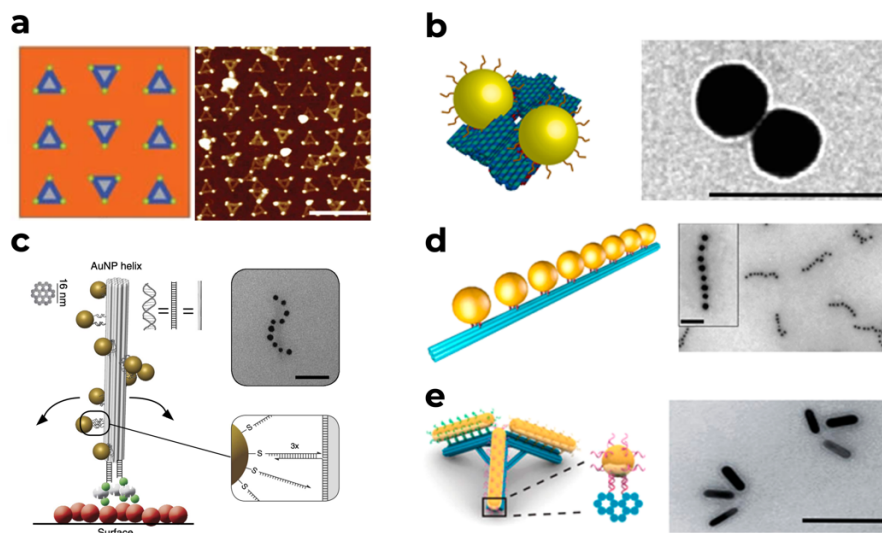


Figure 15. Examples of use of DNA origami for controlled assembly of nanoparticles functionalized by thiolated DNA strands. **a** Sketch (left) and an AFM image (right) of Triangle DNA origami with selective immobilization of NPs on the substrate patterned by electron-beam lithography. Scale bar is at 500 nm. Reproduced from Huang, A. M. et. al. *Nat Nanotechnol* 5, 121-126 (2010) with permission<sup>95</sup> by Springer Nature. **b** Sketch of gold dimer assembled on a DNA origami nanostructure (left) and an exemplary TEM image (right). Scale bar corresponds to 100 nm. Reproduced from Thacker, V. V. et. al. *Nat Commun*, 5, 3448 (2014). with permission<sup>96</sup> by Springer Nature. **c** Chiral assembly of nanoparticles controlled by a DNA origami immobilized on the surface via biotin-avidin interaction and an exemplary TEM image of the construct. Scale bar is at 50 nm. Copyright 2013<sup>97</sup>, published by Springer Nature, licensed under Creative Commons CC-BY-NC-SA. **d** Schematic of a linear arrangement of nanoparticles on DNA origami (left) and the SEM image (right). Scale bar represents 100 nm. Reproduced from Gür, F. N., Schwarz, F. W., Ye, J., Diez, S. & Schmidt, T. L. *ACS Nano* 10, 5374–5382 (2016) with permission<sup>98</sup>. Copyright 2016 by American Chemical Society. **e** Schematic of gold nanorods assembled on a tripod-shaped DNA origami nanostructure on the left and an exemplary TEM image on the right. Scale bar is at 100 nm. Reproduced from Zhan, P. et. al. *ACS Nano* 11, 1172-1179 (2017) with permission<sup>99</sup>. Copyright 2017 by American Chemical Society.

# 2

## THEORETICAL CONCEPTS

### 2.1 FLUORESCENCE

*"It was certainly a curious sight to see the tube instantaneously lighted up when plunged into the invisible rays: it was literally **darkness invisible**."*

*-George Gabriel Stokes<sup>32</sup>*

Fluorescence is a type of luminescence that involves the absorption of light by a molecule followed by the emission of light, typically at a longer wavelength<sup>100</sup>. It is an essential phenomenon in many biological, chemical, and technological applications, from microscopy and diagnostics to pollution detection and optical displays. Fluorescence begins with the absorption of photons, usually from ultraviolet or visible light. This absorbed energy promotes electrons in the molecule from a lower energy state (ground state) to a higher energy state (excited state). The excited electrons are not stable and release this excess energy by emitting photons as they return to their ground state, emitting light at a longer wavelength than the absorbed light. The first observation of fluorescence from a quinine solution in sunlight was reported by Sir John Frederick William Herschel in 1845<sup>33</sup>.

#### 2.1.1 SINGLE MOLECULE FLUORESCENCE: HOW FAR HAVE WE COME?

Detecting single molecules is the ultimate level of sensitivity for analytical methods. Combining it with fluorescence is an obvious choice as it allows detection against a dark background, reducing noise. However, fluorescence-based single-molecule detection is technically challenging, with the first successful demonstration at room temperature occurring in 1990<sup>101</sup>. This method required minimizing the observed volume and using pulsed laser excitation to distinguish the signal from scattered light, yielding a signal of about 50 photons per rhodamine 6G molecule in water. Previously, in 1989, Moerner and Kador pioneered the optical detection of individual chromophores by observing the absorption of pentacene in p-

terphenyl host crystals at extremely low temperatures<sup>102</sup>. Soon after, Orrit and Bernard demonstrated that using laser-induced fluorescence to excite pentacene molecules provided greater sensitivity compared to measuring their absorbance<sup>103</sup>. Despite advancements, detecting single fluorophores, especially in impure biological samples, remains difficult. Earlier efforts by Hirshfeld<sup>104</sup> in 1976 work and Keller<sup>105</sup> and Mathies in 1989<sup>106</sup> involved large molecules with multiple fluorophores. Other reports in the late 1980s involved extreme conditions like liquid helium temperatures or trapped atoms, all of which is impractical for biochemical experiments<sup>102,107,108</sup>. Finally, Yanagida and his team<sup>109</sup>, in 1995, became the first to conduct single-molecule measurements on a biological sample in an aqueous environment at room temperature. They could simultaneously observe hundreds of individual myosin motor proteins labelled with fluorescent markers and track their real-time adenosine triphosphate (ATP) hydrolysis activity (Figure 16a). This laid the foundation for biological samples to be probed at physiologically relevant conditions which opened up a myriad of possibilities. In 1996, Ha et. al. extended the application of FRET to the single-molecule level (called sm-FRET) by studying energy transfer between a donor and an acceptor fluorophore pair connected by a short DNA linker<sup>110</sup>. Another exciting discovery was the use of Green Fluorescent Protein (GFP) as a fluorophore that changed the landscape for fluorescence imaging in the life science area and resulted in a Nobel Prize in Chemistry in 2008<sup>111-120</sup>. Single-molecule experiments also revealed GFP's ability to reversibly switch between non-fluorescent and fluorescent states<sup>121-124</sup>. In 1999, Klar and Hell<sup>125</sup> introduced the concept of stimulated-emission depletion (STED)<sup>126</sup>, a technique that manages to overcome the diffraction limit of light. They used one laser to excite fluorescent molecules in a sample and another, donut-shaped laser to quench the fluorescence around the edges of the illuminated area. This left a much smaller, focused point of light, allowing for the imaging of structures at a higher resolution (Figure 16b, c). Although this enabled sub-diffraction resolution, it was still difficult to distinguish features in a densely labelled sample. The next developmental phase of the field, also known as super-resolution, started in 2006 when Betzig<sup>127</sup> (known as photo activated localization microscopy, PALM), Zhuang<sup>128</sup> (Stochastic optical reconstruction microscopy, STORM) and Hess<sup>129</sup> (Fluorescence photoactivated localization microscopy, FPALM), individually suggested methods to sequentially activate and localize only a few molecules at a time. A few molecules sparsely situated allowed localization with high precision and repeating this process over time resulted in a super-resolved image.

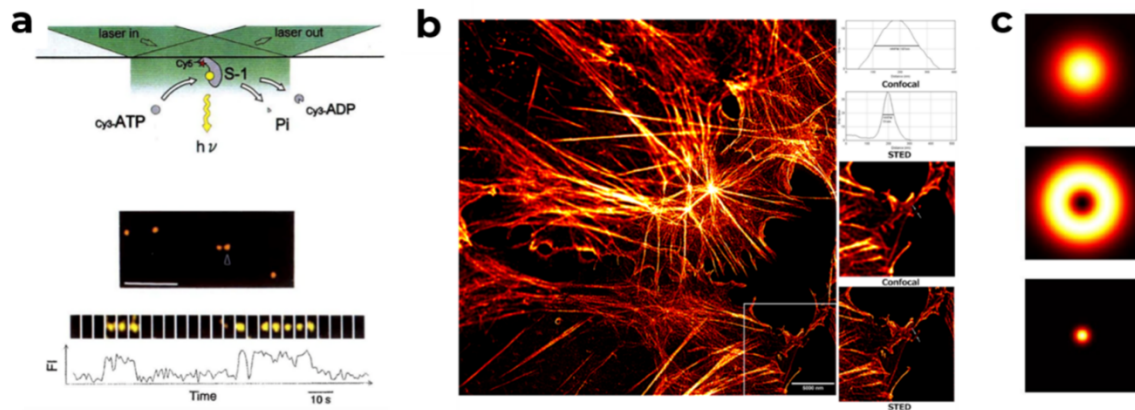


Figure 16. **a** Schematic (top) and fluorescence micrograph (middle) and time trace (bottom) showing individual ATP turnover by single Cy5 labelled S-1 molecules. Scale bar is at 5  $\mu\text{m}$ . Reproduced from Funatsu, T., Harada, Y., Tokunaga, M., Saito, K. & Yanagida, T. *Nature* 374, 555–559 (1995) with permission by Springer Nature<sup>109</sup>. **b** Image resolution in confocal microscopy and in STED microscopy showing actin filaments stained with 647-phalloidin. Image by Howard Vindin, Licensed under CC BY-SA 4.0. **c** Excitation focus (top), de-excitation focus (centre) and the remaining fluorescence beam (bottom) in the case of STED microscopy. Image by Marcel Lauterbach licensed under CC BY-SA 3.0.

In 2014, these efforts were recognized by a Nobel Prize in Chemistry shared between Eric Betzig, W.E. Moerner and Stefan Hell. There are many different strategies now like REversible Saturable Optical Fluorescence Transitions (RESOLFT<sup>130</sup>), Points accumulation for imaging in nanoscale topography (PAINT<sup>131</sup>), DNA-PAINT<sup>132</sup>, Resolution Enhancement by Sequential Imaging (RESI<sup>133</sup>) and others, to overcome the diffraction limit and reach the super-resolution realm with resolution reaching well below 10 nm. Very recently, the Jungmann group developed secondary label-based unlimited multiplexed DNA-PAINT or SUM-PAINT<sup>134</sup>, a high-throughput imaging method enabling multiplexing at better than 15 nm resolution. They showed a 30-plex SUM-PAINT experiment which facilitated the mapping of the super-resolved 3D protein distribution for 30 distinct targets within a single neuron. This brief non-exhaustive account highlights how the single-molecule fluorescence landscape has evolved and how it has enabled us to visualize structures and processes that were unimaginable a few years ago.

## 2.1.2 FUNDAMENTALS OF FLUORESCENCE

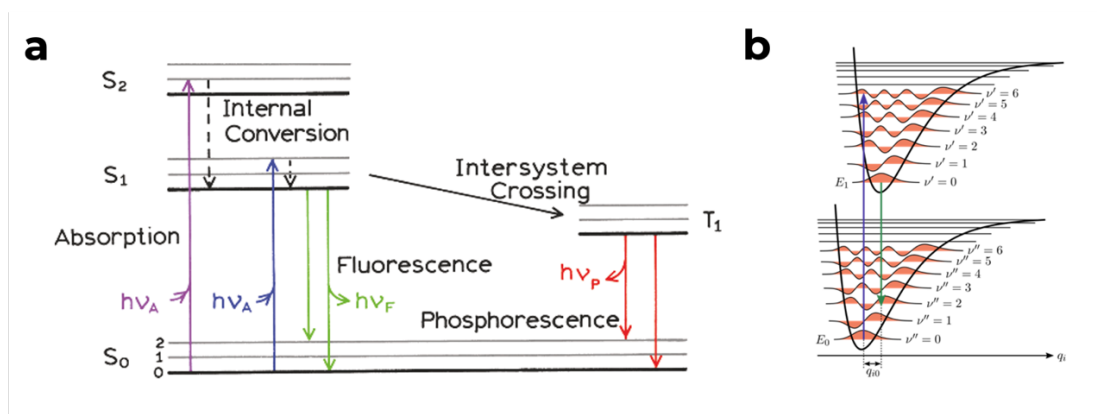


Figure 17 **a** Example of a type of Jablonski diagram. Reused with permission<sup>32</sup> by Springer Nature. **b** Illustration of Franck-Condon principle energy diagram. made by Samoza licensed under CC BY-SA 3.0

The physical process behind fluorescence is best explained by understanding the Jablonski diagram, Frank-Codon principle and Kasha's rule. Starting with the *Jablonski diagram*<sup>35</sup> (Figure 17 a), which is a visual representation of the electronic states of a molecule and the transitions between these states. Named after Professor Alexander Jablonski, the father of fluorescence spectroscopy, these diagrams serve as fundamental tools to explain various molecular processes in excited states. When a molecule absorbs a photon, it excites an electron from the ground state ( $S_0$ ) to one of the higher electronic excited states ( $S_1$ ,  $S_2$ , etc.). Within an electronic state, the molecule may undergo non-radiative relaxation between vibrational levels, which typically occurs very rapidly, leading to the electron settling in the lowest vibrational level of the first excited state ( $S_1$ ). This is known as internal conversion. The electron then returns to a vibrational level of the ground state ( $S_0$ ), emitting a photon in the process. This photon has less energy and thus a longer wavelength than the absorbed photon. Moreover, molecules in  $S_1$  can transition to the first triplet state,  $T_1$ , via intersystem crossing, resulting in phosphorescence, which is generally shifted to longer wavelengths (lower energy) compared to fluorescence. The transition from  $T_1$  to the ground state is forbidden, significantly slowing the rate of triplet emissions. The presence of heavy atoms such as bromine and iodine can facilitate intersystem crossing and thus enhance the yields of phosphorescence. The *Franck-Condon Principle*<sup>36</sup> (Figure 17 b) states that electronic transitions are much faster than nuclear motions of the atoms in a molecule. Therefore, during electronic transitions like absorption and emission, the positions of nuclei in the molecule do not change. The principle explains why the absorption and emission spectra often appear as mirror images-the electronic and vibrational states involved in transitions are similar. *Kasha's Rule*<sup>37</sup> states that

regardless of the excitation level, fluorescence emission always occurs from the lowest vibrational level of the first excited state ( $S_1$ ). This rule helps explain why fluorescence has a relatively uniform emission spectrum even if excitation occurs at different wavelengths.

The Jablonski diagram (Figure 17 a) shows that emission energy is usually lower than absorption energy, resulting in fluorescence at lower energies or longer wavelengths. This phenomenon, known as the Stokes shift, was first observed by Sir G. G. Stokes in 1852. The Stokes shift commonly occurs as fluorophores rapidly decay to the lowest vibrational level of  $S_1$  and typically return to higher vibrational levels of  $S_0$  (Figure 17 a), where they lose excitation energy through thermalization. Additional shifts can also result from solvent effects, excited-state reactions, complex formation, and energy transfer.

Fluorescent substances, also known as *Fluorophores*, are the most important part of fluorescence microscopy. Fluorophores are broadly classified into two types: intrinsic and extrinsic. Intrinsic fluorophores, which are naturally occurring, include fluorescent proteins such as GFP (see Figure 18 a) and mCherry, as well as native fluorophores like NADH (Nicotinamide Adenine Dinucleotide) and Tryptophan. Extrinsic fluorophores, which are added to non-fluorescent samples to induce fluorescence, include quantum dots and synthetic organic dyes (Figure 18 b) such as Rhodamine.

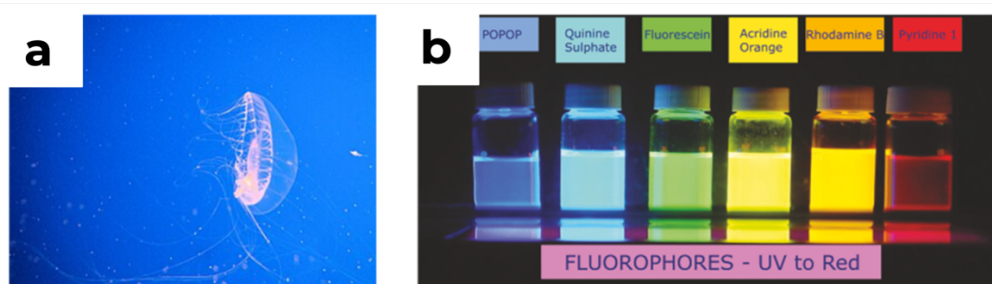


Figure 18. **a** An image of *hydrozoan Aequorea Victoria*- a jellyfish known as a carrier of green fluorescent protein. Image licensed under CC BY 2.0. **b** Examples of commonly used fluorophores covering the spectrum from ultraviolet (UV) to red wavelengths. Image reused with permission<sup>32</sup> by Springer Nature.

The fluorescence lifetime and quantum yield are the most important characteristics of a fluorophore. Quantum yield ( $\phi$ ) measures the ratio of emitted to absorbed photons, with substances like rhodamines displaying bright emissions due to high quantum yields near unity. Fluorescence lifetime ( $\tau$ ) is crucial as it determines how long a fluorophore can interact or diffuse within its environment, influencing the insights gathered from its emission. Fluorescence is always in competition with other processes that occur from the singlet excited state of a molecule. There can be multiple relaxation pathways: energy can be dissipated in a non-radiative manner with the rate  $k_{nr}$ , through fluorescence with the rate  $k_f$ , or through the



possibility for intersystem crossing to the triplet excited state with the rate  $k_{ISC}$ . The quantum yield and the fluorescence lifetime can be influenced by factors that affect either of the rate constants. The fluorescence quantum yield which is the fraction of fluorophores that decay through emission is given by:

$$\phi = \frac{k_{fl}}{k_{fl} + k_{nr} + k_{ISC}} \quad (2.1)$$

The quantum yield can be close to unity if the radiation-less decay rate is much smaller than the rate of radiative decay<sup>32</sup>. Similarly, the fluorescence lifetime ( $\tau$ ) can be described as:

$$\tau_{fl} = \frac{1}{k_{fl} + k_{nr} + k_{ISC}} \quad (2.2)$$

### 2.1.2.1. FLUORESCENCE QUENCHING

Fluorescence quenching refers to a process that leads to a decrease in fluorescence intensity of a fluorophore. This reduction in intensity can result from different mechanisms, often involving interactions between the fluorophore and another molecule or environmental changes affecting the fluorophore. *Collisional or Dynamic quenching* occurs when the fluorophore and a quencher molecule come into contact during the excited state lifetime of the fluorophore. The quencher can deactivate the fluorophore through energy transfer or charge transfer, returning it to the ground state without emission of a photon. The decrease in the fluorescence intensity in case of collisional quenching can be explained by the Stern-Volmer equation as:

$$\frac{F_0}{F} = 1 + K[Q] = 1 + k_q\tau_0[Q] \quad (2.3)$$

where  $F_0$  and  $F$  are the fluorescence intensities in the absence and presence of quencher, respectively,  $K$  is the Stern-Volmer quenching constant,  $k_q$  is the bimolecular quenching constant,  $\tau_0$  is the unquenched lifetime, and  $[Q]$  is the quencher concentration. The constant  $K$  measures a fluorophore's sensitivity to a quencher. Low  $K$  values typically indicate that the fluorophore is embedded within a macromolecule, making it less accessible to water-soluble quenchers. Conversely, higher  $K$  values suggest that the fluorophore is either exposed on a biomolecule's surface or freely dissolved in solution. Interestingly, for collisional quenching, the relative change in the intensity of fluorescence is equivalent to the relative change in the fluorescence lifetime. Molecular oxygen, halogens, and amines are typical quenchers in dynamic quenching.

On the other hand, in case of *static quenching*, the fluorophore and quencher form a less-emissive or non-fluorescent complex in the ground state<sup>35</sup>. In this case, the quenching of the

fluorescence intensity will have a dependence on the association constant for the complex formation ( $K_s$ ):

$$\frac{F_0}{F} = 1 + K_s[Q] \quad (2.4)$$

Where  $[Q]$  is the concentration of the quencher. Unlike collisional quenching, static quenching does not lead to changes to the fluorescence lifetime of the fluorophores as the complexed fluorophores are not fluorescent and the emission is collected only from the free fluorophores in solution<sup>32</sup>. Another interesting difference is that for collisional quenching, the absorption spectrum of the fluorophores remains unchanged as it only affects their excited state, whereas there might be perturbations in the absorption spectra for static quenching due to the ground-state complex formation<sup>32</sup>.

Another relaxation pathway possible is through *Resonance Energy Transfer* (RET) or FRET<sup>138</sup>, which describes energy transfer from a donor fluorophore, in its excited state, to an acceptor fluorophore through non-radiative dipole-dipole coupling<sup>139</sup>.

### 2.1.2.2 MEASURING FLUORESCENCE LIFETIME

Fluorescence lifetime is quantified as the average time a fluorophore remains in its excited state before returning to the ground state by emitting a photon. Time-Correlated Single-Photon Counting (TCSPC) is the most common method for measuring fluorescence lifetimes (Figure 19 a). TCSPC involves exciting the fluorophore with a short pulse of light and then detecting the time it takes for emitted photons to arrive at a detector<sup>140</sup>. This process is repeated many times to build up a statistically significant histogram of photon arrival times. For TCSPC, conditions ensure that less than one photon is detected per laser pulse, typically around one photon for every 100 excitation pulses<sup>32</sup>. The time between the excitation pulse and the detected photon is recorded and plotted in a histogram, with the x-axis representing the time difference and the y-axis showing the count of photons detected at each time interval.

If the fluorophore decays (Figure 19 b) from the excited state to the ground state at a single rate, the decay can be described by a single exponential function:

$$I(t) = I_0 e^{-\frac{t}{\tau}} \quad (2.5)$$

where  $I(t)$  is the intensity at time  $t$ ,  $I_0$  is the initial intensity, and  $\tau$  is the fluorescence lifetime. The fluorescence lifetime is defined as the time it takes the intensity to drop to  $1/e$  ( $\approx 0.368$ ) of its initial value<sup>140</sup>. The formula for a bi-exponential decay, which involves two different lifetimes, is:

$$I(t) = A_1 * e^{\frac{-t}{\tau_1}} + A_2 * e^{\frac{-t}{\tau_2}} \quad (2.6)$$

where  $A_1, A_2$  are amplitudes corresponding to the proportions of each fluorophore population and  $\tau_1, \tau_2$  are different lifetimes associated to each population. Often, the decay profile is more complex and can be better described by a sum of exponential terms:

$$I(t) = \sum_i a_i e^{\frac{-t}{\tau_i}} \quad (2.7)$$

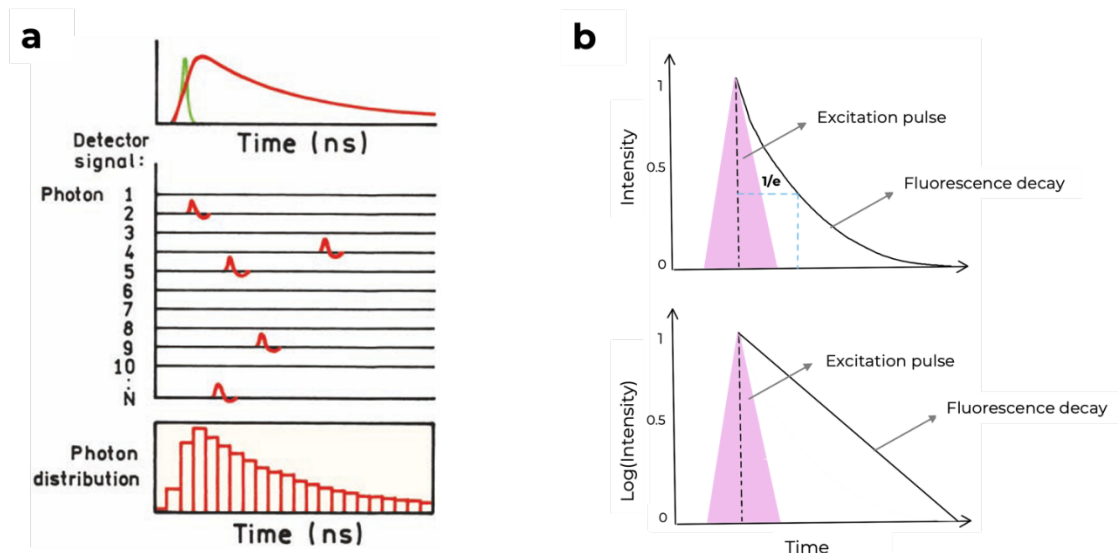


Figure 19. **a** Working principle for TCSPC. Reused with permission<sup>32</sup> by Springer Nature. **b** Sketch showing fluorescence decay curve as commonly plotted in a linear (top) and logarithmic (bottom) scale.

where  $a_i$  are the amplitudes and  $\tau_i$  are the lifetimes associated with each component of the decay. This can occur due to different environments of the fluorophores or different excited states.

The minimum measurable lifetime in TCSPC is determined by the temporal width of the Instrument Response Function (IRF), which reflects the shortest time profile the system can measure. The IRF is typically captured using a dilute scattering solution (e.g. Rayleigh/Raman scattering of water or a colloidal silica solution), without an emission filter. The width of the IRF is indicative of the system's temporal resolution and is influenced by the detector characteristics and timing electronics. In general, narrower IRFs mean better resolution. Especially for shorter lifetimes, it is crucial to deconvolute the IRF from the measured data, to get a more accurate representation of the true signal.

## 2.2 PLASMONICS FOR FLUORESCENCE ENHANCEMENT

A Localized Surface Plasmon (LSP) occurs when surface plasmons are confined within nanoparticles smaller than the wavelength of the exciting light. When light irradiates a small spherical metallic nanoparticle, its electric field causes the conduction electrons to oscillate coherently (Figure 20). Displacement of the electron cloud creates a Coulombic restoring force from the attraction between the electrons and nuclei, leading to further oscillation.

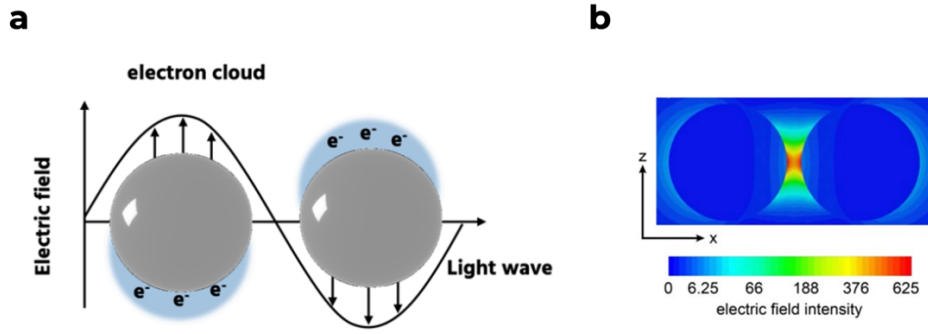


Figure 20. **a** Illustrating the impact of incident light on a metallic nanoparticle with a size smaller than the wavelength of the light. **b** Numerical simulation of the electric field intensity at the equatorial plane of the dimer structure with an interparticle distance of 12 nm at a wavelength of 640 nm and an incident electric field polarization parallel to the dimer orientation. Reproduced from Puchkova, A. et. al. Nano Lett 15, 8354-8359 (2015) with permission<sup>141</sup>. Copyright 2015 American Chemical Society.

The oscillation frequency is influenced by electron density, effective electron mass, and the size and shape of the nanoparticle. LSPs significantly enhance electric fields near the nanoparticle's surface and create maximum optical absorption at the plasmon resonance frequency. The optical properties of nanoparticles are significantly influenced by their material composition (through  $\epsilon_{particle}$ ), size ( $R$ ), and the electromagnetic environment (via  $\epsilon_{medium}$ ). We can describe the scattering and absorption of light by very small spherical nanoparticles using the quasistatic approximation (a framework applicable when the nanoparticle size is much smaller than the wavelength of the incident light). The scattering cross-section ( $\sigma_{scatt}$ ) equation describes how much light is scattered by a nanoparticle. It is given by:

$$\sigma_{scatt} = \frac{8\pi}{3} k^4 R^6 \left| \frac{\epsilon_{particle} - \epsilon_{medium}}{\epsilon_{particle} + 2\epsilon_{medium}} \right|^2 \quad (2.8)$$

where  $k$  is the wavenumber of the incident light,  $R$  is the radius of the nanoparticle,  $\epsilon_{particle}$  and  $\epsilon_{medium}$  are the relative permittivity (or dielectric constants) of the nanoparticle and the surrounding medium, respectively. The absorption cross-section ( $\sigma_{abs}$ ) equation quantifies how much light is absorbed by the nanoparticle:

$$\sigma_{abs} = 4\pi k R^3 \text{Im} \left| \frac{\epsilon_{particle} - \epsilon_{medium}}{\epsilon_{particle} + 2\epsilon_{medium}} \right| \quad (2.9)$$

where  $\text{Im}$  denotes taking the imaginary part of the complex ratio, indicating that absorption depends on the imaginary components of the dielectric functions, which relate to the material's ability to dissipate energy from the electromagnetic field. Equation 2.11 shows a clear  $R^3$  dependence for the absorption, whereas the scattering shows an  $R^6$  dependence. This dependency explains why smaller nanoparticles exhibit less scattering relative to larger ones, and why they demonstrate proportionately greater absorption<sup>142</sup>.

The relative permittivity of the nanoparticle ( $\epsilon_{particle}$ ) is defined by:

$$\epsilon_{particle} = 1 - \frac{\omega_p^2}{\omega^2 + i\omega\gamma} \quad (2.10)$$

This equation is based on the Drude Model for free electrons, where  $\omega_p$  is the plasma frequency,  $\gamma$  is the charge carriers' relaxation frequency, and  $\omega$  is the frequency of the electromagnetic radiation. It models the behaviour of electrons as a harmonic oscillator driven by an electric field, and it simplifies to its most fundamental form when solving the corresponding differential equation. The polarizability of a material experiences a significant boost at resonance when the expression  $\epsilon_{particle} + 2\epsilon_{medium}$  reaches a minimum, which for the case of small or slowly-varying  $\text{Im}[\epsilon]$  around the resonance simplifies to

$$\text{Re}[\epsilon_{particle}(\omega)] = -2\epsilon_{medium} \quad (2.11)$$

This scenario is referred to as the Fröhlich condition, and it describes the dipole surface plasmon mode of a metal nanoparticle when it oscillates in an electromagnetic field<sup>143</sup>. At this point, the scattering and absorption cross-sections are maximized, indicating strong interaction between light and the nanoparticle. These calculations assume single, spherical particles. For non-spherical particles or assemblies of multiple nanoparticles, modifications to these equations are necessary to account for changes in geometry and collective interactions<sup>144</sup>.

## 2.2.1 COUPLING BETWEEN TWO NANOSPHERES

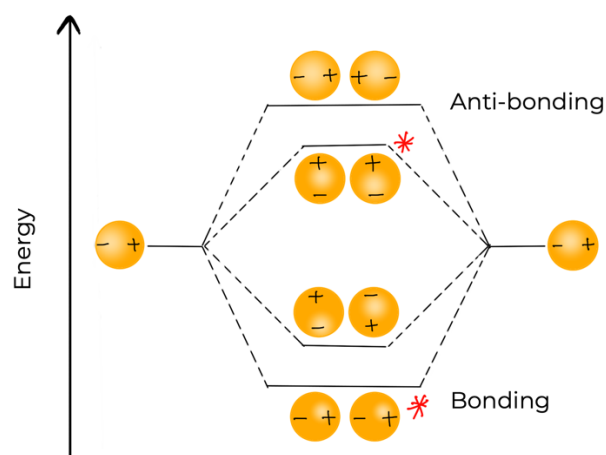


Figure 21. Sketch representing plasmon hybridization model for two gold nanospheres. The asterisk in red represents the bonding or bright modes that can be excited by external electric field, whereas the anti-bonding or dark modes can be excited only under special conditions.

When two or more plasmonic nanoparticles are in close proximity, their plasmonic fields interact through plasmon hybridization. This process, which is analogous to the hybridization of electronic orbitals in molecules, varies depending on the orientation and proximity of the nanoparticles<sup>145,146</sup>. As these particles approach each other within the range of their evanescent fields, the electromagnetic fields between them are significantly enhanced, particularly in the narrow gaps known as "plasmonic hot spots"<sup>44</sup>. These hot spots exhibit much stronger electromagnetic fields than those generated by individual particles<sup>69</sup>.

To analyse these interactions, each nanoparticle is modelled as a simple dipole. Using the plasmon-hybridization model (Figure 21), various coupling modes are predicted, including bright modes, where dipoles are in phase and enhance detectability to incoming light, and dark modes, where out-of-phase dipoles lead to field cancellations. The behaviour of these modes depends on the phase relationships between the dipoles and the symmetry of the particle arrangement, where asymmetric setups can convert dark modes into bright ones. Depending on the polarization of the incident electric field and the arrangement of the nanoparticles, these particles can act either as single plasmonic entities or as a coupled system. Coupled configurations typically result in a red shift<sup>147</sup> in the localized surface plasmon resonance (LSPR) relative to isolated nanoparticles, dependent on the gap size<sup>145,146</sup>.

## 2.2.2 FLUOROPHORE IN A PLASMONIC HOTSPOT

Plasmonic nanoparticles significantly alter the photophysical properties of nearby fluorophores by affecting their excitation and emission processes. The local electromagnetic field generated by these nanoparticles enhances the excitation rate ( $k_{exc}$ ) of fluorophores<sup>61</sup>, which is proportional to the product of the transition dipole ( $\mu$ ) of the fluorophore and the electric field  $E$ :

$$k_{exc} \propto |\mu E|^2 \quad (2.12)$$

The square of this product quantifies how the alignment and strength of the electric field relative to the dipole moment influence the rate at which the fluorophore is excited. In terms of emission, the presence of nanoparticles modifies the fluorophore's relaxation pathways. The nanoparticles introduce additional non-radiative decay routes, where the fluorophore's energy is transferred to the nanoparticle and dissipated as heat, a process known as quenching. The

dominance of either radiative or non-radiative decay is dependent on the proximity of the fluorophore to the nanoparticle: closer distances favour non-radiative decay and quenching, while intermediate distances enhance fluorescence due to increased radiative decay.

The interaction between the fluorophore and the nanoparticles is also influenced by the orientation of the fluorophore's transition dipole moment relative to the nanoparticle. Additionally, the size of the nanoparticle affects these interactions, with larger nanoparticles generally enhancing the emission rate more significantly than smaller ones. The cumulative effects of these factors- orientation, distance, and nanoparticle size- determine the overall impact on the fluorophore's fluorescence intensity, quantum yield, and lifetime. These modifications are quantified using the Purcell factor<sup>148</sup> for radiative decay rates and the fluorescence enhancement (FE) factor for overall fluorescence intensity.

The Purcell Effect refers to the enhancement of a fluorophore's or emitter's spontaneous emission rate when placed in an environment that alters its local density of optical states (LDOS)<sup>148</sup>. The enhancement factor measures the ratio of the fluorescence intensity of a molecule in the presence of a plasmonic nanoparticle compared to its fluorescence in the absence of such structures.

## **2.3 DNA**

Deoxyribonucleic acid (DNA) can be imagined as a giant recipe book that contains all the information needed to build every living thing on Earth. Every plant, animal, and human has its own unique recipe encoded in its DNA. DNA carries the genetic instructions necessary for the development, functioning, growth, and reproduction of all known organisms and many viruses. Together with proteins, lipids, and complex carbohydrates, nucleic acids are one of the four essential types of macromolecules crucial for all known forms of life<sup>149</sup>.

The story of DNA begins in 1869 with Friedrich Miescher, a Swiss biochemist, who discovered a substance containing nitrogen and phosphorus, which he named "nuclein", while studying white blood cells<sup>150</sup>. Later, between 1910-1920, Phoebus Levene, an American biochemist, made significant contributions by discovering that DNA was composed of four nucleotides: adenine (A), thymine (T), cytosine (C), and guanine (G)<sup>151</sup>. Following this in 1950, Erwin Chargaff, an Austrian-American biochemist, discovered that the amounts of adenine and thymine were equal in DNA, as were the amounts of cytosine and guanine<sup>152</sup>. This became known as Chargaff's rules.

The years 1951-1953 marked the crucial discovery of the double helix structure of DNA. Rosalind Franklin, a British biophysicist, together with Raymond Gosling, used X-ray crystallography to photograph DNA fibres. Her images, particularly Photo 51, revealed the helical structure of DNA<sup>153</sup> (Figure 22a). Building on this, James Watson, an American biologist, and Francis Crick, a British physicist, in 1953, created the first model of the double helical structure of DNA, explaining how genetic information is stored and copied<sup>154</sup> (Figure 22b). Together this marking a revolutionary moment in biology.

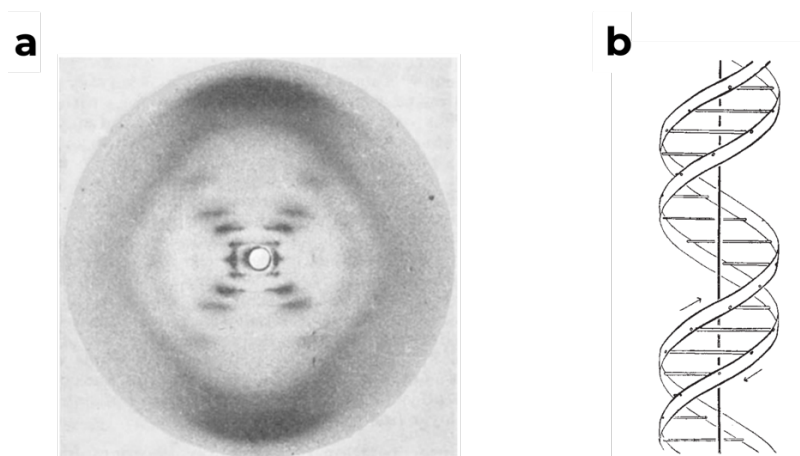


Figure 22. **a** Photo 51. Reproduced from Franklin, R. E. & Gosling, R. G. *Nature* 171, 740-741 (1953) with permission<sup>153</sup> by Springer Nature. **b** First diagram of the double helical structure of DNA. Reproduced from Watson, J. D. & Crick, F. H. C. *Nature* 171, 737-738 (1953) with permission<sup>154</sup> by Springer Nature.

Following these discoveries, the focus shifted towards-how DNA functions? This led to various important discoveries such as -the semi-conservative replication of DNA, where each new DNA molecule consists of one old strand and one new strand in 1958<sup>155</sup>; determining how sequences of nucleotides (codons) specify amino acids, the building blocks of proteins in the 1960s<sup>156,157</sup>; The Human Genome Project, completed in 2003, was an international research effort to map and sequence the entire human genome, and provided a comprehensive blueprint of human DNA, identifying all the genes and their functions. More recently, Jennifer Doudna and Emmanuelle Charpentier developed CRISPR-Cas9, a revolutionary gene-editing technology that allows precise modifications to DNA<sup>158</sup>. Acknowledging the impact, they were awarded a Nobel Prize in Chemistry in 2020.

### 2.3.1 STRUCTURE OF DNA

DNA is a long polymer consisting of two antiparallel strands that coil around each other to create a double-helix configuration. The two strands are called polynucleotides as they are



made of simpler units called nucleotides. Each nucleotide consists of three components: a deoxyribose sugar molecule, a phosphate group, and a nitrogenous base. The sugar and phosphate groups form the backbone of each DNA strand, creating a repeating sugar-phosphate structure (Figure 23a). The nitrogenous bases, adenine (A), thymine (T), cytosine (C), and guanine (G) (Figure 23a), extend from the backbone and pair specifically in the centre of the helix through hydrogen bonding.

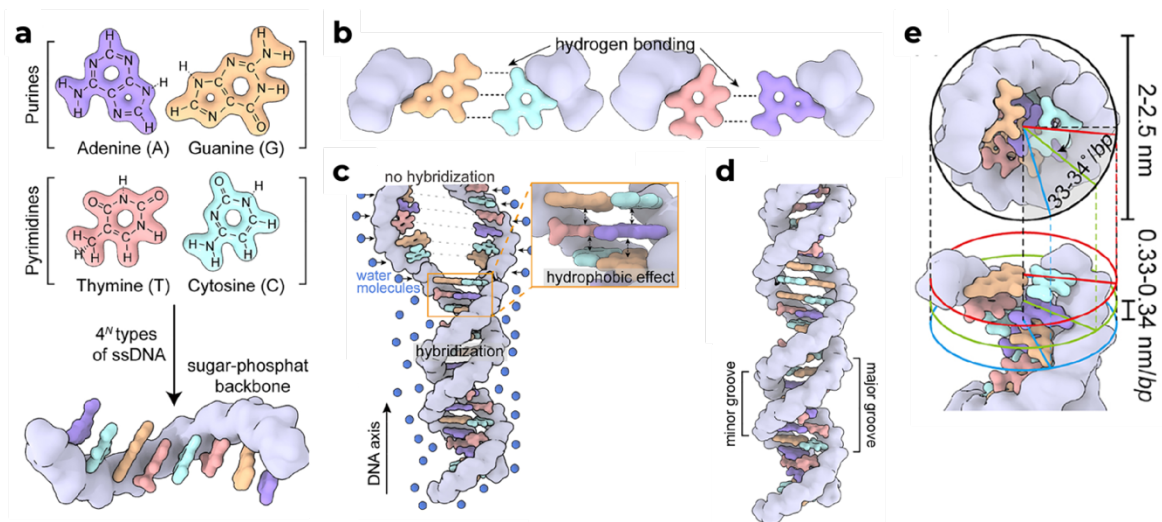


Figure 23. Fundamentals of structure of DNA. Modified and used as licensed under CC BY 4.0<sup>159</sup>. Published by De Gruyter.

Adenine and guanine belong to the group of double-ringed purines, whereas thymine and cytosine belong to the single-ringed pyrimidines group (Figure 23a). Adenine pairs with thymine via two hydrogen bonds, while cytosine pairs with guanine via three hydrogen bonds (Figure 23b). A higher G-C content promotes higher stability. The complementary base pairing means that all the information in double stranded (ds) sequence of a DNA is duplicated in each strand. This is crucial for biological processes such as replication and serves as the foundational property for structural DNA nanotechnology. The stability of the double helix is enhanced by hydrophobic  $\pi - \pi$  interactions between the delocalized electron clouds of neighbouring bases. This phenomenon, known as “base-stacking”<sup>160</sup>, removes water from between the nucleobases and is partly responsible for DNA assuming its helical shape (Figure 23c). The voids formed by the asymmetrical spiral winding of the two strands are the major and minor grooves (Figure 23d). The major groove is wider and deeper, making it a key site for protein binding, and the minor groove is narrower and less accessible, but it still plays a role in the binding of smaller molecules. DNA can exist in many different forms (A-form, Z-form), although B-form is the most common under physiological conditions. A complete turn of the DNA helix, which

encompasses 10.5 base pairs (bp), extends across 3.5 nm, has a diameter of approximately 2 nm, and features a vertical spacing of 0.34 nm between consecutive base pairs (Figure 23e).

### 2.3.2 CONSTRUCTING WITH DNA

*"Just because we can't do it doesn't mean we can't think about doing it."*

*-Ned Seeman, 1995<sup>161</sup>*

DNA is not just a molecule that carries genetic information; it can also be a versatile construction material. This idea was first introduced by Nadrian Seeman in the early 1980s. The principles of complementary base pairing enable the self-assembly of carefully designed sequences into complex structures, which justifies the name 'DNA Nanotechnology' for this field. It mirrors the bottom-up approach used in Nanotechnology, where molecular components arrange themselves into larger structures.

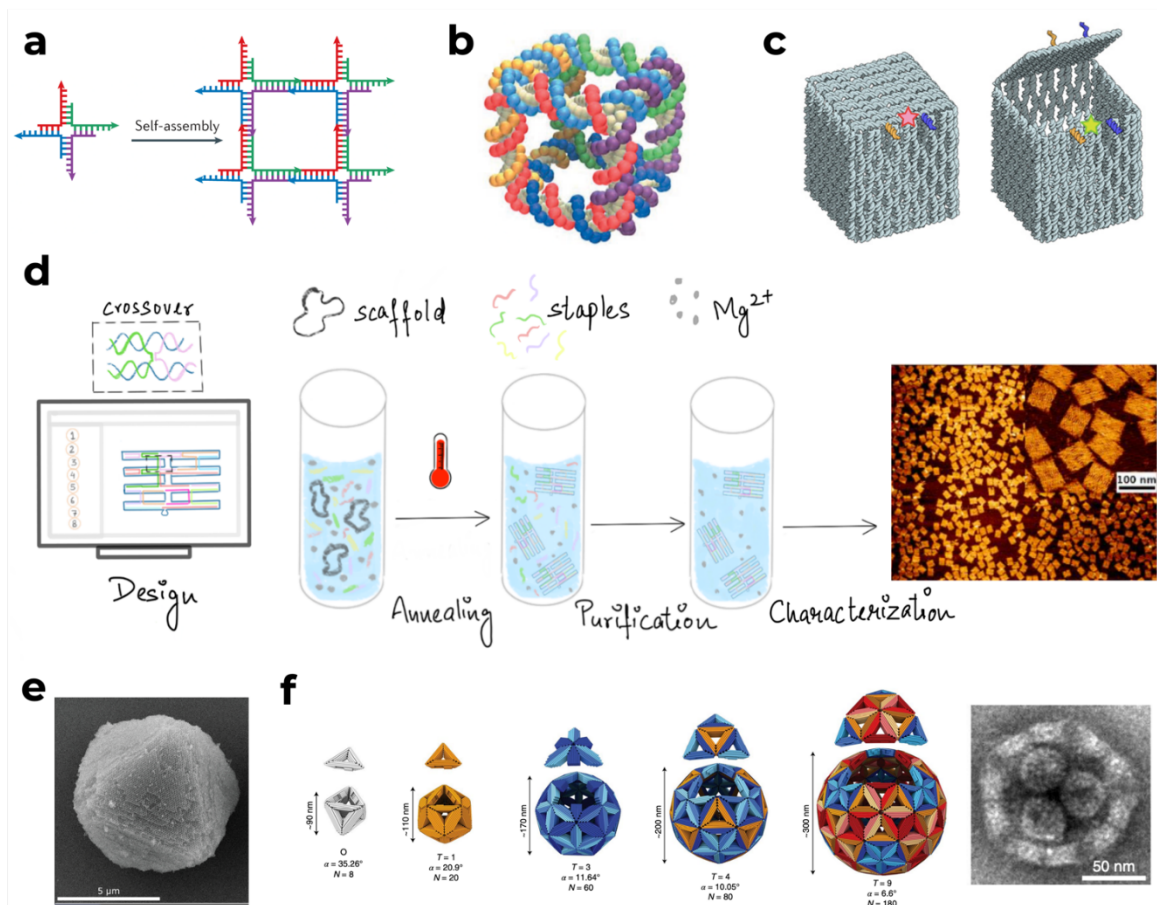


Figure 24. **a** Four-way DNA junction with self-complementary, single-stranded ends that assemble into a quadrilateral shape. Reproduced from Seeman, N. C. & Sleiman, H. F. *Nat Rev Mater* 3, 17068 (2017) with permission<sup>162</sup> by Springer Nature. **b** Reproduced from Seeman, N. C. *Biochemistry* 42, 7259-7269 (2003) with permission<sup>163</sup>. Copyright 2003 American Chemical Society. **c** A DNA box with a controllable lid.

Reproduced from Andersen, E. S. et. al. Nature 459, 73-76 (2009) with permission<sup>86</sup> by Springer Nature. Copyright 2009, Macmillan Publishers Limited. **d** Schematic workflow of DNA origami design, folding, purification and characterization by AFM. An exemplary image of a 2D rectangle origami imaged by AFM is shown<sup>164</sup>. The AFM image is reused with permission. Copyright 2019 American Chemical Society. **e** SEM image of DNA origami cubic diamond crystal covered with a layer of SiO<sub>2</sub>. From [ Posnjak, G. et. al. Science (1979) 384, 781-785 (2024)<sup>165</sup>]/Reprinted with permission from AAAS. **f** Variations in icosahedral shell designs and a TEM image showing three particles enclosed within one of the shell types. Reproduced from Sigl, C. et. al. Nat Mater 20, 1281-1289 (2021) with permission. Copyright 2021, The Author(s),<sup>166</sup> under exclusive licence to Springer Nature Limited.

A crucial development in DNA-based 3D nanostructures was creating immobile junctions<sup>167,168</sup> (Figure 24a). These junctions between DNA strands remain stable and do not undergo branch migration, serving as solid joints for complex constructions. In 1991, Seeman and his team built upon this and successfully demonstrated the assembly of DNA into cube-like structures<sup>169</sup> (Figure 24b). This transformed the field, leading to the rapid development of numerous 2D and 3D DNA nanotechnology constructs in subsequent years<sup>162</sup>. In 2006, Paul Rothemund introduced a new concept for building DNA constructs- DNA Origami<sup>83</sup>. The simplicity of this method helped expand the field of DNA Nanotechnology<sup>162,170-178</sup> with applications in biomedicine<sup>179-182</sup>, optics<sup>183-185</sup>, photonics<sup>186-190</sup>, biotechnology<sup>191-196</sup> and nanofabrication<sup>197-200</sup>. Initially many different 2D shapes were demonstrated such as smileys, stars, triangles, showcasing the possibility of creating virtually any 2D shape<sup>83</sup>. This was soon expanded to 3D structures mostly by two strategies- one involved joining 2D sheets at the edges to assemble a 3D box with a controllable lid<sup>86</sup> (Figure 24c), and the other involved pleated sheets of helices arranged in a honeycomb lattice to create 3D shapes<sup>92</sup>.

The word 'Origami' is the Japanese word for the art of paper folding. DNA origami is analogous to paper origami in the way complex structures are folded from a simple, flat sheet. In DNA origami (Figure 24d), a long, viral single-stranded DNA molecule (called *scaffold*) serves as the "paper", while short, custom-designed '*staple*' strands act as the "folds". These staple strands with complementary sequences are designed to specifically bind at various points along the scaffold strand, effectively folding it into a precise and pre-designed shape. As the sequence of the scaffold strand is known, one can precisely program how staple strands would hybridize. The process starts with designing the scaffold route to create the backbone of the structure on a software called caDNAno<sup>201</sup>. The software automatically suggests staple strands that are complementary to specific sections of the scaffold and crossover points where strands cross and switch helices. Once the design is complete, the software generates a list of all the staple

sequences needed to fold the scaffold into the desired shape. Folding involves a one-pot reaction, where a mixture of scaffold and a 5-10 times excess of staple strands is first heated to 65°C to denature, then slowly cooled, allowing the structures to assume their thermodynamically stable forms. The mixture also contains buffer to stabilize the pH and cations to screen the negatively-charged backbone of DNA. The addressability offered by the technique has allowed the field to progress rapidly with recent articles showing 3D supramolecular assemblies like crystals made of DNA origami<sup>165,202,203</sup> (Figure 24e) or a virus-trapping concept developed by assembling 8-180 triangular DNA-origami monomers into larger constructs with an internal cavity of up to 280 nm<sup>166</sup> (Figure 24f).

To create such 3D structures, the honeycomb lattice can be used which typically refers to an arrangement where each helix has neighbours at two sides, forming a continuous network of hexagons (Figure 25a). Another commonly used lattice is the square lattice, where each helix has neighbours at four sides<sup>204</sup> (Figure 25b). Furthermore, twists and curvatures were introduced in the 3D structures by targeted insertions or deletions of base pairs<sup>204</sup> (Figure 25c). Higher order assemblies were demonstrated using shape-complementary base-stacking<sup>206</sup> and with sticky-ends approach<sup>207</sup> (Figure 25d).

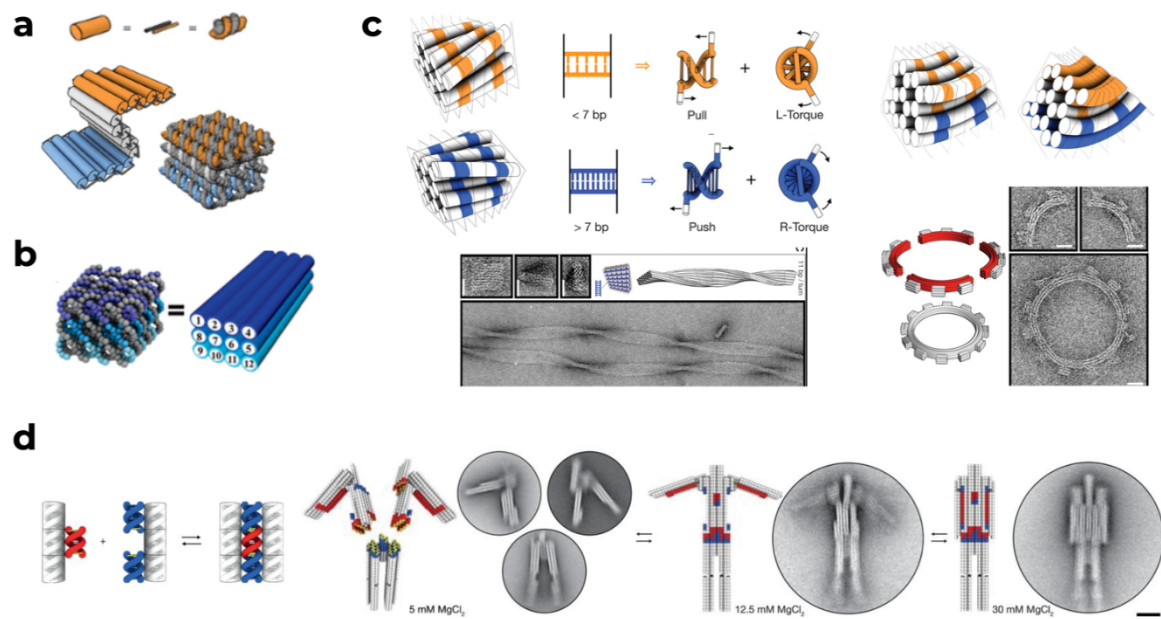


Figure 25. **a** Cylinder in orange represents double helices formed by scaffold (grey) and staple strands (orange, white, blue). A cylinder model of a partially rolled intermediate, where cylinders are connected by unpaired scaffold strand loops at the ends of adjacent helices. An atomistic DNA model of the shape follows this representation. Reproduced from Douglas, S. M. *et al. Nature* 459, 414–418 (2009) with permission<sup>82</sup>. Copyright 2009, Macmillan Publishers Limited. **b** The helices arranged in a square lattice,

with the scaffold strand shown in grey and the staple strands in blue. Each cylindrical rod on the right represents a DNA double helix, and the numbers at the helical ends denote the sequential order of the scaffold strand segments threading through the helices. Reproduced from Ke, Y. *et al. J Am Chem Soc* 131, 15903–15908 (2009) with permission<sup>204</sup>. Copyright 2009, American Chemical Society. **c** Design principles for adding twist or curvature to DNA bindles with example origami structures and their TEM images. From [Dietz, H., Douglas, S. M. & Shih, W. M. *Science (1979)* 325, 725–730 (2009).<sup>205</sup>]/Reprinted with permission by AAAS. **d** Schematic of a heterotrimeric nanorobot (15 MD) that shifts between three states—disassembled, and assembled with either open or closed arms—by adjusting cation concentrations. TEM micrographs show the nanorobot at various MgCl<sub>2</sub> levels, altered by adding or diluting MgCl<sub>2</sub> stock solution. From [Gerling, T., Wagenbauer, K. F., Neuner, A. M. & Dietz, H. *Science (1979)* 347, 1446–1452 (2015).<sup>206</sup>]/Reprinted with permission by AAAS.

DNA origami has also been applied to create dynamic structures. One of the examples is the use of 'toe-hold mediated strand displacement', wherein one of the two strands in the dsDNA duplex carries a short ssDNA sequence at the end that acts like a "handle" or "toe-hold", allowing the complementary ssDNA to initially bind. Once the ssDNA binds to the toe-hold, it begins to displace the shorter original strand in the DNA duplex through branch migration. This is a process where the invading strand pairs with its complementary bases on the duplex, gradually displacing the original complementary strand<sup>208</sup> (Figure 26a). The toe-hold is typically 4-12 nucleotides long and is crucial because its length and sequence can be designed to control the reaction kinetics. A variety of DNA-based molecular switches and devices were developed based on this method, finding applications in sensing, gene regulation and nanofabrication, to name a few<sup>209,210</sup>. In an alternate strategy, flexibility can be induced by leaving single-stranded regions in the DNA origami, resulting in dynamic behaviour. This was quickly adopted to create structures that could open and release cargo on addition of trigger strands<sup>211</sup>, nanostructures mimicking a hinge or a joint<sup>212</sup> (Figure 26b), and more recently, dynamic DNA robotic arm controlled by electric field<sup>213</sup>, a nanoscale rotary motor<sup>214</sup> (Figure 26c), DNA origami turbines<sup>215</sup> (Figure 26d) etc.

Beyond its structural capabilities, DNA origami's addressability is uniquely valuable, enabling the introduction of modifications or functionalities with nm precision. Often likened to a 'molecular breadboard'<sup>185</sup>, this technique supports a range of base modifications through advanced nucleic acid synthesis, including biotin for immobilization on glass coverslips<sup>10,45</sup>, thiols for nanoparticle binding<sup>98</sup>, pyrenes for immobilization on graphene<sup>164,216,217</sup>, cholesterol for interaction with lipid membranes and vesicles<sup>218,219</sup>, as well as optically active moieties like fluorophores<sup>220</sup>.

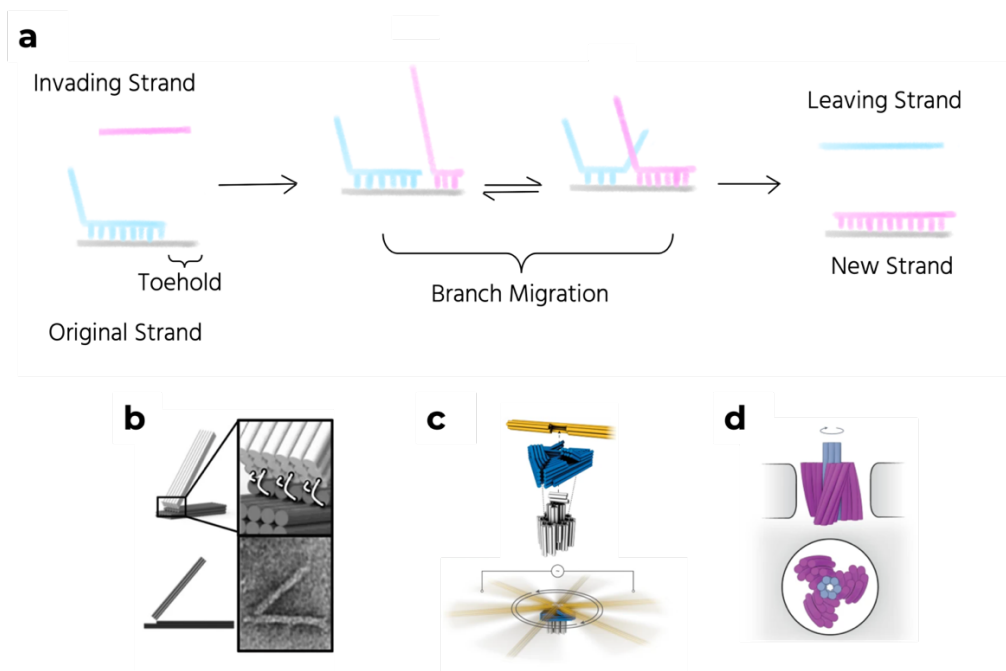


Figure 26. **a** Mechanism of toe-hold mediated strand displacement. **b** Leaving single-stranded regions in the DNA origami can be used to induce flexibility. Published<sup>212</sup>, Copyright 2015 National Academy of Sciences. **c** DNA origami-based nanoscale rotary motor. CC BY 4.0. Copyright 2022, The Author(s)<sup>214</sup>, published by Springer Nature. **d** Sketch of a DNA origami-based turbine. CC BY 4.0. Copyright 2023, The Author(s)<sup>215</sup>

## 2.4 MICROSCOPY SETUPS

### 2.4.1. CONFOCAL MICROSCOPY

Confocal microscopy is an advanced optical imaging method that enhances the resolution and contrast, by employing a spatial pinhole to filter out-of-focus light during image formation<sup>221</sup>. The concept, patented in 1957 by Marvin Minsky<sup>222</sup>, was developed to address some limitations of traditional wide-field fluorescence microscopes<sup>223</sup>, where the entire specimen is uniformly illuminated and all parts are excited simultaneously, resulting in a high background in the images. Confocal microscopy (Figure 27) utilizes point illumination and a strategically placed pinhole in the optically conjugate plane in front of the detector, which allows only the light from the focal plane very close to the point of fluorescence to be detected, effectively eliminating out-of-focus signals. This method significantly enhances the optical resolution, especially in the depth direction of the sample, compared to wide-field microscopes. To compensate for the reduced light, confocal systems use highly sensitive detectors, such as



photomultiplier tubes (PMT) or avalanche photodiodes, which convert the diminished light signals into electrical ones, ensuring detailed and high-resolution imaging<sup>224</sup>.

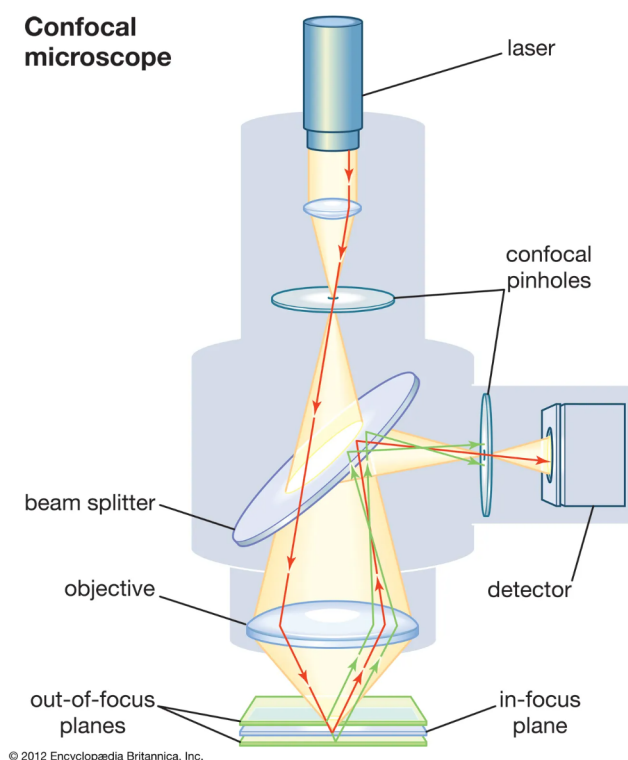


Figure 27. Schematic of a confocal microscope taken from Encyclopædia Britannica<sup>225</sup>

In this thesis, two different confocal setups were used for single-molecule fluorescence imaging:

**Setup 1:** A home-built confocal setup utilizing an Olympus IX71 microscope was employed for measurements<sup>10</sup>. Red and green lasers (LDH-D-C-640 and LDH-P-FA-530B, PicoQuant GmbH, Germany) were operated using a PDL 828 “Sepia II” controller from PicoQuant GmbH, Germany. The green laser light was transmitted through a polarization-maintaining fibre, then cleaned using a Z532/10X filter (Chroma Technology, USA) and combined with red laser light via a 640 LPXR dichroic mirror (Chroma Technology, USA). The lasers were merged using a P3-488PM-FC fibre (Thorlabs) and modified for circular polarization with a WP12L-Vis linear polarizer (Thorlabs) and an AQWP05M-600 quarter-wave plate (Thorlabs). The combined beam was then focused on the samples using a UPLSAPO 100 XO oil immersion objective (Olympus Corporation, Japan). Sample positioning was controlled with a P-527.3CD piezo-stage and an E-727 controller from Physik Instrumente GmbH & Co. KG, Germany. The collected light was narrowed through a 50  $\mu\text{m}$  pinhole (Linos) and collimated with a lens (AC050-150-A-ML, Thorlabs). After passing a dichroic beam splitter (640LPXR, Chroma Technology, USA) and a combination of two filters (red: 731/137 BrightLine HC, Semrock Inc., USA, and Razor Edge 647

nm, Semrock Inc., USA; green: 582/75 BrightLine HC, Semrock Inc., USA, and Razor Edge 532 nm, Semrock Inc., USA), the beam is focused via a lens (AC080-020-B-ML, Thorlabs) on an APD (SPCM-AQRH-TR-14, Excelitas). Signals were processed using a HydraHarp 400 and managed via SymPhoTime 64 software from PicoQuant GmbH, Germany.

**Setup 2:** Measurements were conducted using a home-built confocal setup based on an IX-83 inverted microscope (Olympus Corporation, Japan) and a SuperK Extreme EXW-12 pulsed supercontinuum white light laser (NKT Photonics A/S, Denmark) with selected 532 nm and 639 nm wavelengths via an acousto-optically tuneable filter SuperK Dual AOTF (NKT Photonics A/S, Denmark)<sup>5</sup>. This is controlled through an AODS 20160 8R digital controller (Crystal Technology, USA) and supplementary LabVIEW (National Instruments, USA) software for the AOTFs (AA.AOTF.ns: TN, AA Opto-Electronic, France). Laser intensity and polarization were managed with a neutral density filter and a  $\lambda/4$  plate. The excitation beam was directed onto the sample using a UPlanSApo 100 $\times$  objective (Olympus Corporation, Japan) and ZT532/640rpc dichroic beam splitter (Chroma Technology, USA). A P-517.3CL piezo-stage (Physik Instrumente GmbH & Co. KG, Germany) facilitated micropositioning. The emitted light was initially filtered through the same objective and dichroic beam splitter, then further focused through a 50  $\mu\text{m}$  pinhole (Linos AG, Germany) and detected by avalanche photodiodes (SPCM, AQR 14, PerkinElmer, Inc., USA) using a TCSPC system (HydraHarp 400, PicoQuant GmbH, Germany) after additional spectral filtering (RazorEdge 647, Semrock Inc., USA for the red channel and BrightLine HC 582/75, Semrock Inc., USA for the green channel)

## 2.4.2. TIRF MICROSCOPE

Introduced in 1910, widefield fluorescence was an optical imaging technique that included illumination of the entire sample<sup>226</sup>. This type of imaging was prone to high background signal. Later in the 1980s, a new type called total internal reflection fluorescence microscope (TIRFM) was introduced, which reduced the background signal significantly by only illuminating a thin section of the sample<sup>227</sup>. TIRFM employs an evanescent wave<sup>N</sup> to excite fluorophores specifically in a restricted region near the glass-water interface of the specimen (Figure 28a). This evanescent electromagnetic field exponentially decreases from the interface, penetrating merely about 100 nm into the sample medium.

---

<sup>N</sup> An *evanescent wave* is a non-propagating electromagnetic wave that occurs during total internal reflection when the wave encounters a medium boundary at an angle greater than the critical angle. This wave decays exponentially with distance from the interface and does not transmit energy into the second medium.



There are two common setups based on TIRFM namely, Prism-based TIRFM and Objective-based TIRFM (Figure 28b). In prism-based TIRFM, a light beam is directed through a prism to strike the interface between two media (typically a glass slide and a sample medium) at angles greater than the critical angle for total internal reflection. This method is advantageous for its stability and the ability to achieve very shallow penetration depths, but it limits access to the sample and can be complex to set up. Objective-based TIRFM utilizes a high numerical aperture microscope objective to direct excitation light into a sample at supercritical angles directly through the microscope slide. This technique is more commonly used due to its integration with standard fluorescence microscopes, ease of use, and flexibility in handling live cell samples. It also allows for dynamic control over the incident angle and focal plane. In this thesis, a commercial objective-based TIRF microscope was used- Nanoimager from ONI, UK.

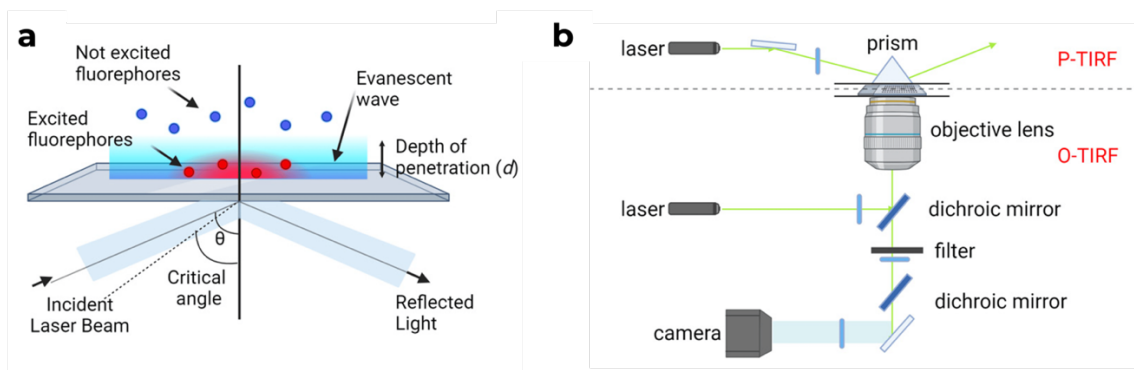


Figure 28. **a** Working principle of TIRFM. **b** The two types of TIRFM- prism (P) and objective (O). Images licensed under CC BY 4.0. Copyright 2023 by the authors<sup>228</sup>.

TIRFM relies on total internal reflection, a phenomenon where light is entirely reflected back into a medium (medium 1) with a higher refractive index and does not transmit into a second medium (medium 2) with a lower refractive index<sup>229</sup>. This occurs when light strikes the interface at angles greater than the critical angle, determined by Snell's law:

$$\theta_c = \sin^{-1} \frac{n_1}{n_2} \quad (2.13)$$

where  $n_1$  is the refractive index of the glass coverslip and  $n_2$  is that of the sample solution. Alongside total internal reflection, an evanescent wave forms at the interface, extending perpendicularly into medium 2 and decaying exponentially. This decay is influenced by the wavelength, refractive index, and the angle of incidence. The evanescent wave, penetrating only about 100 nm, selectively excites fluorophores near the surface, reducing unnecessary excitation within the bulk of the solution.

In objective-based TIRFM, the coverslip is often placed close to the lens with immersion oil to minimize refraction through air. The intensity of the evanescent wave  $I(z)$  is modelled as:

$$I(z) = I_0 e^{-z/d} \quad (2.14)$$

The penetration depth  $d$  can be described as:

$$d = \frac{\lambda_0}{4\pi} \sqrt{n_2^2 \sin^2 \theta - n_1^2} \quad (2.15)$$

To control the excitation within the sample, the wavelength  $\lambda_0$  and the range of incidence angles  $\theta$  are tailored through the objective's numerical aperture (NA), which must exceed the refractive index  $n$ . The refractive indices of the cover slip and solution are either measured or provided by the manufacturer. This setup allows TIRFM to achieve highly localized fluorescence imaging with minimal background noise.

## INTRODUCING DNA ORIGAMI NANOANTENNAS

### 3.1 A SHORT REVIEW

By arranging plasmonic nanoparticles on the DNA scaffold, DNA origami is used to create plasmonic nanoantennas that localize and enhance electromagnetic fields, allowing a significant enhancement in fluorescence<sup>84</sup> and Raman signals<sup>230</sup>. For additional information on enhancing Raman signals, the reader is encouraged to check these articles<sup>96,231–245</sup>. Here, I highlight the evolution of nanoantenna designs, primarily focusing on how modifications have led to improved fluorescence enhancement.

The early designs of DNA-assembled nanoantennas (DANs) utilized gold nanoparticles (AuNPs) due to their favourable plasmonic properties. Acuna et al. developed one of the first DANs by arranging two 100 nm AuNPs with a 23 nm gap on a 3D DNA origami pillar, placing a single fluorophore (ATTO 647N) in the plasmonic hotspot (Figure 29a)<sup>4</sup>. This configuration achieved up to a 117-fold enhancement in fluorescence intensity, demonstrating the potential of DNA origami for precise NP positioning and fluorescence enhancement

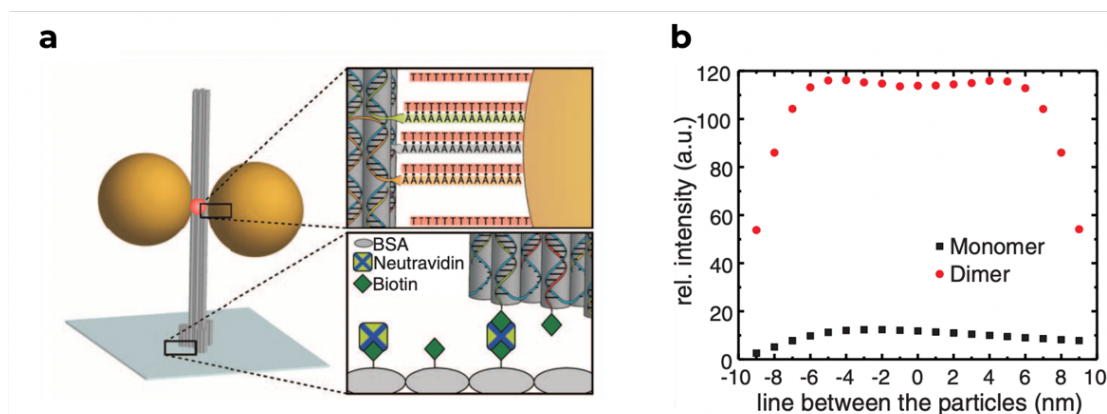


Figure 29. **a** Schematic of a 3D DNA origami pillar capturing two AuNPs forming a dimer nanoantenna, with a fluorophore (in red) at the hotspot. The NPs are captured by complementary strand hybridization and the structure is immobilized on glass via biotin-avidin chemistry. **b** Numerical simulations predicting the fluorescence enhancement values along the gap connecting the NPs for a fluorophore oriented

radially. From [Acuna, G. P. et. al. Science (1979) 338, 506-510 (2012)<sup>41</sup>]/Reprinted with permission from AAAS.

Recognizing that fluorescence enhancement depends on the size, shape, and material of the plasmonic NPs, as well as the distance and orientation between the fluorophore and the NPs (Figure 29b)<sup>62</sup>, researchers explored various configurations. Larger NPs, such as 100 nm AuNPs, offer higher field enhancement<sup>45,84</sup> compared to smaller ones. Efforts were made to reduce the gap between NPs to intensify the plasmonic hotspot. The top part of the DNA origami nanostructure was made thinner to allow particles to allow NPs to come closer<sup>141</sup>. Using a zipper configuration<sup>141</sup> and functionalizing NPs with 20-nucleotide ssDNA<sup>246</sup> strands reduced the gap between NPs from 23 nm to 12-17 nm, increasing fluorescence enhancement up to 471-fold for a 100 nm AuNP dimer nanoantenna<sup>141,247</sup>.

Nanoantennas utilizing AuNPs typically show fluorescence enhancement in the red to near-infrared (NIR) spectral regions. Silver nanoparticles (AgNPs), on the other hand, exhibit plasmon resonance in the violet-blue spectral region, which can be red-shifted upon dimerization, enabling coupling with dyes across a broad spectral range<sup>85,142,248</sup>. To extend the operational wavelength range, AgNPs were used. Vietz et al. demonstrated that AgNP-based nanoantennas provided superior performance across a broad spectral range, achieving significant fluorescence enhancement for dyes like Alexa 488, ATTO 542, and ATTO 647N<sup>248</sup>. AuNRs with high aspect ratios and sharp tips generate stronger localized fields. Design modifications incorporated AuNRs into DNA origami nanoantennas, leading to enhancements of up to 473-fold for ATTO 655<sup>249</sup> dye and up to 1600-fold<sup>250</sup> for near-infrared dyes in advanced configurations like NanoAntennas with Cleared Hotspots (NACHOS).

The evolution of nanoantenna design (Figure 30) continued with innovations aimed at maximizing fluorescence enhancement. For instance, maintaining a vertical orientation of the DNA origami structures helps align the NP dipoles with the incident light polarization<sup>45,251</sup>, optimizing the excitation of plasmonic modes. Next, the NACHOS design involves creating a cleared space in the DNA origami scaffold between the NPs, allowing the fluorophore to reside closer to the plasmonic hotspot without steric hindrance as well as incorporation of bioassays or larger biomolecules<sup>5,252</sup>. The latest design of nanoantennas which is also used for this thesis is a second generation NACHOS 2.0 (Figure 30) with a gap of 19 nm between the external origami pillars compared to 6.5 nm in the previous design<sup>253</sup>.

The advancements in DNA origami nanoantenna design have led to several key benefits. The nanoantennas significantly reduce the excitation volume to the zeptoliter ( $10^{-21}$ ) scale, which

is a million times smaller than typical confocal volumes<sup>45</sup>. This reduction minimizes background fluorescence and enables single-molecule measurements even in high-concentration environments relevant to biological systems<sup>141</sup>. The increased radiative decay rates<sup>254</sup> within plasmonic hotspots lead to shorter fluorescence lifetimes and reduce the time fluorophores spend in reactive excited states<sup>255</sup>. This results in enhanced photostability and allows fluorophores to emit more photons before photobleaching<sup>254,256,257</sup>. These advancements deepened our understanding of light-matter interactions at the nanoscale and paved the way for practical applications in ultra-sensitive biosensing and diagnostics.



Figure 30. Sketch portraying the evolution of the 3D nanoantenna design in the Tinnefeld lab.

### 3.2 APPLICATION IN BIOSENSING

As DNA Origami Nanoantennas (DONs) allow physical amplification of the fluorescence signal from a single molecule, they can boost the assay with improved speed, robustness and multiplexing capabilities<sup>45</sup>. They also overcome the problem of a low SNR caused by the background signal from the large number of impurities present in the observation volume contributing to scattering, autofluorescence and unspecific binding<sup>258</sup>.

One of the first examples of a bioassay using DONs featured a pillar-shaped DNA origami with a fluorescence-quenching hairpin (FQH) near an 80 nm AgNP<sup>259</sup>. In the closed state, ATTO 647N fluorescence was quenched by a BlackBerry quencher 650 (BBQ650) (Figure 31a). Binding to the target molecule (synthetic Zika virus DNA and RNA) opened the hairpin, separating the dye and quencher, restoring the fluorescence signal amplified by the AgNP. This enabled specific detection of DNA targets in buffer and heat-deactivated human serum, with fluorescence enhancement values of 7.3 and 4.9, respectively (Figure 31b). Multiplexing was demonstrated by incorporating different fluorophores at the base of the DNA origami structure as barcodes, allowing simultaneous detection of two DNA sequences (Figure 31c)<sup>259</sup>.

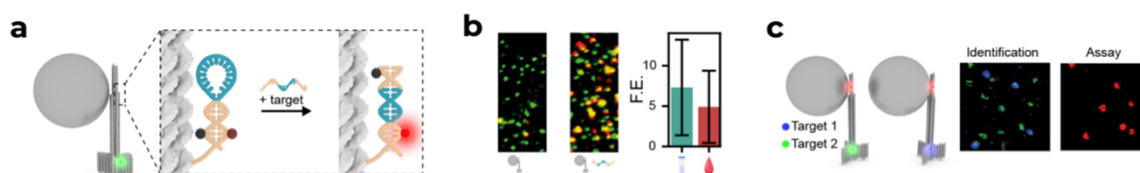


Figure 31. **a** Sketch of the FQH assay incorporated in the DNA origami nanoantenna and its working principle. **b** Confocal fluorescence scans before and after detection of the Zika-specific target strand in heat-deactivated human serum and the fluorescence enhancement (FE) values in buffer and serum. **c** Strategy for multiplexing by barcoding the DNA origami structures with two different localization dyes (green and blue). Copyright 2021<sup>45</sup>. Published by American Chemical Society, licensed under CC-BY-NC-ND 4.0

This study laid the foundation for future applications in diagnostics but also highlighted challenges. The FQH in the hotspot reduced accessibility and increased steric hindrance, preventing the binding of a second nanoparticle for dimer formation, resulting in modest signal enhancement<sup>98,259</sup>. Optimizing the pillar-shaped DNA origami design to enhance nanoparticle binding is a potential future direction. Additionally, significant false positives in the FQH assay call for improved specificity in target recognition<sup>259</sup>. Studies indicate that a plasmonic hotspot might accelerate selective photobleaching of the quencher, leading to higher false positives<sup>256,260</sup>. Future assays should consider eliminating the quencher to reduce this issue. Addressing these challenges could advance the use of DONs for diagnostics in low-resource point-of-care settings.

Before we go deeper into diagnostics, let's discuss what is point-of-care (POC) diagnostics and why is it important? POC diagnostics are essential tools that facilitate rapid and efficient detection of genetic material from pathogens or genetic markers for diseases, directly at or near the site of patient care<sup>261</sup>. This approach is vital for timely decision-making in clinical and field settings, reducing the reliance on centralized laboratories. Especially for nucleic acids, methods such as PCR and loop-mediated isothermal amplification (LAMP) and more recently CRISPR are commonly used, as we also briefly discussed in Chapter 1. While these methods are designed to be fast, require minimal sample preparation and are often integrated into user-friendly devices, they have certain disadvantages. PCR, for example, can suffer from both false negatives due to degradation, or due to the presence of inhibitors, and false positives due to contamination during the collection and processing of the samples<sup>262</sup>. Furthermore, PCR requires thermal cyclers, which are sophisticated and can be challenging to miniaturize and maintain for point-of-care settings. Although isothermal, LAMP still requires precise temperature control, and the need for multiple primers, increasing the complexity of test

design and potential for non-specific amplification<sup>263</sup>. Two major challenges limit CRISPR-based diagnostics for POC and home use- lengthy sample processing requiring instrumentation and the need for ultralow temperature storage<sup>264</sup>.

Utilizing the intrinsic signal amplification capability of nanoantennas could enable single-molecule detection using simple, low numerical aperture optics, opening new applications in point-of-care technology. Previous studies indicate that detecting a signal equivalent to at least 16 single emitters is necessary for effective use with low-numerical aperture microscope configurations, such as those based on smartphones<sup>265</sup>. This would require tackling the following challenges:

1. a change of design for more efficient nanoparticle binding.
2. an assay that allows specific target recognition.
3. ways to overcome the concentration barrier problem and detect trace amounts of target molecules efficiently.
4. a low-tech device that is capable of single-molecule readout enabled by DONs.

Implementing these steps would advance point-of-care diagnostics using DNA Origami Nanoantennas, enabling a user-friendly process where adding the patient's sample is the primary requirement, and the subsequent assay steps, data acquisition, and analysis are automated or require minimal expertise.

### **3.2.1 CAN WE USE A LOW-TECH DEVICE TO SEE SINGLE MOLECULES?**

In 2021, led by Kateryna Trofymchuk and Viktorija Glembockyte, we developed the next generation of DONs, NanoAntennas with Cleared HOtSpots (NACHOS), that allowed high fluorescence enhancement (up to 417-fold with an average of  $74 \pm 3$ -fold) and bioassay incorporation in the nanoantenna hotspot<sup>5</sup>. The new design featured a novel three-dimensional DNA origami structure with two pillars, each having extensions to bind 100 nm AgNPs (Figure 32). The design created a plasmonic hotspot at the bifurcation in the gap between the two pillars and the nanoparticles, leaving the hotspot space free for binding targets needed for nucleic acid bioassays.

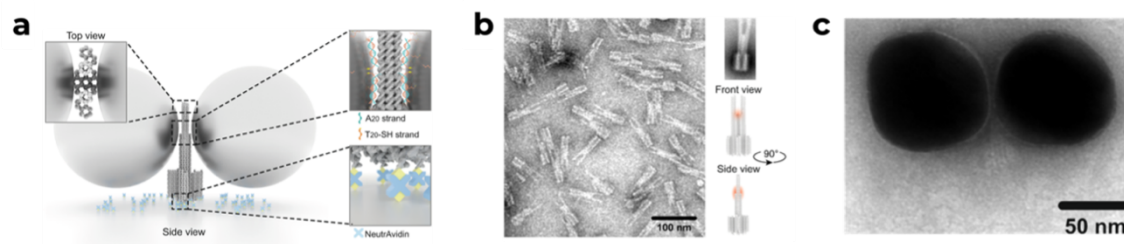


Figure 32. **a** Design of NACHOS. **b** TEM image of the pillared structure. **c** TEM image of a fully assembled NACHOS. Reproduced with permission<sup>5</sup>. CC Attribution 4.0 International License. Published by Springer Nature.

We designed a sandwich binding assay to detect a DNA fragment specific to OXA-48, a gene responsible for carbapenemase production in antibiotic-resistant *Klebsiella pneumoniae* (Figure 33). Three capture strands specific to the target DNA were incorporated, extending into the plasmonic hotspot of the NACHOS to optimize target binding (Figure 33a). The assay's principle involves a 17-nt capture strand complementary to half of the 34-nt target DNA strand (Figure 33a). Binding of the target DNA provides an overhang for a 17-nt dye-labelled imager strand, which is then incorporated into the plasmonic hotspot, where the signal is amplified by the nanoantenna (Figure 33a, b). Binding efficiencies of 66% in NACHOS and 84% in the reference structures indicated that attaching two 100 nm silver nanoparticles did not significantly compromise hotspot accessibility for the target DNA sequence<sup>5</sup>. Moreover, ~60% of NACHOS contained one imager strand in the hotspot, one-third contained two strands, and 8-11% had three strands, quantified using single-step bleaching analysis<sup>5</sup>. The assay showed similar performance in target-spiked, heat-inactivated human serum.

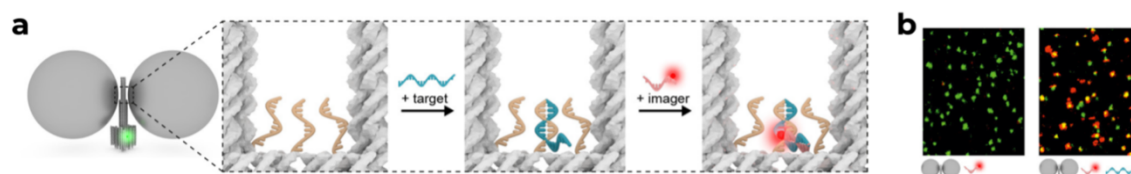


Figure 33. **a** Sketch of the sandwich binding assay incorporated in the hotspot of NACHOS and its working principle. **b** Confocal fluorescence scans before and after the target capture. Copyright 2021<sup>45</sup>. Published by American Chemical Society, licensed under CC-BY-NC-ND 4.0

A key advantage of using NACHOS for the sandwich binding assay is that it amplifies only the signal from specific binding to the target sequence within the nanoantenna hotspot<sup>5</sup>. Signals from non-specific binding to the DNA origami scaffold or glass coverslip are not amplified, as seen in Figure 34a. Next, we developed a portable smartphone-based microscope that uses the camera of a smartphone for detection, a battery-driven laser for excitation and a 0.25 NA objective lens<sup>5</sup> (Figure 34b). We successfully observed 1-3 bleaching steps in the assay, while



control measurements without NPs showed no signal (Figure 34c). This demonstrated that DONs can be effectively used to democratize single-molecule detection with a low-tech and cost-effective device, relevant for point-of-care applications<sup>5</sup>.

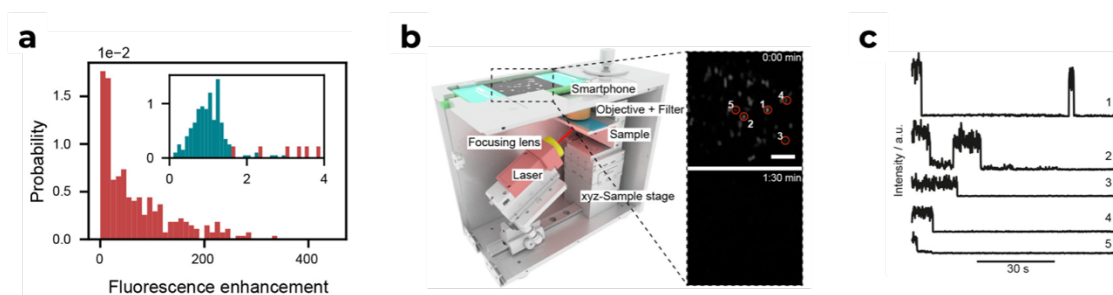


Figure 34. **a** FE values for the sandwich binding assay in the NACHOS in red compared to the intensity distribution from a single fluorophore in the inset (blue) clearly distinguishing the target-specific signal from single molecule impurities. **b** portable smartphone-based microscope capable of detecting single molecules and snapshots from the movie. **c** Exemplary fluorescence intensity vs time transients for the sandwich binding assay extracted from the movie, showing one, two or three bleaching steps corresponding to the number of target molecules captured. Copyright 2021<sup>45</sup>. Published by American Chemical Society, licensed under CC-BY-NC-ND 4.0

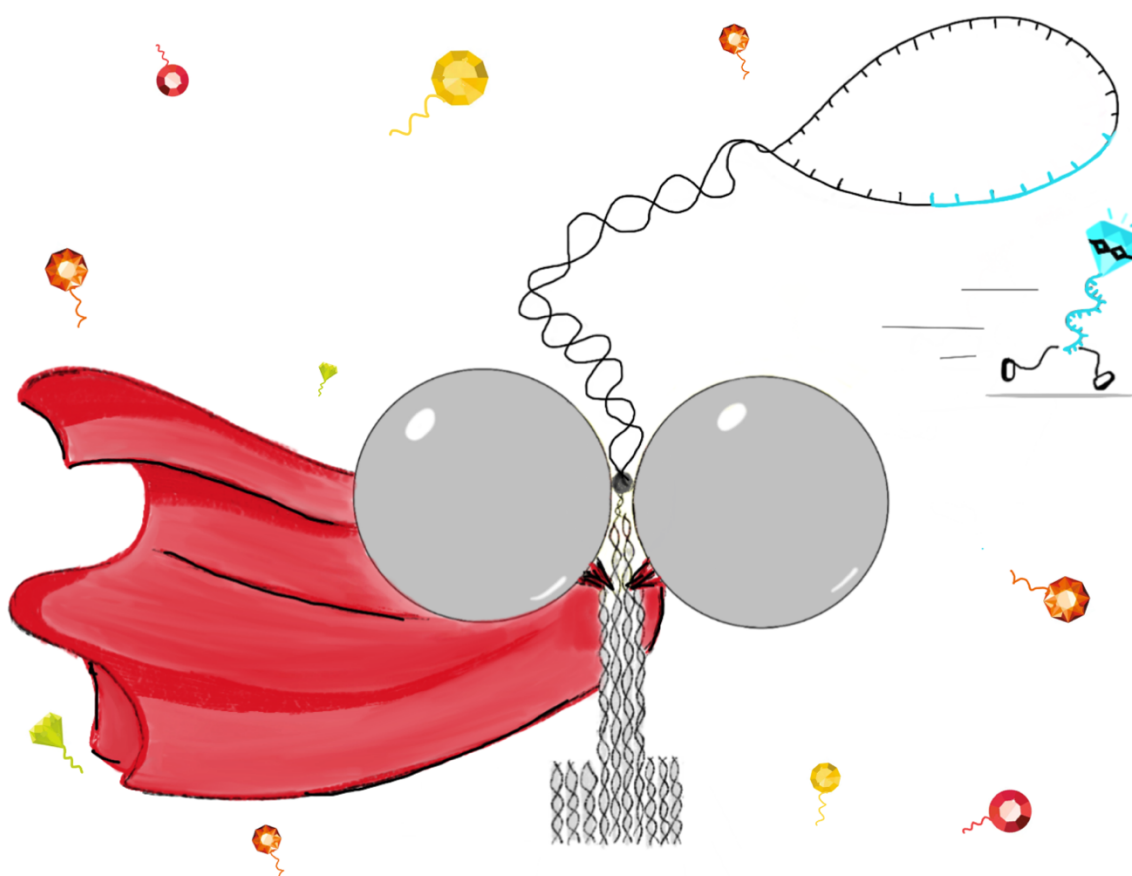
This section was a brief summary of the publication- *Addressable nanoantennas with cleared hotspots for single-molecule detection on a portable smartphone microscope* by Kateryna Trofymchuk, Viktorija Glembockyte, Lennart Grabenhorst, Florian Steiner, Carolin Vietz, Cindy Close, Martina Pfeiffer, Lars Richter, Max L. Schütte, Florian Selbach, **Renukka Yaadav**, Jonas Zähringer, Qingshan Wei, Aydogan Ozcan, Birka Lalkens, Guillermo P. Acuna & Philip Tinnefeld, published in *Nature Communications* (2021).

**Author Contributions:** P.T., A.O. and G.P.A. conceived the project, L.G. and B.L. developed the DNA origami structure, K.T., V.G. and M.P. optimized the solution synthesis procedure, F.Se. performed the TEM measurements, K.T., V.G., C.C., M.P. and **R.Y. developed the sandwich assay and prepared samples, performed and analyzed the measurements on the confocal microscope**, C.V., L.R., M.L.S., Q.W., A.O. and G.P.A. worked on an earlier version of the smartphone microscope, K.T., V.G., F.St. and J.Z. constructed the portable smartphone microscope, K.T., V.G. and F.St. performed and analyzed the measurements on the smartphone microscope, K.T., V.G., L.G., F.St. and P.T. wrote the manuscript. All authors have read and approved the final manuscript.

# 4

## BRINGING ATTOMOLAR DETECTION TO POC DIAGNOSTICS

### 4.1 OVERVIEW



Point-of-care testing signifies a transformative approach in medical diagnostics, where evaluations are conducted promptly at or near the site of patient interaction. This method is pivotal in streamlining clinical decision-making, enabling the selection of precise treatments, and ensuring the judicious use of healthcare resources through timely medical interventions. Particularly in developing regions, POC diagnostics are crucial, extending critical healthcare services to underserved populations and significantly reducing reliance on expansive, centralized laboratory facilities.

We set out to develop DNA origami NanoAntennas as a tool to amplify the signal of fluorophores reporting the presence of an infectious DNA or RNA. The goal was twofold: enhance the assay's sensitivity, ensuring that even weak signals from target molecules could be discerned against the complex matrix of bodily fluids, and develop a system compatible with point-of-care use without the necessity for costly, sophisticated microscopy equipment. Over a decade, the Tinnefeld group achieved various milestones in this direction, with the most recent being detection of single molecules enhanced by the NanoAntennas on a smartphone-based device<sup>5</sup>. This breakthrough motivated us to ask the question- can we develop DNA origami nanoantenna-based biosensing chips for highly sensitive single-molecule detection at the point of care? The answer- Yes!

In the associated publication P1, we first start with the assay and focus on how to maximise the specific interaction and how to minimise the unspecific interaction. To maximise the specific interaction, we increased the number of recognition units (capture strands) per DNA origami, which allowed us to catch more target strands per origami. To reduce the unspecific interaction, we design a temporary blocking strand that hybridizes with the capture strand in absence of the target strand. This blocker reduces the interaction of the fluorophore (imager strand) in the hotspot region in the absence of target, thus reducing false-positives. The next step is to increase the number of NanoAntennas on the surface. We do this by employing DNA origami placement (DOP) method<sup>6</sup> that allows placement of individual NanoAntennas in a hexagonal array of hydrophilic placement sites. Each site is 400 nm apart from each other which renders a high surface density of functional NanoAntennas. Next, we integrate a self-adhesive microfluidic chip to perform repetitive back and forth flow during target incubation. This plays a significant role in improving the kinetics of the assay. Then, we develop a fluorescence reader that is capable of automated fluidics, has a 2.5 mm x 3 mm FOV and an in-built software for single-molecule detection and analysis. We use the DOP to restrict the immobilization of NanoAntennas only to the FOV, further improving the chance of counting most of the molecules captured. With these elements combined, we detect 5 aM concentration as the lowest detectable concentration above blank, of a synthetic 151-nucleotide DNA sequence specific to antibiotic-resistant *Klebsiella pneumoniae*, in a 100  $\mu$ l of sample. In other words, we detect ~100 out of ~300 molecules within an hour of incubation. Furthermore, biosensing requires detection compatibility in clinically relevant fluids like blood, urine, or saliva, which are full of impurities unlike the carefully optimized buffers. To address this, we coated the NanoAntennas with silica in a process called silicification<sup>7,8,266</sup>. This creates

a 3-5 nm thin shell of silica around the double stranded regions of DNA, protecting it against degradation by enzymes, fluctuations in ionic strengths, pH and temperature. This selective coating doesn't interact with single stranded regions which means the recognition sites for the assay remain unaffected<sup>9</sup>. We achieve 10 aM limit of detection after silicification of NanoAntennas in untreated human blood plasma.

The cost of a diagnostic test often determines its accessibility to those most in need. Making the chips reusable and offering users the ability to modify the same chip for detecting various target sequences can thus benefit PoC applications. We use toehold-mediated strand-displacement<sup>208</sup> to displace the bound target-imager duplex from the capture strand, making the capture strand accessible for the next round of use.

Through these advances, we hope to set a new standard for integrating nanotechnology with molecular diagnostics at the point of care. This approach holds promise for a wide range of applications, including but not limited to, infectious disease diagnostics, cancer screening, and monitoring of biomarkers for various other diseases, making it a versatile tool in the global health arsenal.

## 4.2 ASSOCIATED PUBLICATION. 1

### **Bringing Attomolar Detection to the Point-of-Care with Nanopatterned DNA Origami NanoAntennas**

by

Renukka Yaadav, Kateryna Trofymchuk, Mihir Dass, Vivien Behrendt, Benedikt Hauer,  
Jan Schütz, Cindy Close, Michael Scheckenbach, Giovanni Ferrari, Leoni Maeurer,  
Sophia Sebina, Viktorija Glembockyte, Tim Liedl, Philip Tinnefeld

uploaded to

*bioRxiv 2024.10.14.618183. 10.1101/2024.10.14.618183*

This publication is licensed under CC BY-NC 4.0..

# Bringing Attomolar Detection to the Point-of-Care with Nanopatterned DNA Origami Nanoantennas

Renukka Yaadav<sup>1</sup>, Kateryna Trofymchuk<sup>1</sup>, Mihir Dass<sup>2</sup>, Vivien Behrendt<sup>3</sup>, Benedikt Hauer<sup>3</sup>, Jan Schütz<sup>3</sup>, Cindy Close<sup>1</sup>, Michael Scheckenbach<sup>1</sup>, Giovanni Ferrari<sup>1</sup>, Leoni Maeurer<sup>1</sup>, Sophia Sebina<sup>1</sup>, Viktorija Glembockyte<sup>1</sup>, Tim Liedl<sup>2</sup>, Philip Tinnefeld<sup>1,\*</sup>

<sup>1</sup>Department of Chemistry and Center for NanoScience, Ludwig-Maximilians-University, Butenandtstraße 5–13, 81377 Munich, Germany

<sup>2</sup>Faculty of Physics and Center for NanoScience, Ludwig-Maximilians-University, 80539 Munich, Germany

<sup>3</sup>Fraunhofer Institute for Physical Measurement Techniques IPM, Georges-Köhler-Allee 301, 79110 Freiburg, Germany

KEYWORDS: DNA origami NanoAntenna, Point-of-Care, single-molecule detection, biosensing, fluorescence enhancement

Corresponding author email: Philip.tinnefeld@cup.lmu.de

## Abstract

Creating increasingly sensitive and cost-effective nucleic acid detection methods is critical for enhancing point-of-care (POC) applications. This involves capturing all desired biomarkers in a sample with high specificity and transducing the capture events to a detector. However, the signal from biomarkers present at extremely low amounts often falls below the detection limit of typical fluorescence-based methods, making molecular amplification a necessary step. Here, we present a nucleic acid detection assay of a 151-nucleotide sequence specific to antibiotics-resistant *Klebsiella pneumoniae*, based on single-molecule fluorescence detection of non-amplified DNA down to the attomolar level, using Trident NanoAntennas with Cleared HOtSpots (NACHOS). Our NACHOS-diagnostics assay leverages a compact microscope with a large field-of-view and cost-efficient components, including microfluidic flow to enhance capturing efficiency. Fluorescence enhancement is provided by DNA origami NanoAntennas,

arranged in a dense array using a combination of nanosphere lithography and site-specific DNA origami placement. Our method can detect  $200 \pm 50$  out of 600 molecules in a  $100 \mu\text{L}$  sample volume within an hour. This represents typical number of pathogens in clinical samples commonly detected by Polymerase Chain Reaction but without the need for molecular amplification. We achieve similar sensitivity in untreated human blood plasma, enhancing the practical applicability of the system. Our platform can be adapted to detect shorter nucleic acid fragments that are not compatible with traditional amplification-based technologies. This broadens its potential for diverse diagnostic and healthcare applications, providing a robust and scalable solution for sensitive nucleic acid detection in various clinical settings.

## Introduction

Single-molecule methods are gaining ground in bioanalytical applications like nucleic acid sequencing and sensitive analyte detection.<sup>1-4</sup> For Point-of-Care (POC) detection in low-technology environments, however, single-molecule approaches, are still considered prohibitively expensive due to their reliance on sophisticated setups. For instance, single-molecule detection using fluorescence often requires either molecular multiplication to detect the target's signal against background noise or expensive instrumentation to detect single fluorescent molecules directly.<sup>1,5,6</sup> Advances in plasmonic fluorescence enhancement,<sup>7-9</sup> utilizing DNA origami nanostructures,<sup>10-12</sup> have facilitated signal amplification of fluorophores captured in the hotspot, improving the distinction of the real signal from background impurities and enabling single-molecule detection using a portable, battery-driven smartphone microscope.<sup>13</sup> But their use for target detection at clinically relevant nucleic acid concentrations below the picomolar range<sup>14</sup> has remained elusive.

Arguably, analytical methods cannot get more sensitive than detecting a single molecule and concentration determination cannot become more direct than digitally counting all molecules in a sample.<sup>2,15-17</sup> Single-molecule detection is thus swiftly moving towards the development of affordable, portable devices, making it accessible outside of specialized laboratories and into POC and field settings.<sup>13,18-23</sup> The challenge here is not to detect the single molecule present in a (typically very small) detection volume, but to find all molecules in the patient sample. At  $1 \text{ aM}$  ( $10^{-18} \text{ mol/L}$ ) concentration,  $100 \mu\text{L}$  of blood serum contains  $\sim 60$  molecules that need to be detected. It is impractical to rely solely on Brownian motion to transport these molecules through the minuscule detection volumes of e.g. a focused laser beam or a nanopore.<sup>1</sup> To address this, most detection methods rely on a pre-concentration step<sup>2,24,25</sup> or

utilize molecular amplification strategies<sup>26–28</sup>. For nucleic acids, dPCR (digital polymerase chain reaction) has been a game changer. dPCR works by partitioning the sample into many reaction chambers or droplets and diluting until each chamber contains one or zero target molecule. The molecules are then amplified by thermal cycling, and the positive droplets are detected using fluorescence-based methods, determining an absolute number of target nucleic acids.<sup>20</sup> However, practical use of commercially available dPCR devices, especially in low-resource settings is still limited by complex workflow, need for trained personnel and advanced equipment.<sup>29</sup>

Building on addressable NanoAntennas with Cleared HOtSpots (NACHOS)<sup>13</sup> we present NACHOS-diagnostics, a POC-compatible amplification-free detection approach for nucleic acids that addresses these challenges. Specifically, we target a synthetic DNA sequence specific to carbapenem-resistant *Klebsiella pneumoniae*, a bacterium which has been directly linked to 1.27 million deaths and contributing to 4.95 million deaths annually.<sup>30</sup> The fluorescence enhancement by NanoAntennas not only facilitates single-molecule detection with simple optics but it also creates a contrast against an unavoidable background of single-molecule impurities, thus minimizing false positive signals.<sup>13</sup> NACHOS diagnostics utilizes a sandwich assay<sup>13</sup> with a capturing sequence and a dye-labeled imager strand to detect DNA target strands over a broad concentration range from attomolar to nanomolar.

## Results

At nucleic acid concentrations where only a few molecules are present in the sample volume, detection systems face significant challenges—background noise from impurities, sensitivity of the assay and long response times.<sup>24</sup> Employing NanoAntennas allows us to tackle the first challenge by physically amplifying the fluorescence signal of a fluorophore captured in the hotspot of plasmonic nanoparticles (NPs). Resolving the latter two challenges requires maximizing the probability of capturing the target molecules in the shortest possible time. We address this with an integrated NACHOS-diagnostic approach involving several steps of development (Figure 1). These include optimization of the DNA origami NanoAntenna design; integrating nanopatterning and microfluidics; and engineering of a fluorescence reader with single-molecule detection software.



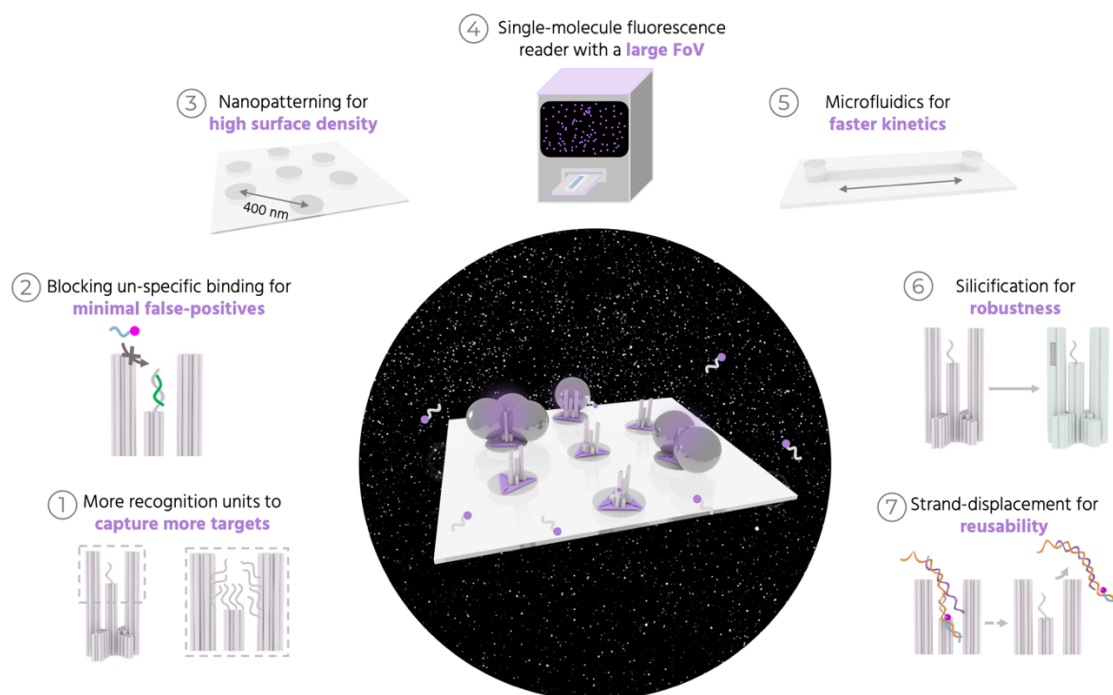


**Figure 1: Overview of the different components for NACHOS diagnostics.** Different components involved in our approach to develop fluorescence enhanced single-molecule detection into a POC-compatible method for detecting low target concentrations of nucleic acids. An abstract image in the center showing a purple glow upon capturing DNA in the NanoAntennas with a snapshot of thousands of single molecules detected on our fluorescence reader as the background. Panels 1-7 show the different steps we employed, to address the challenges in achieving high sensitivity.

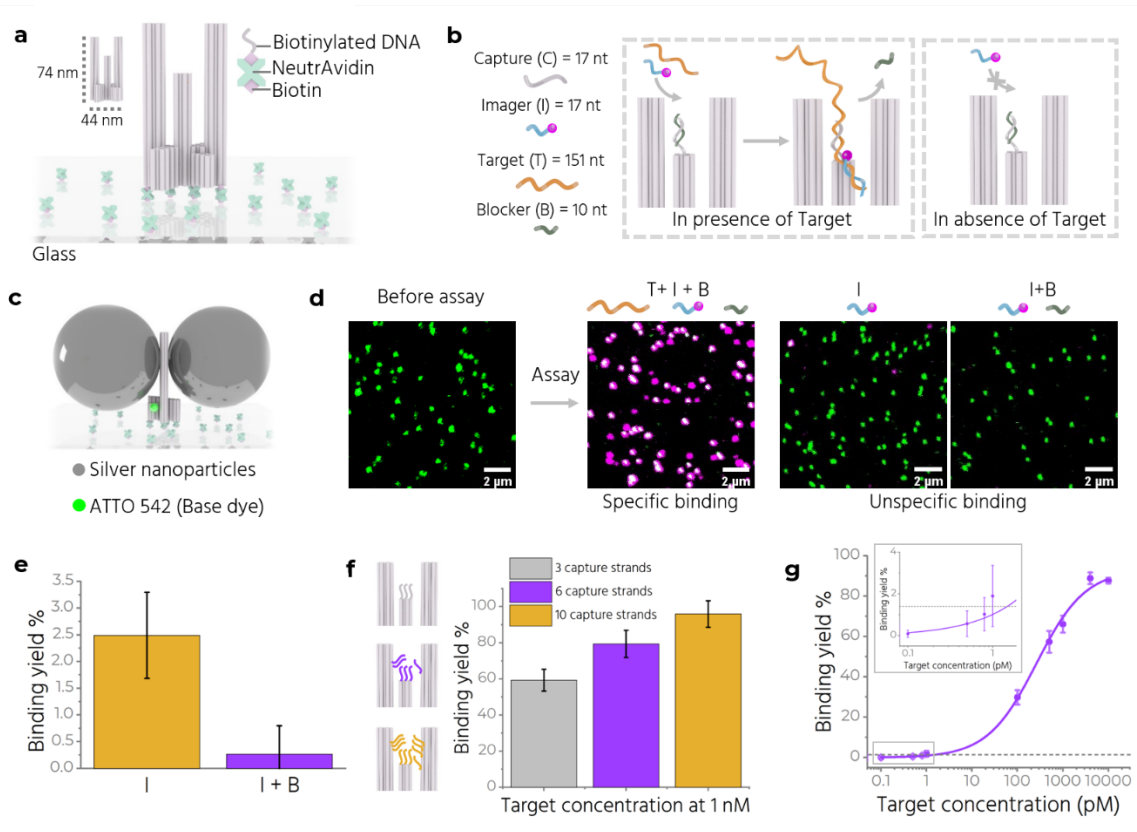
**NanoAntenna design and nucleic acid assay optimization.** We use the second generation of NACHOS<sup>31</sup> for the NanoAntenna assembly as its larger gap (19 nm) between side pillars compared to the first generation (6.5 nm<sup>13</sup>), allows more room for integrating multiple capture strands (Figure 1, panel 1). The DNA origami structure, called *Trident*, consists of a central pillar (51 nm in height) flanked on two sides by longer pillars (74 nm in height). The pillars emerge from a 44 nm wide cross-shaped base (Figure 2a and Figure S1). We modify the base of the Trident to extend twelve biotinylated single-stranded DNA (ssDNA) extensions from the bottom face, which are used to immobilize the structure on glass coverslips using Biotin-NeutrAvidin linkages (Figure 2a). The sandwich-type hybridization assay<sup>13</sup> involves four strands – capture, target, imager, and blocker (Figure 2b). The ‘capture’ strands are extended staple strands that protrude from the Trident and hybridize to the ‘target’ strand (which is 151 nt long) via a 17 nucleotide (nt) complementary sequence. The ‘imager’ strand, labelled with Alexa Fluor 647, has a 17 nt sequence complementary to another part of the target. The ‘blocker’ strand is shorter (10 nt) and is complementary to a portion of the capture strand. It prevents unspecific interaction between the imager and capture strands in the absence of the target (Figure 2b,

Figure S2 and Figure 1, panel 2). The target, when added, can displace the blocker (Figure 2b). We utilize a synthetic target sequence specific to the OXA-48 gene, used for diagnosing carbapenem-resistant *Klebsiella pneumoniae* infection (Supplementary Note 1.1).<sup>32</sup> The gram-negative bacterium can cause various infections, including pneumonia and others of the bloodstream and urinary tract.<sup>33</sup>

We use 80 nm silver nanoparticles (AgNPs) functionalized with thiolated T<sub>20</sub> strands for plasmonic enhancement. We modify each side pillar to incorporate six A<sub>20</sub> extensions to capture two AgNPs, one on each pillar, assembling the NanoAntenna (Figure 2c). An ATTO 542 at the base of the Trident acts as an internal reference to determine the position of the nanostructure during confocal measurements (Figure 2c). Detailed characterization of the NanoAntenna is included in the supporting information (Figure S3). We assess the specificity and efficiency of the assay by taking single-molecule confocal fluorescence scans before and after performing the assay. Initially, we observe only green spots corresponding to the reference ATTO 542 (Figure 2d). After incubation with target (4 nM), imager (12 nM), and blocker (12 nM) strands for one hour at 37°C and subsequent washing, we detect magenta (absence of reference dye due to limited labelling efficiency) and white spots (colocalization of two dyes on the structure) (Figure 2d). To quantify the assay, we calculate the specific 'binding yield' as

$$\text{Binding yield} = \frac{\text{Number of magenta and white (colocalized) spots}}{\text{Number of total spots}}$$

To quantify 'unspecific binding', we perform the assay without the target. We obtain fewer colocalized spots when both imager and blocker are present compared to imager alone (Figure 2d and 2e).



**Figure 2. Optimization of nucleic acid assay detection with NACHOS.** **a** Sketch of the Trident nanostructure immobilized on a BSA-Biotin-NeutrAvidin modified glass coverslip. **b** Working principle of the assay in presence and absence of target. A single capture strand is shown for simplified visualization. **c** Sketch of a fully assembled Trident NACHOS with 80 nm silver nanoparticles and an ATTO 542 dye at the base. **d** Confocal fluorescence scans before and after the assay. Scale bars: 2  $\mu$ m. **e** Binding yield or colocalization percentage comparison after incubation with imager only (in yellow) and with imager and blocker (in purple). **f** (Left, insets) Schematic showing the positions of 3, 6 and 10 capture strands on the Trident. (Right) Target binding yield in the three cases upon incubation with target, imager and blocker. **g** Target binding yield at varying target concentrations. Inset shows a magnified view between 0.1 - 1 pM target concentration. For each data point, at-least 3 (20  $\mu$ m x 20  $\mu$ m) confocal scans with at-least 300 molecules per scan are analyzed. The error bars represent standard deviation. The purple line represents logistic fit. The grey dashed line indicates the minimum detectable target concentration above the blank.

As predicted, the larger gap between the two side pillars in the Trident allows integration of more capture strands in the hotspot region. Increasing the number of capture strands increases the binding yield (Figure 2f). Bleaching step analysis confirms that a single Trident NACHOS with 10 capture strands can capture up to 8 target strands at higher concentrations (4 nM) (Figure S4). This supports the increased accessibility of the hotspot in the current design

compared to the previous design, where more than 70% structures captured only a single target strand.<sup>13</sup> We also examine whether including more capture strands affects nanoparticle binding due to steric hindrance. We compare Trident variants with zero and 10 capture strands, and do not observe a loss in enhancement with the introduction of more capture strands (Figure S5). Hence, we employ 10 capture strands for subsequent experiments. Next, we measure the target binding yield at varying target concentrations from 100 fM to 10 nM (Figure 2g). The imager and blocker concentrations were kept constant at 12 nM for each sample (See Figure S6 for example fluorescence scans). In this setting, the limit of detection (LoD) for the assay is determined to be ~1 pM using the formula:

$$\text{LoD} = \text{Mean value of blank} + 3 * \text{Standard Deviation of blank}$$

### **Optimizing the cross-section for binding with DNA origami NanoAntenna placement.**

Besides increasing the cross-section for target binding by increasing the number of capture strands per NanoAntenna, we aim next at increasing the surface density of NanoAntennas. The challenge here is to achieve dense placement of NanoAntennas on a substrate without them interacting with each other and aggregating into clusters with uncontrolled properties.<sup>34</sup> We adapt the combination of DNA origami placement (DOP)<sup>35-37</sup> and nanosphere lithography<sup>38</sup> to regularly arrange NanoAntennas at 400 nm distances (Figure 1, panel 3). The method involves drop-casting polystyrene (PS) nanospheres (400 nm diameter) onto a hydrophilic coverslip and then passivating the surface to render the unmasked areas hydrophobic. The spheres are then lifted off, revealing a hexagonal array of hydrophilic *placement sites* (Figure 3a). DNA origami nanostructures are selectively placed on these sites through electrostatic interactions. A high-quality DOP, defined as one origami per placement site, is achieved by optimizing Mg<sup>2+</sup> concentration, pH, incubation time, and DNA origami concentration (Figure 3b). Our modified DOP protocol involves two placement steps. First, a two-dimensional *Triangle* origami is placed on the substrate. We use a modified version of the 'Rothenmund triangle' with a side length of ~127 nm (Figure S7),<sup>39</sup> which corresponds well to the placement sites of ~120 nm diameter.<sup>35</sup> Second, the Trident is introduced with six ssDNA strands extending from its bottom face that are complementary to the six protruding sequences on the Triangle. The two-step placement prevents direct interaction of the Trident with placement sites, which otherwise results in the placement of multiple Tridents per placement site in random orientations (Figure S8). We use atomic force microscopy (AFM) (Figure S9) and DNA-PAINT (Point Accumulation In Nanoscale Topography)<sup>40,41</sup> to characterize the quality of placement. DNA-PAINT, as a super-resolution microscopy technique, allows single-molecule localization of freely diffusing short,

labelled DNA probes (imager) transiently binding to complementary ssDNA (docking strand) on the origami. We incorporate six docking strands (60 nm apart) (Figure S10) on the outer rim of the Triangle and perform DNA-PAINT imaging with an 8 nt imager labelled with ATTO 655. We observe a hexagonal placement pattern with Triangles placed ~400 nm apart (Figure 3c). We also observe geometric defects consistent with those observed in scanning electron microscopy (SEM) images of self-assembled nanospheres on glass (Figure S11).

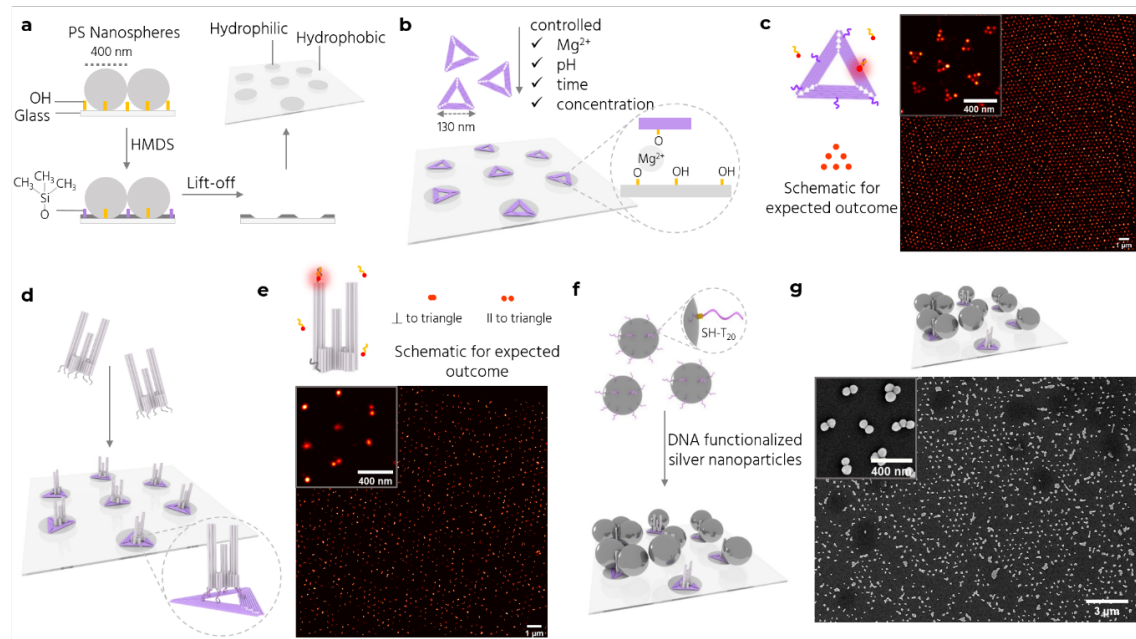


**Figure 3. Site-specific nanopatterning of Trident NanoAntennas.** **a** Fabrication of a nanopatterned surface via nanosphere lithography involving nanospheres deposition, vapor-phase passivation by HMDS, and lift-off. **b** DOP of Triangle DNA origami nanostructures on the hydrophilic placement sites through electrostatic interactions between the placement sites and the Triangle (inset). **c** (Left) Triangle with 6 docking sites (purple) for DNA-PAINT experiments and a schematic of the expected outcome. (Right) DNA-PAINT image of the triangle placed on a nanopatterned surface with a zoom-in (inset). **d** DNA hybridization between the Trident and the Triangle. **e** Trident with 2 docking sites (dark gray) for DNA-PAINT experiments and a schematic of the expected outcome (top) for upright Tridents (correct orientation) or fallen Tridents (undesired orientation) on the Triangle. A single strand per docking site is shown for simplicity. DNA-PAINT image of the Trident bound to the Triangle is shown with a zoom-in (inset). **f** Incubation with functionalized AgNPs (dark gray spheres) results in full NanoAntenna assembly. **g** SEM image of NanoAntennas on a patterned surface with a zoom-in (inset).

After the Triangles are placed, we add the Trident. The extensions at the base of the Trident hybridize with the protrusions on the Triangle (Figure 3d). The extensions are placed at the inner hole, protruding in the plane of the Triangle, to make sure they are accessible irrespective of which face of the Triangle lands on the placement site. We use DNA-PAINT to study the

orientation of the Tridents after placement by incorporating six docking strands (three near the top and three near the bottom of one outer pillar). Tridents in the desired upright orientation are observed as one overlapping spot, while those lying parallel to the surface show up as two spots (Figure 3e). We achieve more than 80% upright Tridents after optimizations (Figure S12).

Next, we incubate the patterned Tridents with thiolated-DNA functionalized 80 nm AgNPs to complete the NanoAntenna assembly (Figure 3f). Under ideal conditions, each NanoAntenna would contain two AgNPs to create a 'dimer'. To achieve this, it is imperative to refine the functionalization protocol to minimize NP aggregation (Figure S13). Although aggregation does not compromise the assay and can even yield elevated enhancement factors,<sup>42</sup> it poses a challenge for achieving uniform, closely spaced assemblies. We employ the freeze and thaw functionalization method to increase the DNA loading on each NP,<sup>43</sup> followed by an agarose gel-based purification step to separate single AgNPs from aggregates and free thiol-DNA strands. SEM imaging reveals the hexagonal array of NanoAntennas on the coverslips (Figure 3g and S14). As a control, we perform DOP with Triangles and incubate the surface with functionalized NPs, observing minimal or no binding. This confirms the selective binding of NPs to the Trident (Figure S15). Adding Tridents directly to a surface with empty placement sites results in the placement of multiple Tridents per placement site, many of which are misoriented or have fallen. Adding AgNPs to this sample results in minimal binding or aggregation (Figure S16). This suggests that it is crucial to have at least one Trident bound to the Triangle in the desired orientation for proper assembly of the NanoAntenna. Additional Tridents bound to the Triangle in random orientations are unable to capture NPs to form the plasmonic hotspot due to steric hindrance and are rendered unfunctional.

**Single-molecule fluorescence reader.** To enable POC detection of single molecules on a cost-efficient device that also provides a large field-of-view (FOV) to count all the single molecules captured by NanoAntennas, we developed a fluorescence reader (Figure 4a and Figure 1, panel 4). The reader uses four spectrally filtered LEDs to excite the Alexa Fluor 647 and a CMOS camera for detection. It is sensitive enough to detect single molecules when their fluorescence is enhanced by NanoAntennas (Figure 4b and S17). At our standard settings of 2 W/cm<sup>2</sup> excitation power density and an integration time of 300 ms, single molecules not enhanced by NanoAntennas remain dark. This creates an intrinsic filter against false positive signals, as unspecific binding in the ultra-small volumes of the NanoAntenna hotspot is minimal, whereas an unavoidable background of not-enhanced single-molecule impurities is

invisible.<sup>13</sup> The reader also includes two white LEDs to collect scattering light from NPs. An integrated computer with a touchscreen serves as the user interface, running a custom software that can control all components and execute script-based processes. The software also performs image processing to detect single molecules based on their intensity and temporal blinking behavior. A detailed description of the reader is provided in Supplementary Note 2.

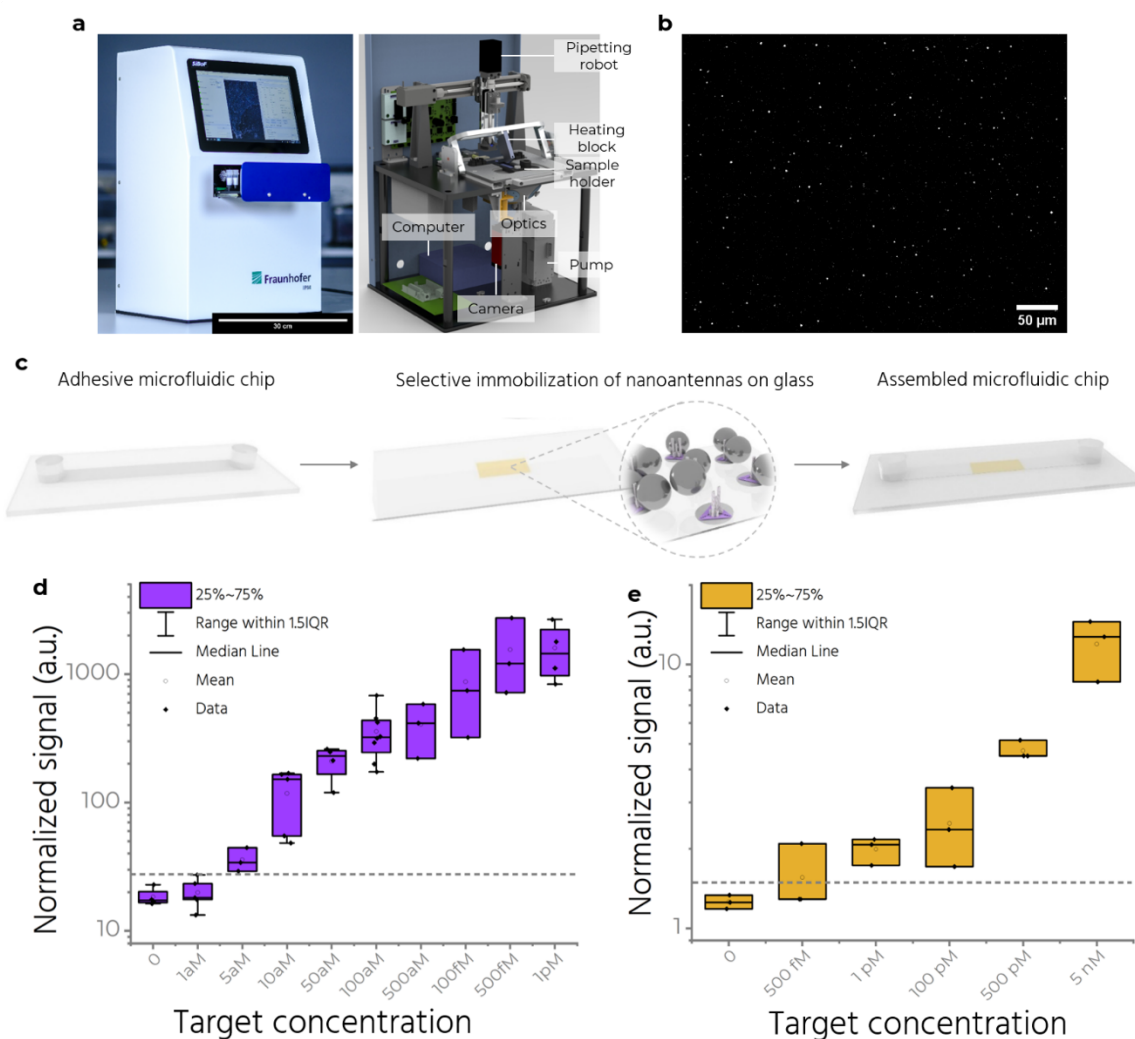


**Figure 4. Microfluidics and a simple fluorescence reader.** **a** (left) The single-molecule fluorescence reader and (right) a sketch showing its components. Scale bar: 30 cm. **b** A zoom-in view of an exemplary image captured on the reader after sandwich assay with target concentration of 1 pM. Scale bar: 50  $\mu\text{m}$ . **c** A self-adhesive microfluidic chip is attached on top of the coverslip with patterned NanoAntennas. The yellow rectangle depicts the area where DOP of NanoAntennas is performed. **d** Measurements showing efficiency of the assay at target concentrations from 1 aM to 1 pM, performed on the reader and analyzed by spot picking. The grey dashed line indicates the minimum target concentration

detectable above the blank. **e** Measurements on the reader analyzed by intensity averaging between target concentrations of 500 fM-5 nM. The box plots in d and e show the 25/75 percentiles and the whisker represents the 1.5\*IQR (inter quartile range) length, the center lines represent the average values. The grey dashed line indicates the minimum target concentration detectable above the blank in d and e.

For finding all target molecules in our 100  $\mu$ L sample solutions, the reader features a field-of-view (FOV) of 3 mm x 2.5 mm. This matches the self-adhesive microfluidic chip that features a channel (Width: 2.5 mm, Depth: 150  $\mu$ m, Length: 58.5 mm), inlet and outlet ports for easy pipetting, and can attach to glass substrates (Figure 4c). This selective placement (Figure S18) allows us to detect most of what we capture, minimizing the loss of target strands outside the detection FOV. Besides the high density of capturing strands and the increased density of NanoAntennas, the large FOV further enhances the interactions of sample volume with the NanoAntennas. Next, we employ fluidics housed in the reader- a simple, automated repetitive back and forth flow within the narrow channel in the microfluidic chip, to further increase the binding kinetics beyond purely diffusive interactions (Figure 1, panel 5). Applying flow allows us to achieve a ~10-fold increase in target capture. We demonstrate this by comparing assays on chips patterned with NanoAntennas and comparing the two cases—one performed with flow and the other without (Figure S19), both with an incubation time of one hour and a target concentration of 500 fM.

**Achieving attomolar sensitivity.** Combining the various elements (Figure 1, panels 1-5) into the NACHOS chip, we use the reader to characterize assays performed at target concentrations ranging from 1 aM to 5 nM, achieving an LoD of ~5 aM (Figure 4e and S20).

We determine this by counting the number of spots detected in each sample normalized to the Nanoantenna surface density (see Supplementary Note 2, Normalized signal). Measurements were repeated at least three times to obtain a standard deviation. In our reader, with an optical resolution of ~ 2.7  $\mu$ m (Supplementary Note 2, reader specifications), a single molecule is detected as a spot (Point Spread Function) with a diameter of 3 pixels, with each pixel corresponding to 0.8  $\mu$ m. Within the aM-fM concentration range, the probability of spatially overlapping signals from two different target molecules remains low, so each detected spot is assumed to correspond to a single molecule. Specifically, at 1 pM, we estimate the average proportion of double molecules among the detected spot to be 0.5-1.5% (Supplementary Note 2, double-event estimate). Thus, throughout the aM-fM range, the proportion of unaccounted double molecules is safely below 1%. At concentrations above 1



pM, the spots are too closely spaced to accurately distinguish them individually (Figure E, Supplementary Note 2). We therefore use an intensity-based analysis - which calculates an average intensity value over the whole image - to analyze data from 500 fM- 5nM. Using average intensity alone, we calculate an LoD of approximately 1 pM, further highlighting the advantage of single-molecule counting over averaging. It is worth noting that the combination of the two detection strategies (in their respective ranges of applicability) preserves accuracy in the full concentration range, from aM to nM regime.<sup>44</sup>

**Silicification for stability in clinically relevant fluids.** Biological fluids like plasma contain many components in addition to target molecules. These components can interact unspecifically with substrates and add to the noise, reducing the sensitivity of our assay. We use buffers containing monovalent electrostatic ions like Na<sup>+</sup> to reduce such interactions and wash away weakly-bound unspecific molecules (Figure S21). But the same Na<sup>+</sup>-containing buffers also lift-off the DNA origami structures placed through DOP (Figure S22). To overcome these issues, we employ silicification (Figure 1, panel 6), which involves the formation of a robust silica coating on the DNA origami nanostructure. The inorganic coating significantly enhances the stability of the structure and keeps them 'glued' to the surface (Figure S23) over a wide range of pH, temperature and salt concentrations.<sup>45,46</sup> Importantly, silicification does not affect the accessibility of ssDNA extensions (capture strands), which is crucial for the assay's functionality (Figure 5a).<sup>47</sup>

We introduce a pre-hydrolyzed precursor - prepared by mixing *N*-trimethoxysilylpropyl-*N,N,N*-trimethylammonium chloride (TMAPS) and tetraethoxysilane (TEOS) solutions in Mg<sup>2+</sup> buffer<sup>48</sup> - to the surface with DNA origami, incubate for desired durations, wash with water and ethanol and air-dry to complete the process. We use AFM to compare the height of the base of the Trident prior to silicification, and after one and four days of silicification to determine optimal silicification parameters (Figure S24). We observe a thickness increase of ~3 nm after one and ~7 nm after four days of silicification, consistent with other studies.<sup>47,48</sup> After 4 days of silicification, we could not reasonably resolve the structural features of the Trident with AFM, and observed an increase in formation of unidentified clusters. We chose the 1-day incubation period for further experiments.

Next, we check the effect of silicification on fluorescence enhancement by silicifying NanoAntennas immobilized on glass using BSA-biotin-NeutrAvidin. These NanoAntennas are folded with an Alexa Fluor 647-modified staple strand which positions the dye in the hotspot, in addition to the base dye (ATTO 542). We record single-molecule confocal fluorescence scans

and measure the intensity of the Alexa Fluor 647, computing a maximum enhancement factor of 126 and 102 for non-silicified and silicified NanoAntennas respectively (Figure 5b). We also check if silicifying the origami adversely affects the accessibility of the capture strand in the hotspot. Results show similar target-capture binding yields in silicified and non-silicified NanoAntennas at all tested target strand concentrations (Figure 5c). We then test the performance of silicified NanoAntennas in untreated human blood plasma. Plasma - a clear, slightly yellow liquid composed of blood without red blood cells, white blood cells and platelets - is ubiquitously used in diagnostics.

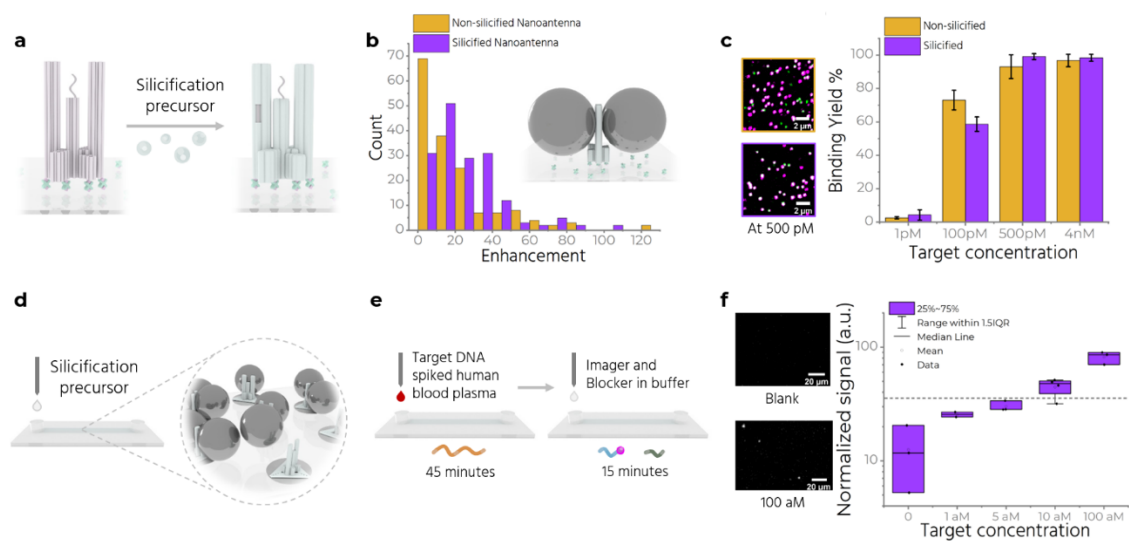


**Figure 5. Silicification and measuring in human blood plasma.** **a** Coating of the double stranded regions of the Trident with silica. **b** Enhancement values are compared for non-silicified and silicified NanoAntennas. (inset) Schematic of a silicified NanoAntenna. **c** (left) Exemplary confocal fluorescence scans for silicified and non-silicified NanoAntenna after incubating with 500 pM target concentration on the left. (right) Column plot comparing target binding yield at different target concentration in case of silicified and non-silicified NanoAntennas. **d** Silicification of nanopatterned NanoAntennas assembled in the microfluidic chip. **e** The microfluidic chip is incubated first with target spiked plasma for 45 minutes, washed with buffer and then incubated with imager and blocker for 15 minutes. **f** Measurements on the reader with target spiked plasma at target concentrations 0, 1 aM, 5 aM, 10 aM and 100 aM, with silicified NanoAntennas. Grey dashed line indicates the lowest detectable signal above blank. Zoom-in snapshots from the blank and 100 aM chip is shown on the left. Scale bar at 20  $\mu$ m.

We start by silicifying NanoAntennas immobilized using BSA-biotin-NeutrAvidin chemistry. We then incubate the sample for one hour with plasma spiked with 5 nM of target and 12 nM of both imager and blocker and measure the imager and base dye colocalization (Figure S25). We observe only green spots, consistent with the base dye, indicating the presence of stable

origami on the surface. Absence of other colored spots suggests degradation of the target and/or imager by enzymes in the plasma. Next, we perform an assay under the same buffer conditions by incubating with plasma spiked only with the target for an hour, wash the sample with buffer to remove the plasma, and then incubate with the imager and blocker for 15 minutes (Figure S25). We observe colocalized spots confirming proper functioning of the assay and suggesting that the imager gets quickly degraded in plasma but not the target. Additionally, we introduce 1  $\mu\text{M}$  of random DNA sequence (sacrificial DNA) during the target incubation. This results in a 94.6% binding yield, an improvement over the 90.8% yield without sacrificial DNA (Figure S25). The target's longer sequence (151 nt) and its tendency to form secondary structures<sup>49</sup> make it less prone to enzymatic degradation (Figure S26). Shorter sacrificial DNA strands appear to further slow this degradation process. We adapt this strategy and incubate the NACHOS chip (Figure 5d) with target-spiked plasma for 45 minutes, put it in the reader with fluidics and wash the chip to remove any unspecifically bound residues originating from the plasma. We then re-incubate the chip with the imager and blocker for 15 minutes while performing fluidics, and wash with fresh buffer (Figure 5e). We measure target concentrations from 1 aM to 100 aM and observe the lowest detectable concentration above the blank to be  $\sim 10$  aM after silicification (Figure 5f and S27), compared to 5 aM in assays performed with unsilicified NanoAntennas. Silicification thus significantly increases the stability of the structures without impacting the sensing performance, enabling assays in clinically relevant fluids.

Finally, we use toehold-mediated strand-displacement<sup>50</sup> to displace the bound target-imager duplex from the capture strand, making the capture strand accessible for the next round of use (Figure 1, panel 7 and Figure S28). As the cost of a diagnostic test often determines its accessibility to those most in need, making the chips reusable and offering users the ability to modify the same chip for detecting various target sequences can benefit POC applications.

## Conclusion

In this work, we have developed an amplification-free POC-compatible nucleic acid detection assay capable of attomolar sensitivity, targeting a 151-nucleotide sequence specific to antibiotics-resistant *Klebsiella pneumoniae*. DNA origami NanoAntennas, particularly NACHOS, excel in distinguishing signals from background noise. We merged the strengths of NACHOS with nanopatterning and microfluidics to offer an integrated approach that addressed key challenges in detecting low-abundance targets.

A nanopatterned surface densely populated with NanoAntennas combined with microfluidics to overcome the effects of slow kinetics at low target concentrations, increases the probability of target capture. We develop a single-molecule fluorescence reader boasting a larger FOV to efficiently detect captured targets. Silicification reduces the dependence of our system on ionic concentrations, pH, temperature as well as protects against degrading enzymes. Finally, a strand displacement strategy is optimized to be able to re-use our chips. We use a sandwich-type assay to detect target DNA bearing the sequence specific to a clinically relevant microbe and achieve a detection limit of 5 aM in buffer and 10 aM in untreated human blood plasma within one hour. It should be possible to modify our chip to target any DNA target by extending an 'adapter' sequence from the origami to which a part of a capture strand can bind, allowing the user to choose the sequence for the capture and thus the target.

Overall, our method offers a robust and scalable solution for sensitive nucleic acid detection in various clinical settings, with potential applications in diagnosing antibiotic-resistant infections, cancer biomarkers, and neurodegenerative diseases. By providing a simple, amplification-free approach with high sensitivity and specificity, our platform addresses critical needs in rapid, on-site diagnostics, potentially improving patient outcomes and aiding in the global fight against antimicrobial resistance. Finally, NACHOS-diagnostics has the potential to evolve into an alternative to digital PCR for quantifying nucleic acid molecules, as it may eliminate the need for separation into small reaction vessels.

## **Methods**

**DNA Origami:** We design DNA origami structures using caDNA<sub>no2</sub>,<sup>51</sup> assembling and purifying them with protocols adapted from Wagenbauer et al.<sup>52</sup> We mix 30 nM of in-house produced p8064 scaffold for Trident and p7249 for Triangle with 300 nM unmodified staples (pooled from an original 100  $\mu$ M concentration) and 750 nM modified staples (also pooled from 100  $\mu$ M). Integrated DNA Technologies Europe GmbH, Germany; Eurofins Genomics GmbH, Germany and biomers.net GmbH, Germany supply all staples, and their exact sequences are in Supplementary Note 3. We add 10 x of folding buffer (FoB) (200 mM MgCl<sub>2</sub>, 50 mM Tris, 50 mM NaCl, 10 mM EDTA) to this mixture and subject it to a thermal annealing ramp for 16.5 hours (detailed in Supplementary Table S2). For purification, we use 100 kDa MWCO Amicon Ultra filters (Merck KGaA, Germany), washing the samples four times with a lower ionic strength buffer (5 mM MgCl<sub>2</sub>, 5 mM Tris, 5 mM NaCl, 1 mM EDTA) for 5 minutes at 10,000 x g, 4 °C. We

invert the filter and collect the purified origami in a fresh tube after centrifuging at 1000 x g for 5 minutes.

**Nanoparticle functionalization:** We adapt a freeze and thaw approach from the work of Liu et. al.<sup>43</sup> Typically we take 100  $\mu$ l of 1 mg/ml 80 nm BioPure AgNPs from nanoComposix, USA, into a low-bind 1.5 ml Eppendorf tube. We reconstitute two tubes of lyophilized thiol-modified ssDNA (5'-thiol-20T-3') at 4 nmol from Ella Biotech GmbH in 670  $\mu$ l of nuclease-free water each. Gradually, we add the thiolated-DNA strands to the NPs while mixing with a pipette. Next, we introduce 60  $\mu$ l of 5 M NaCl and mix gently. We then freeze the mixture at -20 °C for a minimum of 1 hour. For purification, we thaw the mixture and centrifuge at 2800 x g, 4 °C for 15 minutes. After discarding the supernatant, we add 1x BlueJuice loading dye (Merck, Germany) and pipette to mix. We load a 1.2 % agarose gel and perform electrophoresis at 100 V for 45 minutes to isolate the monomer functionalized NPs from aggregates and excess ssDNA. We cut and squeeze the band to get the NPs. We mix this with an equal volume of nuclease-free water and centrifuge again under same conditions. We remove the supernatant, check the concentration at Nanodrop 2000 (Thermo Fisher, USA) and store at 4 °C for later use.

**Surface preparation for immobilizing NanoAntennas with Biotinylated strands:** We rinse 24 mm x 60 mm, 170  $\mu$ m thick microscope coverslips (Carl Roth GmbH, Germany) with Milli-Q water and isopropanol, dry them with an air stream and treat them in a UV-Ozone cleaner (PSD-UV4, Novascan Technologies, USA) for 30 min at 100 °C. After applying SecureSeal™ Hybridization Chambers (2.6 mm depth, Grace BioLabs, USA) to the cleaned coverslips, we wash the chambers thrice with Phosphate-buffered saline (PBS) and incubate them for at least 5 minutes with BSA-biotin (0.5 mg/ml, Sigma Aldrich, USA), followed by 5 minutes with NeutrAvidin (0.2 mg/ml, Thermo Fisher Scientific, USA). We add 100 pM of Trident DNA origami (in 5 mM Tris, 2M NaCl, 1 mM EDTA) with twelve biotinylated ssDNA extensions at the base to bind to NeutrAvidin and wash off excess origami after one and a half minutes. Next, we add functionalized NPs at 0.05 OD (measured at a path length of 1 mm) and incubate overnight in the dark at room temperature in the buffer (5 mM Tris, 2M NaCl, 1 mM EDTA). The following day, we wash 4-5 times with the same buffer to remove unbound nanoparticles.

**Nucleic acid assay:** We fold Trident DNA origami with 10 capture strands protruding from the hotspot to detect a 151 nt synthetic DNA sequence specific to the OXA-48 gene carrying an

antibiotic resistance (see Supplementary Note 1.1). We assemble the NanoAntennas as mentioned above and incubate with 4 nM of the target strand with 12 nM of an Alexa Fluor 647- labelled imager strand (17 nt) and 12 nM of a blocker strand (10 nt) in a buffer containing 5 mM Tris, 2M NaCl, 1 mM EDTA, at 37 °C for 1 hour. After incubation, we wash off the unbound strands with the same buffer.

**Surface preparation for patterned NanoAntennas:** We adapt and modify the DNA origami placement method by Shetty et. al.<sup>35</sup> We rinse 25 mm x 75 mm, 170 µm thick microscope coverslips (Electron Microscopy Sciences, Pennsylvania, USA) with Milli-Q water and isopropanol, dry them with an air stream. We mark a rectangle of ~7 mm x 5 mm with a marker in the center of one side and prepare samples on the reverse. We cover the unmarked area with extra glass coverslips and treat the marked region in an UV-Ozone cleaner for 30 min at 100 °C to make it hydrophilic. We centrifuge 350 µl of 400 nm polystyrene (PS) nanospheres (Thermo Scientific™ Nanosphere™ Size standard 3400A) for 5 minutes at 10,000 x g at room temperature, discard the supernatant, re-suspend in 350 µl of Milli-Q water, and repeat the centrifugation twice. We re-suspend the final pellet in 100 µl of 25 % ethanol/water and drop-cast 10 µl onto the marked area at a ~30° angle. After heating at 60 °C for 4-5 minutes, we expose the coverslips to hexamethyldisilazane (HMDS) vapors for 30 minutes in a sealed glass chamber. We then ultrasonicate in water to lift-off spheres, dry with nitrogen stream and annealed at 120 °C for 5 minutes. We dilute the Triangle DNA origami to 150 pM, add ~200 µl to the marked area and incubate for 1 hour at room temperature in placement buffer (PB, 40 mM Tris, 40 mM MgCl<sub>2</sub> at pH~8.4). After washing with placement buffer and Tween20, we add 350 pM Trident DNA origami and incubate for another 1 hour, followed by repeated washing. Finally, we add 50 µl of 0.2 OD (measured at a path length of 1 mm) functionalized 80 nm AgNPs in placement buffer with Tween and incubate overnight in the dark. We wash the coverslips 5-6 times in placement buffer containing Tween.

**Sample preparation for measurements on the reader:** We wash and keep the patterned area moist, place an adhesive microfluidic chip (Straight channel chip with adhesive tape, Fluidic 268, channel width: 2500 µm, channel depth: 150 µm, channel length: 58.5 mm, material: Zeonor™, from microfluidic ChipShop GmbH, Germany) over the coverslip, and flush the channel with placement buffer containing Tween before further measurements.

## Acknowledgements

R.Y. thanks Dr. Lorena C. Manzanares, Dr. Alan Szalai, Julian Bauer and Dr. Ece Büber for fruitful discussions. P.T. gratefully acknowledges financial support from the DFG (TI 329/9-2 (project number 267681426), INST 86/1904-1 FUGG, INST 86/2224-1 FUGG, excellence cluster e-conversion EXC 2089/1-390776260), Sino-German Center for Research Promotion (grant agreement C-0008), BMBF (Grants POCEMON, 13N14336, and SIBOF, 03VP03891). K.T. acknowledges the support by Humboldt Research Fellowships from the Alexander von Humboldt Foundation. P.T. and M.D. acknowledge funding by the Federal Ministry of Education and Research (BMBF, 13N16929) and the Free State of Bavaria under the Excellence Strategy of the Federal Government and the Länder through the ONE MUNICH Project Munich Multiscale Biofabrication, and by the Center for NanoScience (CeNS).

## Author contributions

The manuscript was written through contributions of all authors. All authors have given approval to the final version of the manuscript.

## Competing interests

P.T. is an inventor on an awarded patent of the described bottom-up method for fluorescence enhancement in molecular assays, EP1260316.1, 2012, US20130252825 A1. The remaining authors declare no competing interests.

## References

1. Holzmeister, P., Acuna, G. P., Grohmann, D. & Tinnefeld, P. Breaking the concentration limit of optical single-molecule detection. *Chem. Soc. Rev.* 43, 1014–1028 (2014).
2. Walt, D. R. Optical Methods for Single Molecule Detection and Analysis. *Anal Chem* 85, 1258–1263 (2013).
3. Bizuayehu, T. T. et al. Long-read single-molecule RNA structure sequencing using nanopore. *Nucleic Acids Res* 50, e120–e120 (2022).
4. Gooding, J. J. & Gaus, K. Single-Molecule Sensors: Challenges and Opportunities for Quantitative Analysis. *Angewandte Chemie International Edition* 55, 11354–11366 (2016).
5. Howorka, S. & Hesse, J. Microarrays and single molecules: an exciting combination. *Soft Matter* 10, 931 (2014).
6. Mayr, R. et al. A microfluidic platform for transcription- and amplification-free detection of zepto-mole amounts of nucleic acid molecules. *Biosens Bioelectron* 78, 1–6 (2016).

7. Punj, D. et al. A plasmonic 'antenna-in-box' platform for enhanced single-molecule analysis at micromolar concentrations. *Nat Nanotechnol* 8, 512–516 (2013).
8. Anger, P., Bharadwaj, P. & Novotny, L. Enhancement and Quenching of Single-Molecule Fluorescence. *Phys Rev Lett* 96, 113002 (2006).
9. Curto, A. G. et al. Unidirectional Emission of a Quantum Dot Coupled to a Nanoantenna. *Science* (1979) 329, 930–933 (2010).
10. Rothemund, P. W. K. Folding DNA to create nanoscale shapes and patterns. *Nature* 440, 297–302 (2006).
11. Acuna, G. P. et al. Fluorescence Enhancement at Docking Sites of DNA-Directed Self-Assembled Nanoantennas. *Science* (1979) 338, 506–510 (2012).
12. Glembockyte, V., Grabenhorst, L., Trofymchuk, K. & Tinnefeld, P. DNA Origami Nanoantennas for Fluorescence Enhancement. *Acc Chem Res* 54, 3338–3348 (2021).
13. Trofymchuk, K. et al. Addressable nanoantennas with cleared hotspots for single-molecule detection on a portable smartphone microscope. *Nat Commun* 12, 950 (2021).
14. Kelley, S. O. What Are Clinically Relevant Levels of Cellular and Biomolecular Analytes? *ACS Sens* 2, 193–197 (2017).
15. Punj, D. et al. Plasmonic antennas and zero-mode waveguides to enhance single molecule fluorescence detection and fluorescence correlation spectroscopy toward physiological concentrations. *WIREs Nanomedicine and Nanobiotechnology* 6, 268–282 (2014).
16. Peng, S., Wang, W. & Chen, C. Breaking the Concentration Barrier for Single-Molecule Fluorescence Measurements. *Chemistry – A European Journal* 24, 1002–1009 (2018).
17. White, D. S., Smith, M. A., Chanda, B. & Goldsmith, R. H. Strategies for Overcoming the Single-Molecule Concentration Barrier. *ACS Measurement Science Au* 3, 239–257 (2023).
18. Rissin, D. M. et al. Single-molecule enzyme-linked immunosorbent assay detects serum proteins at subfemtomolar concentrations. *Nat Biotechnol* 28, 595–599 (2010).
19. Bell, N. A. W. & Keyser, U. F. Digitally encoded DNA nanostructures for multiplexed, single-molecule protein sensing with nanopores. *Nat Nanotechnol* 11, 645–651 (2016).
20. Hindson, B. J. et al. High-Throughput Droplet Digital PCR System for Absolute Quantitation of DNA Copy Number. *Anal Chem* 83, 8604–8610 (2011).
21. Loretan, M. et al. Direct single-molecule detection and super-resolution imaging with a low-cost portable smartphone-based microscope. *bioRxiv* 2024.05.08.593103 (2024)  
doi:10.1101/2024.05.08.593103.
22. Brown, J. W. P. et al. Single-molecule detection on a portable 3D-printed microscope. *Nat Commun* 10, 5662 (2019).
23. Moya Muñoz, G. G. et al. Single-molecule detection and super-resolution imaging with a portable and adaptable 3D-printed microscopy platform (Brick-MIC). *Sci Adv* 10, (2024).
24. Wu, Y., Tilley, R. D. & Gooding, J. J. Challenges and Solutions in Developing Ultrasensitive Biosensors. *J Am Chem Soc* 141, 1162–1170 (2019).

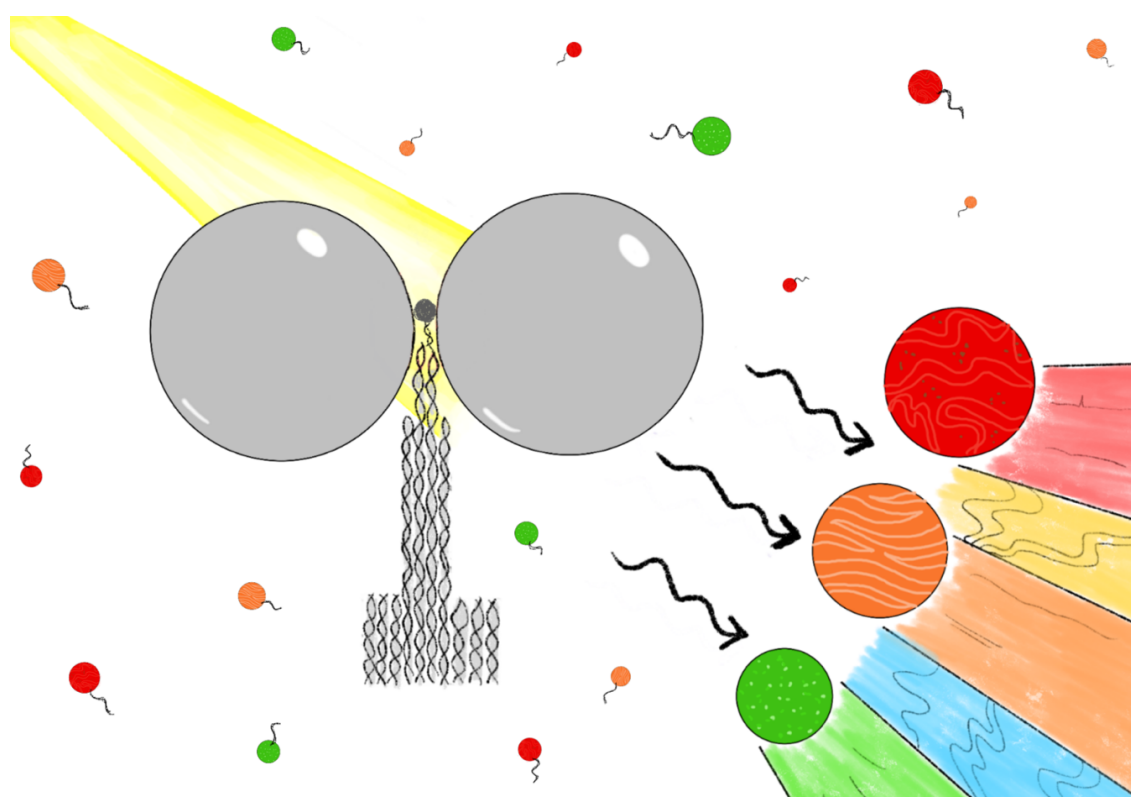


25. Wanunu, M. et al. Rapid electronic detection of probe-specific microRNAs using thin nanopore sensors. *Nat Nanotechnol* 5, 807–814 (2010).
26. Giljohann, D. A. & Mirkin, C. A. Drivers of biodiagnostic development. *Nature* 462, 461–464 (2009).
27. Yan, L. et al. Isothermal amplified detection of DNA and RNA. *Mol Biosyst* 10, 970 (2014).
28. Kaminski, M. M., Abudayyeh, O. O., Gootenberg, J. S., Zhang, F. & Collins, J. J. CRISPR-based diagnostics. *Nat Biomed Eng* 5, 643–656 (2021).
29. Mirabile, A. et al. Advancing Pathogen Identification: The Role of Digital PCR in Enhancing Diagnostic Power in Different Settings. *Diagnostics* 14, 1598 (2024).
30. Murray, C. J. L. et al. Global burden of bacterial antimicrobial resistance in 2019: a systematic analysis. *The Lancet* 399, 629–655 (2022).
31. Close, C. et al. Maximizing the Accessibility in DNA Origami Nanoantenna Plasmonic Hotspots. *Adv Mater Interfaces* 9, (2022).
32. Poirel, L., Bonnin, R. A. & Nordmann, P. Genetic Features of the Widespread Plasmid Coding for the Carbapenemase OXA-48. *Antimicrob Agents Chemother* 56, 559–562 (2012).
33. Budia-Silva, M. et al. International and regional spread of carbapenem-resistant *Klebsiella pneumoniae* in Europe. *Nat Commun* 15, 5092 (2024).
34. Leake, M. C. The physics of life: one molecule at a time. *Philosophical Transactions of the Royal Society B: Biological Sciences* 368, 20120248 (2013).
35. Shetty, R. M., Brady, S. R., Rothemund, P. W. K., Hariadi, R. F. & Gopinath, A. Bench-Top Fabrication of Single-Molecule Nanoarrays by DNA Origami Placement. *ACS Nano* 15, 11441–11450 (2021).
36. Martynenko, I. V. et al. Site-directed placement of three-dimensional DNA origami. *Nat Nanotechnol* 18, 1456–1462 (2023).
37. Dass, M. R. L.; P. C.; S. C.; H. L.; T. J.; M. I. V.; R. U.; P. G.; L. T. Self-assembled physical unclonable function labels based on plasmonic coupling. *ArXiv* (2023).
38. Vogel, N., Weiss, C. K. & Landfester, K. From soft to hard: the generation of functional and complex colloidal monolayers for nanolithography. *Soft Matter* 8, 4044–4061 (2012).
39. Gopinath, A. & Rothemund, P. W. K. Optimized Assembly and Covalent Coupling of Single-Molecule DNA Origami Nanoarrays. *ACS Nano* 8, 12030–12040 (2014).
40. Jungmann, R. et al. Single-Molecule Kinetics and Super-Resolution Microscopy by Fluorescence Imaging of Transient Binding on DNA Origami. *Nano Lett* 10, 4756–4761 (2010).
41. Sharonov, A. & Hochstrasser, R. M. Wide-field subdiffraction imaging by accumulated binding of diffusing probes. *Proceedings of the National Academy of Sciences* 103, 18911–18916 (2006).
42. Li, S., He, J. & Xu, Q.-H. Aggregation of Metal-Nanoparticle-Induced Fluorescence Enhancement and Its Application in Sensing. *ACS Omega* 5, 41–48 (2020).

43. Liu, B. & Liu, J. Freezing Directed Construction of Bio/Nano Interfaces: Reagentless Conjugation, Denser Spherical Nucleic Acids, and Better Nanoflakes. *J Am Chem Soc* 139, 9471–9474 (2017).
44. Zang, F. et al. Ultrasensitive Ebola Virus Antigen Sensing via 3D Nanoantenna Arrays. *Advanced Materials* 31, (2019).
45. Liu, X. et al. Complex silica composite nanomaterials templated with DNA origami. *Nature* 559, 593–598 (2018).
46. Nguyen, L., Döblinger, M., Liedl, T. & Heuer-Jungemann, A. DNA-Origami-Templated Silica Growth by Sol–Gel Chemistry. *Angewandte Chemie International Edition* 58, 912–916 (2019).
47. Wassermann, L. M., Scheckenbach, M., Baptist, A. V., Glembockyte, V. & Heuer-Jungemann, A. Full Site-Specific Addressability in DNA Origami-Templated Silica Nanostructures. *Advanced Materials* 35, (2023).
48. Jing, X. et al. Solidifying framework nucleic acids with silica. *Nat Protoc* 14, 2416–2436 (2019).
49. Chandrasekaran, A. R. Nuclease resistance of DNA nanostructures. *Nat Rev Chem* 5, 225–239 (2021).
50. Yurke, B., Turberfield, A. J., Mills, A. P., Simmel, F. C. & Neumann, J. L. A DNA-fuelled molecular machine made of DNA. *Nature* 406, 605–608 (2000).
51. Douglas, S. M. et al. Rapid prototyping of 3D DNA-origami shapes with caDNAo. *Nucleic Acids Res* 37, 5001–5006 (2009).
52. Wagenbauer, K. F. et al. How We Make DNA Origami\_supplement. *ChemBioChem* 18, 1873–1885 (2017).

## QUANTUM DOTS: AN ALTERNATE EMITTER

### 5.1 OVERVIEW



Quantum Dots (QDs) are semiconducting nanoparticles that are typically in the range of 1-8 nm in diameter. The small size of QDs allows them to exhibit unique electronic and optical properties, that are very different from their bulk counterparts. In the case of bulk semiconductors, electrons can move freely as they have continuous energy bands. However, in the case of QDs, these energy bands split into discrete energy levels because the electrons are tightly confined (Quantum confinement<sup>o</sup>) in a small space in all three dimensions such that they behave more like electrons in isolated atoms rather than in a continuous solid<sup>267</sup>. Such

---

<sup>o</sup> Quantum Confinement is the spatial confinement of electron-hole pairs or excitons in one or more dimensions within a material.

quantization of energy levels is similar to that observed in atoms which is why QDs are often referred to as 'artificial atoms'<sup>268,269</sup>.

When a QD is illuminated with light and a photon is absorbed, it excites an electron from the valence band to the conduction band, leaving behind a positively charged hole in the valence band. The electron in the conduction band and the hole in the valence band together form an 'exciton', which is a bound state due to Coulomb attraction. The exciton exists until recombination of the electron and hole by releasing energy in form of a photon in a process known as radiative recombination.

The most fascinating thing about QDs is that they exhibit size-dependent optoelectronic properties. The size of QDs determines the spacing between the energy levels. Smaller QDs experience stronger confinement effects causing larger energy gap between the valence and conduction bands, which in turn means that smaller QDs will absorb and emit photons of higher energy or shorter wavelength, whereas larger QDs will interact with lower energy or longer wavelength photons. Thus, QDs made from the same material can be tuned to exhibit different emission wavelengths depending on their size.

QDs can be prepared using top-down or bottom-up approaches. In case of top-down methods, electron-beam lithography, reactive-ion etching, and wet chemical etching are commonly used to thin the bulk semiconductor to form QDs<sup>270</sup>. Bottom-up approaches include wet-chemical methods such as microemulsion, sol-gel, hot-solution decomposition and electrochemistry, and vapor-phase methods such as molecular beam epitaxy, sputtering, liquid metal ion sources or aggregation of gaseous monomers<sup>270</sup>.

One of the crucial aspects in QD synthesis is the surface passivation. Defects on the surface of QDs can trap charge carriers resulting in quenched radiative recombination and reduced quantum yields<sup>270</sup>. Most commonly, a semiconductor core such as cadmium selenide (CdSe), lead selenide (PbSe), or indium arsenide (InAs) is passivated by another semiconducting material like zinc sulfide (ZnS), particularly with a larger band gap, to create a shell around the QDs<sup>271</sup>. The thickness of the shell or the passivation must be optimized to efficiently confine charge carriers without causing a big change in the size of QDs. For example, a monolayer of an inorganic passivating shell may increase the quantum yield of a QD by a factor of 3, on the other hand, a very thick shell can lead to reduction in the quantum yield due to dislocations formed upon lattice mismatch and strain which can cause non-radiative recombination<sup>272</sup>.

While QDs have proven to be a game-changer for applications like light emitting diodes (LEDs), photovoltaic devices and photodetectors, their use in biological applications has also been on

the rise. Organic dyes are generally the most common emitters used in fluorescence imaging; however, as applications evolve and demand higher sensitivity and versatility, alternative emitters are increasingly being sought. QDs make an excellent candidate. For example, organic dyes have narrow absorption ranges, broad emission spectra, are prone to quick photobleaching, whereas QDs have broad absorption ranges, narrow emission spectra, and are significantly more photostable and their optical and electronic properties can be tuned by varying the size. ZnS capped CdSe QDs were shown to be 20 times brighter and 100 times more photostable than organic dyes like rhodamine<sup>273</sup>.

In the associated publication P2<sup>10</sup>, we explored the incorporation of DNA-tagged CdTe:Zn<sup>2+</sup> QDs of three different sizes (QD-green~2.8 nm, QD-orange~3.5 nm and QD-red~3.8 nm) into the plasmonic hotspot formed between two 100 nm silver nanoparticles, examining their effects on the fluorescence intensity and lifetime of QDs. Using NanoAntennas with Cleared HotSpots (NACHOS), we precisely positioned the nanoparticles at a certain distance, with the unique addressability offered by the self-assembly technique of DNA origami, as discussed in the previous chapters. We showed successful capturing of QDs in the hotspot via DNA hybridization and observed an enhancement in fluorescence intensity, along with the characteristic shortening of the fluorescence lifetime in the presence of nanoparticles<sup>42,102,176</sup>. Owing to the broad plasmonic spectra of silver nanoparticles<sup>248</sup>, we observed broad-band fluorescence enhancement for all sizes of QDs. The maximum enhancement factors observed were approximately 200, 30 and 70 for QD-green, QD-orange and QD-red respectively. We observed frequent 'blinking' (intermittent on/off behaviour) of QDs which is well-documented<sup>271</sup>, however the frequency of blinking reduced in the presence of nanoparticles which resulted in longer dark states. This suggested a high sensitivity of the QDs used to their immediate environment.

Although QDs have several advantages over organic dyes, their synthesis and the quality of their passivation layer play critical roles in their performance. In our case, the QDs were smaller than 5 nm, necessitating a very thin passivation layer. While crucial for maintaining a small size for certain applications (for example, limited incorporation space in the plasmonic hotspot in this case), this thin passivation layer also raises the risk of incomplete surface coverage, leading to increased non-radiative recombination. Overall, this work increased our understanding of interaction of QDs with plasmonic hotspots and the potential challenges associated, which is useful for the development of advanced photonic devices and biosensing applications.

## 5.2 ASSOCIATED PUBLICATION. 2

### **Broad-Band Fluorescence Enhancement of QDs Captured in the Hotspot of DNA Origami Nanonantennas**

by

Renukka Yaadav, Kateryna Trofymchuk, Feng Gong, Xinghu Ji, Florian Steiner, Philip Tinnefeld, and Zhike He

published in

*The Journal of Physical Chemistry C* 2024

as

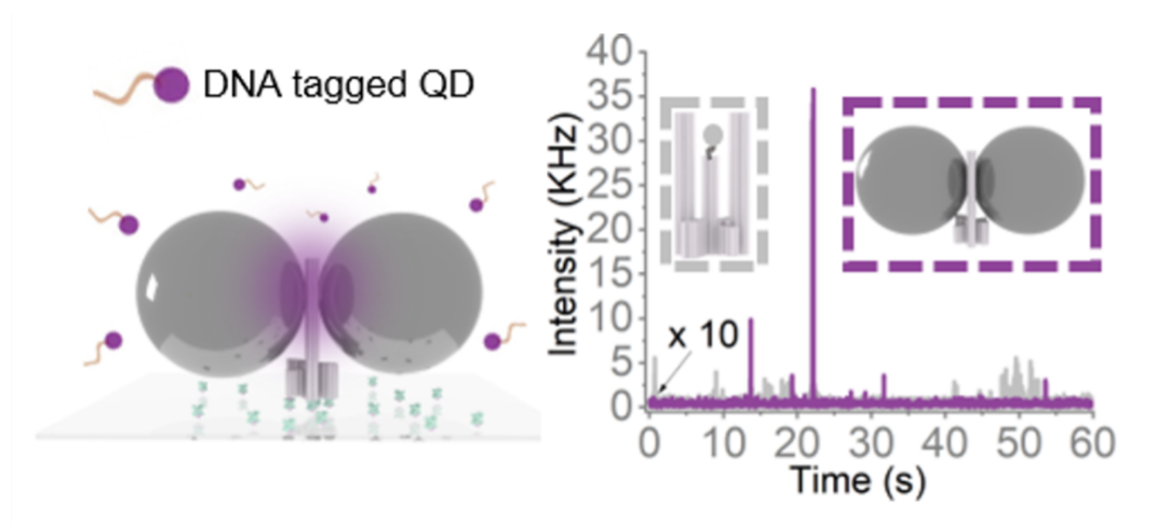
Renukka Yaadav, Kateryna Trofymchuk, Feng Gong, Xinghu Ji, Florian Steiner, Philip Tinnefeld, and Zhike He. *The Journal of Physical Chemistry C* 2024 128 (22), 9154-9160.

DOI: 10.1021/acs.jpcc.4c01797

Copyright © 2024, American Chemical Society

## Abstract

The integration of the DNA origami technique with plasmonic nanostructures has led to the development of optical antennas capable of significantly enhancing the excitation and emission rates of proximal fluorophores by offering precise control over their spatial positioning. However, despite these advancements, conventional fluorophores still face challenges due to their susceptibility to photobleaching. This limitation highlights the need for more stable alternatives. Quantum dots (QDs), also known as “artificial atoms”, emerge as a promising candidate, offering an array of distinctive size-dependent spectral qualities, encompassing broad absorption ranges, tight emission bands, adjustable fluorescence, and better photostability. The pivotal challenge is ensuring the QDs’ precise placement within plasmonic hotspots to unlock maximal signal enhancement. To tackle this, we used DNA origami-based NanoAntennas with Cleared HOTspots (NACHOS) to successfully incorporate divalent DNA-tagged QDs of different sizes within the hotspot of two 100 nm silver nanoparticles. Known for their broad-band optical properties, silver nanoparticles enabled fluorescence enhancement for three spectrally different QDs, with more than 100-fold enhancement for the smallest QDs, alongside a reduction in their fluorescence lifetime. This integration deepens our understanding of nanoscale interactions and charts a path for the development of advanced plasmonic devices, establishing a robust framework for tailored bioassays.



## Introduction

In the realm of nanotechnology, DNA origami nanoantennas have emerged as a groundbreaking tool for signal enhancement in fluorescence [\(1\)](#) and Raman detection. [\(2\)](#) Using the DNA origami technique for constructing nanoantennas, [\(3\)](#) a long, single-stranded viral scaffold strand and a set of short artificial oligonucleotides are self-assembled into a three-dimensional nanostructure. [\(4\)](#) The nanostructure is immobilized on a coverslip using biotin–avidin chemistry and incubated with DNA-functionalized silver nanoparticles (NPs). The single-stranded (ss) protrusions on the nanostructure capture the NPs at a defined position creating a plasmonic “hotspot”. Such an assembly acts as an optical antenna, propagating light into highly enhanced and localized electric fields. [\(5,6\)](#) An emitter placed in the hotspot experiences dramatic change in the local environment leading to photophysical effects such as fluorescence enhancement, [\(7,8\)](#) reduced fluorescence lifetime, [\(4\)](#) altered quantum yield, [\(9\)](#) and increased photostability. [\(10,11\)](#)

Over the past decade, several groups [\(1,12–15\)](#) have not only developed but also extensively applied DNA origami nanoantennas across various scientific fields, particularly for diagnostics. One of the major challenges in fluorescence-based diagnostics is differentiating the signal from the background, especially in complex biological samples. DNA origami nanoantennas have shown remarkable capabilities in this regard. For instance, they have enabled single-molecule measurements even in solutions with dye concentrations as high as 25  $\mu\text{M}$ . [\(8\)](#) Another example is their use in detecting Zika-specific RNA through a fluorescence quenching hairpin assay. [\(16\)](#) Despite these advancements, challenges remain, particularly concerning the fluorophores used in these assays. For instance, it was observed that in a fluorescence quenching assay, the quencher can experience accelerated photobleaching when placed in the hotspot, leading to an increase of false positive signals. [\(17\)](#) Moreover, while DNA origami nanoantennas enhance the photon budget of organic fluorophores, they do not overcome intrinsic limitations such as dim state formation and photoinduced isomerization, thus curtailing their utility. [\(17\)](#) This highlights the necessity for careful selection and study of fluorescent components. In addressing these challenges, quantum dots (QDs) emerge as a compelling alternative.

QDs are semiconducting nanoparticles with typical diameters ranging from 1 to 8 nm. QDs have properties intermediate between those of bulk semiconductors and discrete atoms or molecules. Furthermore, they exhibit size-dependent spectral properties, including broad



absorption spectra, narrow emission bands, and tunable fluorescence, earning extensive applications in bioimaging, photovoltaics, quantum computing, and as emitters in single-molecule spectroscopy. Compared to conventional dyes, QDs possess large dipole moments (up to 10 times larger [\(18\)](#)) emerging as ideal candidates for studies focusing on optical coupling with plasmonic devices. In this realm, the coupling strength between QDs and plasmonic structures can vary, depending on parameters like the size of the plasmonic cavity and energy scales, thereby resulting in complex optical behaviors. [\(18\)](#) Recognizing their importance in nanotechnology, the Nobel Prize in Chemistry 2023 was awarded to Moungi G. Bawendi, Louis E. Brus, and Aleksey Yekimov for the discovery and development of QDs. Various methods have been explored to position QDs within plasmonic cavities, ranging from spin coating on silver films [\(19\)](#) to lithographical techniques [\(20\)](#) and atomic force microscopy (AFM). [\(21\)](#) However, the advent of DNA nanotechnology has revolutionized our ability to organize nanoscale entities with unprecedented precision. [\(22–27\)](#)

In this article, we employ a recently developed DNA origami nanoantenna design, termed NanoAntenna with Cleared HotSpot (NACHOS), [\(28\)](#) to position individual QDs between two 100 nm silver (Ag) NPs. AgNPs were chosen due to their broad plasmonic spectra providing broad-band enhancement, [\(29\)](#) aligned with the emission spectra of three differently sized QDs. The DNA-functionalized QDs of different sizes were synthesized by a simple hydrothermal method under different reaction times. [\(30\)](#) The resultant system shows more than a 100-fold increase in fluorescence, substantiating the utility of DNA origami nanoantennas for investigating complex light–matter interactions. This work paves the way for the utilization of QDs within DNA origami nanoantenna hotspots, offering promising avenues for tailored bioassays and other applications.

## Methods

### DNA Origami

DNA origami nanostructures were designed in caDNAno2. [\(31\)](#) For the folding, 25  $\mu\text{L}$  of p8064 scaffold (produced in-house) at 100 nM was mixed with 18  $\mu\text{L}$  of unmodified staples pooled from 100  $\mu\text{M}$  original concentration and 2  $\mu\text{L}$  of modified staples, pooled from 100  $\mu\text{M}$  original concentration. All staples were purchased from Eurofins Genomics GmbH (Germany); for the exact sequences, see [Tables S2](#). 5  $\mu\text{L}$  of folding buffer (200 mM  $\text{MgCl}_2$ , 50 mM Tris, 50 mM NaCl, 10 mM EDTA) was added, and the mixture was subjected to a thermal annealing ramp ([Table S3](#)). Samples were purified using 100 kDa MWCO Amicon Ultra filters (Merck KGaA, Germany)

with four washing steps with a lower ionic strength buffer (5 mM MgCl<sub>2</sub>, 5 mM Tris, 5 mM NaCl, 1 mM EDTA) for 5 min at 10 krcf, 20 °C. Finally, the Amicon filter was flipped and placed in a new tube. By centrifuging it for 5 min at 1 krcf and 20 °C, the DNA origami was extracted.

### **Synthesis of DNA-QDs**

DNA-functionalized CdTe:Zn<sup>2+</sup> QDs of three different colors were prepared according to Ma et al. (30) Typically, under a nitrogen stream, 1 mL of ultrapure water was quickly added to a mixture of 20 mg of Te powder and 11 mg of NaBH<sub>4</sub>. The mixture was continued to react in oxygen-free and ice-bath conditions for about 5 h until it became a clear solution of colorless or light pink to obtain the Te precursor. At the same time, 38 mL of solution containing 6.25 mM CdCl<sub>2</sub>, 6.25 mM ZnCl<sub>2</sub> and 25 mM *N*-acetyl-L-cysteine was adjusted to pH 9.0 by NaOH to obtain the Cd precursor. Then, 5 μL of Te precursor, 400 μL of Cd precursor, 1.6 mL of ultrapure water, and 14 OD of phosphorothioate-modified DNA were mixed and reacted in a Teflon-lined-stainless steel autoclave at 200 °C for different times to obtain QDs of different colors. The DNA sequence of the three QDs is TGTCTACATTGCCCGAAAAAAG\*G\*G\*G\*G\*G\*G\*G\*G\*G\*G\*G\*G\*G\*G\*G\*G\*A (\* indicates the phosphorothioate linkage), which is purchased from Sangon Biotechnology Co., Ltd. (Shanghai, China). Specifically, the green emission QD (QD-green) was obtained with a reaction time of 23 min, while 29.5 min was needed for orange-emitting QD (QD-orange) and 34 min was needed for red-emitting QD (QD-red). Finally, the obtained QDs were purified using a 50 kDa MWCO Amicon Ultra filter (Millipore Corp., U.S.A.) with four washing steps with 10 mM Tris-HCl buffer (pH 8.0). The fluorescence emission spectra, UV-vis absorption spectra, and transient fluorescence decay curve of the QD solutions were measured with an RF-6000 fluorescence spectrophotometer (Shimadzu, Japan), UV-2250 spectrophotometer (Shimadzu, Japan), and QM/TM system (Photon Technology International, USA). Transmission electron microscopy (TEM) images of QDs were performed with a JEM 2100 electron microscope (Japan).

### **Functionalization of NPs**

AgNPs were functionalized with T20 ssDNA oligonucleotides with a thiol modification at the 3'-end (Biomers.net GmbH, Germany). Briefly, 2 mL of ~0.025 mg/mL AgNP solution in Milli-Q-water was heated to 40 °C under permanent stirring. 20 μL of 10% Tween 20 and 20 μL of a potassium phosphate buffer (4:5 mixtures of 1 M monobasic and dibasic potassium phosphate, Sigma-Aldrich, USA) were added as well as 10 μL of a 2 nM thiol-modified single-stranded DNA

solution (5'-T20-SH-3') and incubated for 1 h at 40 °C. A salting procedure was then carried out by adding 1× PBS buffer containing 3.3 M NaCl stepwise over 45 min to the stirred 40 °C solution, until a final concentration of 750 mM NaCl was reached. Afterwards, the NPs were mixed 1:1 with 1× PBS, 10 mM NaCl, 2.11 mM P8709 buffer (Sigma Aldrich, USA), 2.89 mM P8584 buffer (Sigma-Aldrich, USA), 0.01% Tween 20, and 1 mM EDTA. To remove the excess thiolated ssDNA, the solution was centrifuged for 12 min at 2.8 krcf and 20 °C. A pellet was formed, in which the particles were concentrated. The supernatant was discarded, and the washing step was repeated six more times. After functionalization, NPs were diluted in 1× TE buffer (10 mM Tris, 1 mM EDTA) containing 2 M NaCl to reach the final extinction of ~0.1 (0.1 mm path length) at the extinction maximum on a UV-vis spectrometer (NanoDrop 2000, Thermo Fisher Scientific, USA).

### **Sample Preparation on the Coverslip for Single-Molecule Confocal Measurements**

Microscope coverslips of 24 × 60 mm size and 170 μm thickness (Carl Roth GmbH, Germany) were cleaned with a UV-Ozone cleaner (PSD-UV4, Novascan Technologies, USA) for 30 min at 100 °C. Adhesive SecureSeal hybridization chambers (2.6 mm depth, Grace Bio-Laboratories, USA) were glued on the clean coverslips. The created wells were washed three times with 1xPBS buffer and then incubated with BSA-biotin (0.5 mg/mL, Sigma-Aldrich, USA) and NeutrAvidin (0.2 mg/mL, Thermo Fisher Scientific, USA). The DNA origami (50–100 pM in 1× TE buffer containing 750 mM NaCl) was immobilized on the biotin-NeutrAvidin surfaces using covalently attached biotin modifications on the six staple strands on the base. Density of NACHOS on the surface suitable for single-molecule measurements was checked with a microscope. The binding of NPs was then performed by incubating the surfaces with 150 μL of T20-functionalized particles in 1× TE buffer containing 2 M NaCl overnight at room temperature. Afterwards, 2 nM QDs bearing ssDNA was incubated with reference and nanoantenna sample overnight in 1× Tris buffer containing 14 mM MgCl<sub>2</sub> at room temperature. To prevent the evaporation, samples were kept in sealed humidity chambers during the incubation. The nanoantennas were then stored in 1× TE buffer containing 14 mM MgCl<sub>2</sub>.

### **Confocal Measurements and Data Analysis**

Measurements were performed on a home-built confocal setup with an Olympus IX71 microscope. The red and green lasers (LDH-D-C-640 and LDH-P-FA-530B, Picoquant) were controlled by a PDL 828 “Sepia II” (Picoquant). The green fiber (polarization maintaining fiber

with FC/APC output connector) coupled laser light is decoupled via a F220APC-532 collimator (Thorlabs) and cleaned up with a 532/2 (Z532/10X, Chroma) filter before passing a dichroic mirror (640 LPXR, Chroma) for combination with the already cleaned up (Z640/10X, Chroma) red laser. Both lasers are overlapped with a fiber (P3-488PM-FC, Thorlabs), which is entered through a collimator (PAF2-2A, Thorlabs) and exited via a collimator (G169015000, Qioptics). A linear polarizer (WP12L-Vis, Thorlabs) and a quarter-wave plate (AQWP05M-600, Thorlabs) are combined to obtain circularly polarized light. After passing a second dichroic mirror (zt532/640rpc, Chroma) the beam is focused via an oil immersion objective (UPLSAPO 100 XO, NA 1.40, Olympus) onto the samples. The sample is scanned with a piezo-stage (P-527.3CD, Physik Instrumente), which is controlled by an E-727 controller (Physik Instrumente). The emitted light is focused on a 50  $\mu\text{m}$  pinhole (Linos) and collimated with a lens (AC050-150-A-ML, Thorlabs). After passing a dichroic beam splitter (640LPXR, Chroma) and a combination of two filters (red: 731/137 BrightLine HC, Semrock, and Razor Edge 647 nm, Semrock; green: 582/75 BrightLine HC, Semrock, and Razor Edge 532 nm, Semrock), the beam is focused via a lens (AC080-020-B-ML, Thorlabs) on an APD (SPCM-AQRH-TR-14, Excelitas). The APD signal is processed with a HydraHarp 400 instrument (Picoquant) and controlled with the software SymPhoTime 64 (Picoquant). The FLIM images ( $10 \times 10 \mu\text{m}$ ;  $100 \times 100$  pixels, monodirectional) were taken with a laser power of  $1 \mu\text{W}$  for imaging the localization dye and for QDs in reference samples and 100 nM for QDs in NA. The homemade Python software was used to process the acquired data. Background correction was performed for each transient. Fluorescence lifetime decays were extracted, IRF deconvoluted, and multiexponentially fitted for the shortest lifetime component. The extracted data were analyzed in OriginPro 2019.

## Results and Discussion

### Synthesis and Characterization of QDs

QDs of different sizes were used to investigate their universality of fluorescence enhancement in DNA origami NACHOS. The QDs were synthesized and functionalized by a simple hydrothermal method as described by Ma et al. (30) Divalent DNA-tagged QDs (modified with two DNA strands) were used to improve the binding efficiency of QDs in the hotspot. The number of modified DNA on a QD can be regulated by the number of phosphorothioate on the DNA strand and the concentration of DNA used in the synthesis. (30) QDs of three different sizes each exhibit wide excitation spectra and narrow emission spectra (40–50 nm full width

at the half-maximum) (Figure 1a), which indicate that the synthesized QDs are excellent materials for studying broad-band fluorescence enhancement in DNA origami NACHOS. The characteristic absorption peaks of QD-green, QD-orange, and QD-red were 522, 581.5, and 615 nm, respectively (Figure 1b). The absorption peak of QD-green at 256 nm was caused by the modification of DNA on its surface. For QD-orange and QD-red, the absorption peaks for DNA are not obvious because of the increase in the size of QDs. Two peaks in the UV-vis absorption spectra (Figure 1b) of QDs indicate the successful modification of the DNA on QDs. The TEM images (Figure 1d) of QDs show that the average sizes of QD-green, QD-orange, and QD-red are 2.8, 3.5, and 3.8 nm, respectively. Fluorescence lifetime measurements (Figure 1c) yield a fluorescence lifetime of 16.6 ns for QD-green, 27.0 ns for QD-orange, and 33.6 ns for QD-red, respectively, that were extracted by fitting the decay curves with a single exponential fit. Compared to conventional dyes having fluorescence lifetimes in the range of 0.1–10 ns, (32) the longer lifetime of QDs is more conducive to the observation of the shortening of fluorescent lifetime in the hotspot.

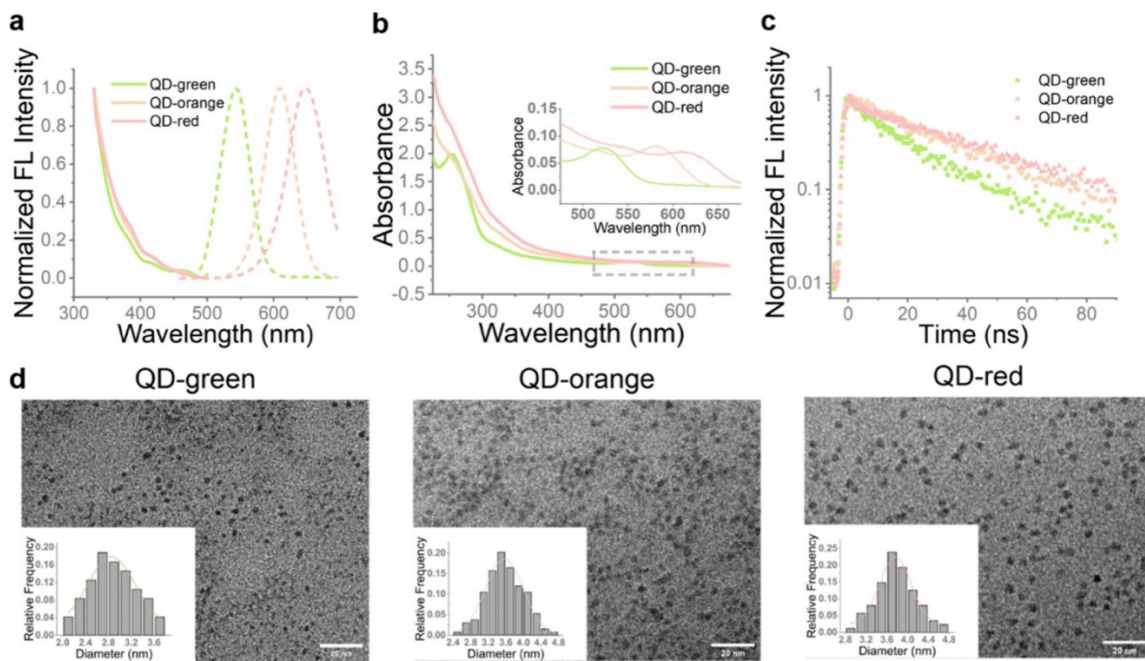


Figure 1. Characterization of the QDs. (a) Fluorescence excitation and emission spectra (the solid line indicates the excitation spectrum, and the dashed line indicates the emission spectrum), (b) UV-vis absorption spectra, (c) fluorescence decay curve of the QDs in solution, (d) TEM images of QD-green, QD-orange, and QD-red (inset: corresponding size distribution of the QD).

## Capturing QDs in the DNA Origami Nanostructure

We utilize a new design of the recently introduced 3D DNA origami NACHOS structure, which features a three-pillar structure and provides an accessible region known as the “hotspot” for

positioning nanoscale objects of interest (33) (as detailed in Figure 2, Figure S1, and Tables S2 and S3). DNA origami structures were designed to incorporate a localization dye to identify the presence of the structure on the surface (ATTO647N for QD-green and QD-orange and ATTO542 for QD-red; Figure 2 and Figure S2). This dye serves dual function: It not only indicates the location of DNA origami structures but also acts as a marker for successful NP binding, a feature confirmed by the observed shortening of the dye's lifetime in proximity to NPs<sup>9</sup> (Figure S3).

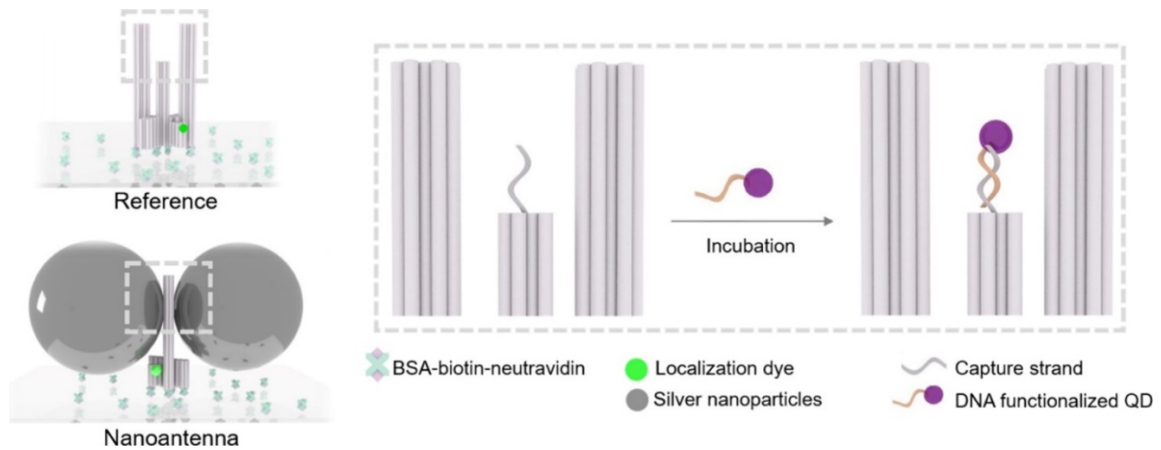


Figure 2. Labeling approach to capture QDs. For the reference measurements, the origami structure was first immobilized on a glass coverslip (top left) and then incubated with QDs (inset). For the nanoantenna measurements, the full nanoantenna assembly was carried out first (bottom left), followed by incubation with QDs (inset).

To capture the QDs in the hotspot region of the DNA origami nanostructure, we first immobilized the DNA origami nanostructure on a glass coverslip and then incubated the sample with an excess of QDs (Figure 2). The origami structure was engineered to include three capture strands that are complementary to the DNA sequence present on the QDs (Table S1). The approach aims to maximize the probability of each DNA origami capturing a QD. (34) Our previous investigations have shown that this approach results in ~ 60% binding yield of one dye molecule in the NACHOS structures. (28)

We tested the capturing of QDs in the DNA origami hotspot region without the presence of NPs to get a reference value. For this, DNA origami structures that were immobilized on a coverslip through a biotin–neutravidin interaction (refer to Methods Section for more details) were incubated with a 2 nM concentration of QDs overnight.

A key challenge in these experiments stems from the stochastic blinking behavior of QDs during emission (35) (as illustrated in Figure 3), a characteristic that prevents direct assessment of QD immobilization efficiency through dual-color fluorescence scans (as shown in Figure S2).

To combat this, we employed a two-step approach for quantification. First, a scan was conducted to pinpoint the location of DNA origami structures based on their integrated localization dye. Subsequently, we recorded fluorescent transients from these identified locations for a duration of 60 s while using a laser specifically tuned for QD excitation ([Figure S4](#)). We used a 532 nm excitation wavelength for QD-green and QD-orange, and 640 nm for QD-red. Our results indicate that 75, 93, and 73% of these transients displayed the characteristic blinking fluorescent transients ([Figures S5 and S6](#)) for green, orange, and red QDs, respectively. These figures closely align with previously reported values for dye incorporation via a sandwich assay method. ([28](#))

In contrast, control measurements carried out in an identical manner but on structures devoid of QDs revealed substantially lower transient percentages, ranging between 6 and 11%. These much lower intensity transients ([Figure S6](#)) could be attributed either to isomeric forms of the localization dyes or to dim impurities in the system.

### **QD-DNA Origami Nanoantenna**

Subsequently, we assembled nanoantennas on the substrate by incubating immobilized DNA origami structures with oligo-functionalized AgNPs. ([4](#)) Fluorescence lifetime imaging microscopy (FLIM) scans of the localization dye confirmed the successful association of the AgNPs (as evidenced in [Figure S3](#)). We then carried out the immobilization of QDs under conditions identical to those used for DNA origami alone. To quantify QD behaviors, we adapted the previous measurement methodology but reduced the excitation power from 1  $\mu$ W to 100 nW to mitigate saturation effects within the hotspot ([17](#)) ([Figure S4](#)). The resulting binding efficiencies for green, orange, and red QDs were 88, 67, and 40%, respectively ([Figure S5](#))—values that are slightly lower than those observed in reference structures, likely due to increased spatial constraints. ([28](#)) Control measurements indicated transients in only 4–6% of instances ([Figure S6](#)), a reduction likely attributable to the lower excitation power employed. Next, we investigated the influence of the plasmonic hotspot on QD photophysics. Consistent with observed transients and in accordance with previous studies, ([27,36](#)) we noted an elevation in the fluorescence intensity of the QDs ([Figure 3b](#)). To quantify the fluorescence enhancement, we first determined the fluorescence intensity of QDs bound to DNA origami by identifying the maximum value of the intensity in each transient and subtracting the average background intensity specific to the trace. This processed value was averaged across all transients to establish a reference intensity for the QDs on DNA origami. These measurements were taken at a laser power (1  $\mu$ W) 10 times greater than that used for the QDs

in DNA origami nanoantennas (100 nW); therefore, we adjusted the reference intensity by dividing it by 10 for consistency. Similarly, for the QDs in the nanoantennas, we extracted the maximum intensity from each transient, subtracted the mean background intensity specific to the nanoantenna trace and then normalized these values by the previously determined reference intensity of the QDs in DNA origami without NPs.

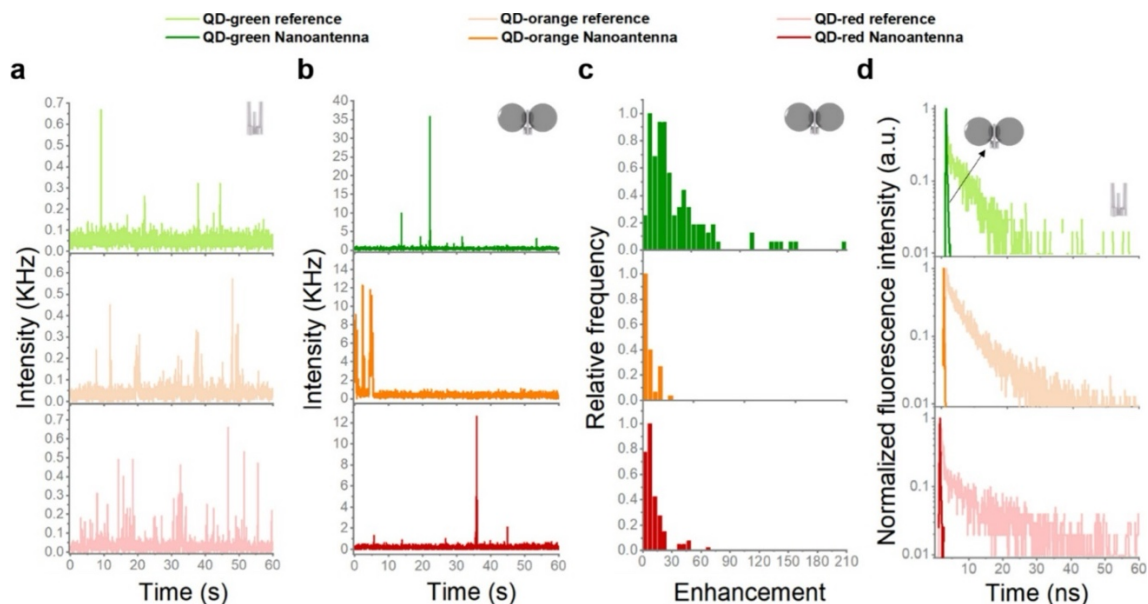


Figure 3. (a) Exemplary transients of the QDs of different sizes on the DNA origami (reference) and (b) in the hotspot of nanoantennas. (c) Measured fluorescence enhancement for QDs of different sizes in the hotspot of the nanoantennas. (d) Exemplary fluorescent lifetime decays of QDs of different sizes on the DNA origami (reference) and in the hotspot of nanoantennas.

We plotted the histogram of the distribution of the enhancement of QDs in the nanoantenna (Figure 3c). The maximum enhancement factor observed was approximately 200, 30, and 70 for QD-green, QD-orange, and QD-red, respectively (Figure 3c). We were unable to pinpoint the exact cause of the reduced fluorescence enhancement observed in QD-orange and QD-red. Their larger size, compared to QD-green, might have contributed to this phenomenon since their incorporation efficiency within the hotspot was also lower. However, this does not fully explain why QD-orange, despite being medium-sized, displayed the lowest enhancement values. The overall heterogeneity in enhancement values observed could have resulted from heterogeneity in the NPs size and shape, or from intrinsic variability in the emission of individual QDs, or from varying orientations of the nanoantennas relative to the excitation field; additionally, the presence of a subpopulation of nanoantennas with either monomeric or multimeric NPs cannot be ruled out.<sup>(1)</sup> We also observed fewer on-states in the



nanoantennas compared to the reference DNA origami structures (Figure 3a,b). This observation can be attributed to the sensitivity of QDs to their immediate environment. (27) The QDs employed in this study were smaller than 5 nm, which necessitated a very thin passivating layer. It is well established that the photophysical properties of QDs are significantly influenced by the thickness of the passivating shell, among other factors, leading to longer off-states and reduced blinking. (37,38)

Furthermore, we observed and compared the fluorescence lifetime of QDs in the nanoantenna as one of the hallmark behaviors of emitters situated in a plasmonic cavity is reduced fluorescent lifetime. (1,4,9,17,29) In the nanoantennas, the fluorescence lifetime decay for QDs was similar to the instrument response function due to the enhancement of radiative and non radiative rates and could not be determined by single-photon counting. This trend was consistent for all the three sizes of QDs, corroborating prior studies. (18,27,39) Lifetime decay analysis of QDs on DNA origami revealed a multiexponential decay curve with characteristic lifetimes (35) (Figure 1c,d). Variances in decay compared to solution-phase measurements (Figure 1c) are attributed to differences in the local environmental conditions and the use of different measurement instruments and methods. Importantly, all QDs situated in the plasmonic hotspot exhibited a dramatic shortening of fluorescent lifetime, which was significantly shorter than reference DNA Origami nanostructures (Figure 3d).

## Conclusions

In the present work, we demonstrate the synthesis of DNA-labeled QDs, which were successfully incorporated into the hotspot of self-assembled DNA NanoAntennas with Cleared HOtSpot (NACHOS). Utilizing 100 nm AgNPs for their broad-band fluorescent enhancement capabilities, we investigated the behavior of QDs of different size, observing up to 100-fold increase in fluorescence for green QDs. The findings highlight the significant potential of QDs, with their unique size-dependent spectral tuning properties, as an alternative to conventional dyes provided they are carefully fabricated to suit specific applications. Notably, smaller-sized QDs, while advantageous due to their smaller band gaps and resultant higher enhancement effects, necessitate a very thin passivating shell, which can compromise their photostability. (27) Adding a thicker passivating shell of a higher band gap material can minimize the interaction with the surface and substantially improve the stability of QDs, enhancing their utility. (37) The results indicate two significant avenues for future

research and applications. On the one hand, they suggest that QDs could be effectively employed for specialized bioassays [\(12,16,28,30,33\)](#) in plasmonic hotspots. On the other hand, the findings demonstrate the utility of self-assembled 3D DNA origami nanoantennas for the precise positioning and study of a variety of emitters, extending beyond conventional organic dyes, in plasmonic hotspots with NPs of diverse sizes and shapes.

## Author Contributions

R.Y. and K.T. contributed equally.

The manuscript was written through contributions of all authors. All authors have given approval to the final version of the manuscript. †These authors contributed equally.

## Acknowledgments

P.T. gratefully acknowledges financial support from the DFG (TI 329/9-2 (project number 267681426), INST 86/1904-1 FUGG, excellence cluster e-conversion EXC 2089/1-390776260), Sino-German Center for Research Promotion (grant agreement C-0008), and BMBF (Grants POCEMON, 13N14336, and SIBOF, 03VP03891). K.T. acknowledges the support by Humboldt Research Fellowships from the Alexander von Humboldt Foundation.

## References

1. Glembockyte, V.; Grabenhorst, L.; Trofymchuk, K.; Tinnefeld, P. DNA Origami Nanoantennas for Fluorescence Enhancement. *Acc. Chem. Res.* **2021**, *54*, 3338– 3348, DOI: 10.1021/acs.accounts.1c00307
2. Mehmandoust, S.; Eskandari, V.; Karooby, E. A Review of Fabrication of DNA Origami plasmonic Structures for the Development of Surface-Enhanced Raman Scattering (SERS) Platforms. *Plasmonics* **2023**, 1– 13, DOI: 10.1007/s11468-023-02064-9
3. Rothmund, P. W. K. Folding DNA to create nanoscale shapes and patterns. *Nature* **2006**, *440*, 297– 302, DOI: 10.1038/nature04586
4. Acuna, G. P.; Möller, F. M.; Holzmeister, P.; Beater, S.; Lalkens, B.; Tinnefeld, P. Fluorescence enhancement at docking sites of DNA-directed self-assembled nanoantennas. *Science* **2012**, *338*, 506– 510, DOI: 10.1126/science.1228638
5. Novotny, L.; van Hulst, N. Antennas for light. *Nat. Photonics* **2011**, *5*, 83– 90, DOI: 10.1038/nphoton.2010.237

6. Bharadwaj, P.; Deutsch, B.; Novotny, L. *Optical Antennas. Adv. Opt. Photon.* **2009**, *1*, 438– 483, DOI: 10.1364/AOP.1.000438
7. Kinkhabwala, A.; Yu, Z.; Fan, S.; Avlasevich, Y.; Müllen, K.; Moerner, W. E. Large single-molecule fluorescence enhancements produced by a bowtie nanoantenna. *Nat. Photonics* **2009**, *3*, 654– 657, DOI: 10.1038/nphoton.2009.187
8. Puchkova, A.; Vietz, C.; Pibiri, E.; Wünsch, B.; Sanz Paz, M.; Acuna, G. P.; Tinnefeld, P. DNA Origami Nanoantennas with over 5000-fold Fluorescence Enhancement and Single-Molecule Detection at 25  $\mu\text{m}$ . *Nano Lett.* **2015**, *15*, 8354– 8359, DOI: 10.1021/acs.nanolett.5b04045
9. Holzmeister, P.; Pibiri, E.; Schmied, J. J.; Sen, T.; Acuna, G. P.; Tinnefeld, P. Quantum yield and excitation rate of single molecules close to metallic nanostructures. *Nat. Commun.* **2014**, *5*, 5356, DOI: 10.1038/ncomms6356
10. Kaminska, I.; Vietz, C.; Cuartero-González, Á.; Tinnefeld, P.; Fernández-Domínguez, A. I.; Acuna, G. P. Strong plasmonic enhancement of single molecule photostability in silver dimer optical antennas. *Nanophotonics* **2018**, *7*, 643– 649, DOI: 10.1515/nanoph-2017-0081
11. Pellegrotti, J. V.; Acuna, G. P.; Puchkova, A.; Holzmeister, P.; Gietl, A.; Lalkens, B.; Stefani, F. D.; Tinnefeld, P. Controlled Reduction of Photobleaching in DNA Origami–Gold Nanoparticle Hybrids. *Nano Lett.* **2014**, *14*, 2831– 2836, DOI: 10.1021/nl500841n
12. Pfeiffer, M.; Trofymchuk, K.; Ranallo, S.; Ricci, F.; Steiner, F.; Cole, F.; Glembockyte, V.; Tinnefeld, P. Single antibody detection in a DNA origami nanoantenna. *iScience* **2021**, *24*, 103072 DOI: 10.1016/j.isci.2021.103072
13. Yeşilyurt, A. T. M.; Huang, J.-S. Emission Manipulation by DNA Origami-Assisted plasmonic Nanoantennas. *Adv. Opt. Mater.* **2021**, *9*, 2100848, DOI: 10.1002/adom.202100848
14. Xu, Y.; Zhang, Q.; Chen, R.; Cao, H.; Tang, J.; Wu, Y.; Lu, X.; Chu, B.; Song, B.; Wang, H. NIR-II Photoacoustic-Active DNA Origami Nanoantenna for Early Diagnosis and Smart Therapy of Acute Kidney Injury. *J. Am. Chem. Soc.* **2022**, *144*, 23522– 23533, DOI: 10.1021/jacs.2c10323
15. Dass, M.; Gür, F. N.; Kołtąj, K.; Urban, M. J.; Liedl, T. DNA Origami-Enabled plasmonic Sensing. *J. Phys. Chem. C* **2021**, *125*, 5969– 5981, DOI: 10.1021/acs.jpcc.0c11238
16. Ochmann, S. E.; Vietz, C.; Trofymchuk, K.; Acuna, G. P.; Lalkens, B.; Tinnefeld, P. Optical Nanoantenna for Single Molecule-Based Detection of Zika Virus Nucleic Acids without Molecular Multiplication. *Anal. Chem.* **2017**, *89*, 13000– 13007, DOI: 10.1021/acs.analchem.7b04082
17. Grabenhorst, L.; Trofymchuk, K.; Steiner, F.; Glembockyte, V.; Tinnefeld, P. Fluorophore photostability and saturation in the hotspot of DNA origami nanoantennas. *Methods Appl. Fluoresc.* **2020**, *8*, 24003, DOI: 10.1088/2050-6120/ab6ac8
18. Bitton, O.; Gupta, S. N.; Haran, G. *Quantum dot plasmonics: from weak to strong coupling.* **2019**, *8*, 559– 575, DOI: 10.1515/nanoph-2018-0218

19. Gómez, D. E.; Vernon, K. C.; Mulvaney, P.; Davis, T. J. Surface Plasmon Mediated Strong Exciton–Photon Coupling in Semiconductor Nanocrystals. *Nano Lett.* **2010**, *10*, 274– 278, DOI: 10.1021/nl903455z
20. Santhosh, K.; Bitton, O.; Chuntanov, L.; Haran, G. Vacuum Rabi splitting in a plasmonic cavity at the single quantum emitter limit. *Nat. Commun.* **2016**, *7*, 11823, DOI: 10.1038/ncomms11823
21. Ratchford, D.; Shafiei, F.; Kim, S.; Gray, S. K.; Li, X. Manipulating Coupling between a Single Semiconductor Quantum Dot and Single Gold Nanoparticle. *Nano Lett.* **2011**, *11*, 1049– 1054, DOI: 10.1021/nl103906f
22. Seeman, N. C.; Sleiman, H. F. DNA nanotechnology. *Nat. Rev. Mater.* **2017**, *3*, 17068, DOI: 10.1038/natrevmats.2017.68
23. Samanta, A.; Deng, Z.; Liu, Y.; Yan, H. A perspective on functionalizing colloidal quantum dots with DNA. *Nano Res.* **2013**, *6*, 853– 870, DOI: 10.1007/s12274-013-0367-x
24. Banerjee, A.; Pons, T.; Lequeux, N.; Dubertret, B. Quantum dots-DNA bioconjugates: synthesis to applications. *Interface Focus* **2016**, *6*, 20160064, DOI: 10.1098/rsfs.2016.0064
25. Zhang, H.; Li, M.; Wang, K.; Tian, Y.; Chen, J.-S.; Fontaine, K. T.; DiMarzio, D.; Liu, M.; Cotlet, M.; Gang, O. Polarized Single-Particle Quantum Dot Emitters through Programmable Cluster Assembly. *ACS Nano* **2020**, *14*, 1369– 1378, DOI: 10.1021/acsnano.9b06919
26. Majewski, P. W.; Michelson, A.; Cordeiro, M. A. L.; Tian, C.; Ma, C.; Kisslinger, K.; Tian, Y.; Liu, W.; Stach, E. A.; Yager, K. G.; Gang, O. Resilient three-dimensional ordered architectures assembled from nanoparticles by DNA. *Sci. Adv.* **2021**, *7*, eabf0617 DOI: 10.1126/sciadv.abf0617
27. Nicoli, F.; Zhang, T.; Hübner, K.; Jin, B.; Selbach, F.; Acuna, G.; Argyropoulos, C.; Liedl, T.; Pilo-Pais, M. DNA-Mediated Self-Assembly of plasmonic Antennas with a Single Quantum Dot in the Hot Spot. *Small* **2019**, *15*, 1804418, DOI: 10.1002/smll.201804418
28. Trofymchuk, K.; Glembockyte, V.; Grabenhorst, L.; Steiner, F.; Vietz, C.; Close, C.; Pfeiffer, M.; Richter, L.; Schütte, M. L.; Selbach, F. Addressable Nanoantennas with Cleared Hotspots for Single-Molecule Detection on a Portable Smartphone Microscope. *Nat. Commun.* **2021**, *12*, 950, DOI: 10.1101/2020.04.09.032037
29. Vietz, C.; Kaminska, I.; Sanz Paz, M.; Tinnefeld, P.; Acuna, G. P. Broadband Fluorescence Enhancement with Self-Assembled Silver Nanoparticle Optical Antennas. *ACS Nano* **2017**, *11*, 4969– 4975, DOI: 10.1021/acsnano.7b01621
30. Ma, Y.; Mao, G.; Huang, W.; Wu, G.; Yin, W.; Ji, X.; Deng, Z.; Cai, Z.; Zhang, X.-E.; He, Z. Quantum Dot Nanobeacons for Single RNA Labeling and Imaging. *J. Am. Chem. Soc.* **2019**, *141*, 13454– 13458, DOI: 10.1021/jacs.9b04659
31. Douglas, S. M. Rapid prototyping of 3D DNA-origami shapes with caDNA. *Nucleic Acids Res.* **2009**, *37*, 5001– 5006, DOI: 10.1093/nar/gkp436

32. J.R., L. *Principles of Fluorescence Spectroscopy*. (Springer: New York, NY, 2006). doi: DOI: 10.1007/978-0-387-46312-4 .
33. Close, C.; Trofymchuk, K.; Grabenhorst, L.; Lalkens, B.; Glembockyte, V.; Tinnefeld, P. Maximizing the Accessibility in DNA Origami Nanoantenna plasmonic Hotspots. *Adv. Mater. Interfaces* **2022**, *9*, 2200255, DOI: 10.1002/admi.202200255
34. Strauss, M. T.; Schueder, F.; Haas, D.; Nickels, P. C.; Jungmann, R. Quantifying absolute addressability in DNA origami with molecular resolution. *Nat. Commun.* **2018**, *9*, 1600, DOI: 10.1038/s41467-018-04031-z
35. Resch-Genger, U.; Grabolle, M.; Cavaliere-Jaricot, S.; Nitschke, R.; Nann, T. Quantum dots versus organic dyes as fluorescent labels. *Nat. Methods* **2008**, *5*, 763– 775, DOI: 10.1038/nmeth.1248
36. Qin, W.; Shah, R. A.; Guyot-Sionnest, P. CdSeS/ZnS Alloyed Nanocrystal Lifetime and Blinking Studies under Electrochemical Control. *ACS Nano* **2012**, *6*, 912– 918, DOI: 10.1021/nn2044388
37. Nirmal, M.; Dabbousi, B. O.; Bawendi, M. G.; Macklin, J. J.; Trautman, J. K.; Harris, T. D.; Brus, L. E. Fluorescence intermittency in single cadmium selenide nanocrystals. *Nature* **1996**, *383*, 802– 804, DOI: 10.1038/383802a0
38. Lim, S. J.; Ma, L.; Schleife, A.; Smith, A. M. Quantum Dot Surface Engineering: Toward Inert Fluorophores with Compact Size and Bright, Stable Emission. *Coord. Chem. Rev.* **2016**, *320–327*, 216– 237, DOI: 10.1016/j.ccr.2016.03.012
39. Schedlbauer, J.; Wilhelm, P.; Grabenhorst, L.; Federl, M. E.; Lalkens, B.; Hinderer, F.; Scherf, U.; Höger, S.; Tinnefeld, P.; Bange, S. Ultrafast Single-Molecule Fluorescence Measured by Femtosecond Double-Pulse Excitation Photon Antibunching. *Nano Lett.* **2020**, *20*, 1074– 1079, DOI: 10.1021/acs.nanolett.9b043

# 6

## SUMMARY AND OUTLOOK

And we are at the end! Before we delve into the future, let's have a quick recap. In this thesis, I combine the fields of DNA nanotechnology and plasmonics to advance biosensing applications, particularly focusing POC diagnostics. From day one of my PhD, I got the opportunity to be a part of an ongoing project regarding detection of single molecules on a smartphone-based device enabled by DNA origami nanoantennas<sup>5</sup>. This experience helped me grasp fundamental concepts and allowed me to build a line of research that excites me the most: applying nanotechnology tools to healthcare.

**In associated publication P1**, we aimed to develop a high-sensitivity assay based on DNA origami NanoAntennas and a reader capable of running the assay and analysing the results for POC diagnostics. We designed a sandwich hybridization assay to detect single DNA strands specific to carbapenem-resistant *Klebsiella pneumoniae*, regarded as a critical pathogen by the WHO. We modified the assay to include more capture strands to increase target capture efficiency. We introduced a short strand (blocker) that prevents the fluorophore from interacting with the hotspot in the absence of the target, significantly reducing false positives. We adapted DNA origami placement<sup>6</sup> to create a densely packed surface with NanoAntennas. We integrated a self-adhesive microfluidic chip to create a channel for repetitive back-and-forth flow during target incubation, helping to overcome slow kinetics at lower target concentrations. In parallel, we developed a simple fluorescence reader with a 2.5 mm × 3 mm field of view, fluidics pump, automated pipetting robot, touchscreen interface, and built-in software to detect and analyse single molecules bound in the NanoAntennas. These elements combined allowed us to detect as low as 5 attomolar concentration above the blank.

To further improve the assay, we coated the NanoAntennas with a thin layer of silica to protect against fluctuations in ionic strength and temperature, as well as from degrading enzymes in biological fluids. With silicified NanoAntennas, we detected 10 aM in target-spiked human blood plasma. In the spirit of making POC diagnostics universally accessible, we demonstrated

that a simple strand-displacement reaction could render the chips reusable, significantly lowering the barriers to advanced diagnostics.

**For associated publication P2<sup>10</sup>,** we explored the use of three different sizes of DNA-tagged quantum dots (QDs) ranging from 2 to 4 nm and studied the effect of incorporating them into the hotspot of DNA origami NanoAntennas on their fluorescence lifetime and intensity. Our aim was to investigate QDs as alternative emitters to traditional organic dyes, which have narrow absorption ranges, broad emission spectra, and are prone to quick photobleaching. In contrast, QDs offer broad absorption ranges, narrow emission spectra, and significantly greater photostability. Moreover, QDs are excellent candidates for multiplexing, as different sizes can be excited at the same wavelength but emit at different wavelengths.

We successfully captured QDs in the hotspot and observed a maximum fluorescence enhancement value of 200 for the smallest QDs. The enhanced QDs exhibited characteristic shortening of fluorescence lifetime and increased intensity. We also recorded frequent blinking typical for QDs, which reduced once the QDs were captured in the hotspot. Throughout the experiments, we noticed the sensitivity of the QDs to their immediate environment, which could be attributed to improper surface passivation. Overall, we learned about the interaction of QDs with plasmonic hotspots and the associated challenges, which is useful for developing advanced photonic devices and biosensing applications.

## **FUTURE DIRECTIONS AND CHALLENGES**

**Miniaturizing the Reader:** The development of a simple fluorescence reader in this thesis represents a significant step towards accessible diagnostics. Future iterations of the reader could leverage advances in microfluidics, optoelectronics, and data processing to create a compact, user-friendly device. The integration of artificial intelligence and machine learning algorithms could enhance data analysis, providing users with rapid and accurate results without the need for specialized training. Furthermore, connectivity features could enable seamless data transmission to healthcare providers, facilitating remote monitoring and telemedicine applications. Ensuring affordability and ease of use will be crucial for adoption in resource-limited settings.

**Multiplexing and disease panels:** One of the most promising avenues is the development of multiplexed detection systems capable of simultaneously identifying multiple biomarkers or pathogens. By designing nanoantennas with different capture strands and

incorporating distinct fluorophores or quantum dots, we can create a platform that detects a panel of diseases or genetic variations in a single assay. Potential applications include infectious disease panels for simultaneous detection of multiple pathogens such as bacteria or viruses. This is particularly valuable in clinical settings where rapid identification of the causative agent is crucial for appropriate treatment.

Combining DNA origami nanoantennas with spotting technologies can lead to the creation of high-density biochips or microarrays. By precisely placing nanoantennas on substrates using techniques such as dip-pen nanolithography or microcontact printing, we can fabricate chips with thousands of individually addressable spots, each designed to detect a specific target.

**Detection of miRNAs and SNPs:** miRNAs are small, non-coding RNA molecules typically 18-25 nucleotides long, playing crucial roles in gene regulation and serving as biomarkers for various diseases, including cancers and neurodegenerative disorders<sup>274</sup>. The 2024 Nobel Prize in Physiology or Medicine to

Victor Ambros and Gary Ruvkun, for the discovery of microRNA and its role in post-transcriptional gene regulation, further highlights its role in the future of diagnostics.

Detecting miRNAs poses significant challenges due to their short length, low abundance, and sequence similarities among family members. The detection of short nucleic acids like miRNAs requires highly specific and sensitive assays. The limited number of nucleotides reduces the specificity of hybridization-based detection methods, increasing the risk of cross-reactivity and false positives. To this end, we can explore the use of modified nucleic acids, such as locked nucleic acids (LNAs) or peptide nucleic acids (PNAs), which have higher binding affinities and specificity for short RNA sequences<sup>275</sup>. Incorporating these into the DNA origami structures could enhance the capture efficiency of miRNAs. Furthermore, LNAs and PNAs have higher melting temperatures and are more sensitive to mismatches<sup>276</sup>. Smartly utilizing this could open ways for single nucleotide polymorphisms (SNPs) detection using DNA origami nanoantennas. SNPs help in understanding complex diseases such as heart disease, diabetes, and cancer, and also play a crucial role in pharmacogenomics, or the study of how genes affect a person's response to drugs.

**Commercialization and Startup Potential:** The successful development and validation of the biosensing platform in this thesis have garnered interest for commercialization. The potential to establish a startup based on this technology offers an exciting pathway to bring advanced diagnostics to market. By translating the research into a viable product, we can address real-world healthcare challenges, particularly in early disease



detection and management. Collaborations with industry partners and investors will be essential to navigate the regulatory landscape, scale up production, and ensure the technology meets the needs of end-users.

**Towards Widespread At-Home Testing:** The ultimate vision is to empower individuals with the ability to monitor their health through personalized diagnostic devices that can be used at home, enabling early detection and monitoring of diseases. DNA origami nanoantennas, with their high sensitivity and specificity, could be central to this vision. However, several challenges regarding scalability, stability and storage, standardization of protocols etc. must be addressed.

In a nutshell, this thesis has advanced the understanding and application of DNA origami nanoantennas in biosensing, demonstrating their potential for highly sensitive and specific detection of biomolecules. By envisioning and pursuing the future directions outlined above, we can contribute to the development of next-generation diagnostics that are accessible, affordable, and transformative for global health. The journey from laboratory research to real-world applications is challenging but filled with opportunities to make a significant impact. Through continued innovation, collaboration, and dedication, the dream of personalized, at-home diagnostics powered by nanotechnology can become a reality, ushering in a new era of proactive and personalized healthcare.

## REFERENCES

1. Mousa, S. Biosensors: the new wave in cancer diagnosis. *Nanotechnol Sci Appl* 1 (2010) doi:10.2147/NSA.S13465.
2. Murray, C. J. L. et al. Global burden of bacterial antimicrobial resistance in 2019: a systematic analysis. *The Lancet* 399, 629–655 (2022).
3. White, D. S., Smith, M. A., Chanda, B. & Goldsmith, R. H. Strategies for Overcoming the Single-Molecule Concentration Barrier. *ACS Measurement Science Au* 3, 239–257 (2023).
4. Acuna, G. P. et al. Fluorescence Enhancement at Docking Sites of DNA-Directed Self-Assembled Nanoantennas. *Science* (1979) 338, 506–510 (2012).
5. Trofymchuk, K. et al. Addressable nanoantennas with cleared hotspots for single-molecule detection on a portable smartphone microscope. *Nat Commun* 12, 950 (2021).

6. Shetty, R. M., Brady, S. R., Rothmund, P. W. K., Hariadi, R. F. & Gopinath, A. Bench-Top Fabrication of Single-Molecule Nanoarrays by DNA Origami Placement. *ACS Nano* 15, 11441–11450 (2021).
7. Nguyen, L., Döblinger, M., Liedl, T. & Heuer-Jungemann, A. DNA-Origami-Templated Silica Growth by Sol–Gel Chemistry. *Angewandte Chemie International Edition* 58, 912–916 (2019).
8. Jing, X. et al. Solidifying framework nucleic acids with silica. *Nat Protoc* 14, 2416–2436 (2019).
9. Wassermann, L. M., Scheckenbach, M., Baptist, A. V., Glembockyte, V. & Heuer-Jungemann, A. Full Site-Specific Addressability in DNA Origami-Templated Silica Nanostructures. *Advanced Materials* 35, (2023).
10. Yaadav, R. et al. Broad-Band Fluorescence Enhancement of QDs Captured in the Hotspot of DNA Origami Nanonantennas. *The Journal of Physical Chemistry C* (2024) doi:10.1021/acs.jpcc.4c01797.
11. Wikipedia. 'Life.' Wikimedia Foundation. (2024).
12. UPDIKE, S. J. & HICKS, G. P. The Enzyme Electrode. *Nature* 214, 986–988 (1967).
13. Shukla, S., Hong, S.-Y., Chung, S. H. & Kim, M. Rapid Detection Strategies for the Global Threat of Zika Virus: Current State, New Hypotheses, and Limitations. *Front Microbiol* 7, (2016).
14. Verma, M. K. et al. Rapid diagnostic methods for SARS-CoV-2 (COVID-19) detection: an evidence-based report. *J Med Life* 14, 431–442 (2021).
15. Fleischmann-Struzek, C. & Rudd, K. Challenges of assessing the burden of sepsis. *Med Klin Intensivmed Notfmed* 118, 68–74 (2023).
16. Goodsell, D. S. Zika Virus. *RCSB Protein Data Bank* (2020) doi:10.2210/rcsb\_pdb/goodsell-gallery-015.
17. Goodsell, D. S. Coronavirus. *RCSB Protein Data Bank* (2020) doi:10.2210/rcsb\_pdb/goodsell-gallery-019.
18. Kang, C.-I. et al. Bloodstream Infections Caused by Antibiotic-Resistant Gram-Negative Bacilli: Risk Factors for Mortality and Impact of Inappropriate Initial Antimicrobial Therapy on Outcome. *Antimicrob Agents Chemother* 49, 760–766 (2005).
19. Kumar, A. et al. Duration of hypotension before initiation of effective antimicrobial therapy is the critical determinant of survival in human septic shock\*. *Crit Care Med* 34, 1589–1596 (2006).
20. Kaprou, G. D., Bergšpica, I., Alexa, E. A., Alvarez-Ordóñez, A. & Prieto, M. Rapid Methods for Antimicrobial Resistance Diagnostics. *Antibiotics* 10, 209 (2021).
21. Kellner, M. J., Koob, J. G., Gootenberg, J. S., Abudayyeh, O. O. & Zhang, F. SHERLOCK: nucleic acid detection with CRISPR nucleases. *Nat Protoc* 14, 2986–3012 (2019).

22. Chen, J. S. et al. CRISPR-Cas12a target binding unleashes indiscriminate single-stranded DNase activity. *Science* (1979) 360, 436–439 (2018).
23. Kaminski, M. M., Abudayyeh, O. O., Gootenberg, J. S., Zhang, F. & Collins, J. J. CRISPR-based diagnostics. *Nat Biomed Eng* 5, 643–656 (2021).
24. Branton, D. et al. The potential and challenges of nanopore sequencing. *Nat Biotechnol* 26, 1146–1153 (2008).
25. Kaminski, M. M., Abudayyeh, O. O., Gootenberg, J. S., Zhang, F. & Collins, J. J. CRISPR-based diagnostics. *Nat Biomed Eng* 5, 643–656 (2021).
26. Gines, G., Menezes, R., Xiao, W., Rondelez, Y. & Taly, V. Emerging isothermal amplification technologies for microRNA biosensing: Applications to liquid biopsies. *Mol Aspects Med* 72, 100832 (2020).
27. Naresh, Varnakavi. & Lee, N. A Review on Biosensors and Recent Development of Nanostructured Materials-Enabled Biosensors. *Sensors* 21, 1109 (2021).
28. Binnig G.; Rohrer, H. Scanning tunneling microscopy". *IBM J Res Dev* 30 (4): 35, (1986).
29. Abbe, E. Beiträge zur Theorie des Mikroskops und der mikroskopischen Wahrnehmung. *Archiv für Mikroskopische Anatomie* 9, 413–468 (1873).
30. Lichtman, J. W. & Conchello, J.-A. Fluorescence microscopy. *Nat Methods* 2, 910–919 (2005).
31. Walt, D. R. Optical Methods for Single Molecule Detection and Analysis. *Anal Chem* 85, 1258–1263 (2013).
32. Joseph R. Lakowicz. *Principles of Fluorescence Spectroscopy*. (Springer New York, NY). doi:<https://doi.org/10.1007/978-0-387-46312-4>.
33. Herschel, J. F. W. IV. 'Ἀμόρφωτα, no. I.— on a case of superficial colour presented by a homogeneous liquid internally colourless. *Philos Trans R Soc Lond* 135, 143–145 (1997).
34. Berlman IB. *Handbook of Fluorescence Spectra of Aromatic Molecules*. (Academic Press, New York., 1971).
35. Glembockyte, Viktorija. *Photoprotection of Fluorophores used for single-molecule imaging: a battle for more photons*. (McGill University, 2017).
36. Holzmeister, P., Acuna, G. P., Grohmann, D. & Tinnefeld, P. Breaking the concentration limit of optical single-molecule detection. *Chem. Soc. Rev.* 43, 1014–1028 (2014).
37. Eid, J. et al. Real-time DNA sequencing from single polymerase molecules. *Science* 323, 133–138 (2009).
38. Luchowski, R. et al. Single Molecule Studies of Multiple-Fluorophore Labeled Antibodies. Effect of Homo-FRET on the Number of Photons Available Before Photobleaching. *Curr Pharm Biotechnol* 9, 411–420 (2008).
39. Valeur, B. & Berberan-Santos, M. N. *Molecular Fluorescence*. (Wiley, 2012). doi:[10.1002/9783527650002](https://doi.org/10.1002/9783527650002).

40. Farka, Z. et al. Advances in Optical Single-Molecule Detection: En Route to Supersensitive Bioaffinity Assays. *Angewandte Chemie International Edition* 59, 10746–10773 (2020).
41. Rissin, D. M. et al. Single-molecule enzyme-linked immunosorbent assay detects serum proteins at subfemtomolar concentrations. *Nat Biotechnol* 28, 595–599 (2010).
42. Kelly, K. L., Coronado, E., Zhao, L. L. & Schatz, G. C. The Optical Properties of Metal Nanoparticles: The Influence of Size, Shape, and Dielectric Environment. *J Phys Chem B* 107, 668–677 (2003).
43. Bharadwaj, P., Deutsch, B. & Novotny, L. Optical Antennas. *Adv. Opt. Photon.* 1, 438–483 (2009).
44. Novotny, L. & van Hulst, N. Antennas for light. *Nat Photonics* 5, 83–90 (2011).
45. Glembocckyte, V., Grabenhorst, L., Trofymchuk, K. & Tinnefeld, P. DNA Origami Nanoantennas for Fluorescence Enhancement. *Acc Chem Res* 54, 3338–3348 (2021).
46. Punj, D. et al. A plasmonic ‘antenna-in-box’ platform for enhanced single-molecule analysis at micromolar concentrations. *Nat Nanotechnol* 8, 512–516 (2013).
47. Curto, A. G. et al. Unidirectional Emission of a Quantum Dot Coupled to a Nanoantenna. *Science* (1979) 329, 930–933 (2010).
48. Wei, Q. et al. Fluorescent Imaging of Single Nanoparticles and Viruses on a Smart Phone. *ACS Nano* 7, 9147–9155 (2013).
49. Wei, Q. et al. Imaging and Sizing of Single DNA Molecules on a Mobile Phone. *ACS Nano* 8, 12725–12733 (2014).
50. Kühnemund, M. et al. Targeted DNA sequencing and in situ mutation analysis using mobile phone microscopy. *Nat Commun* 8, 13913 (2017).
51. Chung, S. et al. Smartphone-Based Paper Microfluidic Particulometry of Norovirus from Environmental Water Samples at the Single Copy Level. *ACS Omega* 4, 11180–11188 (2019).
52. Brown, J. W. P. et al. Single-molecule detection on a portable 3D-printed microscope. *Nat Commun* 10, 5662 (2019).
53. Taminiau, T. H., Stefani, F. D. & van Hulst, N. F. Enhanced directional excitation and emission of single emitters by a nano-optical Yagi-Uda antenna. *Opt. Express* 16, 10858–10866 (2008).
54. Tang, L. et al. Nanometre-scale germanium photodetector enhanced by a near-infrared dipole antenna. *Nat Photonics* 2, 226–229 (2008).
55. Cao, L., Park, J.-S., Fan, P., Clemens, B. & Brongersma, M. L. Resonant Germanium Nanoantenna Photodetectors. *Nano Lett* 10, 1229–1233 (2010).
56. Pillai, S., Catchpole, K. R., Trupke, T. & Green, M. A. Surface plasmon enhanced silicon solar cells. *J Appl Phys* 101, (2007).

57. Cubukcu, E., Kort, E. A., Crozier, K. B. & Capasso, F. Plasmonic laser antenna. *Appl Phys Lett* 89, (2006).
58. Anker, J. N. et al. Biosensing with plasmonic nanosensors. *Nat Mater* 7, 442–453 (2008).
59. Mühlischlegel, P., Eisler, H.-J., Martin, O. J. F., Hecht, B. & Pohl, D. W. Resonant Optical Antennas. *Science* (1979) 308, 1607–1609 (2005).
60. Ghenuche, P., Cherukulappurath, S., Taminiau, T. H., van Hulst, N. F. & Quidant, R. Spectroscopic Mode Mapping of Resonant Plasmon Nanoantennas. *Phys Rev Lett* 101, 116805 (2008).
61. Kinkhabwala, A. et al. Large single-molecule fluorescence enhancements produced by a bowtie nanoantenna. *Nat Photonics* 3, 654–657 (2009).
62. Anger, P., Bharadwaj, P. & Novotny, L. Enhancement and Quenching of Single-Molecule Fluorescence. *Phys Rev Lett* 96, 113002 (2006).
63. Kalkbrenner, T. et al. Optical Microscopy via Spectral Modifications of a Nanoantenna. *Phys Rev Lett* 95, 200801 (2005).
64. Grzelczak, M., Pérez-Juste, J., Mulvaney, P. & Liz-Marzán, L. M. Shape control in gold nanoparticle synthesis. *Chem Soc Rev* 37, 1783 (2008).
65. Turkevich, J., Stevenson, P. C. & Hillier, J. A study of the nucleation and growth processes in the synthesis of colloidal gold. *Discuss Faraday Soc* 11, 55 (1951).
66. Nikoobakht, B. & El-Sayed, M. A. Preparation and Growth Mechanism of Gold Nanorods (NRs) Using Seed-Mediated Growth Method. *Chemistry of Materials* 15, 1957–1962 (2003).
67. Jana, N. R., Gearheart, L. & Murphy, C. J. Wet Chemical Synthesis of High Aspect Ratio Cylindrical Gold Nanorods. *J Phys Chem B* 105, 4065–4067 (2001).
68. Liu, M. & Guyot-Sionnest, P. Mechanism of Silver(I)-Assisted Growth of Gold Nanorods and Bipyramids. *J Phys Chem B* 109, 22192–22200 (2005).
69. Halas, N. J., Lal, S., Chang, W.-S., Link, S. & Nordlander, P. Plasmons in Strongly Coupled Metallic Nanostructures. *Chem Rev* 111, 3913–3961 (2011).
70. Jimenez de Aberasturi, D. et al. Surface Enhanced Raman Scattering Encoded Gold Nanostars for Multiplexed Cell Discrimination. *Chemistry of Materials* 28, 6779–6790 (2016).
71. Wu, H.-L., Kuo, C.-H. & Huang, M. H. Seed-Mediated Synthesis of Gold Nanocrystals with Systematic Shape Evolution from Cubic to Trisoctahedral and Rhombic Dodecahedral Structures. *Langmuir* 26, 12307–12313 (2010).
72. González-Rubio, G. et al. Disconnecting Symmetry Breaking from Seeded Growth for the Reproducible Synthesis of High Quality Gold Nanorods. *ACS Nano* 13, 4424–4435 (2019).

73. Scarabelli, L., Coronado-Puchau, M., Giner-Casares, J. J., Langer, J. & Liz-Marzán, L. M. Monodisperse Gold Nanotriangles: Size Control, Large-Scale Self-Assembly, and Performance in Surface-Enhanced Raman Scattering. *ACS Nano* 8, 5833–5842 (2014).
74. Hanske, C. et al. Large-Scale Plasmonic Pyramidal Supercrystals via Templated Self-Assembly of Monodisperse Gold Nanospheres. *The Journal of Physical Chemistry C* 121, 10899–10906 (2017).
75. Sánchez-Iglesias, A. et al. High-Yield Seeded Growth of Monodisperse Pentatwinned Gold Nanoparticles through Thermally Induced Seed Twinning. *J Am Chem Soc* 139, 107–110 (2017).
76. de la Encarnación, C., Jimenez de Aberasturi, D. & Liz-Marzán, L. M. Multifunctional plasmonic-magnetic nanoparticles for bioimaging and hyperthermia. *Adv Drug Deliv Rev* 189, 114484 (2022).
77. Gates, B. D. et al. New Approaches to Nanofabrication: Molding, Printing, and Other Techniques. *Chem Rev* 105, 1171–1196 (2005).
78. Huang, J.-S. et al. Atomically flat single-crystalline gold nanostructures for plasmonic nanocircuitry. *Nat Commun* 1, 150 (2010).
79. Rechberger, W. et al. Optical properties of two interacting gold nanoparticles. *Opt Commun* 220, 137–141 (2003).
80. Aćimović, S. S., Kreuzer, M. P., González, M. U. & Quidant, R. Plasmon Near-Field Coupling in Metal Dimers as a Step toward Single-Molecule Sensing. *ACS Nano* 3, 1231–1237 (2009).
81. Ueno, K., Mizeikis, V., Juodkasis, S., Sasaki, K. & Misawa, H. Optical properties of nanoengineered gold blocks. *Opt Lett* 30, 2158–2160 (2005).
82. Douglas, S. M. et al. Self-assembly of DNA into nanoscale three-dimensional shapes. *Nature* 459, 414–418 (2009).
83. Rothemund, P. W. K. Folding DNA to create nanoscale shapes and patterns. *Nature* 440, 297–302 (2006).
84. Taylor, A. B. & Zijlstra, P. Single-Molecule Plasmon Sensing: Current Status and Future Prospects. *ACS Sens* 2, 1103–1122 (2017).
85. Dass, M., Gür, F. N., Kołataj, K., Urban, M. J. & Liedl, T. DNA Origami-Enabled Plasmonic Sensing. *The Journal of Physical Chemistry C* 125, 5969–5981 (2021).
86. Andersen, E. S. et al. Self-assembly of a nanoscale DNA box with a controllable lid. *Nature* 459, 73–76 (2009).
87. Kopperger, E. et al. A self-assembled nanoscale robotic arm controlled by electric fields. *Science* (1979) 359, 296–301 (2018).
88. Mirkin, C. A., Letsinger, R. L., Mucic, R. C. & Storhoff, J. J. A DNA-based method for rationally assembling nanoparticles into macroscopic materials. *Nature* 382, 607–609 (1996).

89. Alivisatos, A. P. et al. Organization of 'nanocrystal molecules' using DNA. *Nature* 382, 609–611 (1996).
90. Liu, B. & Liu, J. Methods for preparing DNA-functionalized gold nanoparticles, a key reagent of bioanalytical chemistry. *Analytical Methods* 9, 2633–2643 (2017).
91. Cutler, J. I., Auyeung, E. & Mirkin, C. A. Spherical Nucleic Acids. *J Am Chem Soc* 134, 1376–1391 (2012).
92. Liu, J. & Lu, Y. Preparation of aptamer-linked gold nanoparticle purple aggregates for colorimetric sensing of analytes. *Nat Protoc* 1, 246–252 (2006).
93. Liu, B., Wu, T., Huang, Z., Liu, Y. & Liu, J. Freezing-directed Stretching and Alignment of DNA Oligonucleotides. *Angewandte Chemie International Edition* 58, 2109–2113 (2019).
94. Liu, B. & Liu, J. Freezing-Driven DNA Adsorption on Gold Nanoparticles: Tolerating Extremely Low Salt Concentration but Requiring High DNA Concentration. *Langmuir* 35, 6476–6482 (2019).
95. Hung, A. M. et al. Large-area spatially ordered arrays of gold nanoparticles directed by lithographically confined DNA origami. *Nat Nanotechnol* 5, 121–126 (2010).
96. Thacker, V. V. et al. DNA origami based assembly of gold nanoparticle dimers for surface-enhanced Raman scattering. *Nat Commun* 5, 3448 (2014).
97. Schreiber, R. et al. Chiral plasmonic DNA nanostructures with switchable circular dichroism. *Nat Commun* 4, 2948 (2013).
98. Gür, F. N., Schwarz, F. W., Ye, J., Diez, S. & Schmidt, T. L. Toward Self-Assembled Plasmonic Devices: High-Yield Arrangement of Gold Nanoparticles on DNA Origami Templates. *ACS Nano* 10, 5374–5382 (2016).
99. Zhan, P. et al. Reconfigurable Three-Dimensional Gold Nanorod Plasmonic Nanostructures Organized on DNA Origami Tripod. *ACS Nano* 11, 1172–1179 (2017).
100. Wikipedia. Fluorescence. <https://en.wikipedia.org/wiki/Fluorescence> (2024).
101. Shera EB Seitzinger NK, D. L. M. K. R. A. S. S. A. Detection of single fluorescent molecules. *Chem Phys Lett* (1990) doi:10.1016/0009-2614(90)85485-U.
102. Moerner, W. E. & Kador, L. Optical detection and spectroscopy of single molecules in a solid. *Phys Rev Lett* 62, 2535–2538 (1989).
103. Orrit, M. & Bernard, J. Single pentacene molecules detected by fluorescence excitation in a p-terphenyl crystal. *Phys. Rev. Lett.* 65, 2716–2719 (1990).
104. Hirschfeld, T. Optical microscopic observation of single small molecules. *Appl Opt* 15, 2965–2966 (1976).
105. Nguyen, D. C., Keller, R. A., Jett, J. H. & Martin, J. C. Detection of single molecules of phycoerythrin in hydrodynamically focused flows by laser-induced fluorescence. *Anal Chem* 59, 2158–2161 (1987).

106. Peck, K., Stryer, L., Glazer, A. N. & Mathies, R. A. Single-molecule fluorescence detection: autocorrelation criterion and experimental realization with phycoerythrin. *Proc Natl Acad Sci U S A* 86, 4087–4091 (1989).
107. Bergquist, J. C., Hulet, R. G., Itano, W. M. & Wineland, D. J. Observation of Quantum Jumps in a Single Atom. *Phys. Rev. Lett.* 57, 1699–1702 (1986).
108. Diedrich, F. & Walther, H. Nonclassical radiation of a single stored ion. *Phys. Rev. Lett.* 58, 203–206 (1987).
109. Funatsu, T., Harada, Y., Tokunaga, M., Saito, K. & Yanagida, T. Imaging of single fluorescent molecules and individual ATP turnovers by single myosin molecules in aqueous solution. *Nature* 374, 555–559 (1995).
110. Ha, T. et al. Probing the interaction between two single molecules: fluorescence resonance energy transfer between a single donor and a single acceptor. *Proc Natl Acad Sci U S A* 93, 6264–6268 (1996).
111. SHIMOMURA, O., JOHNSON, F. H. & SAIGA, Y. Extraction, purification and properties of aequorin, a bioluminescent protein from the luminous hydromedusa, *Aequorea*. *J Cell Comp Physiol* 59, 223–239 (1962).
112. Prasher, D. C., Eckenrode, V. K., Ward, W. W., Prendergast, F. G. & Cormier, M. J. Primary structure of the *Aequorea victoria* green-fluorescent protein. *Gene* 111, 229–233 (1992).
113. Chalfie, M., Tu, Y., Euskirchen, G., Ward, W. W. & Prasher, D. C. Green fluorescent protein as a marker for gene expression. *Science* 263, 802–805 (1994).
114. Heim, R. & Tsien, R. Y. Engineering green fluorescent protein for improved brightness, longer wavelengths and fluorescence resonance energy transfer. *Curr Biol* 6, 178–182 (1996).
115. Cubitt, A. B. et al. Understanding, improving and using green fluorescent proteins. *Trends Biochem Sci* 20, 448–455 (1995).
116. Heim, R., Prasher, D. C. & Tsien, R. Y. Wavelength mutations and posttranslational autooxidation of green fluorescent protein. *Proc Natl Acad Sci U S A* 91, 12501–12504 (1994).
117. Kremers, G.-J., Goedhart, J., van Munster, E. B. & Gadella, T. W. J. Cyan and Yellow Super Fluorescent Proteins with Improved Brightness, Protein Folding, and FRET Förster Radius. *Biochemistry* 45, 6570–6580 (2006).
118. Kremers, G.-J., Goedhart, J., van den Heuvel, D. J., Gerritsen, H. C. & Gadella, T. W. J. Improved green and blue fluorescent proteins for expression in bacteria and mammalian cells. *Biochemistry* 46, 3775–3783 (2007).
119. Nagai, T. et al. A variant of yellow fluorescent protein with fast and efficient maturation for cell-biological applications. *Nat Biotechnol* 20, 87–90 (2002).



120. Griesbeck, O., Baird, G. S., Campbell, R. E., Zacharias, D. A. & Tsien, R. Y. Reducing the environmental sensitivity of yellow fluorescent protein. Mechanism and applications. *J Biol Chem* 276, 29188–29194 (2001).
121. Douglass, A. D. & Vale, R. D. Single-molecule imaging of fluorescent proteins. *Methods Cell Biol* 85, 113–125 (2008).
122. Blum, C. & Subramaniam, V. Single-molecule spectroscopy of fluorescent proteins. *Anal Bioanal Chem* 393, 527–541 (2009).
123. Pierce, D. W., Hom-Booher, N. & Vale, R. D. Imaging individual green fluorescent proteins. *Nature* 388, 338 (1997).
124. Dickson, R. M., Cubitt, A. B., Tsien, R. Y. & Moerner, W. E. On/off blinking and switching behaviour of single molecules of green fluorescent protein. *Nature* 388, 355–358 (1997).
125. Klar, T. A. & Hell, S. W. Subdiffraction resolution in far-field fluorescence microscopy. *Opt. Lett.* 24, 954–956 (1999).
126. Hell, S. W. & Wichmann, J. Breaking the diffraction resolution limit by stimulated emission: stimulated-emission-depletion fluorescence microscopy. *Opt. Lett.* 19, 780–782 (1994).
127. Betzig, E. et al. Imaging intracellular fluorescent proteins at nanometer resolution. *Science* 313, 1642–1645 (2006).
128. Rust, M. J., Bates, M. & Zhuang, X. Sub-diffraction-limit imaging by stochastic optical reconstruction microscopy (STORM). *Nat Methods* 3, 793–796 (2006).
129. Hess, S. T., Girirajan, T. P. K. & Mason, M. D. Ultra-high resolution imaging by fluorescence photoactivation localization microscopy. *Biophys J* 91, 4258–4272 (2006).
130. Hofmann, M., Eggeling, C., Jakobs, S. & Hell, S. W. Breaking the diffraction barrier in fluorescence microscopy at low light intensities by using reversibly photoswitchable proteins. *Proceedings of the National Academy of Sciences* 102, 17565–17569 (2005).
131. Sharonov, A. & Hochstrasser, R. M. Wide-field subdiffraction imaging by accumulated binding of diffusing probes. *Proceedings of the National Academy of Sciences* 103, 18911–18916 (2006).
132. Jungmann, R. et al. Single-Molecule Kinetics and Super-Resolution Microscopy by Fluorescence Imaging of Transient Binding on DNA Origami. *Nano Lett* 10, 4756–4761 (2010).
133. Reinhardt, S. C. M. et al. Ångström-resolution fluorescence microscopy. *Nature* 617, 711–716 (2023).
134. Eduard M. Unterauer Sayedali Shetab Boushehri Kristina Jevdokimenko et al. Spatial proteomics in neurons at single-protein resolution. *Cell* 187, (2024).
135. Jabłoński, A. Über den Mechanismus der Photolumineszenz von Farbstoffphosphoren. *Zeitschrift für Physik* 94, 38–46 (1935).

136. Franck, J. & Dymond, E. G. Elementary processes of photochemical reactions. *Transactions of the Faraday Society* 21, 536 (1926).
137. Kasha, M. Characterization of electronic transitions in complex molecules. *Discuss Faraday Soc* 9, 14 (1950).
138. Förster, Th. Zwischenmolekulare Energiewanderung und Fluoreszenz. *Ann Phys* 437, 55–75 (1948).
139. Szabó, Á., Szöllősi, J. & Nagy, P. Principles of Resonance Energy Transfer. *Curr Protoc* 2, (2022).
140. Jameson, D. M. *Introduction to Fluorescence*. (CRC Press, 2014). doi:10.1201/b16502.
141. Puchkova, A. et al. DNA Origami Nanoantennas with over 5000-fold Fluorescence Enhancement and Single-Molecule Detection at 25  $\mu\text{m}$ . *Nano Lett* 15, 8354–8359 (2015).
142. Coronado, E. A., Encina, E. R. & Stefani, F. D. Optical properties of metallic nanoparticles: manipulating light, heat and forces at the nanoscale. *Nanoscale* 3, 4042 (2011).
143. Maier, S. A. *Plasmonics: Fundamentals and Applications*. (Springer US, New York, NY, 2007). doi:10.1007/0-387-37825-1.
144. Wikipedia contributors. Plasmonic nanoparticles. *Wikipedia, The Free Encyclopedia*. [https://en.wikipedia.org/w/index.php?title=Plasmonic\\_nanoparticles&oldid=1221216883](https://en.wikipedia.org/w/index.php?title=Plasmonic_nanoparticles&oldid=1221216883) (2024).
145. Huang, J.-S. et al. Mode Imaging and Selection in Strongly Coupled Nanoantennas. *Nano Lett* 10, 2105–2110 (2010).
146. Myroshnychenko, V. et al. Modelling the optical response of gold nanoparticles. *Chem Soc Rev* 37, 1792 (2008).
147. Jain, P. K. & El-Sayed, M. A. Plasmonic coupling in noble metal nanostructures. *Chem Phys Lett* 487, 153–164 (2010).
148. Purcell, E. M. *Proceedings of the American Physical Society. Physical Review* 69, 674–674 (1946).
149. Wikipedia contributors. DNA. In *Wikipedia* <https://en.wikipedia.org/wiki/DNA>.
150. Dahm, R. Discovering DNA: Friedrich Miescher and the early years of nucleic acid research. *Hum Genet* 122, 565–581 (2008).
151. Levene, P. A. THE STRUCTURE OF YEAST NUCLEIC ACID. *Journal of Biological Chemistry* 40, 415–424 (1919).
152. Chargaff, E. Chemical specificity of nucleic acids and mechanism of their enzymatic degradation. *Experientia* 6, 201–209 (1950).
153. FRANKLIN, R. E. & GOSLING, R. G. Molecular Configuration in Sodium Thymonucleate. *Nature* 171, 740–741 (1953).

154. WATSON, J. D. & CRICK, F. H. C. Molecular Structure of Nucleic Acids: A Structure for Deoxyribose Nucleic Acid. *Nature* 171, 737–738 (1953).
155. Meselson, M. & Stahl, F. W. The replication of DNA in *Escherichia coli*. *Proceedings of the National Academy of Sciences* 44, 671–682 (1958).
156. Nirenberg, M. W. & Matthaei, J. H. The dependence of cell-free protein synthesis in *E. coli* upon naturally occurring or synthetic polyribonucleotides. *Proceedings of the National Academy of Sciences* 47, 1588–1602 (1961).
157. Caruthers, M. & Wells, R. Har Gobind Khorana (1922–2011). *Science* (1979) 334, 1511–1511 (2011).
158. Jinek, M. et al. A Programmable Dual-RNA–Guided DNA Endonuclease in Adaptive Bacterial Immunity. *Science* (1979) 337, 816–821 (2012).
159. Cho, Y., Park, S. H., Huh, J.-H., Gopinath, A. & Lee, S. DNA as grabbers and steerers of quantum emitters. *Nanophotonics* 12, 399–412 (2023).
160. Yakovchuk, P. Base-stacking and base-pairing contributions into thermal stability of the DNA double helix. *Nucleic Acids Res* 34, 564–574 (2006).
161. Hargittai, I. & Hargittai, B. Nadrian C. Seeman (1945–2021): pioneer of DNA nanotechnology. *Struct Chem* 33, 631–633 (2022).
162. Seeman, N. C. & Sleiman, H. F. DNA nanotechnology. *Nat Rev Mater* 3, 17068 (2017).
163. Seeman, N. C. Biochemistry and Structural DNA Nanotechnology: An Evolving Symbiotic Relationship. *Biochemistry* 42, 7259–7269 (2003).
164. Kaminska, I. et al. Distance Dependence of Single-Molecule Energy Transfer to Graphene Measured with DNA Origami Nanopositioners. *Nano Lett* 19, 4257–4262 (2019).
165. Posnjak, G. et al. Diamond-lattice photonic crystals assembled from DNA origami. *Science* (1979) 384, 781–785 (2024).
166. Sigl, C. et al. Programmable icosahedral shell system for virus trapping. *Nat Mater* 20, 1281–1289 (2021).
167. Seeman, N. C. Nucleic acid junctions and lattices. *J Theor Biol* 99, 237–247 (1982).
168. Kallenbach, N. R., Ma, R.-I. & Seeman, N. C. An immobile nucleic acid junction constructed from oligonucleotides. *Nature* 305, 829–831 (1983).
169. Chen, J. & Seeman, N. C. Synthesis from DNA of a molecule with the connectivity of a cube. *Nature* 350, 631–633 (1991).
170. Hong, F., Zhang, F., Liu, Y. & Yan, H. DNA Origami: Scaffolds for Creating Higher Order Structures. *Chem Rev* 117, 12584–12640 (2017).
171. Tørring, T., Voigt, N. V., Nangreave, J., Yan, H. & Gothelf, K. V. DNA origami: a quantum leap for self-assembly of complex structures. *Chem Soc Rev* 40, 5636 (2011).
172. Saccà, B. & Niemeyer, C. M. DNA Origami: The Art of Folding DNA. *Angewandte Chemie International Edition* 51, 58–66 (2012).

173. Linko, V. & Dietz, H. The enabled state of DNA nanotechnology. *Curr Opin Biotechnol* 24, 555–561 (2013).
174. Simmel, S. S., Nickels, P. C. & Liedl, T. Wireframe and Tensegrity DNA Nanostructures. *Acc Chem Res* 47, 1691–1699 (2014).
175. Pinheiro, A. V., Han, D., Shih, W. M. & Yan, H. Challenges and opportunities for structural DNA nanotechnology. *Nat Nanotechnol* 6, 763–772 (2011).
176. Wang, P., Meyer, T. A., Pan, V., Dutta, P. K. & Ke, Y. The Beauty and Utility of DNA Origami. *Chem* 2, 359–382 (2017).
177. Pugh, G. C., Burns, J. R. & Howorka, S. Comparing proteins and nucleic acids for next-generation biomolecular engineering. *Nat Rev Chem* 2, 113–130 (2018).
178. Wang, Z.-G. & Ding, B. Engineering DNA Self-Assemblies as Templates for Functional Nanostructures. *Acc Chem Res* 47, 1654–1662 (2014).
179. Okholm, A. H. & Kjems, J. DNA nanovehicles and the biological barriers. *Adv Drug Deliv Rev* 106, 183–191 (2016).
180. Song, L., Jiang, Q., Wang, Z. & Ding, B. Self-Assembled DNA Nanostructures for Biomedical Applications. *ChemNanoMat* 3, 713–724 (2017).
181. Zhu, B., Wang, L., Li, J. & Fan, C. Precisely Tailored DNA Nanostructures and their Theranostic Applications. *The Chemical Record* 17, 1213–1230 (2017).
182. Ke, Y., Castro, C. & Choi, J. H. Structural DNA Nanotechnology: Artificial Nanostructures for Biomedical Research. *Annu Rev Biomed Eng* 20, 375–401 (2018).
183. Vogelsang, J. et al. Make them Blink: Probes for Super-Resolution Microscopy. *ChemPhysChem* 11, 2475–2490 (2010).
184. Albinsson, B., Hannestad, J. K. & Börjesson, K. Functionalized DNA nanostructures for light harvesting and charge separation. *Coord Chem Rev* 256, 2399–2413 (2012).
185. Schlichthaerle, T., Strauss, M. T., Schueder, F., Woehrstein, J. B. & Jungmann, R. DNA nanotechnology and fluorescence applications. *Curr Opin Biotechnol* 39, 41–47 (2016).
186. Acuna, G., Grohmann, D. & Tinnefeld, P. Enhancing single-molecule fluorescence with nanophotonics. *FEBS Lett* 588, 3547–3552 (2014).
187. Samanta, A., Banerjee, S. & Liu, Y. DNA nanotechnology for nanophotonic applications. *Nanoscale* 7, 2210–2220 (2015).
188. Lee, H., Ahn, H., Lee, J. & Nam, K. T. Biomolecule-Enabled Chiral Assembly of Plasmonic Nanostructures. *ChemNanoMat* 3, 685–697 (2017).
189. Zhou, C., Duan, X. & Liu, N. DNA-Nanotechnology-Enabled Chiral Plasmonics: From Static to Dynamic. *Acc Chem Res* 50, 2906–2914 (2017).
190. Liu, N. & Liedl, T. DNA-Assembled Advanced Plasmonic Architectures. *Chem Rev* 118, 3032–3053 (2018).
191. Bell, N. A. W. & Keyser, U. F. Nanopores formed by DNA origami: A review. *FEBS Lett* 588, 3564–3570 (2014).

192. Yang, Y. R., Liu, Y. & Yan, H. DNA Nanostructures as Programmable Biomolecular Scaffolds. *Bioconjug Chem* 26, 1381–1395 (2015).
193. Chandrasekaran, A. R., Anderson, N., Kizer, M., Halvorsen, K. & Wang, X. Beyond the Fold: Emerging Biological Applications of DNA Origami. *ChemBioChem* 17, 1081–1089 (2016).
194. Linko, V. et al. DNA-Based Enzyme Reactors and Systems. *Nanomaterials* 6, 139 (2016).
195. Rajendran, A., Nakata, E., Nakano, S. & Morii, T. Nucleic-Acid-Templated Enzyme Cascades. *ChemBioChem* 18, 696–716 (2017).
196. Endo, M. & Sugiyama, H. Single-Molecule Imaging of Dynamic Motions of Biomolecules in DNA Origami Nanostructures Using High-Speed Atomic Force Microscopy. *Acc Chem Res* 47, 1645–1653 (2014).
197. Zhang, G., Surwade, S. P., Zhou, F. & Liu, H. DNA nanostructure meets nanofabrication. *Chem. Soc. Rev.* 42, 2488–2496 (2013).
198. Pillers, M., Goss, V. & Lieberman, M. Electron-Beam Lithography and Molecular Liftoff for Directed Attachment of DNA Nanostructures on Silicon: Top-down Meets Bottom-up. *Acc Chem Res* 47, 1759–1767 (2014).
199. Shen, B., Tapio, K., Linko, V., Kostianen, M. & Toppari, J. Metallic Nanostructures Based on DNA Nanoshapes. *Nanomaterials* 6, 146 (2016).
200. Julin, S., Nummelin, S., Kostianen, M. A. & Linko, V. DNA nanostructure-directed assembly of metal nanoparticle superlattices. *Journal of Nanoparticle Research* 20, 119 (2018).
201. Douglas, S. M. et al. Rapid prototyping of 3D DNA-origami shapes with caDNAo. *Nucleic Acids Res* 37, 5001–5006 (2009).
202. Wang, Y. et al. DNA origami single crystals with Wulff shapes. *Nat Commun* 12, 3011 (2021).
203. Zhang, T. et al. 3D DNA Origami Crystals. *Advanced Materials* 30, (2018).
204. Ke, Y. et al. Multilayer DNA Origami Packed on a Square Lattice. *J Am Chem Soc* 131, 15903–15908 (2009).
205. Dietz, H., Douglas, S. M. & Shih, W. M. Folding DNA into Twisted and Curved Nanoscale Shapes. *Science* (1979) 325, 725–730 (2009).
206. Gerling, T., Wagenbauer, K. F., Neuner, A. M. & Dietz, H. Dynamic DNA devices and assemblies formed by shape-complementary, non-base pairing 3D components. *Science* (1979) 347, 1446–1452 (2015).
207. Li, Z. et al. Molecular Behavior of DNA Origami in Higher-Order Self-Assembly. *J Am Chem Soc* 132, 13545–13552 (2010).
208. Yurke, B., Turberfield, A. J., Mills, A. P., Simmel, F. C. & Neumann, J. L. A DNA-fuelled molecular machine made of DNA. *Nature* 406, 605–608 (2000).

209. Guo, Y. et al. Recent advances in molecular machines based on toehold-mediated strand displacement reaction. *Quantitative Biology* 5, 25–41 (2017).
210. Simmel, F. C. Nucleic acid strand displacement – from DNA nanotechnology to translational regulation. *RNA Biol* 20, 154–163 (2023).
211. Douglas, S. M., Bachelet, I. & Church, G. M. A Logic-Gated Nanorobot for Targeted Transport of Molecular Payloads. *Science* (1979) 335, 831–834 (2012).
212. Marras, A. E., Zhou, L., Su, H.-J. & Castro, C. E. Programmable motion of DNA origami mechanisms. *Proceedings of the National Academy of Sciences* 112, 713–718 (2015).
213. Kopperger, E. et al. A self-assembled nanoscale robotic arm controlled by electric fields. *Science* (1979) 359, 296–301 (2018).
214. Pumm, A.-K. et al. A DNA origami rotary ratchet motor. *Nature* 607, 492–498 (2022).
215. Shi, X. et al. A DNA turbine powered by a transmembrane potential across a nanopore. *Nat Nanotechnol* 19, 338–344 (2024).
216. Krause, S. et al. Graphene-on-Glass Preparation and Cleaning Methods Characterized by Single-Molecule DNA Origami Fluorescent Probes and Raman Spectroscopy. *ACS Nano* 15, 6430–6438 (2021).
217. Kamińska, I. et al. Graphene Energy Transfer for Single-Molecule Biophysics, Biosensing, and Super-Resolution Microscopy. (2021) doi:10.1002/adma.202101099.
218. Khmelinskaia, A., Mücksch, J., Petrov, E. P., Franquelim, H. G. & Schwille, P. Control of Membrane Binding and Diffusion of Cholesteryl-Modified DNA Origami Nanostructures by DNA Spacers. *Langmuir* 34, 14921–14931 (2018).
219. Büber, E. et al. DNA Origami Curvature Sensors for Nanoparticle and Vesicle Size Determination with Single-Molecule FRET Readout. *ACS Nano* 17, 3088–3097 (2023).
220. Schmied, J. J. et al. DNA origami–based standards for quantitative fluorescence microscopy. *Nat Protoc* 9, 1367–1391 (2014).
221. Inoué, S. Foundations of Confocal Scanned Imaging in Light Microscopy. in *Handbook Of Biological Confocal Microscopy* 1–19 (Springer US, Boston, MA, 2006). doi:10.1007/978-0-387-45524-2\_1.
222. Minsky, M. Microscopy apparatus. (1961).
223. Minsky, M. Memoir on inventing the confocal scanning microscope. *Scanning* 10, 128–138 (1988).
224. Fellers, T. & Davidson, M. Introduction to Confocal Microscopy. <http://www.olympusconfocal.com/theory/confocalintro.html> (2007).
225. Encyclopaedia Britannica. Confocal microscope. Encyclopædia Britannica Media Title confocal microscope Media Type Image Website Name Encyclopædia Britannica <https://www.britannica.com/technology/microscope/Confocal-microscopes#/media/1/380582/136152>.

226. Wikipedia contributors. Total internal reflection fluorescence microscope. In Wikipedia [https://en.wikipedia.org/wiki/Total\\_internal\\_reflection\\_fluorescence\\_microscope](https://en.wikipedia.org/wiki/Total_internal_reflection_fluorescence_microscope).
227. Axelrod, D. Cell-substrate contacts illuminated by total internal reflection fluorescence. *J Cell Biol* 89, 141–145 (1981).
228. Colson, L. et al. Trends in Single-Molecule Total Internal Reflection Fluorescence Imaging and Their Biological Applications with Lab-on-a-Chip Technology. *Sensors* 23, 7691 (2023).
229. Fish, K. N. *Current Protocols in Cytometry*. (John Wiley & Sons, Inc., Hoboken, NJ, USA, 2001). doi:10.1002/0471142956.
230. Kerker, M., Wang, D.-S. & Chew, H. Surface enhanced Raman scattering (SERS) by molecules adsorbed at spherical particles. *Appl Opt* 19, 3373 (1980).
231. Mehmandoust, S., Eskandari, V. & Karooby, E. A Review of Fabrication of DNA Origami Plasmonic Structures for the Development of Surface-Enhanced Raman Scattering (SERS) Platforms. *Plasmonics* (2023) doi:10.1007/s11468-023-02064-9.
232. Tanwar, S., Haldar, K. K. & Sen, T. DNA Origami Directed Au Nanostar Dimers for Single-Molecule Surface-Enhanced Raman Scattering. *J Am Chem Soc* 139, 17639–17648 (2017).
233. Reguera, J., Langer, J., Jiménez de Aberasturi, D. & Liz-Marzán, L. M. Anisotropic metal nanoparticles for surface enhanced Raman scattering. *Chem Soc Rev* 46, 3866–3885 (2017).
234. Fang, W. et al. Quantizing single-molecule surface-enhanced Raman scattering with DNA origami metamolecules. *Sci Adv* 5, (2019).
235. Moeinian, A. et al. Highly Localized SERS Measurements Using Single Silicon Nanowires Decorated with DNA Origami-Based SERS Probe. *Nano Lett* 19, 1061–1066 (2019).
236. Ju, J. et al. Surface Enhanced Raman Spectroscopy Based Biosensor with a Microneedle Array for Minimally Invasive In Vivo Glucose Measurements. *ACS Sens* 5, 1777–1785 (2020).
237. Ren, S. et al. Single-Step Organization of Plasmonic Gold Metamaterials with Self-Assembled DNA Nanostructures. *Research* 2019, (2019).
238. Zhao, M.-Z. et al. DNA origami-templated assembly of plasmonic nanostructures with enhanced Raman scattering. *Nuclear Science and Techniques* 29, 6 (2018).
239. Zhan, P. et al. DNA Origami Directed Assembly of Gold Bowtie Nanoantennas for Single-Molecule Surface-Enhanced Raman Scattering. *Angewandte Chemie* 130, 2896–2900 (2018).
240. Heck, C., Kanehira, Y., Kneipp, J. & Bald, I. Placement of Single Proteins within the SERS Hot Spots of Self-Assembled Silver Nanolenses. *Angewandte Chemie International Edition* 57, 7444–7447 (2018).

241. Simoncelli, S. et al. Quantitative Single-Molecule Surface-Enhanced Raman Scattering by Optothermal Tuning of DNA Origami-Assembled Plasmonic Nanoantennas. *ACS Nano* 10, 9809–9815 (2016).
242. Prinz, J., Heck, C., Ellerik, L., Merk, V. & Bald, I. DNA origami based Au–Ag-core–shell nanoparticle dimers with single-molecule SERS sensitivity. *Nanoscale* 8, 5612–5620 (2016).
243. Kühler, P. et al. Plasmonic DNA-Origami Nanoantennas for Surface-Enhanced Raman Spectroscopy. *Nano Lett* 14, 2914–2919 (2014).
244. Prinz, J. et al. DNA Origami Substrates for Highly Sensitive Surface-Enhanced Raman Scattering. *J Phys Chem Lett* 4, 4140–4145 (2013).
245. Lim, D.-K. et al. Highly uniform and reproducible surface-enhanced Raman scattering from DNA-tailorable nanoparticles with 1-nm interior gap. *Nat Nanotechnol* 6, 452–460 (2011).
246. Zhang, X., Servos, M. R. & Liu, J. Instantaneous and Quantitative Functionalization of Gold Nanoparticles with Thiolated DNA Using a pH-Assisted and Surfactant-Free Route. *J Am Chem Soc* 134, 7266–7269 (2012).
247. Vietz, C., Lalkens, B., Acuna, G. P. & Tinnefeld, P. Functionalizing large nanoparticles for small gaps in dimer nanoantennas. *New J Phys* 18, 045012 (2016).
248. Vietz, C., Kaminska, I., Sanz Paz, M., Tinnefeld, P. & Acuna, G. P. Broadband Fluorescence Enhancement with Self-Assembled Silver Nanoparticle Optical Antennas. *ACS Nano* 11, 4969–4975 (2017).
249. Zhang, T., Gao, N., Li, S., Lang, M. J. & Xu, Q.-H. Single-Particle Spectroscopic Study on Fluorescence Enhancement by Plasmon Coupled Gold Nanorod Dimers Assembled on DNA Origami. *J Phys Chem Lett* 6, 2043–2049 (2015).
250. Trofymchuk, K. et al. Gold Nanorod DNA Origami Antennas for 3 Orders of Magnitude Fluorescence Enhancement in NIR. *ACS Nano* 17, 1327–1334 (2023).
251. Schmied, J. J. et al. DNA Origami Nanopillars as Standards for Three-Dimensional Superresolution Microscopy. *Nano Lett* 13, 781–785 (2013).
252. Pfeiffer, M. et al. Single antibody detection in a DNA origami nanoantenna. *iScience* 24, 103072 (2021).
253. Close, C. et al. Maximizing the Accessibility in DNA Origami Nanoantenna Plasmonic Hotspots. *Adv Mater Interfaces* 9, 2200255 (2022).
254. Pellegrotti, J. V et al. Controlled Reduction of Photobleaching in DNA Origami–Gold Nanoparticle Hybrids. *Nano Lett* 14, 2831–2836 (2014).
255. Schedlbauer, J. et al. Ultrafast Single-Molecule Fluorescence Measured by Femtosecond Double-Pulse Excitation Photon Antibunching. *Nano Lett* 20, 1074–1079 (2020).



256. Grabenhorst, L., Trofymchuk, K., Steiner, F., Glembockyte, V. & Tinnefeld, P. Fluorophore photostability and saturation in the hotspot of DNA origami nanoantennas. *Methods Appl Fluoresc* 8, 024003 (2020).
257. Kaminska, I. et al. Strong plasmonic enhancement of single molecule photostability in silver dimer optical antennas. *Nanophotonics* 7, 643–649 (2018).
258. Wu, Y., Tilley, R. D. & Gooding, J. J. Challenges and Solutions in Developing Ultrasensitive Biosensors. *J Am Chem Soc* 141, 1162–1170 (2019).
259. Ochmann, S. E. et al. Optical Nanoantenna for Single Molecule-Based Detection of Zika Virus Nucleic Acids without Molecular Multiplication. *Anal Chem* 89, 13000–13007 (2017).
260. Holzmeister, P., Wünsch, B., Gietl, A. & Tinnefeld, P. Single-molecule photophysics of dark quenchers as non-fluorescent FRET acceptors. *Photochemical & Photobiological Sciences* 13, 853–858 (2014).
261. Wang, C. et al. Point-of-care diagnostics for infectious diseases: From methods to devices. *Nano Today* 37, 101092 (2021).
262. Afzal, A. Molecular diagnostic technologies for COVID-19: Limitations and challenges. *J Adv Res* 26, 149–159 (2020).
263. Moehling, T. J., Choi, G., Dugan, L. C., Salit, M. & Meagher, R. J. LAMP Diagnostics at the Point-of-Care: Emerging Trends and Perspectives for the Developer Community. *Expert Rev Mol Diagn* 21, 43–61 (2021).
264. Ghouneimy, A., Mahas, A., Marsic, T., Aman, R. & Mahfouz, M. CRISPR-Based Diagnostics: Challenges and Potential Solutions toward Point-of-Care Applications. *ACS Synth Biol* 12, 1–16 (2023).
265. Vietz, C. et al. Benchmarking Smartphone Fluorescence-Based Microscopy with DNA Origami Nanobeads: Reducing the Gap toward Single-Molecule Sensitivity. *ACS Omega* 4, 637–642 (2019).
266. Liu, X. et al. Complex silica composite nanomaterials templated with DNA origami. *Nature* 559, 593–598 (2018).
267. Ashoori, R. C. Electrons in artificial atoms. *Nature* 1996 379:6564 379, 413–419 (1996).
268. Silbey, R. J. ; A. R. A. ; B. M. G. *Physical Chemistry*. (John Wiley & Sons., 2005).
269. Kastner, M. A. Artificial Atoms. *Phys Today* 46, 24–31 (1993).
270. Bera, D., Qian, L., Tseng, T.-K. & Holloway, P. H. Quantum Dots and Their Multimodal Applications: A Review. *Materials* 3, 2260–2345 (2010).
271. Nirmal, M. et al. Fluorescence intermittency in single cadmium selenide nanocrystals. *Nature* 383, 802–804 (1996).
272. Peng, X., Schlamp, M. C., Kadavanich, A. V. & Alivisatos, A. P. Epitaxial Growth of Highly Luminescent CdSe/CdS Core/Shell Nanocrystals with Photostability and Electronic Accessibility. *J Am Chem Soc* 119, 7019–7029 (1997).

273. Chan, W. C. W. & Nie, S. Quantum Dot Bioconjugates for Ultrasensitive Nonisotopic Detection. *Science* (1979) 281, 2016–2018 (1998).
274. Peng, Y. & Croce, C. M. The role of MicroRNAs in human cancer. *Signal Transduct Target Ther* 1, 15004 (2016).
275. Elayadi, A. N., Braasch, D. A. & Corey, D. R. Implications of High-Affinity Hybridization by Locked Nucleic Acid Oligomers for Inhibition of Human Telomerase. *Biochemistry* 41, 9973–9981 (2002).
276. Pradeep, S. P., Malik, S., Slack, F. J. & Bahal, R. Unlocking the potential of chemically modified peptide nucleic acids for RNA-based therapeutics. *RNA* 29, 434–445 (2023).

# 7

## APPENDIX

### 7.1. SUPPORTING INFORMATION FOR P1

Supporting Information

for

Bringing Attomolar Detection to the Point-of-care with  
Nanopatterned DNA Origami Nanoantennas

by

Renukka Yaadav<sup>1</sup>, Kateryna Trofymchuk<sup>1</sup>, Mihir Dass<sup>2</sup>, Vivien Behrendt<sup>3</sup>, Benedikt  
Hauer<sup>3</sup>, Jan Schütz<sup>3</sup>, Cindy Close<sup>1</sup>, Michael Scheckenbach<sup>1</sup>, Giovanni Ferrari<sup>1</sup>, Leoni  
Maeurer<sup>1</sup>, Sophia Sebina<sup>1</sup>, Viktorija Glembockyte<sup>1</sup>, Tim Liedl<sup>2</sup>, Philip Tinnefeld<sup>1,\*</sup>

uploaded to

*bioRxiv 2024.10.14.618183. 10.1101/2024.10.14.618183*

**Figure S1. Trident DNA Origami design**

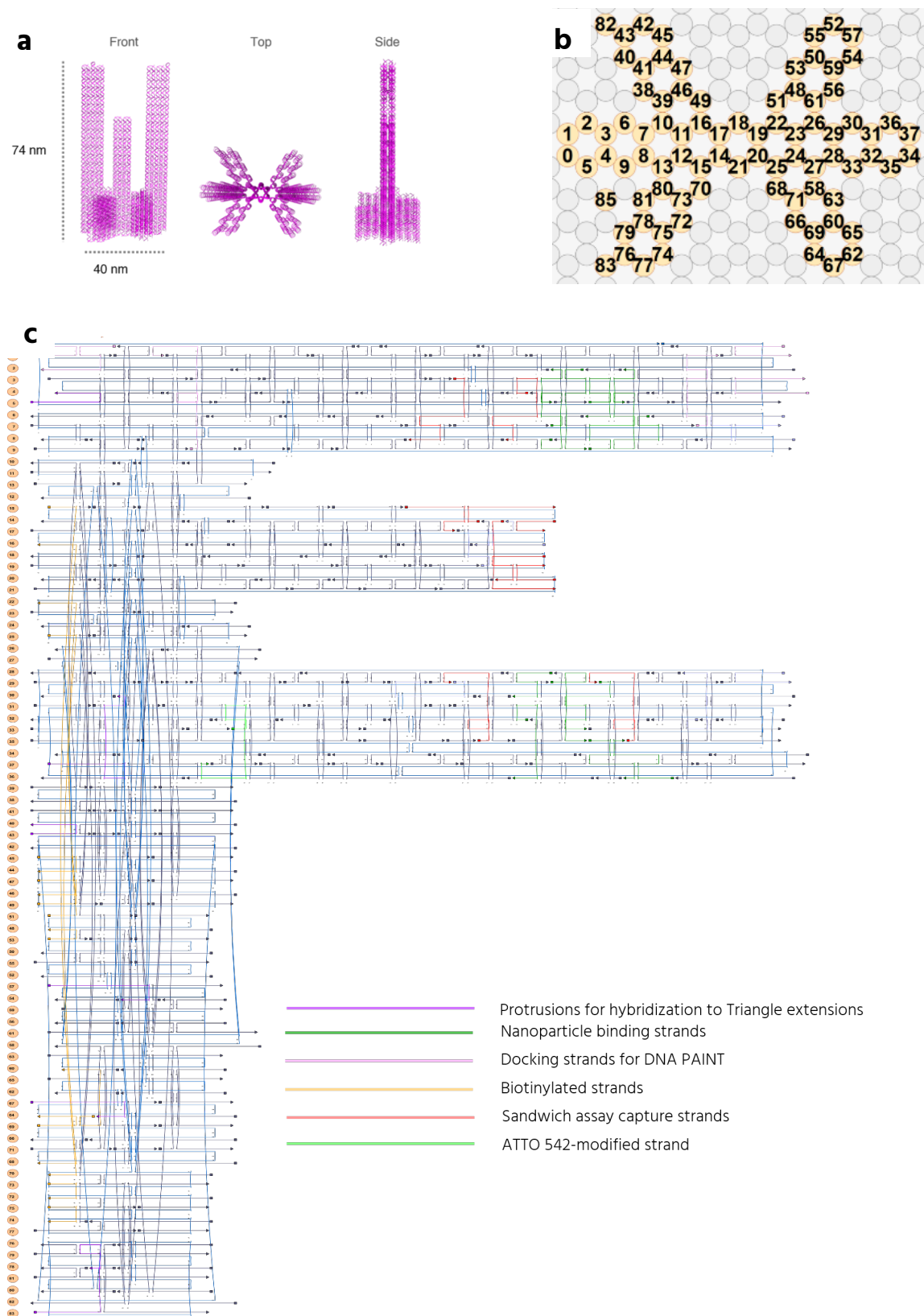


**Figure S1. a** 3D model of the Trident DNA origami. **b** Helical design snapshot from cadnano2<sup>1</sup>. **c** Scaffold routing and staple layout for Trident DNA origami. Scaffold in blue, biotin modified staples in orange,

capture strands in red, nanoparticle binding strands in green, ATTO 542 labelled strand in neon green, PAINT staples in light pink, protrusions for hybridization to triangle in purple.

**Figure S2. Blocker strand.**

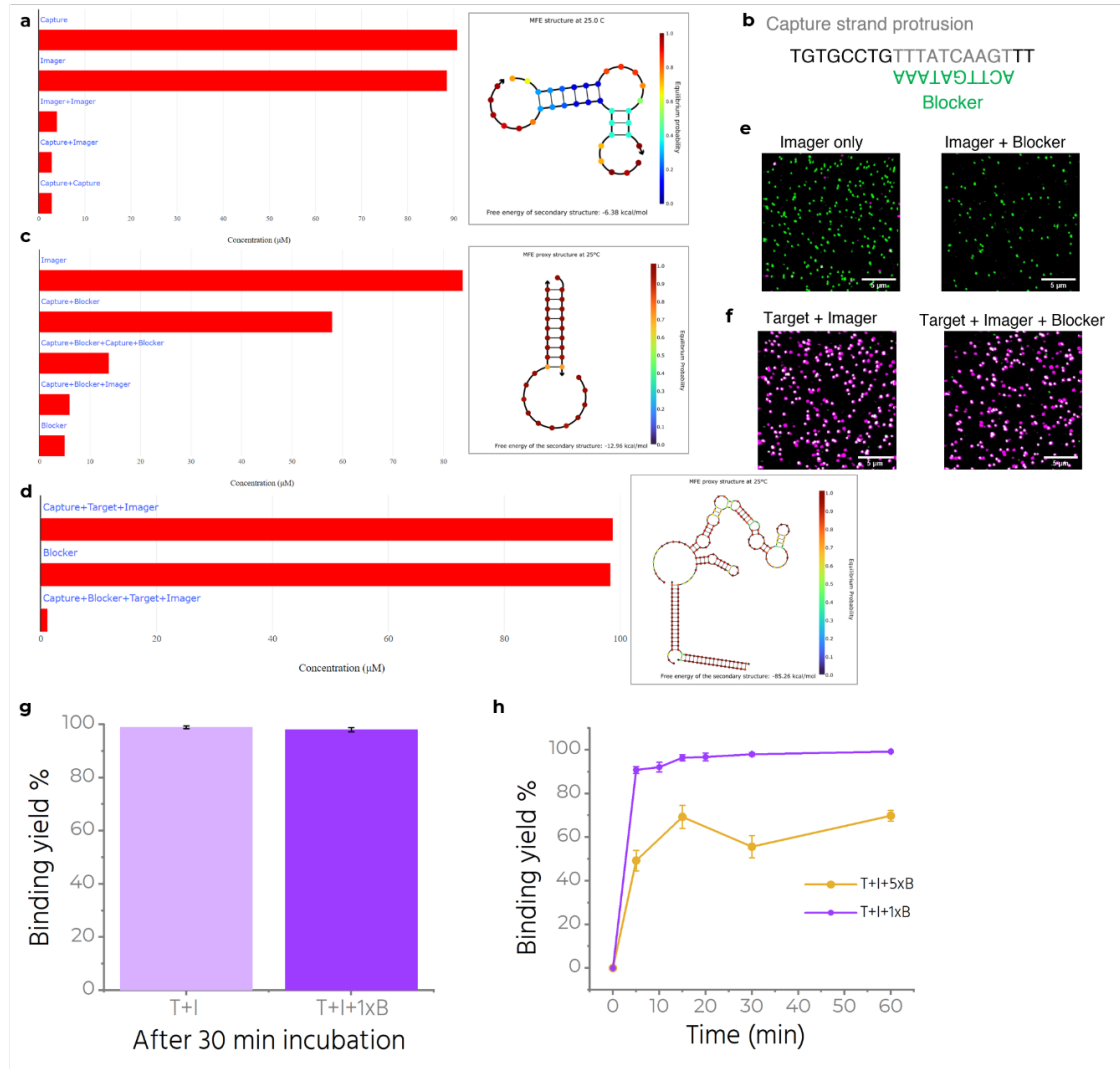


**Figure S2.** NUPACK analysis: **a** Interaction probability histogram and equilibrium probability chart for complexes formed in a solution with capture and imager strand. **b** Designed sequence for blocker strand to restrict interaction between capture and imager strand. **c** Interaction probability histogram for complexes formed in a solution with capture, imager and blocker strand. The equilibrium probability chart shows stable interaction between capture and blocker. **d** Interaction probability histogram for complexes formed in a solution with capture (C), imager (I), blocker (B) and target (T) strand, with equilibrium probability chart showing a stable interaction between capture, target and imager. **e** Confocal fluorescence scans for NanoAntennas incubated with imager only and with imager+blocker. **f** Confocal fluorescence scans for NanoAntennas incubated with target+imager and with target+imager+blocker. **g** Comparing binding yield of two samples after 30 minutes of incubation with

4nM T + 12 nM Imager and 4nM T + 12 nM Imager + 12 nM Blocker. **h** Effect of Blocker concentration on binding kinetics of the assay. We use 1x Blocker (12 nM) throughout the manuscript.

**Figure S3. Trident NanoAntenna characterization.**

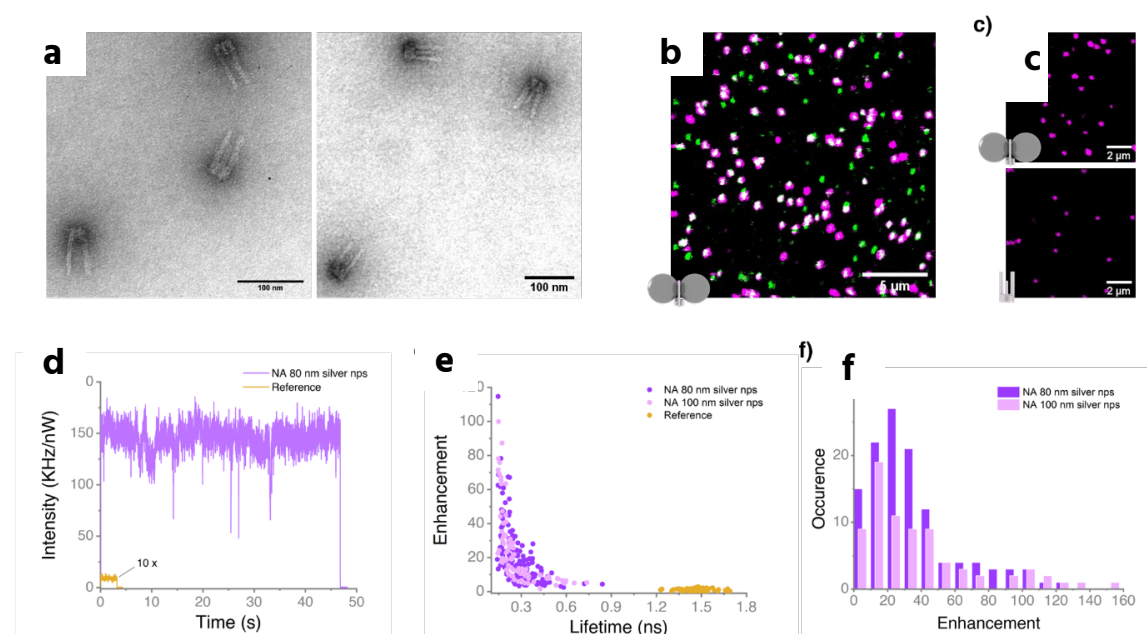


**Figure S3.** **a** TEM images showing successfully folded Trident. **b** Exemplary confocal fluorescence scan for antennas with ATTO 542 (green spots) and co-localized spots in white showing the presence of both ATTO542 and Alexa Fluor 647 dye on the same origami. **c** 10x10  $\mu\text{m}$  exemplary confocal fluorescence scan for Trident with nanoparticles on the top and Trident without nanoparticles on the bottom, measured at 50 nW and 500 nW red laser power respectively. **d** Exemplary transient comparing intensity from a single Alexa F 647 bound to the Trident in presence (NanoAntenna (NA)) and absence of nanoparticles (reference). The reference intensity has been multiplied ten times for better visibility. **e** Enhancement and lifetime correlation for NA with 80 nm silver nanoparticles, with 100 nm silver nanoparticles and without nanoparticles. **f** Enhancement distribution in case of NA with 80 nm silver nanoparticles and 100 nm silver NPs.

**Figure S4. Increased capture strands.**

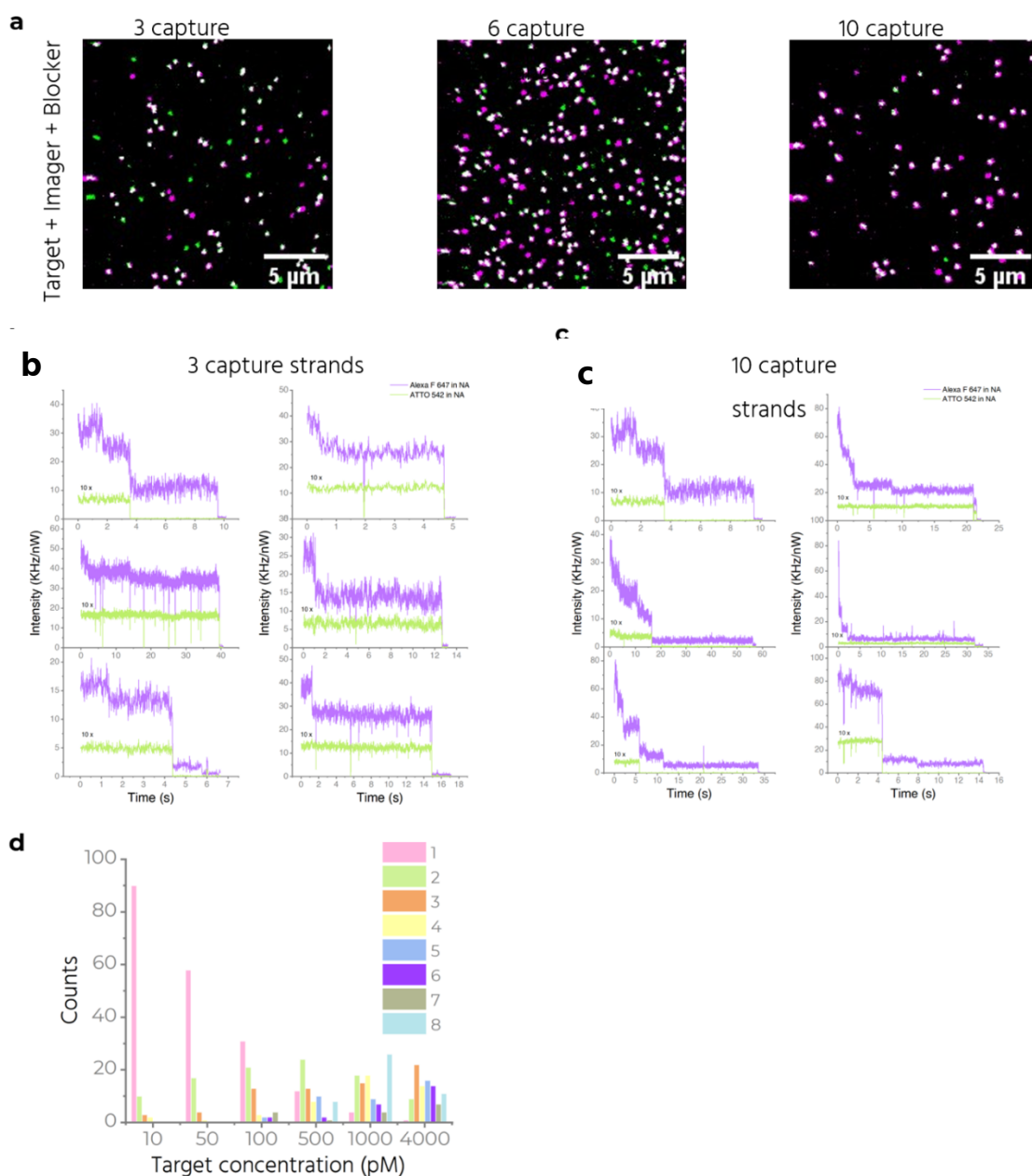


**Figure S4. a** Confocal fluorescence scans recorded after the assay comparing NanoAntennas with 3, 6 and 10 capture strands. **b** Exemplary transients for NA with 3 capture strands. A single step for ATTO 542 (green) represents a single Trident and 1-3 bleaching steps for Alexa Fluor 647 (in purple) represents the number of target strands captured. ATTO 542 is excited at 500 nW and the intensity is multiplied 10 times for better visibility. Alexa F 647 is excited with 50 nW. **c** Exemplary transients for NA with 10 capture strands. **d** Bleaching step analysis for NA with 10 capture strands at different concentrations showing up to 8 bleaching steps recorded at higher concentrations. ATTO 542 is excited at 500 nW and the intensity is multiplied 10 times for better visibility. Alexa F 647 is excited with 50 nW.

**Figure S5. Effect of increased number of capture strands on the fluorescence enhancement.**

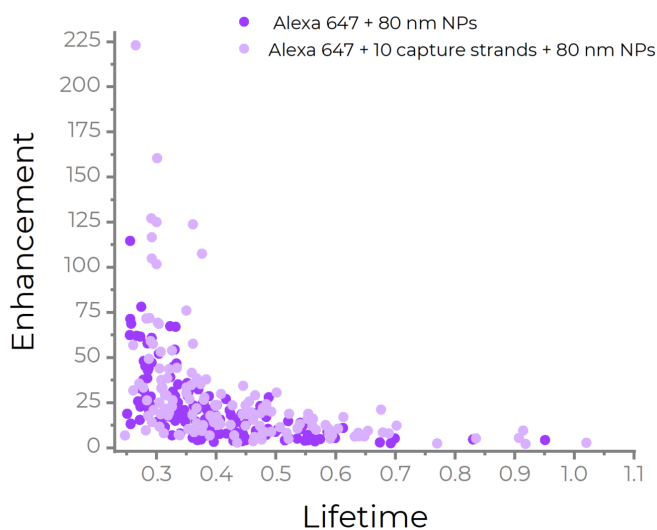


**Figure S5.** Two different Trident are folded, one with a fixed dye in the hotspot and no capture strands, and the other with a fixed dye in the hotspot and additionally 10 capture strands in the hotspot. For each type, NanoAntennas are assembled and confocal fluorescence scans are recorded to analyze and compare the effect of incorporating many capture strands on the binding of nanoparticles. Enhancement vs lifetime is plotted for each case, suggesting a similar trend for both samples.

**Figure S6. Example scans**

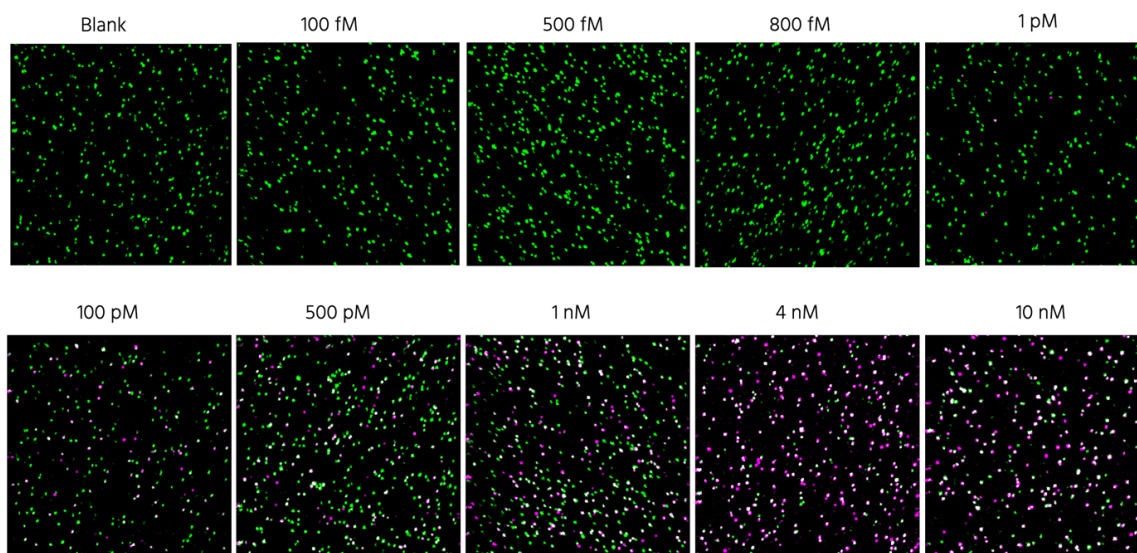


**Figure S6.** Exemplary confocal scans after the assay at different concentrations starting from absence of target (Top, left), to increase in target concentration from 100 fM up to 10 nM. Read from left to right, top to bottom. All samples had imager and blocker at 12 nM during the incubation of 1 hour at 37°C. Green spots represent the base dye on the Trident nanonantenna, and magenta represents the imager labelled with Alexa F 647.



**Figure S7. Triangle DNA origami design**

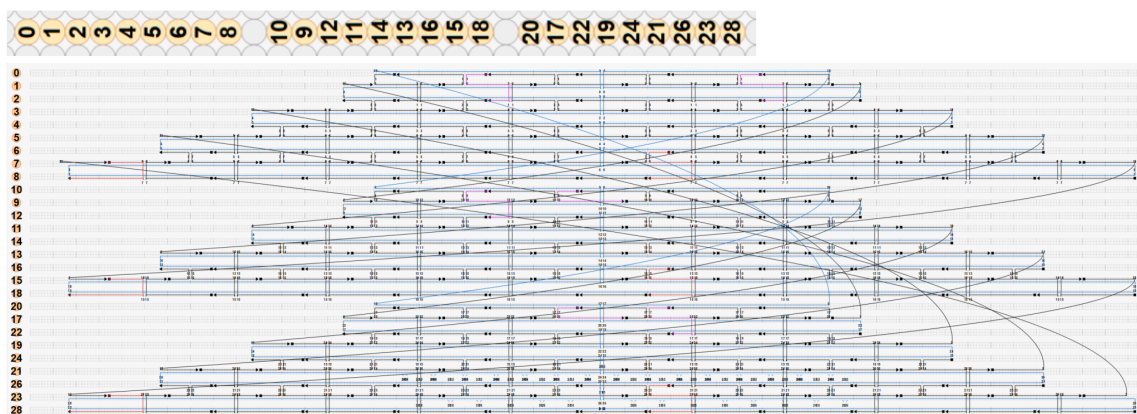


**Figure S7.** Helical design snapshot of the Triangle DNA origami in cadnano2 (above) and scaffold routing (below), showing DNA-PAINT docking sites in red and staples for capturing Trident in pink.

**Figure S8. DNA-PAINT images of Trident directly bound to the binding site**

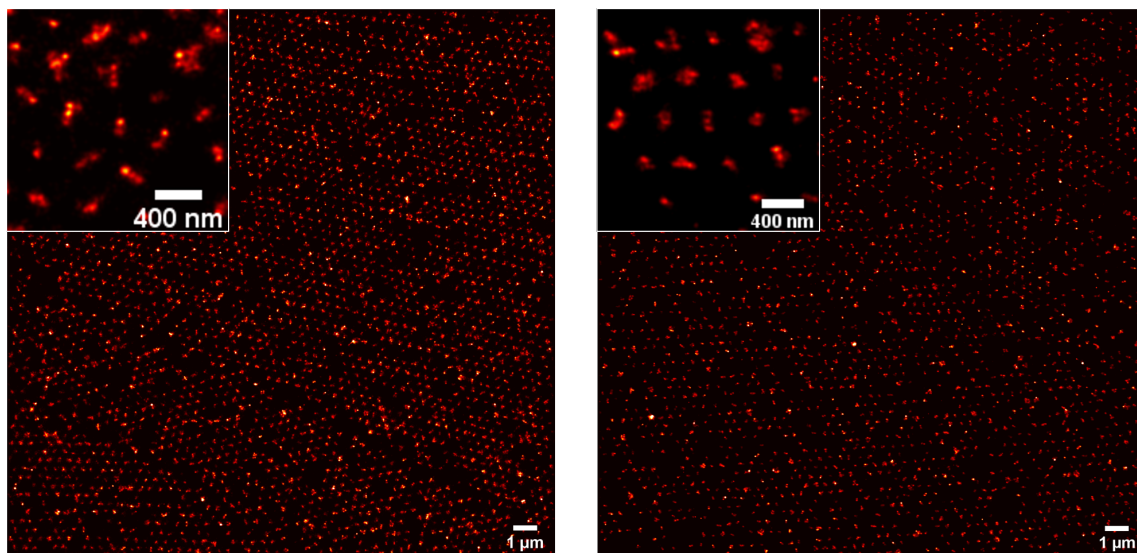
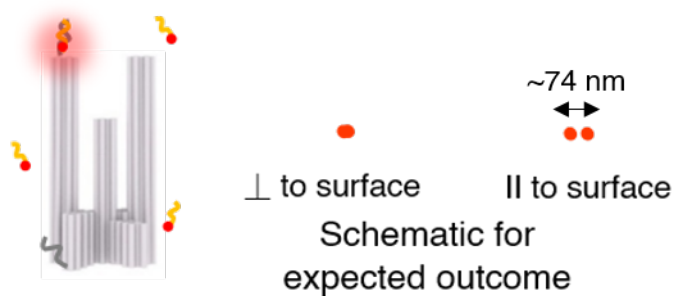


**Figure S8.** Trident is modified to include 3 protruding docking strands from the top of the left pillar-complex and 3 from the bottom. 3 strands per docking site allows to increase the chances of at least one of the strands being incorporated in most structures. (See sketch above. Only one strand at top and one at bottom in grey are shown for simplicity). A 6-nt or an 8-nt imager strand (orange) labelled with

ATTO 655 (red sphere), having a sequence complementary to the docking strands transiently hybridizes to the docking sites. Parameters such as number of frames, exposure time of each frame, laser intensity, imager concentration, are optimized to achieve one hybridization event on each immobilized Trident at a time. Over 10,000 frames, the localization data is collected and analyzed using Picasso Localize and Picasso Render to achieve a super-resolved image as shown here. This design of docking sites allows us to differentiate between an upright orientation of the Trident and other random orientations. In these examples, the Trident is added directly on the coverslip with patterned hydrophilic binding sites. This causes Trident to get placed in random numbers and orientations as the binding sites have a much bigger surface area to cover. The Trident interacts with the binding sites only (no binding on the hydrophobic background) but we don't see defined orientations in this case.

**Figure S9. AFM image of Triangles placed on the binding sites**

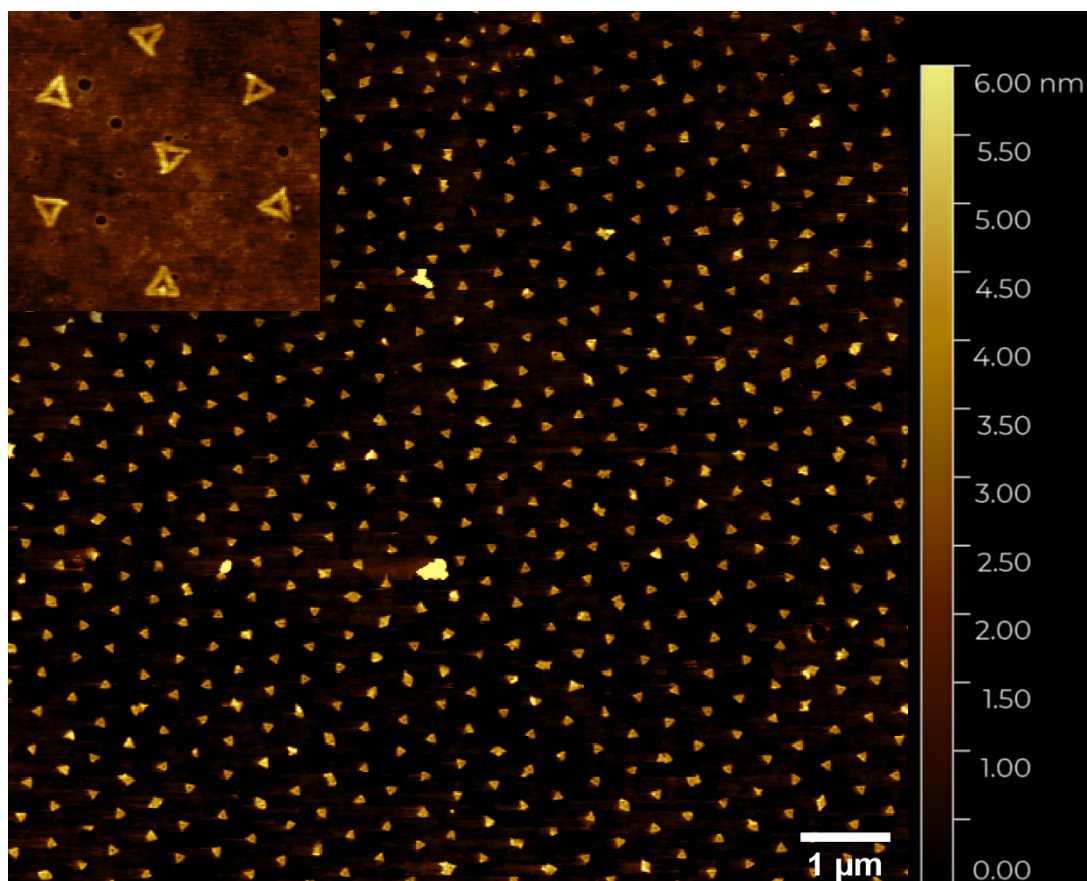
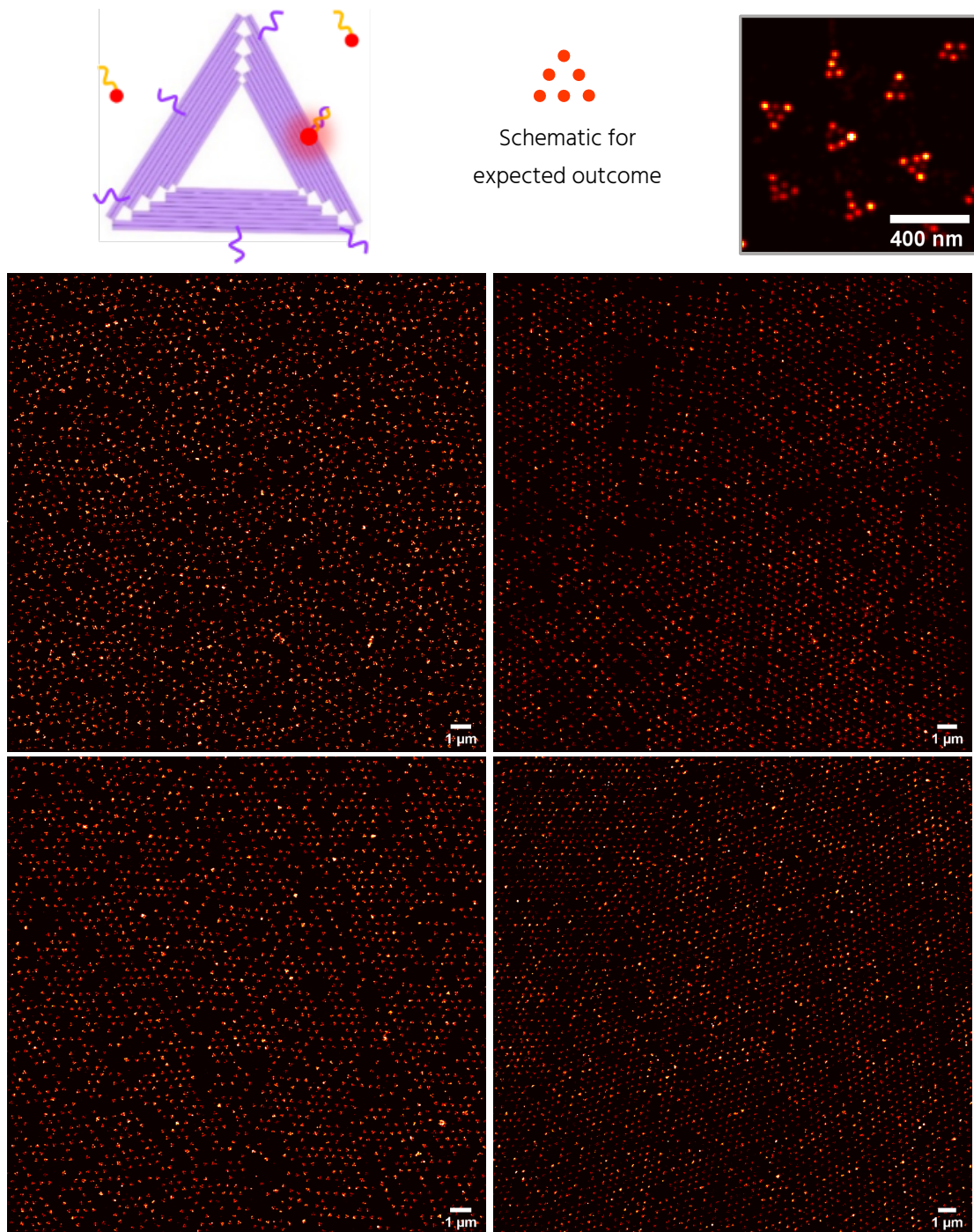
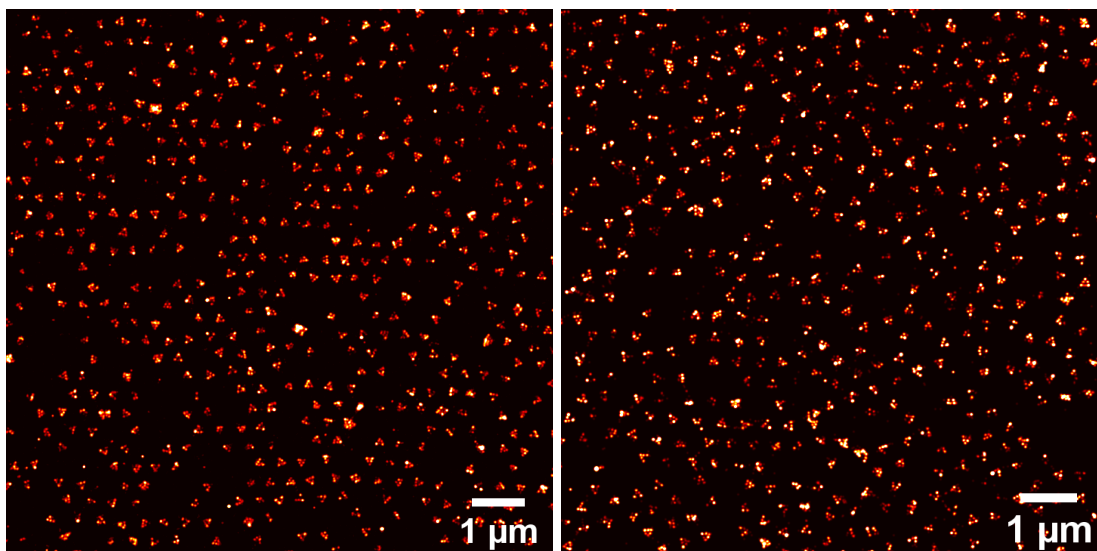


Figure S9. An exemplary AFM image after Triangle placement on the binding sites.

**Figure S10. DNA-PAINT images of Triangle placed on the binding sites**







**Figure S10.** Sketch showing the design of 6 docking strands (purple) in a Triangle shape. 8-nt imager shown in orange was used labelled with ATTO 655 (red sphere) for the measurements. The expected outcome is shown on the top-middle and a zoom-in of a super-resolved image with the Triangle-shaped pattern shown on the top-right. Other example images of Triangles placed on the binding sites specifically.

**Figure S11. SEM images of polystyrene spheres assembled on a glass substrate**

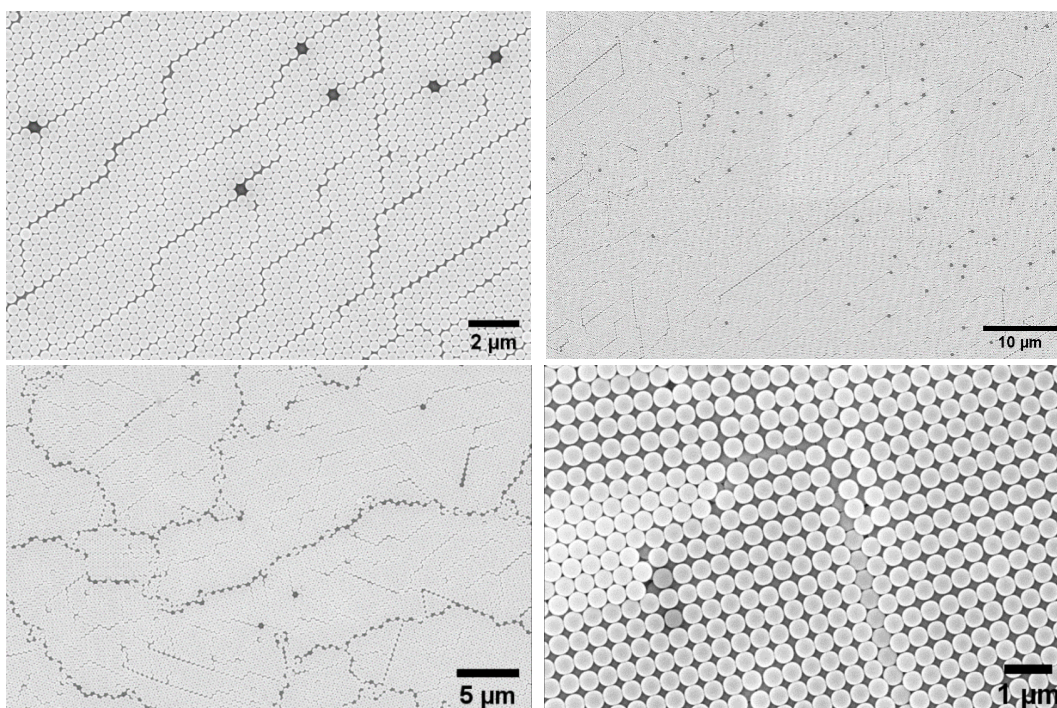


**Figure S11.** SEM images of polystyrene spheres assembled on a glass substrate showing mono- and multi-layer hexagonal assembly. The images reveal point and line defects in the assembly. In a smaller percentage, we also observe areas with a square lattice (last image).

**Figure S12. DNA-PAINT images for Trident placed on a nanopatterned surface and for Trident immobilized on a BSA-biotin-NeutrAvidin surface**

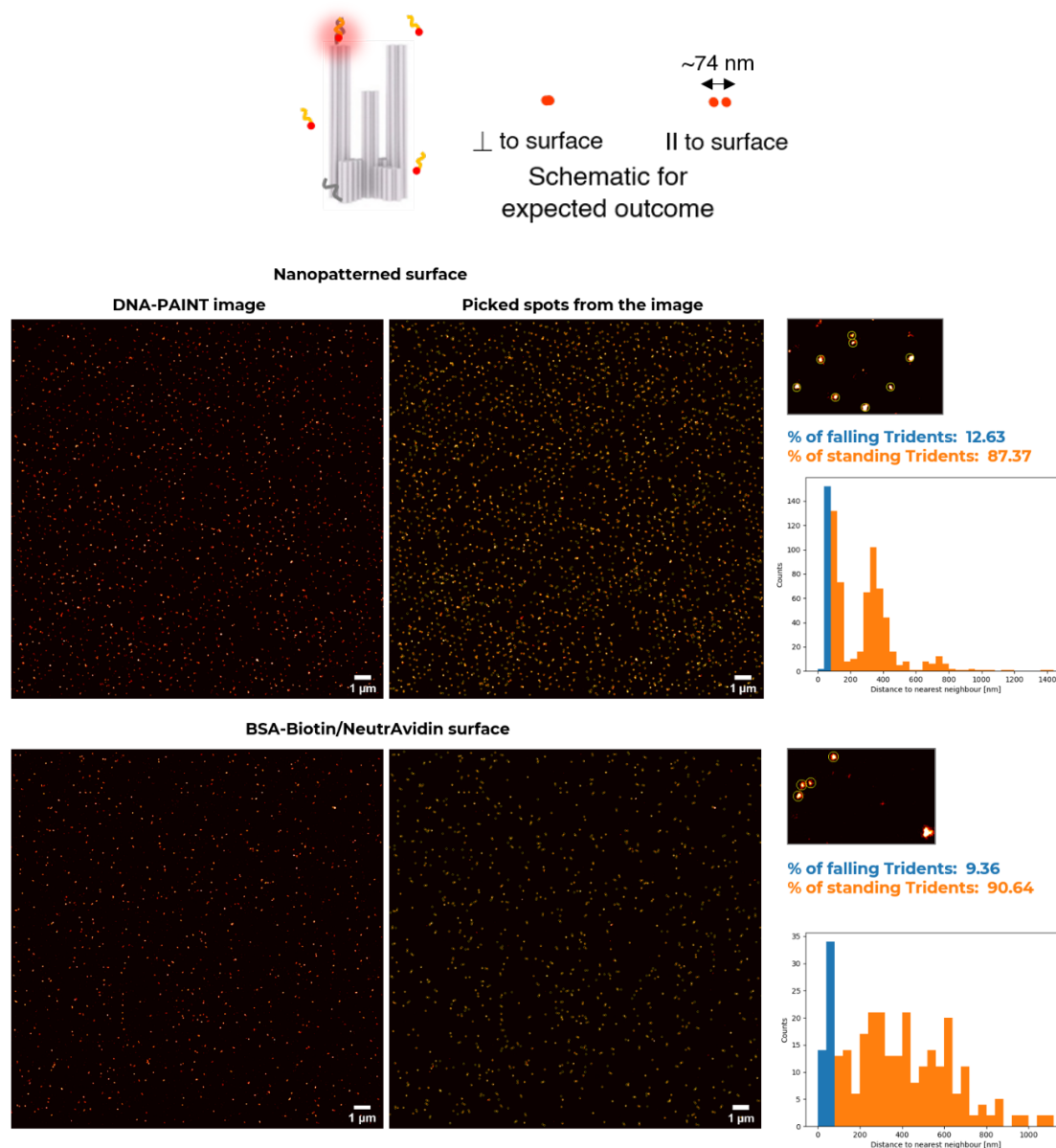
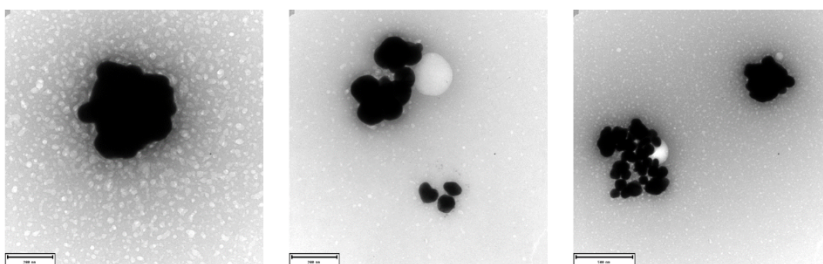


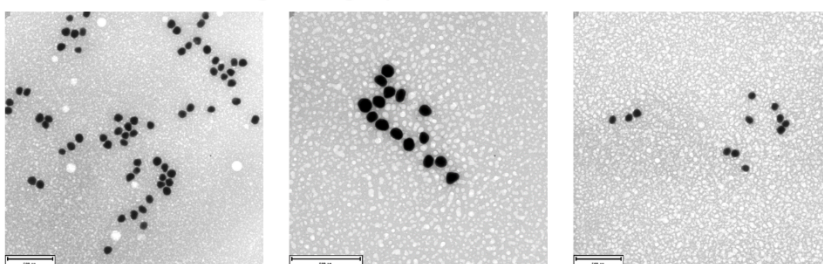
**Figure S12.** DNA-PAINT images are acquired and the % of upright orientation of the Trident is compared for NanoAntennas on a patterned surface vs NanoAntennas immobilized via biotinylated DNA. For the patterned surface, the Trident is bound to the Triangle via DNA hybridization. Individual spots are selected in Picasso Render and the localization information is used to plot the distance between each of those spots. An in-house python script allows segregating the data into ‘% of falling Tridents’ and ‘% of standing Tridents’. According to the design of the docking sites, one spot is expected when the Trident is standing upright and two spots of varying (tilting and falling) distance of ~74 nm is expected when the orientation is not upright. To make it simpler, we assign any distance between two spots below 85 nm as falling (in blue) and any distance above that qualifies as standing (in orange) and plotted a histogram for the distance to nearest neighbor in each case.

### Figure S13. TEM images comparing the two methods for NP functionalization

Salt-aging + centrifugation

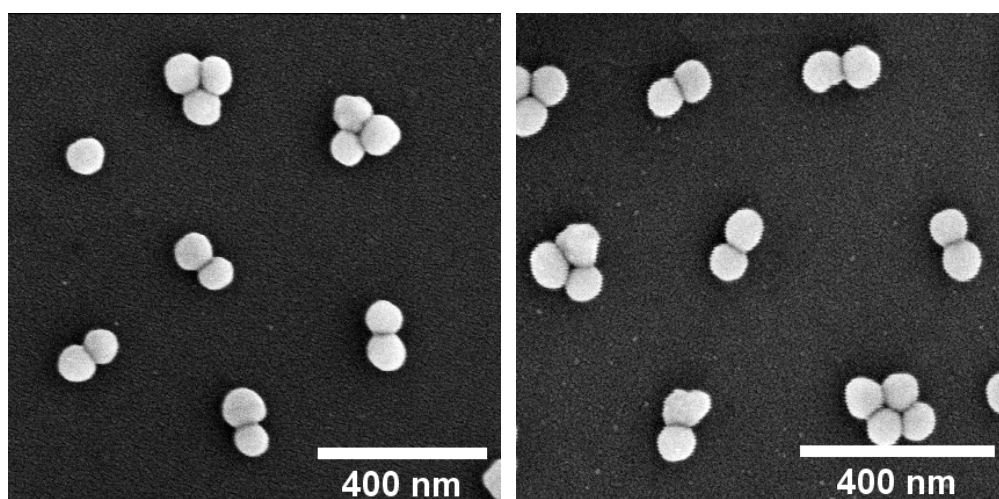


Freeze and thaw + Agarose gel purification

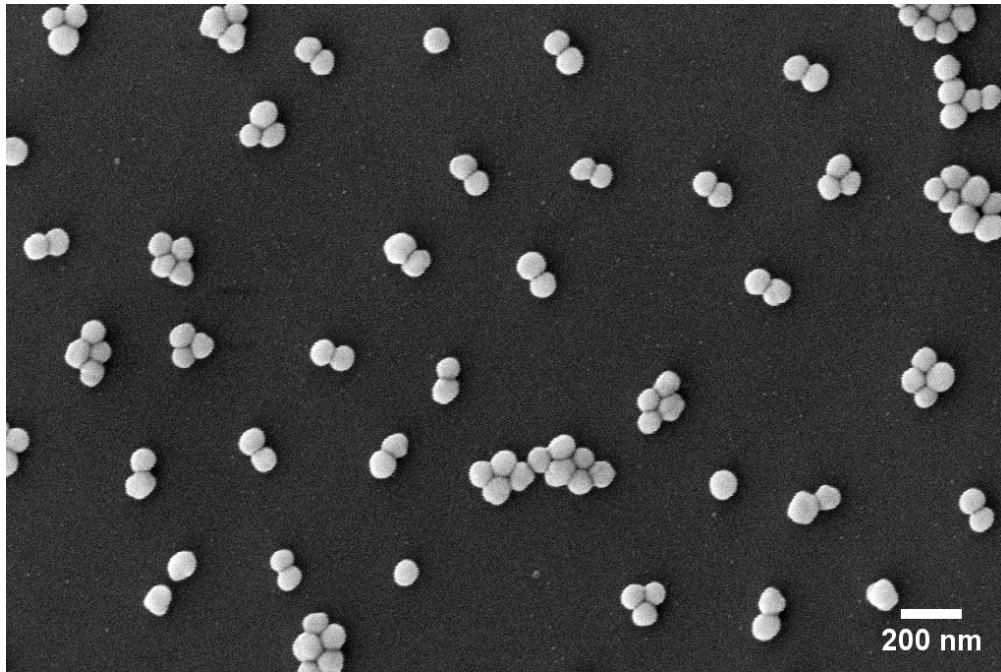
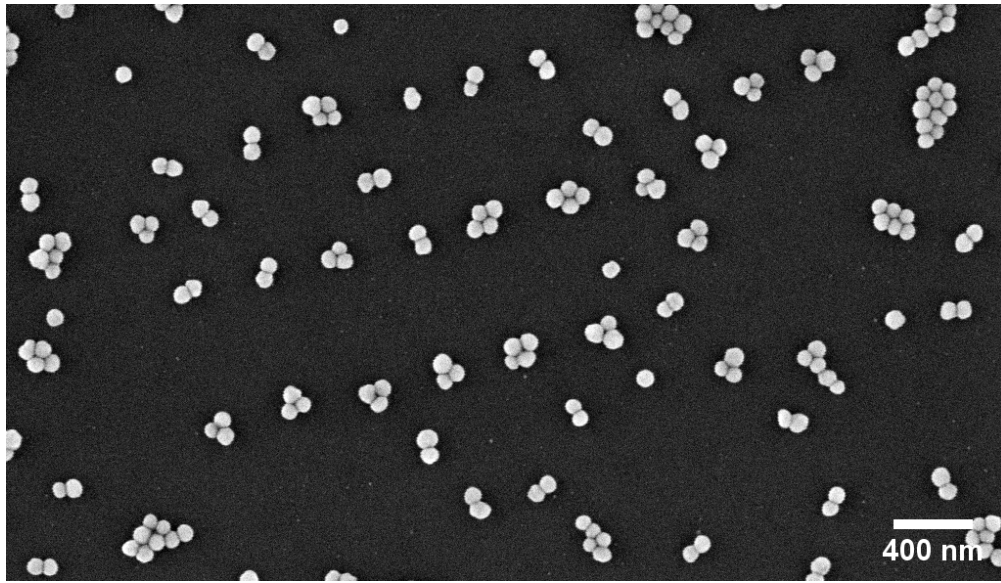


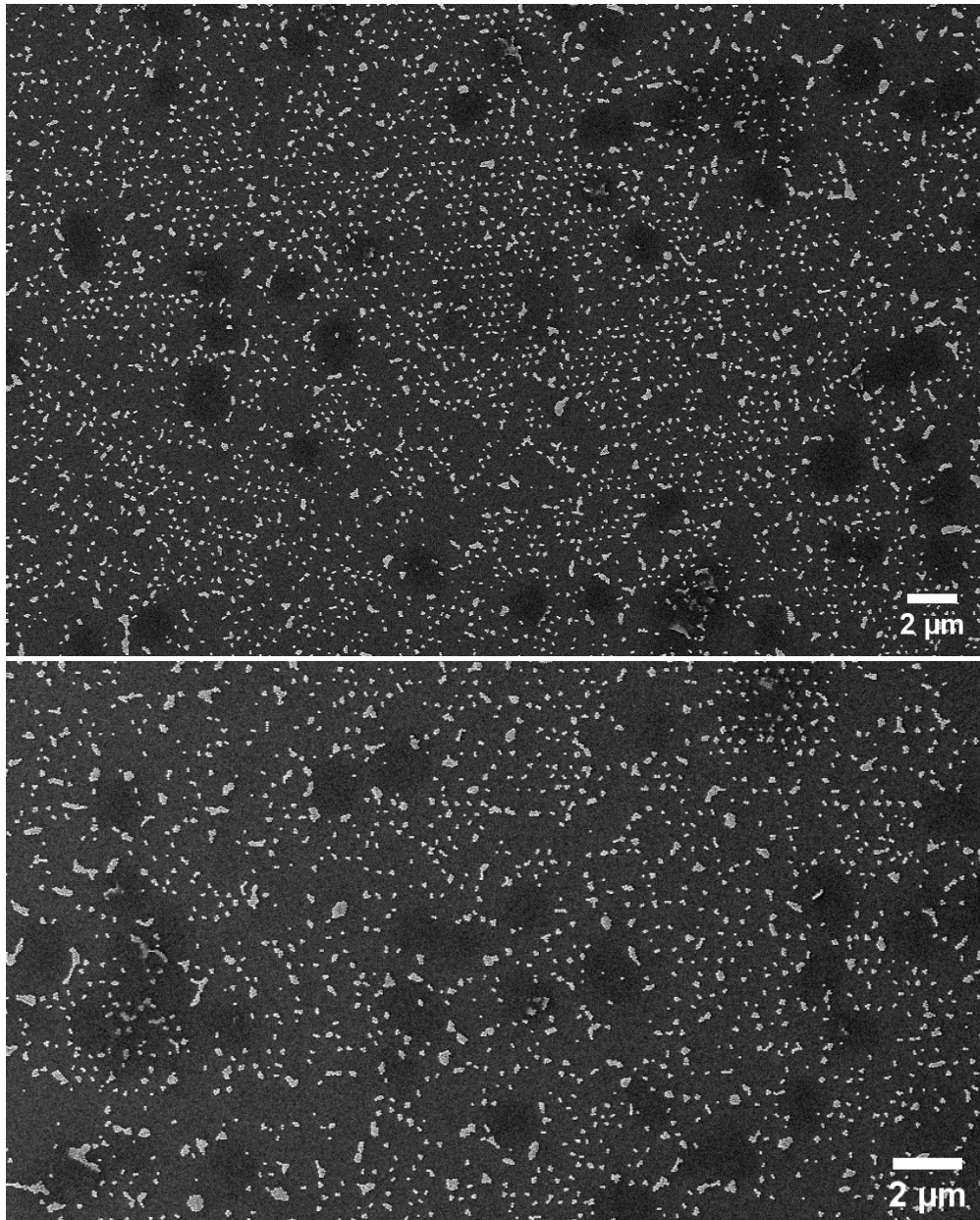
**Figure S13.** TEM images comparing two methods of nanoparticle functionalization and purification. We observe more aggregated chunks when we use the combination of salt-aging followed by centrifugation, to functionalize and purify. NPs look less aggregated after freeze and thaw and purification with agarose gel electrophoresis. We use freeze and thaw followed by gel purification for this article.

### Figure S14. Example SEM images of Nanopatterned NanoAntennas





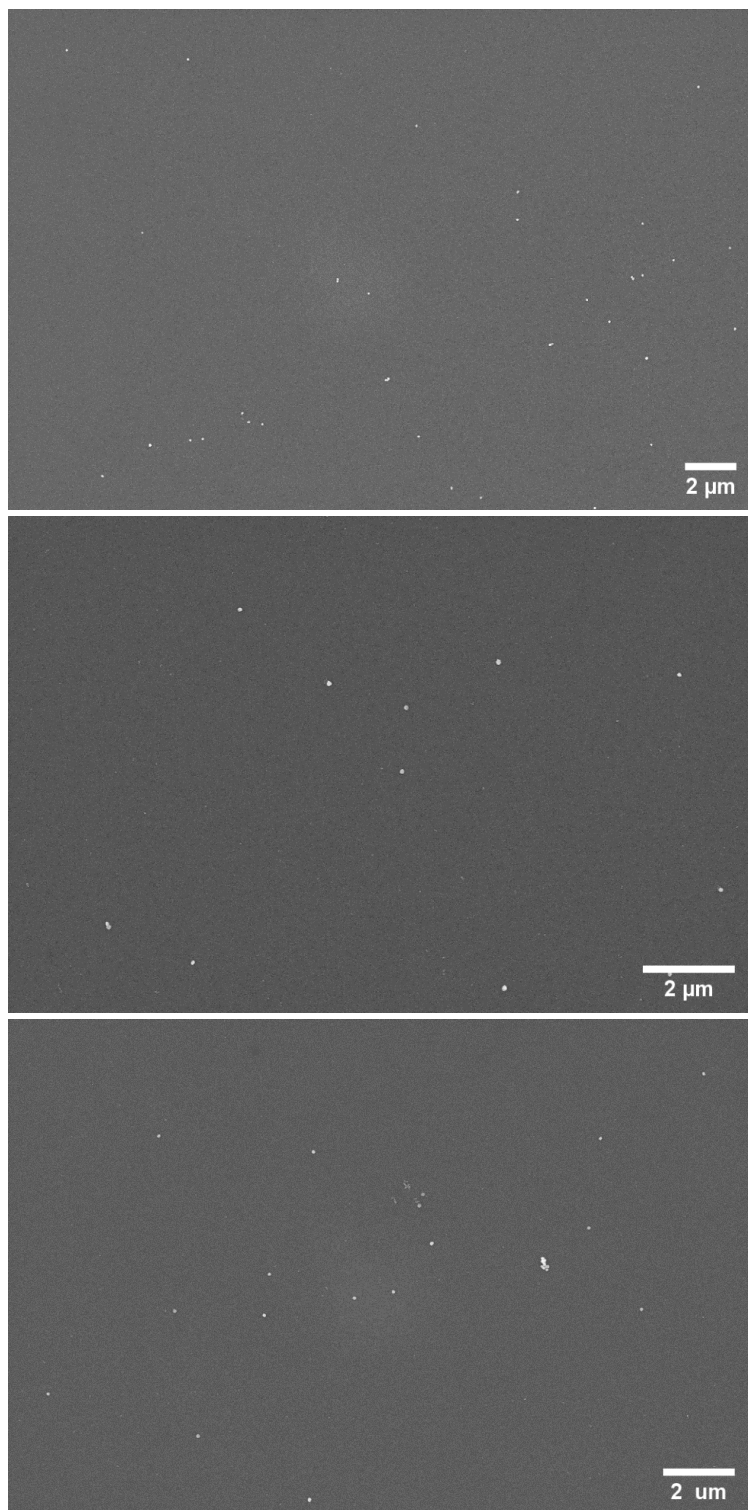




**Figure S14.** Example SEM images from three different coverslips with patterned NanoAntennas.

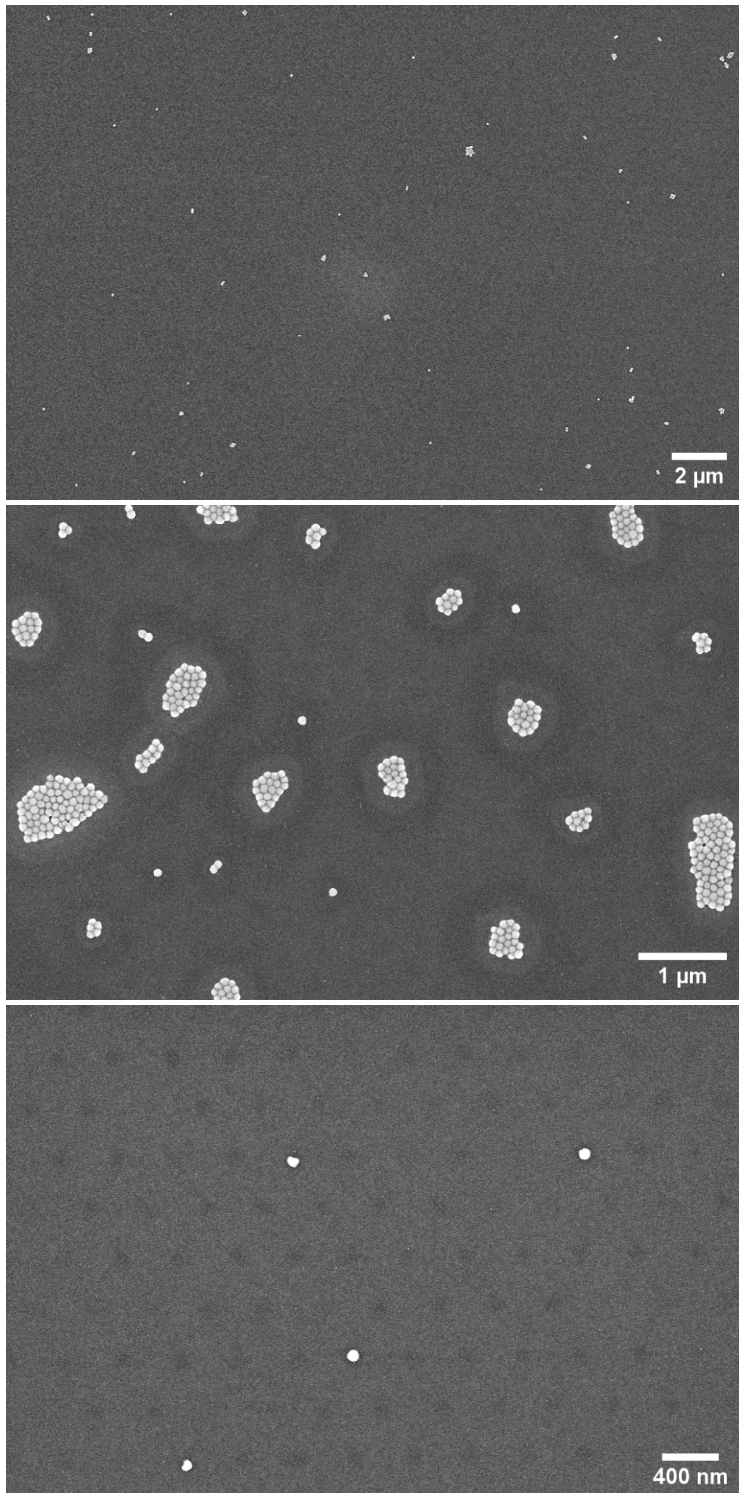


**Figure S15. SEM images after NP incubation with only Triangle placed on the binding site**



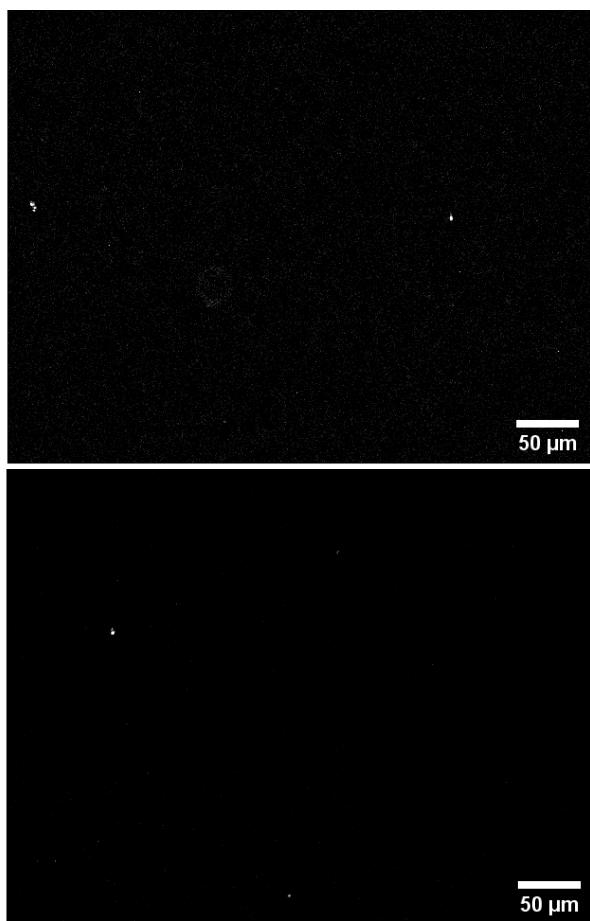
**Figure S15.** As a control, NPs are added to a patterned surface with Triangle placed on the binding sites and incubated overnight, washed and imaged with SEM. We observe no or minimal binding of NPs.

**Figure S16. SEM images after NP incubation with Trident placed directly on the binding site.**



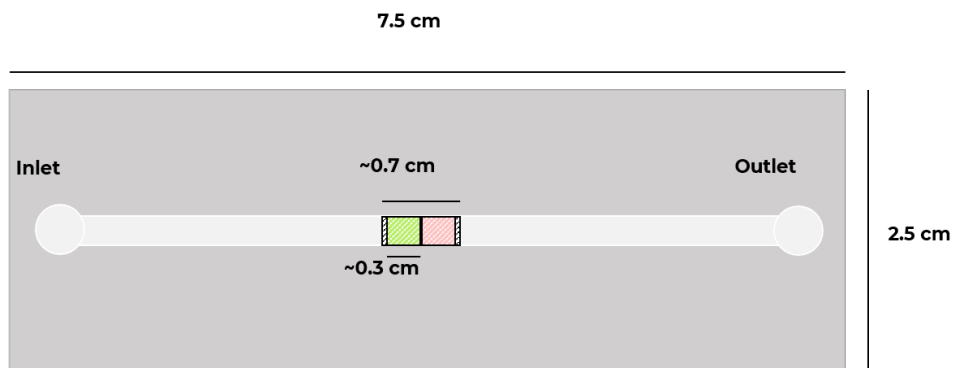
**Figure S16.** As a control, Trident is added directly to the binding sites, which does not allow the Trident to bind in the upright position as seen in DNA-PAINT experiments above, followed by NP incubation. We record SEM images showing minimal binding or formation of large aggregates in certain areas.



**Figure S17. Snapshot after 100 pM assay with Trident without nanoparticles**



**Figure S17.** Zoom-in image from the reader, of scattering (left) and fluorescence (right) channels after running an assay with 100 pM T + 12 nM I + 12 nM B, with Trident immobilized on a BSA-biotin-neutravidin surface, in the absence of nanoparticles. In this case, a total of 9 spots were detected in the entire FOV by the analysis software, with no clear bleaching steps.

**Figure S18. Selective immobilization of antennas to cover two areas for measurements on the reader**



-  Microfluidic chip
-  Patterned Nanoantennas
-  Area 1
-  Area 2

**Figure S18.** A schematic of the microfluidic chip showing the total area patterned (~0.7 cm x 0.3 cm) and the two areas imaged. The FOV of the reader is 2.5 mm x 3mm. The black and white sketched area is marked before patterning to place the NanoAntennas only within this region. Depending on the chip's orientation on the reader, two distinct regions can be imaged, highlighted in green and pink in the schematic. This orientation affects which area is centered within the reader's FOV, as the center alignment is slightly offset.

**Figure S19. Comparing assays on two chips patterned with NanoAntennas—one performed with repetitive flow and the other without.**

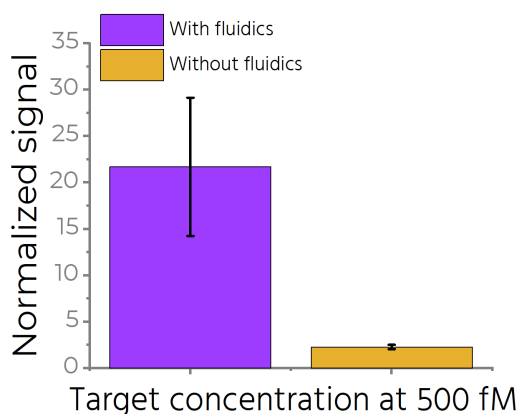
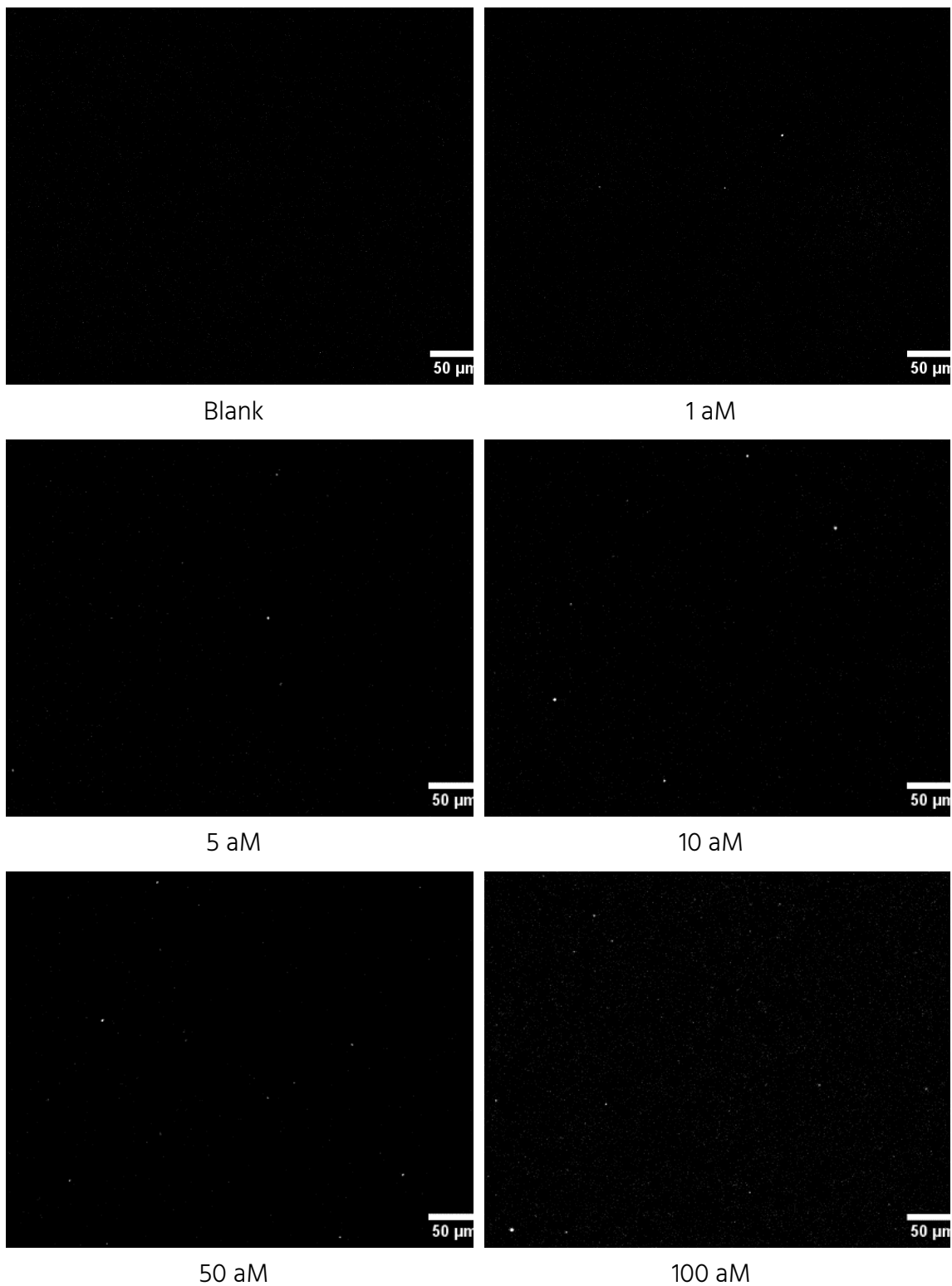


**Figure S19.** Applying flow allows us to achieve a ~10-fold increase in target capture. We demonstrate this by comparing assays on two chips patterned with NanoAntennas—one performed with flows and the other without, both with an incubation time of one hour and a target concentration of 500 fM.

**Figure S20. Exemplary zoomed in snapshots from different concentrations measured on the reader in buffer.**





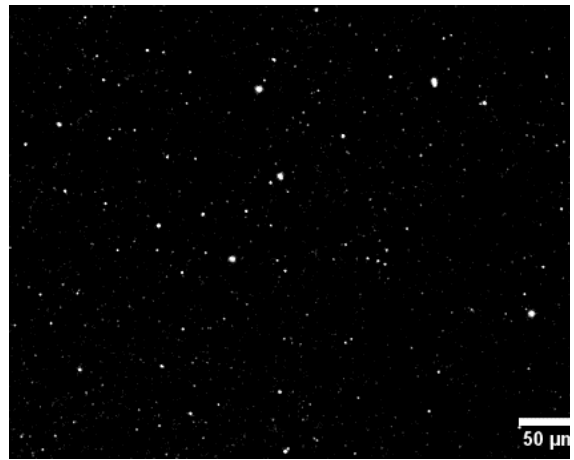
500 aM



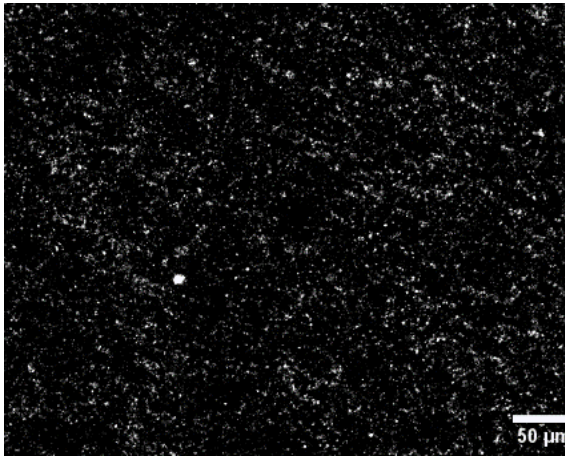
100 fM



500 fM



1 pM

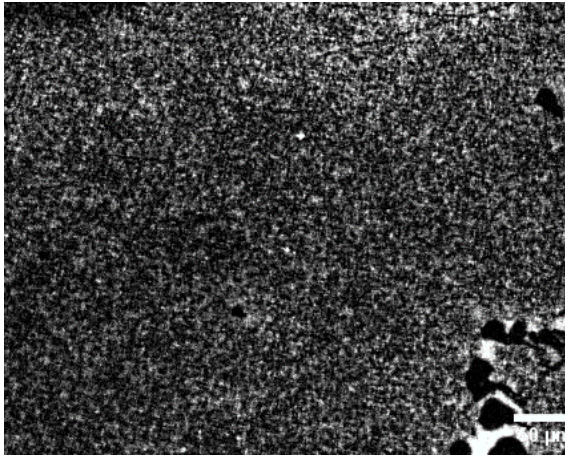


100pM



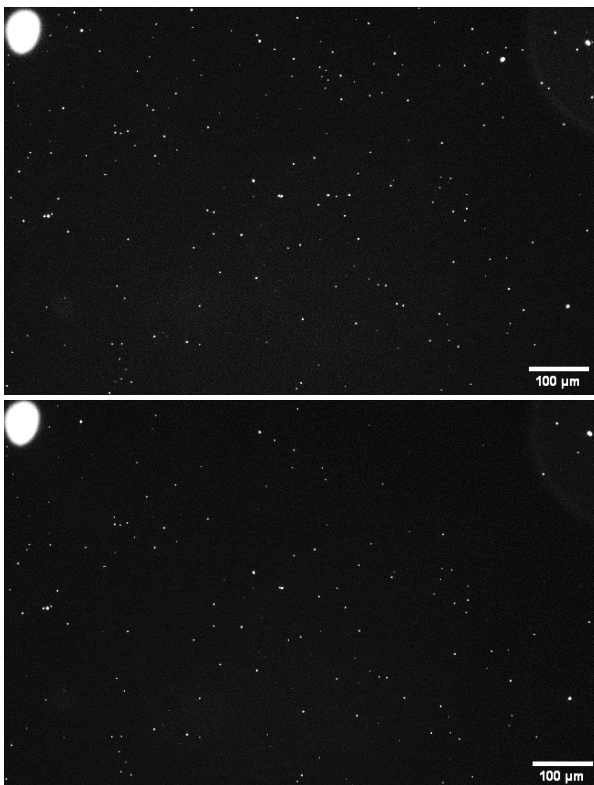
500pM





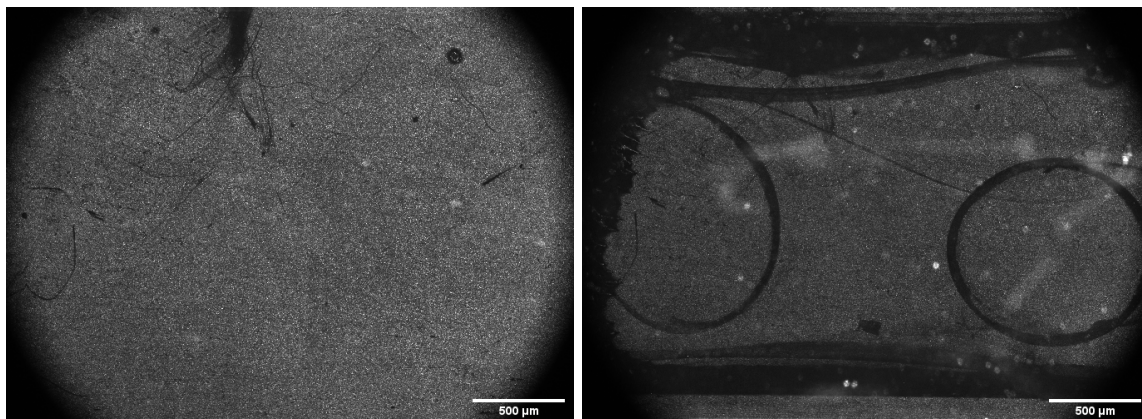
5 nM

**Figure S21. Washing with Sodium buffer helps remove weakly bound or unspecifically bound molecules.**



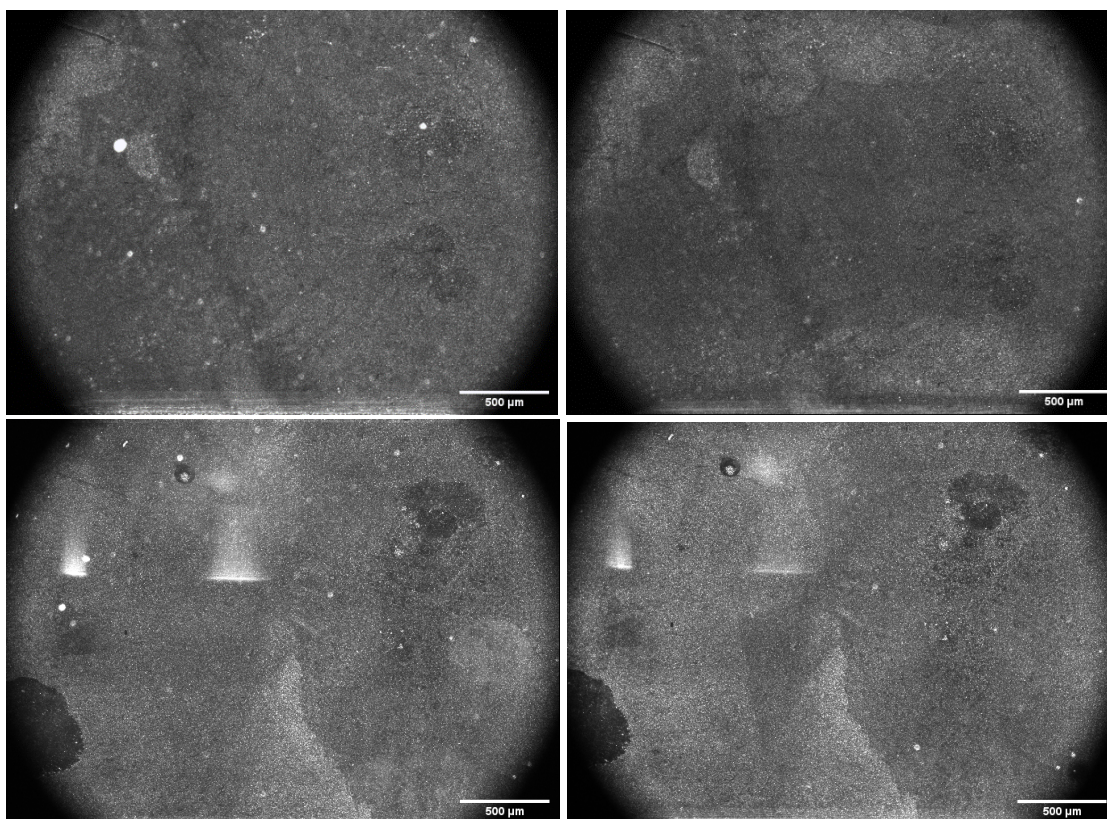
**Figure S21.** Snapshot of the fluorescence channel of a chip with silicified NanoAntennas after assay. Image on the left is after washing with  $\text{Mg}^{2+}$  buffer and the image on the right is after washing the same sample with  $\text{Na}^{+}$  buffer. The reflection of a bubble on the top left is used as a marker to compare the same areas.

**Figure S22. Effect of using Sodium-based buffer on patterning of unsilicified NanoAntennas**



**Figure S22.** Snapshot of the scattering channel of the same area of a chip with un-silicified NanoAntennas before (left) and after (right) washing the chip with TE + 2M NaCl buffer. Washing the channel with sodium-based buffers causes lift-off of patterned NanoAntennas.

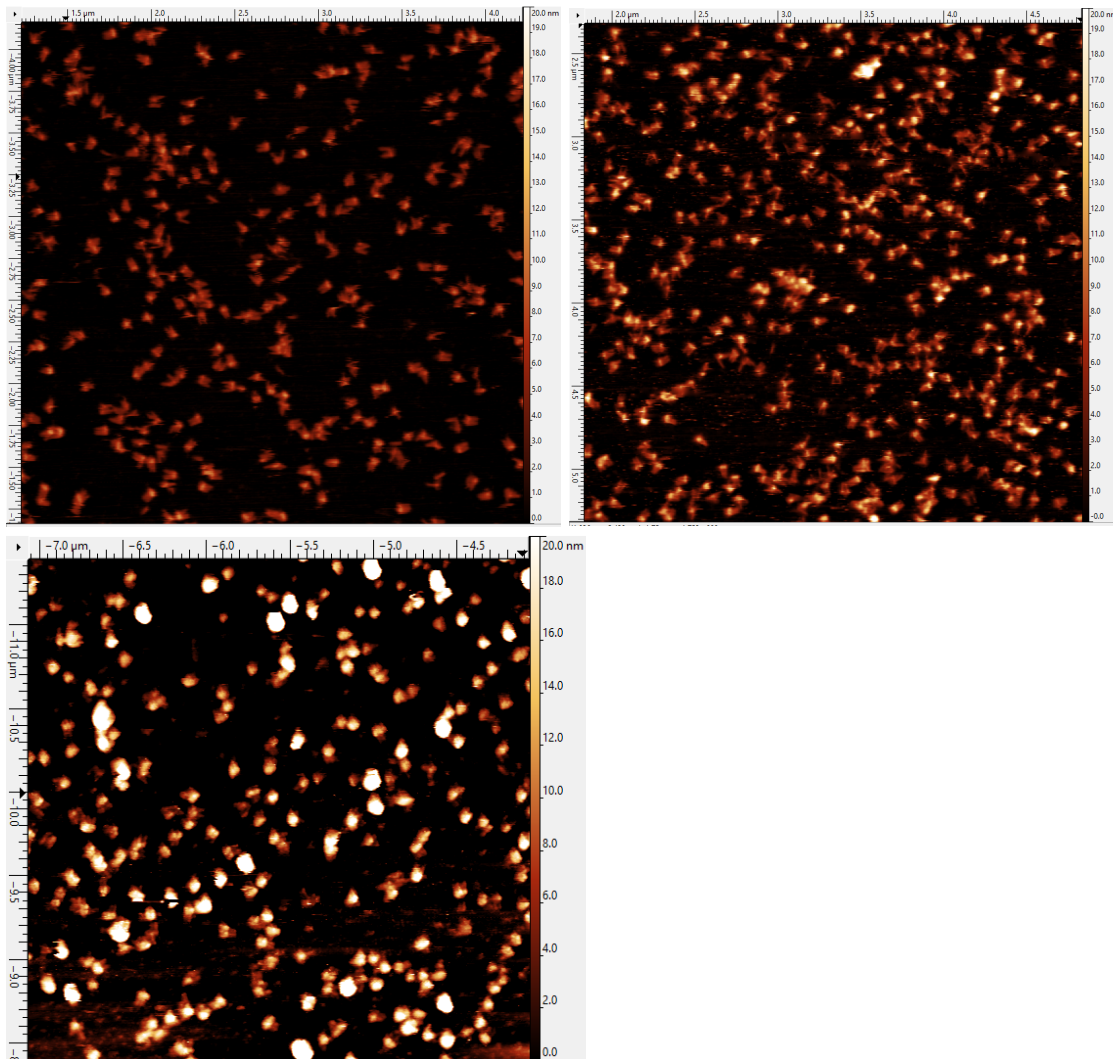
**Figure S23. Effect of using Sodium-based buffer on patterning of silicified NanoAntennas**





**Figure 23.** Snapshot of scattering channel from two silicified samples (top row and bottom row) before (left) and after (right) washing the chip with TE + 2M NaCl buffer. No visible lift-off is observed after silicification.

**Figure S24. AFM showing Trident before and after 1 and 4 days of silicification**



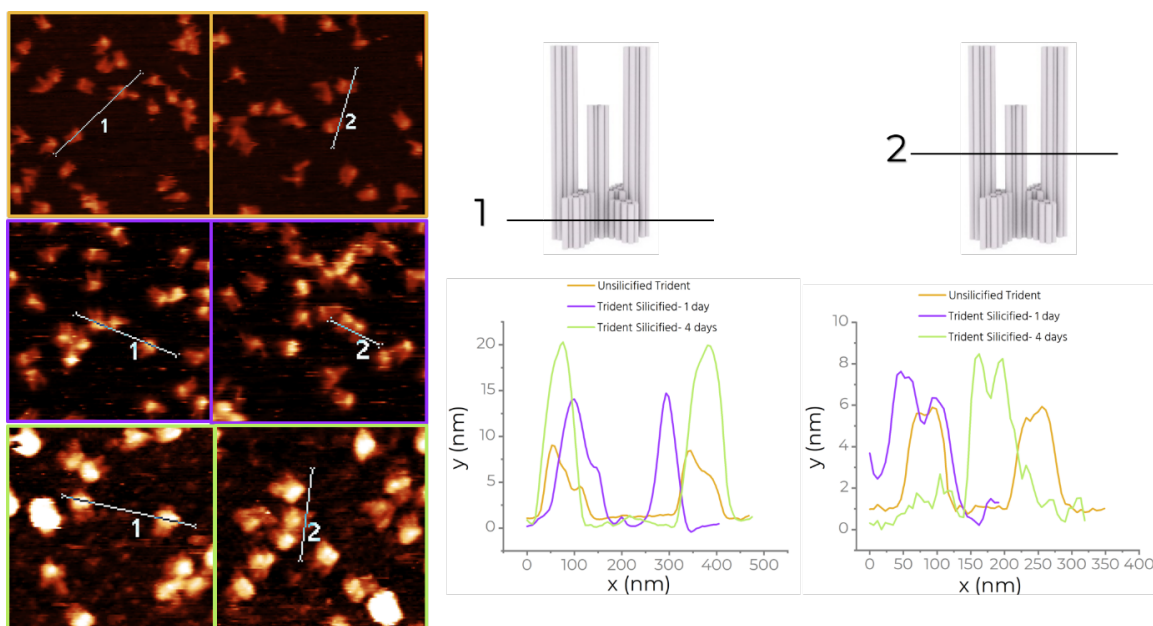


**Figure 24.** Example AFM images of Trident on mica before (left), after 1 day (right) and 4 days (third image, lower panel) of silicification and line scan analysis showing height comparisons for each. After 4 days of silicification, it became difficult to distinguish structural features of the Trident. We also observe larger chunks of silica aggregates in this case.

**Figure S25. Imager degradation in human blood plasma.**

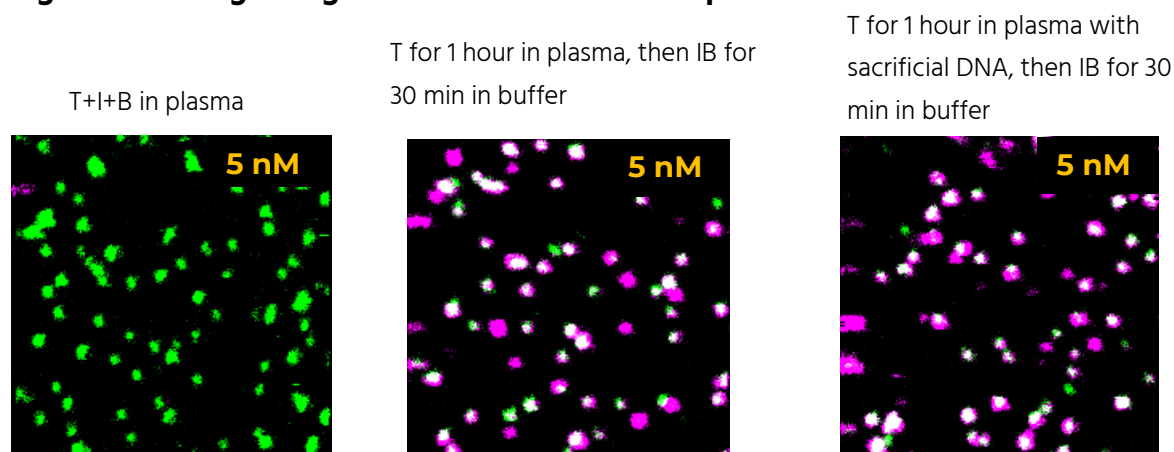


**Figure S25.** Fluorescence scans after incubating Target (5 nM), imager (12 nM) and blocker (12 nM) in human blood plasma for 1 hour with silicified NanoAntennas on the left, after incubating Target in plasma for 1 hour and then incubating imager and blocker in buffer for 30 minutes, after incubating Target with 1  $\mu$ M random (sacrificial) DNA in plasma and then incubating imager and blocker in buffer for 30 minutes. All incubations are done in the incubator at 37°C.

## Figure S26. Secondary structure: Target strand

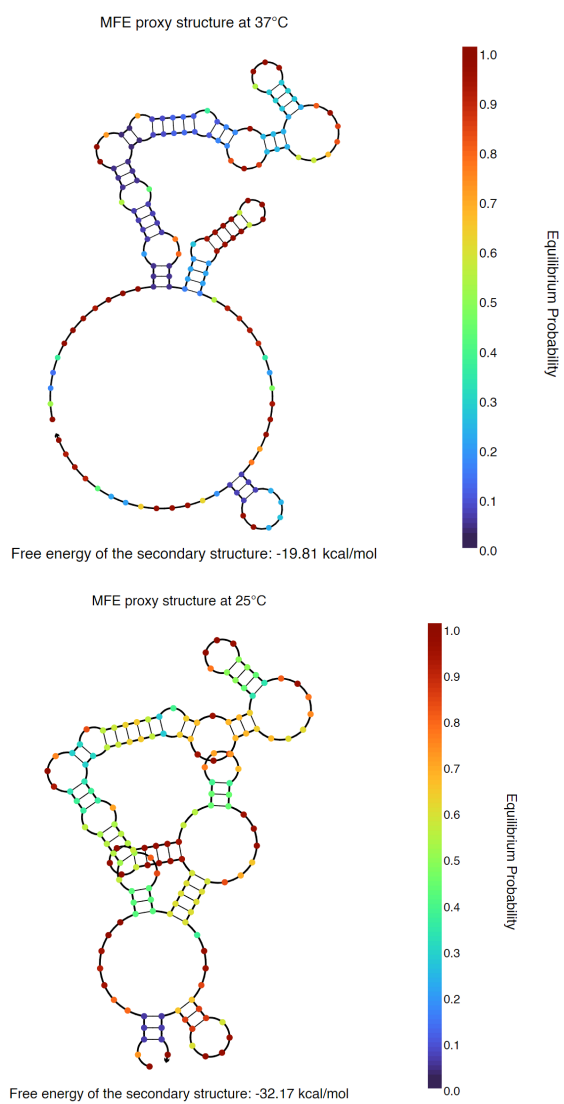
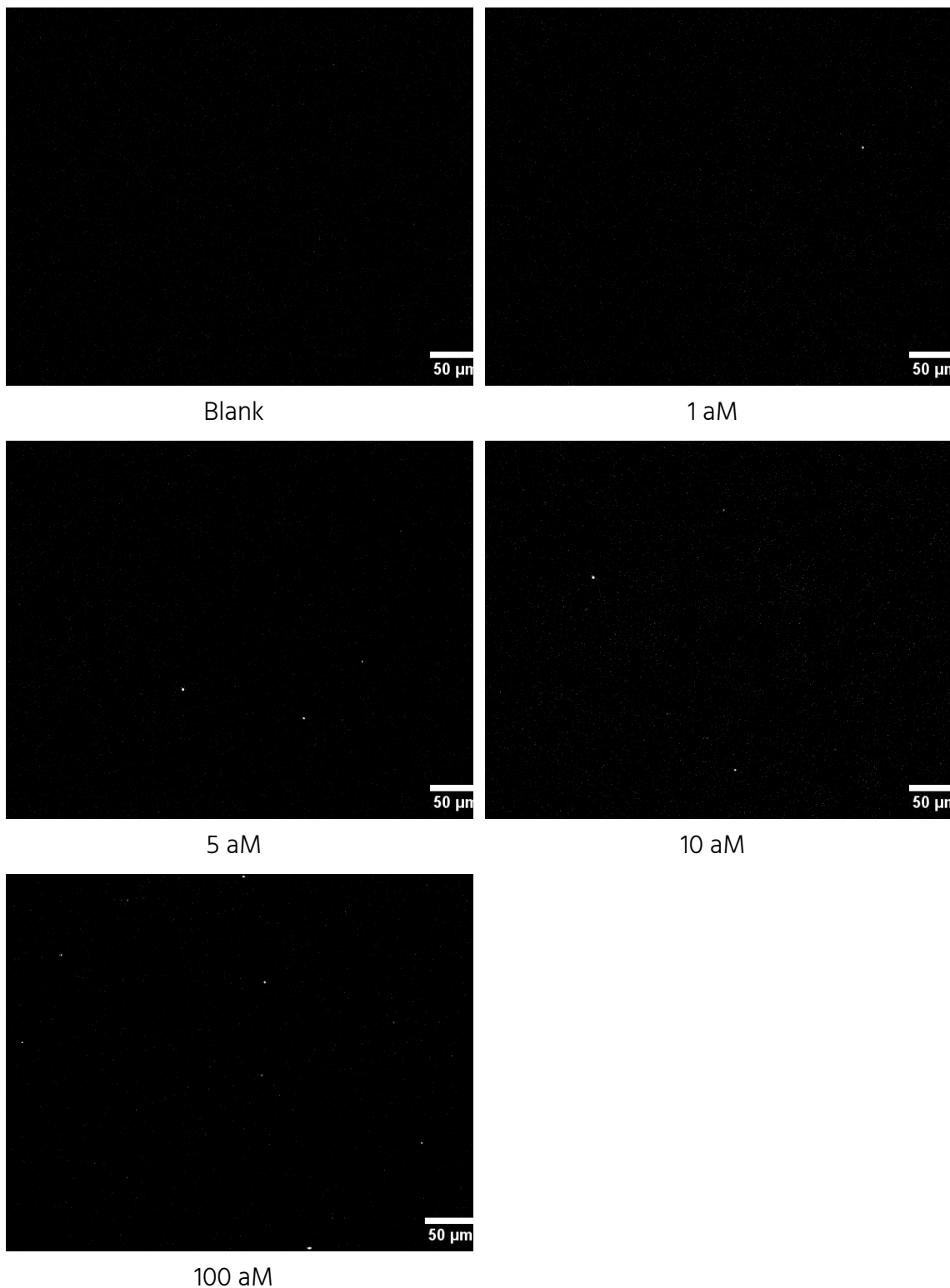
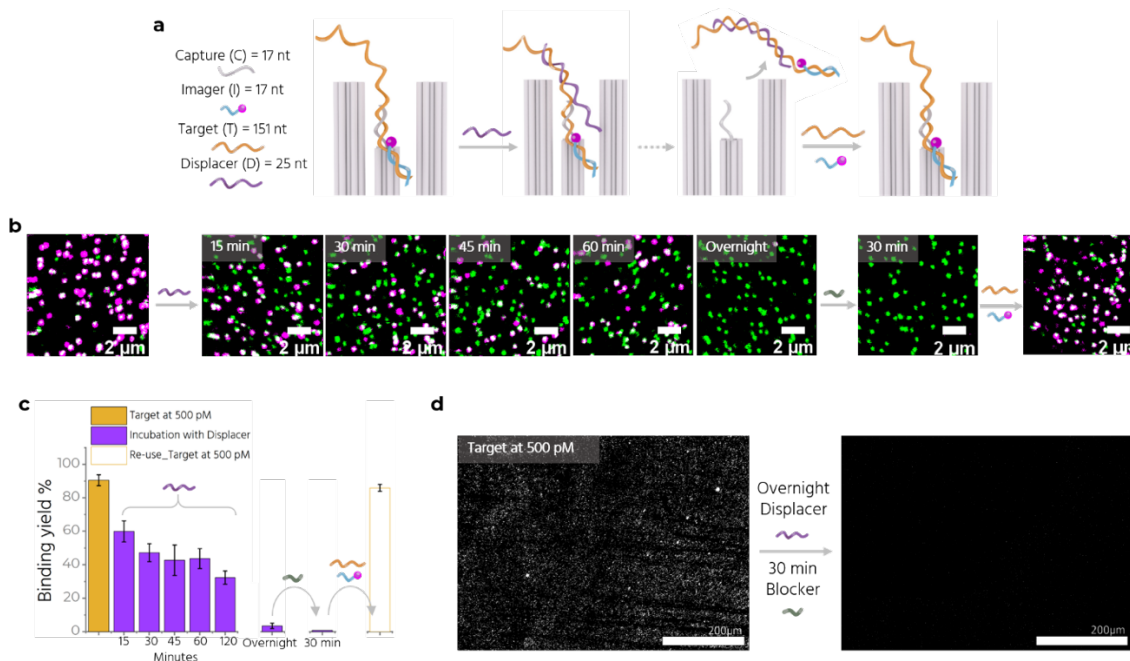


Figure 26. NUPACK analysis for secondary structure of the Target strand at 37°C (left) and at 25°C.

**Figure 27. Exemplary zoomed in snapshots from different concentrations measured on the reader in human blood plasma with silicified NanoAntennas.**



**Figure 28. Reusable chips.** We do this by introducing a ‘displacer’ strand with 25 nt complementary to the target strand, which is thermodynamically more stable than the 17 nt interaction between the capture and target strands. Once displaced, the capture strand is available for use again (Figure 28a). To test this, we immobilize NanoAntennas on a BSA-biotin-NeutrAvidin modified glass substrate and incubate with 500 pM of target along with 12 nM of imager and blocker for one hour and record fluorescence scans (Figure 28b). We observe dye colocalization with a target binding yield of ~90% (Figure 28c). We then incubate the sample with a high concentration (1  $\mu$ M) of displacer for up to two hours, reducing the bound fraction to ~30% (Figure 28b, c). Incubating overnight results in a <2% bound fraction. This likely arises from unspecific attachment of imager strands. We remove them through a short incubation with a high concentration of blocker strands, reducing the bound fraction to nearly zero. Upon re-incubation of the surface with 500 pM target, 12 nM imager and blocker, we achieve ~85% target binding yield. We perform the same protocol on our patterned NACHOS chip and successfully displace the bound target-imager complex, allowing the chip to be reused.



**Figure 28. a** Sketch showing the strand displacement of the target-imager complex by displacer strand, making the chip reusable. **b** Confocal fluorescence scans recorded after the 500 pM assay (left) followed by scans at 15, 30, 45, 60 minutes and overnight incubation with the displacer, after 30-minute incubation with blocker and after re-using the surface for the 500 pM assay. **c** Target binding yield over time. **d** Zoom-In of the fluorescence channel of a patterned NanoAntenna chip after an assay with 500 pM target (left). Incubating overnight with displacer followed by 30 minutes of blocker (right) displaces the target-imager complex, making the chip ready to be used again.

## Supplementary Note. 1

### 1.1 *Klebsiella pneumoniae* strain Kp11978 plasmid pOXA-48

We targeted a 151 nt sequence from the complete sequence that can be found at this link:

<https://www.ncbi.nlm.nih.gov/nuccore/JN626286>

### 1.2. Design and purification of DNA origami nanostructures

**Trident DNA origami nanostructure:** The Trident utilized in this study incorporates a previously characterized design by Close et al.,<sup>1</sup> employing the p8064 scaffold derived from M13mp18 bacteriophages and designed using caDNAo software (version 2.2.0),<sup>2</sup> as depicted in Figure S1. The design integrates various elements including a base dye (ATTO 542), 12 biotin anchors, 12 nanoparticle binding staples, 6 PAINT docking strands, 6 strands for hybridization with the Triangle origami, and 10 capturing strands for assays. The scaffold is produced in-house, while both unmodified and modified staples are sourced from Integrated DNA Technologies, Inc. (IDT). The folding of the DNA origami structures is carried out in a one-pot reaction, mixing 30 nM of scaffold DNA with a 10-fold excess of unmodified oligonucleotides and a 25-fold excess of modified strands relative to the scaffold, in a folding buffer composed of 1x TE and 20 mM MgCl<sub>2</sub>. This mixture underwent a detailed multistep thermocycling protocol, mentioned in Table S2.

**Triangle DNA origami nanostructure:** The Triangle origami is a modified version of the Rothmund Triangle, folded with p7249 scaffold produced in-house, derived from M13mp18 bacteriophages and designed using caDNAo software (version 2.2.0), as depicted in Figure S7. Modified strands in the structure include 6 strands for hybridization to the Trident and 6 strands as docking sites for DNA-PAINT measurements. The folding is carried out in a one-pot reaction, mixing 30 nM of scaffold DNA with a 10-fold excess of unmodified oligonucleotides and a 30-fold excess of modified strands relative to the scaffold, in a folding buffer composed of 1x TE and 12.5 mM MgCl<sub>2</sub>. This mixture underwent a detailed multistep thermocycling protocol, mentioned in Table S2.

**Purification:** The origami structures are purified using Amicon Ultra filters (100 K, Merck, Germany).

1. Add 500  $\mu$ l 1x FoB buffer in the filter tube and spin at 10,000xg at 4°C for 5 minutes.
2. Remove the supernatant collected in the tube and add 100  $\mu$ l of folded origami mix to the filter and add 400  $\mu$ l of 1x FoB buffer and spin again.
3. Repeat Step 2 twice more with 400  $\mu$ l of 1x FoB buffer.
4. Invert the filter and place into a new collection tube. Spin at 1000xg for 5 minutes.
5. Collect and store the purified origami in a low-bind Eppendorf tube.
6. Measure the concentration of the DNA origami using a Nanodrop 2000 spectrophotometer (Thermo Fisher Scientific), and store at -20°C for further use.

### 1.3. Surface preparation: BSA-Biotin/NeutrAvidin coated coverslips

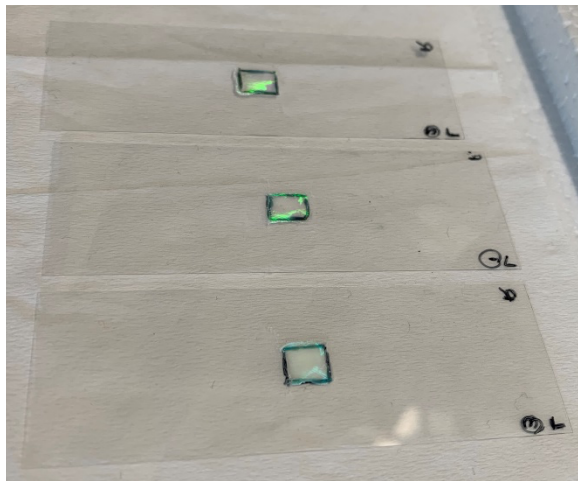
1. Clean the glass coverslips (24mm x 60mm; 170  $\mu$ m thickness from Carl Roth GmbH, Germany or 25mm x 75 mm, 170  $\mu$ m from Electron Microscopy Sciences, PA, USA) by rinsing with Milli-Q water and isopropanol, then dry under a nitrogen stream.
2. Treat in a UV-Ozone cleaner (PSD-UV4, Novascan Technologies, USA) at 100°C for 30 minutes.
3. Affix Adhesive SecureSeal™ Hybridization Chambers (2.6 mm depth, Grace Bio-Labs, USA) to the coverslips and keep on a hotplate at 100°C while pressing on the chamber for 1-2 minutes.
4. Wash the chamber three times with 150  $\mu$ l of 1x PBS buffer.
5. Add 150  $\mu$ l of biotinylated BSA at a concentration of 0.5 mg/mL (Sigma-Aldrich, USA) and incubate for 5 minutes.
6. Wash the chamber three times with 150  $\mu$ l of 1x PBS buffer.
7. Add 150  $\mu$ l of NeutrAvidin (0.2 mg/mL, Thermo Fisher Scientific, USA), and incubate for 5 minutes.
8. Wash the chamber three times with 150  $\mu$ l of 1x PBS buffer.
9. Use the surfaces immediately for DNA origami immobilization.

### 1.4. Surface preparation: Nanopatterned coverslips

The nanopatterning protocol we use was first introduced by Shetty et al.<sup>3</sup>

1. Mark a rectangle (0.7 cm x 0.5 cm) on one face of a 25mm x 75mm glass coverslip with a marker.

2. Wash both faces of the coverslip with Milli-Q water.
3. Wash the unmarked face with isopropanol and dry using an airstream.
4. Place the coverslip in a UV-Ozone cleaner (100°C for 30 minutes) with the unmarked side facing upwards, and position thicker pre-cleaned glass coverslips over them, leaving only the marked area exposed.
5. Take 350  $\mu$ l of 400 nm sized polystyrene nanospheres (DistriLab) in a low-bind Eppendorf and centrifuge at 10,000xg for 5 minutes at 20°C.
6. Discard the supernatant and suspend the spheres in 350  $\mu$ l of Milli-Q water.
7. Centrifuge twice more while washing with Milli-Q water.
8. Discard the supernatant and suspend and suspend the spheres in 100  $\mu$ l of 25% ethanol.
9. Use the ozone-cleaned coverslip immediately.
10. Position it at a slight angle (30-45°) and add 10  $\mu$ l of the cleaned nanospheres solution is to one corner of the marked rectangle and allow the solution to spread and air-dry for 15-20 minutes.
11. Carefully wipe spheres dried outside the marked area using a wipe (Kimtech Science™ wipes by Fisher scientific).



12. Heat the coverslip on a hotplate at approximately 60°C for 5 minutes.
13. Place in a sealed glass chamber with 5-10 ml of Hexamethyldisilazane (HMDS) by Merck, Germany, in a 10 ml glass beaker for 30-40 minutes.
14. Sonicate the coverslip in a beaker filled with Milli-Q water, fully submerging them until the spheres lift off, which usually takes about 30 seconds to a minute (Pipetting in the solution close to the patterned rectangle speeds up the process).
15. Dry with a nitrogen stream.
16. Heat at 120°C for 5-10 minutes, and store in a closed box at room temperature. Use immediately for DNA origami placement.



## 1.5 DNA origami immobilization on BSA-Biotin/NeutrAvidin surface

100 pM of Trident modified with biotin anchors at its base, is diluted in 1xTE +2M NaCl buffer and added to a 150  $\mu$ l chamber (prepared according to section 1.3), incubated for 1.5 minutes and washed 4 times in 1xTE +2M NaCl buffer. This gives a single-molecule density of the origami on the surface and was mostly used for measurements on the confocal microscope.

## 1.6 DNA origami placement on patterned surface

This is a two-step process.

### 1. Triangle placement:

1. Add 200  $\mu$ l of 150 pM Triangle diluted in placement buffer (PB) containing 40 mM Tris, 40 mM MgCl<sub>2</sub> at pH=8.4 to the coverslip (prepared as explained in section 1.4) and incubate for 1 hour.
2. Wash the coverslip 6 times with PB followed by 6 times with PBTween buffer (PB containing 0.05% Tween20) and 8 times (or longer until the surface becomes hydrophobic again) with PB.
3. Check the placement quality by DNA-PAINT (detailed description in section 1.16) using ONI Nanoimager. Assess the surface coverage, repeat the placement if needed.

### 2. Trident placement:

1. Add 200  $\mu$ l of 500 pM Trident in PB to the coverslips with Triangles and incubate for 1 hour, followed by the same washing procedure as for Triangle.
2. Check the placement quality by DNA-PAINT using ONI Nanoimager. Assess the surface coverage, repeat the placement if needed.
3. If most of the Tridents are binding in random orientations on the Triangle (observed using DNA-PAINT), use a two-step, 1-hour long placement each with Trident concentration around 200-250 pM.
4. In case the concentration was too high and the surface has multiple origamis binding at each binding site, incubate the coverslip in a sodium-based buffer (~1 hour) to lift-off the origami and wash with PB 8-10 times and start again from Triangle placement.

## 1.7 Functionalization and purification of nanoparticles

The freeze and thaw method<sup>4</sup> is used to functionalize silver nanoparticles (AgNPs) with DNA and agarose-gel electrophoresis is used to purify.

1. Add 100  $\mu$ l of a 1 mg/ml AgNPs of 80 nm or 100 nm (nanoComposix) into a low-bind Eppendorf tube.
2. Take one tube of lyophilized thiolated-T20 DNA staples (4 nmol) from Ella Biotech, and add 675  $\mu$ l of Sigma water. Mix thoroughly by shaking and vortexing. Slowly add this to the nanoparticle solution with constant pipetting.
3. Two such 675  $\mu$ l aliquots are combined with the 100  $\mu$ l NP solution in one tube.
4. Add 60  $\mu$ l of 5 M NaCl with continuous pipetting.
5. Freeze at -20°C for 1-2 hours. Mostly left frozen overnight or until the day of use.
6. Thaw for 15-20 minutes wrapped in aluminum foil at room temperature on the day of use.
7. Centrifuge at 2800xg for 15 minutes at 4°C, discard the supernatant leaving 80-100  $\mu$ l in the tube.
8. Add a tenth of the loading dye (BlueJuice Gel Loading Buffer, 10x by ThermoFisher scientific) before running in a 1.2% agarose gel at 100 V for 45 minutes.
9. Cut and squeeze the band to retrieve the functionalized nanoparticles.
10. Measure the concentration using Nanodrop 2000 spectrophotometer (Thermo Fisher Scientific). Store in dark at 4°C.
11. Sonicate before using, if not immediately used.

## 1.8 DNA Origami NanoAntennas on BSA-Biotin/NeutrAvidin surface

If the NPs were not functionalized on the same day, they are sonicated before use and the concentration is measured again.

1. Dilute the AgNPs to reach an optical density (O.D.) of 0.05 in 1x TE buffer containing 2M NaCl.
2. Add this to chambers containing Trident DNA origami structures (prepared as described in sections 1.3 and 1.5) and incubate overnight in dark at room temperature.
3. The following day wash 4-5 times with 1x TE buffer with 2M NaCl. The NanoAntenna assembly is complete.

## 1.9 DNA Origami NanoAntennas on patterned surface

If the NPs were not functionalized on the same day, they are sonicated before use and the concentration is measured again.

1. Dilute to an O.D. of 0.2 in PBTween buffer (40 mM Tris, 40 mM MgCl<sub>2</sub>, and 0.05% Tween20).
2. Add 50 µl of this to coverslips containing Trident DNA origami structures bound to Triangle origami (prepared as per sections 1.4 and 1.6) and incubate overnight in the dark at room temperature.
3. The following day, wash 5-6 times with PBTween buffer.
4. Store in PB until use.

## 1.10 Addition of a microfluidic chip

The coverslips with nanonantennas are prepared according to section 1.9. Most of the liquid outside the marked area is carefully removed with a wipe without letting the surface dry. A straight channel microfluidic chip (Fluidic 268 by microfluidicChipShop) with self-adhesive tape is used. The tape is removed, and the chip is pressed onto the coverslip. After the chip is firmly glued to the coverslip, the channel is washed 3-4 times with PBTween. The inlet and outlet are blocked while the center of the chip is sprayed with a black paint (Buntlack Matt from OBI, Germany), to reduce the autofluorescence from the chip. The chip is ready once the paint has dried (~15 minutes air dry).

## 1.11. Silicification

The protocol employed for silicification was adapted from the method outlined in [here](#)<sup>5,6</sup>

1. Take a 10 ml glass vial and add 3 ml PB.
2. Add a magnetic bead and stir at 900 rpm at room temperature. Make sure to keep the stirring unobstructed.
3. Slowly add 60 µl of TMAPS (N-[3-(trimethoxysilyl)propyl]-N,N,N-trimethylammonium chloride, 50% wt/wt in methanol, TCI America) to the mixture and stir for 20 minutes.
4. Slowly add 60 µl of TEOS (Tetraethyl orthosilicate, 98%, Sigma Aldrich) and stir for 20 minutes.

5. Add 100  $\mu$ l of the precursor to each microfluidic chip, gently mix and keep the chips upside-down.
6. Incubate overnight (19-24 hours) at room temperature.
7. Remove the precursor and rinse thrice with Milli-Q water and thrice with absolute ethanol.
8. Let the chips air dry.

### **1.12 Sandwich Assay**

The sandwich assay includes incubation with the 151-nt target strand, 17-nt imager strand and 17-nt blocker strand. The imager and blocker are kept constant at 12 nM concentration. The target concentration varies depending on the experiment.

For measurements with BSA-biotin/NeutrAvidin surfaces, 1xTE 2M NaCl is used during the assay unless stated otherwise. For measurements with patterned surfaces, PBTween was used unless stated otherwise. The target, imager and blocker are incubated at 37°C for 1 hour in an incubator or coupled with back-and-forth microfluidic flow at 36°C for 1 hour on the reader.

Specific signal is determined by the target capture efficiency % in presence of both target and imager strands, while unspecific signal is calculated by the target capture efficiency % in presence of only imager strands.

For measurements with human blood plasma with patterned surfaces on the reader, the target is first incubated with 50% plasma, 40 mM Tris, 40 mM MgCl<sub>2</sub>, 5 mM EDTA, 1  $\mu$ M sacrificial DNA and 2 units of DNase I in water for 45 min with back-and-forth flow (at 36°C), washed 6-8 times with PBTween and with 1xTE 2M NaCl, then incubated 15 minutes with Imager and Blocker in PBTween with back-and-forth flow at 36°C, washed and imaged.

### **1.13. Transmission electron microscopy (TEM)**

The folding of the Trident DNA origami nanostructures was characterized with transmission electron microscopy (TEM). 5  $\mu$ L of a sample was incubated for 30 s – 5 min, depending on concentration, on glow discharged TEM grids (formvar/carbon, 300 mesh Cu; Ted Pella) at room temperature. After incubation on the grids, the sample was wicked off by bringing the grid into contact with a filter paper strip. For the DNA

nanostructures, a 5  $\mu\text{L}$  drop of uranyl formate staining solution (2% uranyl formate aqueous solution containing 25 mM sodium hydroxide) was applied to the grid, immediately wicked off, followed by applying another 5  $\mu\text{L}$  drop of uranyl formate staining solution. This drop was allowed to incubate on the grid for 10 seconds and then wicked off. The grid was dried for 5 minutes before imaging. Imaging was performed with a JEM1011 transmission electron microscope (JEOL) operated at 80 kV.

#### **1.14. SEM**

The SEM instrument used in this work is the Raith eLINE SEM instrument. The beam settings for imaging are 10 kV acceleration and 20  $\mu\text{m}$  aperture. The samples were imaged using the SEM after 20 s sputtering using an Edwards Sputter Coater S150B. The sputter target contained 60% gold and 40% palladium. The process parameters used for sputtering were 5 mbar Argon, 1.5 kV, 11 mA. Here 20 s of sputtering results in the deposition of a layer of gold/palladium with a thickness of a few nanometres. SEM imaging was performed on horizontal samples.

#### **1.15 AFM**

AFM scans in aqueous solution (AFM buffer = 40 mM Tris, 2 mM EDTA, 12.5 mM  $\text{Mg}(\text{OAc})_2 \cdot 4 \text{H}_2\text{O}$ ) were realized on a NanoWizard<sup>®</sup> 3 ultra AFM (JPK Instruments AG). For sample immobilization, a freshly cleaved mica surface (Quality V1, Plano GmbH) was incubated with 10 mM solution of  $\text{NiCl}_2$  for 3 minutes. The mica was washed three times with ultra-pure water to get rid of unbound  $\text{Ni}^{2+}$  ions and blow-dried with air. The dried mica surface was incubated with 1 nM sample solution for 3 minutes and washed with AFM buffer three times. Measurements were performed in AC mode on a scan area of 3 x 3  $\mu\text{m}$  with a BioLeverMini cantilever ( $\nu_{\text{res}}$  = 110 kHz air / 25 kHz fluid,  $k_{\text{spring}}$  = 0.1 N/m, Bruker AFM Probes). Leveling, background correction and extraction of height histograms of obtained AFM images were realized with the software Gwyddion<sup>7</sup> (version 2.60).

#### **1.16 DNA-PAINT**

DNA-PAINT measurements were carried out on a commercial Nanoimager S (ONI Ltd., UK). Red excitation at 640 nm was realized with a 1100 mW laser, green

excitation at 532 nm with a 1000 mW laser, respectively. The microscope was set to TIRF illumination and a pixel size of 117 nm.

**DNA-PAINT with Triangle:** The Triangle DNA origami structure is modified to incorporate six docking sites, each with an 8-nt sequence. These docking sites are positioned to ensure that the super-resolved image represents a triangle shape. The docking sites are oriented towards the interior of the Triangle. This orientation ensures that the docking sites remain accessible for interaction, regardless of which side of the Triangle is facing the surface upon immobilization. For the measurements, ~300 pM of 8 nt Aptamer imager (complementary sequence to the docking site) in PBTween buffer, labeled with ATTO 655 is added to the coverslip and the transient binding of the imager to the docking sites is observed over 10,000 frames at 100 ms exposure time on the ONI Nanoimager. The data is processed using Picasso Localize and Picasso Render.<sup>8</sup>

**DNA-PAINT with Trident:** The Trident consists of 6 docking sites (8-nt long), 3 at the bottom of the left pillar complex and 3 at the top of the left pillar complex such that if the Trident is immobilized perpendicular to the Triangle (desired orientation), the output super-resolved image would be one circular or elliptical (flexibility of the pillar at the top) spot, while a parallel orientation would result in two spots separated by a distance equivalent to the height of the structure ~74 nm. For the measurements ~300 pM of 6-nt fast imager (complementary sequence to the docking site) in PBTween buffer, labeled with ATTO 655 is added to the coverslip and the transient binding of the imager to the docking sites is observed over 10,000 frames at 100 ms exposure time on the ONI Nanoimager. The data is processed using Picasso Localize and Picasso Render.

## 1.17 Confocal measurements

532 nm wavelength is used to excite ATTO 542 and 639 nm for Alexa fluor 647. 20  $\mu\text{m}$  x 20  $\mu\text{m}$  scans are recorded with 1 ms integration time. Samples are excited at 1  $\mu\text{W}$  laser power. For enhancement factor measurements, samples without NPs are excited with 500 nW and samples with NPs at 50 nW. The confocal setup used is as described

by Trofymchuk, Glembocky et al.<sup>9</sup> The data acquired is processed with a custom-made LabVIEW software (National Instruments, USA) and further analysis was done with OriginPro2019.

## Supplementary Note. 2

### Reader specifications

The fluidic automation is implemented with the help of a syringe pump and a needle, whereby the needle can be moved in a motorized manner between liquid reservoirs and a reaction chamber. It is therefore a miniaturized pipetting robot. The cartridge is designed accordingly (Figure A): It has liquid reservoirs that are arranged next to each other and an inlet into a reaction chamber that can be read optically. All reservoirs and the inlet can be closed with septa, which close tightly again after perforation by the needle. The cartridge therefore represents a closed system.

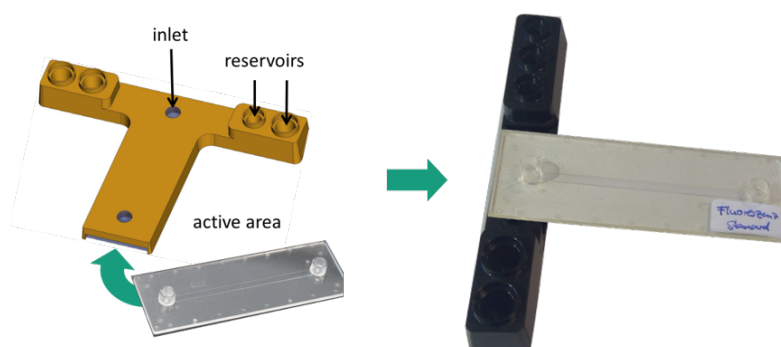


**Figure A.** Sketch of the 3D-printed chip holder with reservoirs on the left and the microfluidic chip shown on right.

Fluidics is implemented as a modular concept for validation purposes. A polymer carrier contains all access points for the needle including the septa. This carrier was created as part of the project using a 3D printer. There are several design variants that particularly affect the reservoirs. These can either be filled with chemicals directly in the carrier or equipped with standard vials. The latter variant is not suitable for mass production, but it has made the laboratory processes in the project easier. The polymer carrier can be produced economically in large quantities as an injection molded part. The fluidic chip with the chamber for optical readout is inserted into the carrier. This is

constructed by first capping the chemically prepared glass substrate with a polymer chip made of Zeonex® cycloolefin polymer (COP) with high optical quality. This creates the flow cell for the detection reaction.

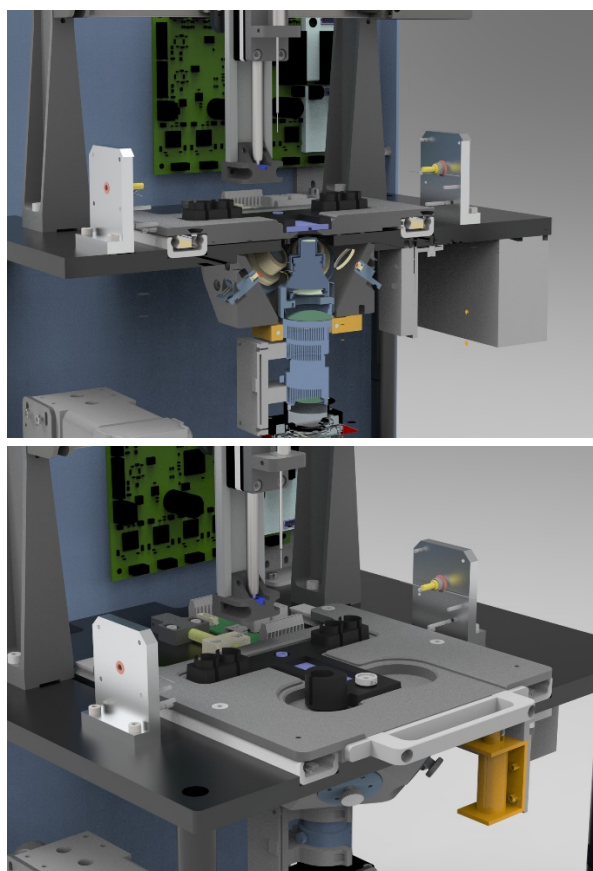


**Figure B.** A sketch of the inside of the reader focusing on the optics unit on the left and pipetting needle and the sample holder on the right.

The optical unit consists of the illumination to stimulate fluorescence and a microscope including a camera for imaging (Figure B). Using spectrally filtered LEDs, an optical power density of  $2 \text{ W/cm}^2$  is achieved, which is sufficient to detect individual molecules. The microscope has a so-called tandem lens - two standard camera lenses arranged in opposite directions. The detection filter is located in the area of the parallel beam path. One of the two lenses has a liquid lens that can be used to electronically adjust the focal plane. By choosing a liquid lens, the entire optical system has no moving parts. The imaging is done on a CMOS camera with 12-megapixel resolution. With a numerical aperture of 0.2, this microscope achieves an optical resolution of  $< 2.7 \mu\text{m}$  ( $0.8 \mu\text{m}$  per pixel) over an image field of  $2.5 \times 3 \text{ mm}^2$ . The optics are extremely compact with a length of only 16 cm and can be set up at a moderate cost. The image



field is large in order to be able to perform multiplexing using several spots and to collect sufficient data for the measurements to be statistically meaningful.

**Reader data and analysis:** Samples are focused using the scattering signal from the NPs (See Figure A). Samples are imaged before doing the assay to ensure there is no unspecific signal in the fluorescence channel (Figure C). The microfluidic chip with the assay mixture is loaded in the sample holder and an automated script allows a pipetting needle to create a back-and-forth flow in the channel. A heating block that touches the chip on top is kept at  $\sim 36^{\circ}\text{C}$  during the incubation. The script is written to continue for 1 hour after which the chip is taken off and washed 5-6 times with PBTween. The sample is excited by spectrally filtered LEDs for several frames at 300 ms exposure time with a 500 ms gap between each frame. To avoid overheating of the sample by the LEDs, the movie recording is done in groups of 15 frames, after which a pause of 1-2 minutes is given before the next 15 frames. This is repeated until most of the single molecules are photobleached.

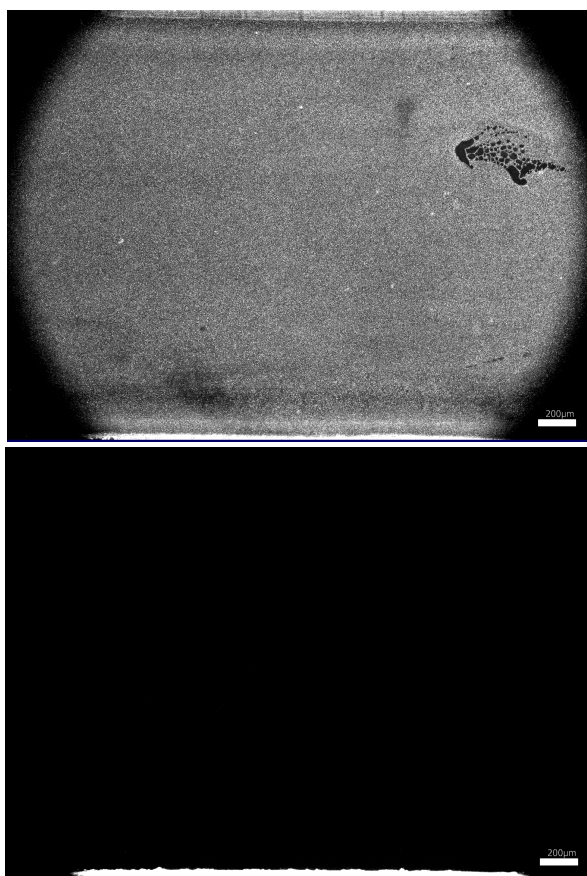


**Figure C.** Image taken on the reader before performing the assay. The left image shows scattering from nanoparticles, allowing us to focus on the right plane. The darker holes are defects from the

nanopatterning. Image on the right is the fluorescence channel (after background subtraction), showing no signal before the assay. The bright part at the bottom of the image is the autofluorescence from the edge of the microfluidic chip.

After recording several frames, the software subtracts the background and counts single molecules (Figure D). The intensity threshold is set to capture most molecules, and if there is significant variation in intensity, two different thresholds can be used, ensuring zero overlap between spots. The software also plots bleaching steps for each identified spot. However, with the current code, the software cannot accurately identify spots that do not blink or bleach. A masking function allows the user to exclude certain spots, which can be useful for eliminating reflections from bubbles that may move over time and cause multiple spots to be counted. Masking these bubbles or similar defects can prevent this issue.



**Figure D.** A snapshot of the software showing a detected single molecule and the time transient on the top right showing a single bleaching step.

At lower target concentrations, the software can automatically detect single molecules (Figure E left). However, at higher concentrations, the surface becomes densely populated, resulting in inaccurate counting due to spots appearing as clusters or continuous bright areas (Figure E right).

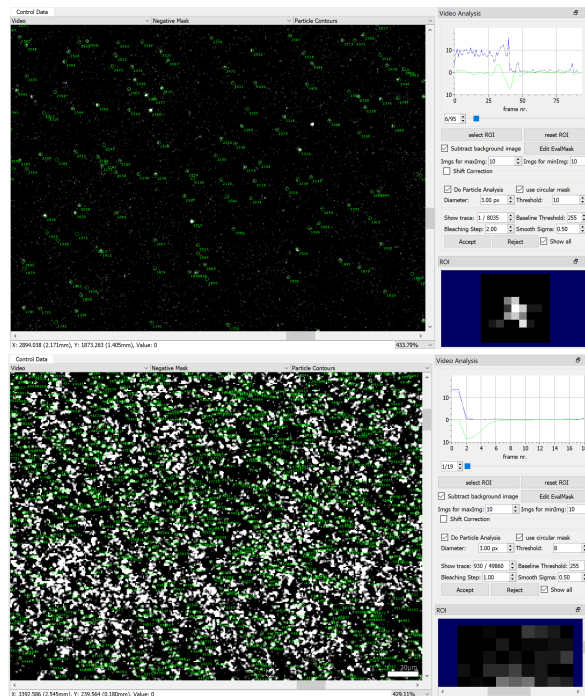
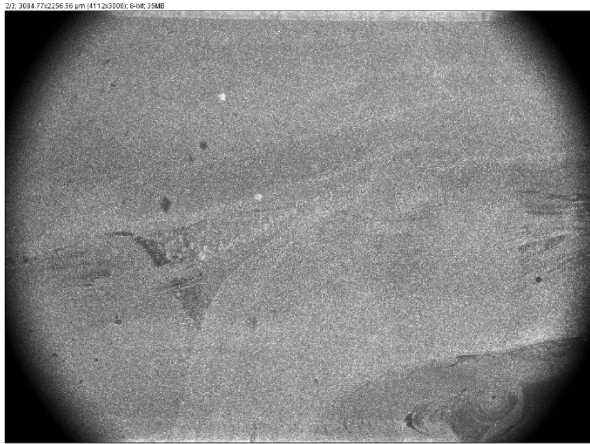


**Figure E.** A snapshot of the software with multiple single molecules identified accurately in case of lower target concentrations on the left, and the inaccurate counting at high target concentrations shown on the right.

### Normalized signal

By observing the scattering from the NPs, we can detect variations in NanoAntenna surface density between the chips due to defects in patterning, as well as varying brightness due to heterogeneity in NP binding. To compensate for this and enable comparison of the chips at different target concentrations, we use a normalization method. By illuminating the surface with white LEDs, we observe scattering from nanoparticles that allows us to focus on the sample without using fluorescence LEDs which would otherwise result in photobleaching of the fluorophore while focusing. This scattering channel also shows the variability in nanoparticle binding across the chip. We use the following process to compute the “normalized signal” by using ImageJ software:

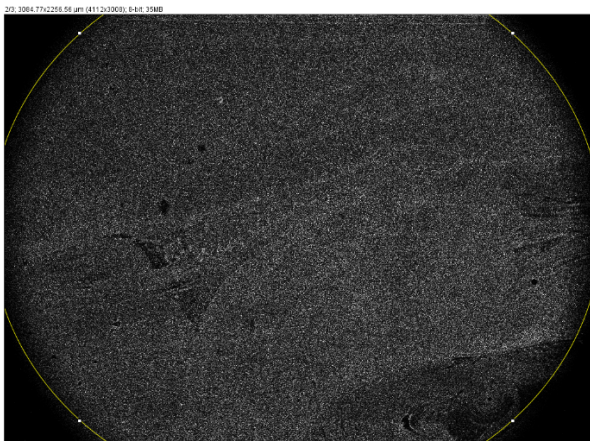
1. Load the image in ImageJ.



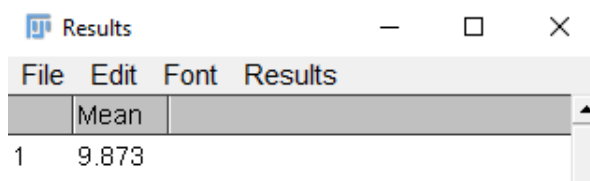
2. Subtract the background by using rolling ball radius.



3. Use the select tool to roughly select the circular FOV.

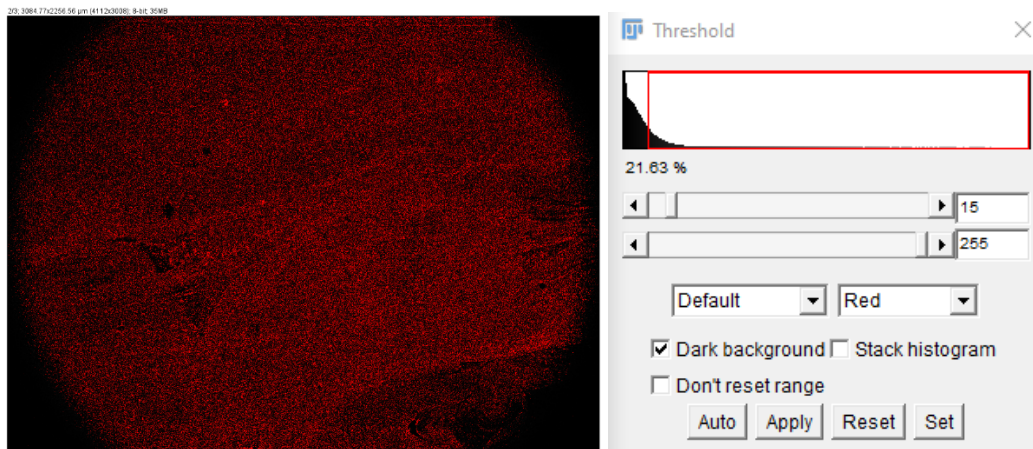


4. Measure the Mean gray value (the mean gray value is the sum of the gray values of all the pixels in the selection divided by the number of pixels.). This gives us an average brightness or B.





- Use the threshold option to select the desired intensity range (included pixels are shown in red). Apply the threshold. This converts the image into a binary image, where pixels are either foreground (typically white) or background (typically black).



- Use the select tool to roughly select the circular FOV and measure the 'area fraction' or the percentage of pixels in the image or selection. This gives us the % area covered or %A.

We convert the %A to decimal before using it for calculations. Normalized signal is thus given by:

$$= \frac{\text{No. of spots in the fluorescence channel}}{\text{Mean scattering brightness } (\bar{B}) * \text{Area fraction } (A)}$$

As we measured two areas (See figure S18) for each sample by changing how the chip was placed in the sample holder, we combine the signal from both areas to arrive at the final signal given as:

$$\text{Normalized signal} = \frac{\text{Total no. of spots in the fluorescence channels}}{(B_1 A_1) + (B_2 A_2)}$$

## Intensity-based analysis

- Open the after-assay image with both scattering and fluorescence channel in ImageJ.
- Look for defects in patterning in the scattering channel, select a circular area, check mean grey value and accordingly set a value to subtract background. This value for our samples was mostly around 20.
- Set rolling ball radius to 20 and subtract the background from both channels.
- Select the image with a rectangle, avoiding edge of the chip from the selection. Keep the same selection for both channels.
- Use the 'transform image to results' option to get xy coordinates for each pixel for the fluorescence channel.

6. Save the files separately as .csv.
7. Import the files in Origin2019.
8. Delete the first column and select the rest of the data. Stack the data in a single column.
9. Select the data to get the sum of pixels.
10. Use the steps from the previous section to get the mean brightness and area covered for the scattering channel.
11. Divide the sum of pixels for the fluorescence channel by the product of mean brightness and area covered to get the 'normalized signal'.

## Double-event estimate

At low target concentrations, compatible with single-molecule counting, the number of fluorescent molecules captured within a single pixel in the reader FOV follows a Poisson distribution, with the huge majority of pixels containing no molecules at all. This is well justified if one considers the high number of capturing strands contained in the area of a pixel, so that the probability of further target captures can be assumed to be independent from the presence of other captured molecules. Let's consider a scenario where  $N_{sp}$  spots have been detected in a field of view (FOV) subdivided in  $N_{pix}$  pixels. Assuming that the probability of capturing a molecule is homogeneous within the sample and if  $N_{sp} \ll N_{pix}$ , the expected number of fluorescent molecules captured within any pixel is approximately  $\sim N_{sp}/N_{pix}$ .

From Poissonian statistics, it is immediate to compute the probability for a pixel to host two molecules as  $e^{-\frac{N_{sp}}{N_{pix}}(N_{sp}/N_{pix})^2/2} \approx (N_{sp}/N_{pix})^2/2$ . On a field of view with  $N_{pix}$  pixels, that corresponds to an average of  $N_{sp}^2/(2N_{pix})$  pixels hosting two molecules within their area.

Given the finite resolution of the setup, two molecules might be detected as a single spot if they are less than 3 pixels apart in any direction. In other words, given a detected molecule, a second one might not be recognized and counted as a distinguished molecule if it sits in a  $5 \times 5$  pixels grid centered on the first one.

So, to estimate the correct number of double events we have to consider, instead of the total number of pixels in the FOV, the number of  $5 \times 5$  pixels grid, which is  $N_{pix}/25$ . This gives a  $25 \times N_{sp}^2/(2N_{pix})$  average number of molecules in the FOV which are not

being counted due to their overlap with other target's signals. Finally, the proportion of molecules that are not being counted with respect to those which are, will be  $\sim 25 \times N_{sp}/(2N_{pix})$ , which turns out to be 0.008% for 5 aM and 0.45% for 1 pM (based on the average of experimental data).

It's important to notice that this calculation holds only in the case  $N_{sp} \ll N_{pix}$  (verified in the whole aM-fM range), because we are neglecting triple or higher order overlap events and treating each additional undetected molecule as statistically independent. Effects such as target molecules depletion in the sample can only make further captures even less likely, diminishing the expected number of double events, so that this can still be considered a good upper bound. Also, if only a proportion  $\alpha$  of the total surface is actually properly functionalized and hence capable of target capturing (let's say 30%, or  $\alpha = 0.3$ ) the final result will have to be divided by  $\alpha$ , leading to the formula  $\sim 25 \times N_{sp}/(2\alpha N_{pix})$ .

### Supplementary Note. 3

**Table S1.** The list of buffers with recipes.

Buffer	Recipe
FoB 5	10 mM Tris-HCl, 1 mM EDTA, 5 mM MgCl <sub>2</sub>
FoB 20	5 mM Tris-HCl, 1 mM EDTA, 20 mM MgCl <sub>2</sub> , pH 8.0
Gel Buffer	40 mM Tris, 20 mM Acetic acid, 1 mM EDTA, 12.5 mM MgCl <sub>2</sub> , pH 8.0
PB	40 mM Tris-HCl, 40 mM MgCl <sub>2</sub> , pH 8.4
PBTween	40 mM Tris-HCl, 40 mM MgCl <sub>2</sub> , 0.05% Tween 20, pH 8.4
TE2MNaCl	10 mM Tris-HCl, 1 mM EDTA, 2 M NaCl

**Table S2.** Folding programs used for the folding of the DNA origami nanostructures.

#### Folding program for Triangle and Trident DNA origami nanostructures

Temperature (°C)	Time per °C (min)	Temperature (°C)	Time per °C (min)
65	2	44	75
64-61	3	43	60
60-59	15	42	45
58	30	41-39	30
57	45	38-37	15
56	60	36-30	8

55	75	29-25	2
54-45	90	4	Storage

**Table S3.** The list of unmodified staples for the Trident.

Plate No.	Well no.	Sequence (5' to 3')
Plate 1	A1	CCCCCTGATATTCAACCGTTCCAA
Plate 1	A2	ATCAAAGGGTGATTAAGACGGAATAGGAAACCAGA
Plate 1	A3	CAAAATCGGCCAACGCGCGGGGTGGAA
Plate 1	A4	CGCCTGTGCAGGTAATGGCATCAGCGGTGGTGCCA
Plate 1	A5	CCTATAAATCCAGGTTGAAGCCCCCAATAGCGTCA
Plate 1	A6	TTCATACATAAGCTTGAGA
Plate 1	A7	CGAGTTGGGAAGAAAAATCCCCC
Plate 1	A8	CCCCCAGTATGTTAGCAAACGAAAGCGCATTAGACCCCC
Plate 1	A9	CCTTCCAGTAAGCGTCTCAGTGCAGGCGGATAA
Plate 1	A10	CCCCCAGGGCGATCGGTAAGGGGGATGTGCCCC
Plate 1	A11	CCCCATTTCTGCTATCGACATACCCCC
Plate 1	A12	AAAACAGGTCTCCAGAGCCACCACCCCCACCCTTAC
Plate 1	B1	CCCCCCTCATTTTCCAGACGATTGGCCCCC
Plate 1	B2	TCATAGGTCTGAGAGACTACCCCC
Plate 1	B3	CTTGTGTCACCAGTTGAGGATCCCAAGCCGGCTTT
Plate 1	B4	CCCCCCCAGAAACCAGGCAAAGCGCCATTCGTAAGCTTTC
Plate 1	B5	CACCTTGCTGGTAATATCCAGACCCCC
Plate 1	B6	AGTGTTTACCGGCCACCAACCGGAATTACCCTGAC
Plate 1	B7	ACCGCCAGACAGAAGTATAGCCCGGACGTCGAGAAGTTTTAACG
Plate 1	B8	CTAGGGCGCTGGGTTTCTGGGCCGTTTTACGGTCCCCC
Plate 1	B9	ATCAAAAGCCTCGCTTCCAGTCGGGTGAGACGCA
Plate 1	B10	CCCCCGCTAACGAAAATAAACACCCCC
Plate 1	B11	ATGAAGGGCGATAAAGAACGTGGACTCCCCC
Plate 1	B12	CTTCTGAATCTTACCAACCCCC
Plate 1	C1	AACGTATCACCGTACTCACAGTACCCTTGAGTAAC
Plate 1	C2	CCCCACGACGGCCAGTACGGATAACCTCCCCC
Plate 1	C3	GCTTAAGAGGTCGTACCTTTAATTGCTCCCCC
Plate 1	C4	AGCTCATATGGGTAATCGGAGCAACTATCAGGCTA
Plate 1	C5	CCCCCAAGAAACATTTTAAAGACCCCC
Plate 1	C6	GCCAACGGCATTAAAAAATCCTTCCGTAATGGGA



Plate 1	C7	AACAATTCATTTGAACCAAGTTTTAGGTCGGAC
Plate 1	C8	AGGCCCTGAACAAGAAAAAGTAATTAATTGCTCC
Plate 1	C9	CCCCCTTTGTCACAATCAGACAAAAGGGCCCCC
Plate 1	C10	CCTTCCTGTAGCTTAATTATAAAGCCCCCATATA
Plate 1	C11	GAATGAGTAACAACCCGTCGGATTCTCCCCC
Plate 1	C12	CCCCCAATGCTGTAGCTCAACATGTTTTATATGGCTTAGA
Plate 1	D1	CGTCGGGGTCCGCCGCTGGAAGAAAGCGAAACTGT
Plate 1	D2	CCCCCGGTGAATTATCACCGTCACCGACTGAAATATTGAC
Plate 1	D3	TATTCACGTTGCGTTAGTAAATGAAAACACTGCAC
Plate 1	D4	TCACTCTGTCCGACAGGAGAATCAGCTAAAGGGAG
Plate 1	D5	CCAATAAAGCGAAGGAAGCAGCGGATAATT
Plate 1	D6	TGATTGTTTGGATTATACAAACAGATTAT
Plate 1	D7	AACTGACCAACCTGATATACGTAACAGCATCCTT
Plate 1	D8	TTATGCTTTCCTGTTAACGGTACTGTGTTGTTG
Plate 1	D9	GACGATAGTGAATTTATCGAAAGCGA
Plate 1	D10	AAAGGAATTGTGGCTATGTAATAAAAGGGACTGAG
Plate 1	D11	GGCGAGAAGAACTCAAACAGGAAAATGAGGCGGTC
Plate 1	D12	CCCCCTGCAAGGCGATCGACGTTGTAAACCCCC
Plate 1	E1	GGCGTTTTAGCGAACCTCCCCC
Plate 1	E2	ATCATTGTTTGCCCTACCG
Plate 1	E3	CCGCGACAACCTTAATACATGAGCCGATGCGGCGCC
Plate 1	E4	ATTCATTATCAGGACACT
Plate 1	E5	TAAACTGAAAGCGTAAGAATACGTTTTAGGAGTTT
Plate 1	E6	GAGCCTTGAATGACCCTCC
Plate 1	E7	CCCCCATACCGGGGCAAGTGTAGCGCCCCC
Plate 1	E8	CTGAACGAACCACTTTTGACGCT
Plate 1	E9	AGAGTTTTTTGGGGTCGCTCA
Plate 1	E10	AAGCATACCGATCTGACCTAAATTTAGAAAACGGT
Plate 1	E11	TCTGTGCTGCGGCCAGAGGTCAGTGCCTTTGAAT
Plate 1	E12	CCCTGTAATACGCATTAACCCATCCTAAT
Plate 1	F1	GTATTTTGCCTTGAATATTACC
Plate 1	F2	GCCTCCTGAGTATAACGGAGCTTGACGGGGACGGG
Plate 1	F3	AAGAGAATACGAGCATTACTAATAGTA
Plate 1	F4	GACTATAGAAATTTCAACAGTTTCAGCCCCC
Plate 1	F5	GGAAGTCTCCATGTTACTTAGCATCCAAGACTTT
Plate 1	F6	GCTCTCTGTGTCGCGTCCGTGAGCAAGGAAGACAG
Plate 1	F7	CAACAATAACAATAAGCA

Plate 1	F8	TAGCTTAGATTAAGACGCTCCCC
Plate 1	F9	CCCCCAGAATCAAGTTTGCCTTAAAGAACAAATAAAAGAGA
Plate 1	F10	CCCCCACATTAATTGCGTTGCGCTTGCCCTTGATC
Plate 1	F11	CCCCCCTTTTGATAATTGCTGAATATCCCC
Plate 1	F12	TCGTCGCTATTAATTAATTCCCC
Plate 1	G1	CTGCAGGTAGCGACGATATAGCGTCCAATACTTG
Plate 1	G2	GATTAACAGTTAATGCCATGGAAAGCCGCCGCAT
Plate 1	G3	TCATGCAAAGACACCACGGCAA
Plate 1	G4	TATAGAAGGCTTATCCGCCCCC
Plate 1	G5	CCCCCTGAAGGGTAAAGTTAAATTTTA
Plate 1	G6	CCCCCAACAGGTCAAGTACGGTGTCCCCC
Plate 1	G7	TTTTTAATGGAAACATTCGCCTATATACAGTAAT
Plate 1	G8	AACTAAGGATTAGACCGGAAGCAAACCTCCCCC
Plate 1	G9	GAGTTGCCCCAGGGCAACGCAAATGAAA
Plate 1	G10	CCCCCCTTTTTAACCTCCGCTTCTGGTGCCCC
Plate 1	G11	CCCCCCTCAGGAAGATCGCACTCCAGCCTTCCTTGAGGG
Plate 1	G12	TCAAACATTACGCGCAGCATT
Plate 1	H1	CCCCCACAAGAAACCACCAGATTATCATATTAATGCAC
Plate 1	H2	TTTTGATAAAGTTATACATGCCTGAGTAATGTGTAGCCCC
Plate 1	H3	ATTAGCTCATTATACCAGCCCAAATCAGACCAGGC
Plate 1	H4	CCCCCAGATTAGTTGCTATTTTGCACCCATAAGCAATAGC
Plate 1	H5	AAGGAAATGCAAAATTCTTCATAATACGTACAGAG
Plate 1	H6	TTAAGCTAAATTTCAATTCAAG
Plate 1	H7	TTCATCAACTAGGCATAGTCCCCCTCAAATGCTTG
Plate 1	H8	CCCCCACCAGAAACAATCCGGAATTTCCCC
Plate 1	H9	CCCCCGGAGTGAGAGTAGCGGTTTTCCCC
Plate 1	H10	CCCCCATCGTAACCGTGCATCTGCCAGTAGGGAGGTCAC
Plate 1	H11	CCCCCTTCCCTTAGAATTGTAGATGGGCGCCCC
Plate 1	H12	AAGGTGCATCATTATTAGCGTTTGGCCAGCATAAC
Plate 2	A1	TTTTCCAGCTATATTTTCAAGCAAATCAGAACTTA
Plate 2	A2	CCCCCTCAGCTCATTTTTAACTCGATGAACTACCCCGCAG
Plate 2	A3	CCCCCGAGAGTTGCAGCAAGCCACCGCCTGGCCCTGACCCCC
Plate 2	A4	CCCCCAGAGCCAGCAAATCACCAGTAGCGAATTTTTGCG
Plate 2	A5	TAGCGAAGCCCATGAAATAGCCCAATAATAAGAGCCCC
Plate 2	A6	AGTAGCCAGCAAGCTGATCACTGCCGGGGTGCTA
Plate 2	A7	AGAAACCGAGTAAAAGAGACGACCATAGTCTTTAA
Plate 2	A8	CGCCCATTCAGGCTGCGCAACTGTTGGGACCCCC

Plate 2	A9	GTTGGCCTTGAAAACATTGGGGTAAA
Plate 2	A10	CCCCCCTTGATATTCACAAACAAATTATTCTGAAACCCCCC
Plate 2	A11	CCCCCGGGTATTAACCTCAAAATATCCCCC
Plate 2	A12	ATCGGCACAGCCAACAGAGATAGACACGCAACCAG
Plate 2	B1	CCCTAGCAATACTTCTTTCTGTCTGATAAAAAATACC
Plate 2	B2	CTCAGAGCCGCCACCCAGTTCAGAAAACGATAATT
Plate 2	B3	CAGGTGAACCATCACCCCGAGCCGGTCGTGCC
Plate 2	B4	TGAATAAGAGCAACACTATAG
Plate 2	B5	CCCCCAACGTCAAGTGAGCTAACTCCCCC
Plate 2	B6	TAAACACCGTTTGAATTCAGAGGTTTTCCAGTCATAAG
Plate 2	B7	TTGCGCGAGGCTGTCTTCTCTAATTTAAGTA
Plate 2	B8	GTTGATCGGAACGAGGCGTAG
Plate 2	B9	GTATCATCGCTTTGAATCA
Plate 2	B10	AGCCTTTATTCAATTCGTAGAAACCAA
Plate 2	B11	CGGCACCGGCTTAGGTTGGCGCAAAA
Plate 2	B12	CTATAATCAGATTCTGGACAATATTTTTGAAAGGA
Plate 2	C1	CCCCCAGTATCATATGCTTAATGCCGCCCCC
Plate 2	C2	AGTGAGAATCGCCATGCTTGAGAGCATGTTAACG
Plate 2	C3	GAGATGGTTGCGAACGTGGCGGAGACTCCTCATGCG
Plate 2	C4	CCCCCGTCACGCTGCGCGTAACCAAATCCGCCGGGCCCCC
Plate 2	C5	ATGTTCCACACAACATAAAAATCAATAGGGTT
Plate 2	C6	CCCCCGTATTCTAAGAACGCGATTAGAAACGCATAAAACTA
Plate 2	C7	CGGTAAAGCCGCACAGGCGGCCTTTAGTGACCCCC
Plate 2	C8	GCCCTAAAACACAATATCGAAGAGGCGGTTTGAAT
Plate 2	C9	CCCCCTAGATTTAGTTTGACCATTAGATAACATTTGATTC
Plate 2	C10	AGACGACGGATAAGTAAGGCAAAGAA
Plate 2	C11	ATTGTTATCCGAGGTGCCAATCAAAGAATAGTCG
Plate 2	C12	ATCCAAAAGAGATTTTTCTGTCTCGTCCGCCCCC
Plate 2	D1	CTGGAAAAACCAAATAGGAACAACGAAAGAGCGC
Plate 2	D2	CCCCCAGGAAGATTGTATAAGGAAA
Plate 2	D3	TTTGAAGCCTTAAATCACCCCC
Plate 2	D4	CCCCCCCCGACTTGCGGGAGGTTAATTTGCCCAATCCAAA
Plate 2	D5	CCCCAAAATAATTCGCGTCTGCTACAAAGGACAAGAGCAC
Plate 2	D6	CCCCCGAGAAGAGTCAACGACAGTATCGGCCCCC
Plate 2	D7	AACGTACCGTTTTTCTGAATA
Plate 2	D8	CCATCGCCACCCTCAGAAGAGACTCTATTTGCGAA
Plate 2	D9	CATGCTAGAAAATACATACCCCCC

Plate 2	D10	GGA	CTT	GT	A	A	C	C	G	C	A	A	C	G	C	A	C	C	C	A	C	C	G
Plate 2	D11	T	G	C	G	A	T	C	A	A	C	A	A	G	C	A	A	T	G	C	C	A	G
Plate 2	D12	G	T	G	C	A	T	A	G	G	T	G	C	C	T	G	T	A	G	C	G	A	T
Plate 2	E1	C	C	C	C	A	T	G	A	A	G	T	A	T	T	A	A	G	A	G	G	C	T
Plate 2	E2	T	T	G	G	A	A	C	A	T	T	T	C	G	A	A	A	T	A	C	C	G	C
Plate 2	E3	T	T	A	T	A	A	A	G	T	A	T	T	A	A	C	G	T	G	A	T		
Plate 2	E4	C	A	G	T	T	A	A	T	T	A	A	C	A	C	G	C	C	A	A	C	A	T
Plate 2	E5	C	C	C	C	C	G	T	G	G	G	A	C	A	A	C	G	G	C	G	G	A	T
Plate 2	E6	T	G	A	T	G	A	T	A	C	A	G	G	A	G	G	G	C	G	C	T	C	A
Plate 2	E7	T	G	A	T	G	C	C	C	G	A	T	A	G	A	T	T	A	T	A	T	A	T
Plate 2	E8	G	A	C	G	A	C	G	A	A	G	T	T	C	A	T	A	A	C	T	T	A	A
Plate 2	E9	C	C	C	C	G	G	G	A	T	A	G	T	C	A	A	C	T	T	A	C	C	C
Plate 2	E10	C	A	G	A	C	A	A	T	T	C	C	A	C	G	G	G	A	G	C	C		
Plate 2	E11	T	T	A	A	T	T	T	T	T	G	T	T	A	A	C	C	C	C				
Plate 2	E12	C	T	T	A	C	A	G	A	G	G	C	T	T	T	G	A	G	A	C	T	A	T
Plate 2	F1	G	G	A	C	A	C	C	A	C	G	T	C	A	C	C	C	G	A	C	A	A	A
Plate 2	F2	C	C	C	C	G	C	G	T	T	T	A	A	T	T	C	G	A	G	C	T	T	C
Plate 2	F3	T	T	T	T	C	A	T	C	G	G	A	T	A	A	G	A	C	A	G	C	A	G
Plate 2	F4	C	C	C	C	A	A	T	A	G	C	A	G	C	T	T	A	T	T	T	T	A	T
Plate 2	F5	A	C	C	T	G	A	A	C	A	A	A	G	T	C	A	G	C	C	C	C		
Plate 2	F6	T	C	A	T	C	G	G	T	T	G	T	A	C	C	A	A	A	T	A	C		
Plate 2	F7	T	G	C	T	G	G	A	G	G	T	T	C	A	C	C	A	G	T	T	C	A	G
Plate 2	F8	C	C	C	C	G	G	T	C	T	G	G	T	C	A	G	C	A	G	C	A	A	C
Plate 2	F9	C	C	C	C	T	A	G	A	C	T	T	A	C	A	C	G	T	G	G	T	C	C
Plate 2	F10	A	A	A	A	C	A	A	A	T	T	A	A	T	T	A	A	G	G	C	G	A	A
Plate 2	F11	C	C	C	C	A	A	A	A	A	T	C	C	C	G	T	A	A	A	T	G	T	A
Plate 2	F12	A	T	A	T	A	C	A	G	A	G	G	G	A	T	C	A	T	A	C	C	C	C
Plate 2	G1	C	C	C	C	A	T	T	T	T	G	T	A	A	A	A	T	C	G	C	T	G	A
Plate 2	G2	C	C	C	C	G	C	G	C	C	A	A	T	A	G	C	A	T	T	T	G	G	T
Plate 2	G3	G	G	T	C	A	A	T	C	A	C	C	G	C	G	A	C	G	T	T	T	C	A
Plate 2	G4	G	C	A	G	G	T	T	G	C	C	C	G	A	G	C	C	G	T	C	A	T	A
Plate 2	G5	T	A	C	G	A	C	G	A	T	C	C	A	G	C	G	C	A	T	G	C	T	C
Plate 2	G6	C	C	C	C	T	A	C	G	T	T	A	A	T	T	A	A	A	C	A	C	T	C
Plate 2	G7	G	G	C	A	A	T	C	A	T	C	A	T	A	T	A	A	G	T	A	G	A	T
Plate 2	G8	A	A	G	G	T	G	C	A	T	T	C	A	A	C	G	T	A	A	C	G	A	G
Plate 2	G9	A	A	A	G	G	T	A	A	T	A	T	A	T	A	T	A	T	C	A	T	C	A
Plate 2	G10	C	C	C	C	C	C	G	G	C	A	A	C	G	C	G	G	T	C	C	G	C	G

Plate 2	G11	GGGCCAGAAGGAGCGGAATTATCATACCT
Plate 2	G12	GTTTCGGAACCAGCGGGAGCTAAACAGGAGTAGTA
Plate 2	H1	CCCCCACAAGAATTGAGTGCTACAATTTTATCCAGAGCC
Plate 2	H2	CGAAATTAAGGGAGACGAGAAACACCAAAT
Plate 2	H3	TTGTTTTTCACGCAAGACAAAGAAGTTATATTCTT
Plate 2	H4	TGAGCCATTTGGGAATTCCTCC
Plate 2	H5	GCATTACCAAGGCAAAGAAAGGCCCCACGCATAA
Plate 2	H6	AGCACGCGTGCGGAGCGGCGCCGCGCTTAATGATT
Plate 2	H7	ATATCAGAGAGATAACCCCCC
Plate 2	H8	CAACGGAACAAACAGGGAGCCGTTTTGGCATGAGA
Plate 2	H9	CCCCTAATCATGTGCCGGTGCCCCCACTGGGCC
Plate 2	H10	AAGCACTAAATCCTGTGTCCGGTTACCTGCACGT
Plate 2	H11	GAACGTGCTTGCCAGAGAACAATAGGAACGCCATCACCCCC
Plate 2	H12	CCCCCGTGAGAGATAGACTATACCAGTCCGGCGAATACTAGATAAGAA
Plate 3	A1	TCACGAGCCAGTAACAGTCATA
Plate 3	A2	CCCCGCCATATTAGTTTAACGTCAAAAATGAACCCCC
Plate 3	A3	TACCAGAAAAGATTACGAAGGGATT
Plate 3	A4	AATTGTAAACGTTAAT
Plate 3	A5	CCCCCTGAGGCTTGCAGGGAGTTAATACACAAAA
Plate 3	A6	ATAAAGGCTAAGTTTTGTCGTCTTACAAACCAGAG
Plate 3	A7	TTGGCTTAAATGTGAGCAACCTTGCTTCTAATACC
Plate 3	A8	ATCATGGTCAGTTGGCAACGAACTGGATTACCCAG
Plate 3	A9	CTTTGAAGCAACCGAAAGAACC
Plate 3	A10	CCCCAACGTCACCAATGAAACCATCGATCAGAACCATTA
Plate 3	A11	TAAATTTGTAAGGTAATAGG
Plate 3	A12	GGATTATTTACCCGTTGTTAGCCGATTAAAGGGGC
Plate 3	B1	AACGACGCCAGCTGGCGAGCGG
Plate 3	B2	CCCCCTGGAAGTTTCATTCCATATAACAGGGGGAATATGC
Plate 3	B3	ATAAATTTTTTTTTATCCAGTTACAGCGT
Plate 3	B4	TAAAGCCAGACCCTGCCCTCAAGAGAAGGATTACAG
Plate 3	B5	CCGAGGGGGTACTTTTGCAAAGAAGTCCCCC
Plate 3	B6	GCCAACTATATGTAATGCTGACCCCC
Plate 3	B7	CCCCCATCGGCATTTTCGGTCATGGCAGGTAGGG
Plate 3	B8	GTCATAGTTAGCGTAACATTCCACACCCTCGCTTT
Plate 3	B9	AAGGGTATCATTCCAAGAACCCCC
Plate 3	B10	GCAACGTATTGATCAAACCCTCAATTCGCCATAAT
Plate 3	B11	TTTACATACGGCAGAGGCATTTTATAATCGCTGAA

Plate 3	B12	ATATATGTGCACGGGAGAAACAACAAGGATAAAAA
Plate 3	C1	ATGTTTCCATCGCGCTTTTGCGGGATCCTAAACATT
Plate 3	C2	GGCGCGTACTGTGTCCAGGTAAAGGCACTAACAAC
Plate 3	C3	AAACCGCCAGCAGCGATGCTGATTGCCGTTCCCCC
Plate 3	C4	CCCCCTGGCAGCCTCCGGAGTAACCTTTCATCAACAGCATG
Plate 3	C5	GCTCGAGGTGAATTTCTCAT
Plate 3	C6	CCATTGAGGGAATTTACCAGCGC
Plate 3	C7	TTCCTGATTATCAGATCAGATGAGATTGCTGGAGA
Plate 3	C8	CCCCCCTTTGACCCCCAGCGATTAAGGCTGGCCGGAT
Plate 3	C9	TAACGATTTTAATCACGCAAATTAATTGGCAATA
Plate 3	C10	ATACCTCAGAGCCACCACCCCCC
Plate 3	C11	CCCCGTAAAGATTCAACCATCAATACCCCC
Plate 3	C12	GGGATACATGAGAGCCAGGAACCGCATAAATCAAAA
Plate 3	D1	AGGATCCCTTTGCATCACGAGCTCGAATTCGCGAT
Plate 3	D2	TCCACCCTTCTGACCGTTTTTGC GGACCCCC
Plate 3	D3	CAAAATAGAAATCAGTAGCGACCCCCC
Plate 3	D4	CCTGAAGCATAAAGTGTCCACTACTTTGGAACAA
Plate 3	D5	TGGTTTGAACGAGCAGAC
Plate 3	D6	CCCCCGCGGTTGCGGTATTTGAGGATTTAGAAGTATCCCCC
Plate 3	D7	GATCTCACGGTCTTCTCCGTGGTGAACCCCC
Plate 3	D8	GTGAATAAGGCGAATTACTGAGATTCATAACTCG
Plate 3	D9	CAACTATCGGCGCTGGTCCACTATAAAAACCGTCT
Plate 3	D10	CAGCTTTAAACAAAAGGAATTACGAATGCAGATGA
Plate 3	D11	CAGAGCGCAGTCTCTGAACCCGTATAGCGGGGTTT
Plate 3	D12	CCCCCGGAGAATTAAGTAACTGAACCTAACCAGAACCCAAAAGA
Plate 3	E1	GGTAGCTTAAACGACCACATACTTTA
Plate 3	E2	GCGTATGGGATTTTGTCTAATAGGTGACAGGTCAT
Plate 3	E3	CCCCGTAATCTTGACAAGAACTGACCTTCATCAAGACCCCC

**Table S4.** The list of modified staples for Trident.

Name	Sequence (5' to 3')	Replace
3' biotin	ATAAAGGTGGAATAAGTTTAT-Biotin	Plate 3, F1
3' biotin	TGAGAGTCTGTAAACTA-Biotin	Plate 3, F2
3' biotin	AAAGTAAGCGAGGAAACG-Biotin	Plate 3, F3
3' biotin	GACATTCAACCGTTATTCATTA-Biotin	Plate 3, F4
5' biotin	Biotin-AGGGTAATTGAGCGCTATATCTTACCCGAACAAAG	Plate 3, F5
3' biotin	GAGAGGGTAGTCATTGCC-Biotin	Plate 3, F6

3' biotin	TTAATTCATCTCCGTGTGATAAA-Biotin	Plate 3, F7
3' biotin	CAATAATAACTCCTTATTACG-Biotin	Plate 3, F8
3' biotin	TGCAAATCCAATAATATATTTTAG-Biotin	Plate 3, F9
3' biotin	GGAAAATTGAGGAGCAAGGCCGGA-Biotin	Plate 3, F10
3' biotin	GCATGTCAACCCAAAAAC-Biotin	Plate 3, F11
3' biotin	TAAGGCGTTAAAAAAGCCTGTTT-Biotin	Plate 3, F12
3' base dye	AAATCGAACCCACAGTTTCGTAGTACCGCCACCCTAG-ATTO 542	Plate 3, G1
NP binding 3'	AATCACAGAGGACGCTCATGAAATCCTGAGTAAAATCCGTTCAAAAAAAAAA AAAAAAAAAAAAAAAAAAAA	Plate 3, H1
NP binding 3'	AGCTGCGGGTGGTTGGTGGTAATAACAAAAAAAAAAAAAAAAAAAAAAAAA A	Plate 3, H2
NP binding 3'	GAGTGTTTGTGATTTTCTTCACCTGAAAAAAAAAAAAAAAAAAAAAAAAA	Plate 3, H3
NP binding 3'	GAACCTCAAATGGCGCCAATTAAAAAAAAAAAAAAAAAAAAAAAAAA	Plate 3, H4
NP binding 3'	GAATGGTAAAAAATTGTGAAAAAAAAAAAAAAAAAAAAAAAAA GAAACAAAGTACGGTGTACAACGTAACAAAGCAGAAAAAAAAAAAAAAAAA	Plate 3, H5
NP binding 3'	AAAAAAAAAA	Plate 3, H6
NP binding 3'	TCATAATATTTAAACAGGGAACGAGAAAAAAAAAAAAAAAAAAAAAAAAA CGCCTCAGCAGCGAAAGATGCCACTCATCAGTCTTATGCAAAAAAAAAA	Plate 3, H7
NP binding 3'	AAAAAAAAAA	Plate 3, H8
NP binding 3'	GATACCGATAGTGCGGAACCTCGTTAAAAAAAAAAAAAAAAAAAAAAAAA	Plate 3, H9
NP binding 3'	CAATGATTAGTCCGAAACCCGAAAAAAAAAAAAAAAAAAAAAAAAA TCACTTGACCTACACAGCAGAAGATAAATAAAGCATTACCAGAAAAAAAAA	Plate 3, H10
NP binding 3'	AAAAAAAAAAAAAAAAAAAA GATTTTATGCTCATAGAGGACAGATGAACAACAAAAAAAAAAAAAAAAA	Plate 3, H11
NP binding 3'	AAAAA	Plate 3, H12
Hybridization to Triangle	ATGTAGGTGGTAGAGTTCACAAGAATTGAGTGCTACAATTTATCCAGAGCC	Plate 2, H1
Hybridization to Triangle	AGCAAGTCCATTACCAAGGATTGGTGAATTATCACCGTCACCGACTGAAATATT GAC	Plate 1, D2
Hybridization to Triangle	GCGCGGTGCAGTCTCGTCCTTAAAAAATCCCGTAAAATGTGTACCATTGCAG CG	Plate 2, F11
Hybridization to Triangle	CTTGCCAGCATTGTAATAGGTTAGGGCGATCGGTAAGGGGGATGTG	Plate 1, A10
Hybridization to Triangle	CACTAAAAGAGTGATGATAATTATGAAAGTATTAAGAGGCTCCGCCACGCAAG CCAAA	Plate 2, E1
Hybridization to Triangle	TCATGAGTGCCGAGCTAAGATTGTCACGCTGCGCGTAACCAAATCCGCCGGGC	Plate 2, C4
Capture Strands	TGTGCCTGTTTATCAAGTTTAAAGCCTCAGAGCATAAGCAAATGTTTAT	Plate 3, G5
Capture Strands	ATTACAACATGTTTCAGCTAATGTTTGTGCCTGTTTATCAAG	Plate 3, G3
Capture Strands	CAGAACGCGCCTAAGCAATATTTGTGCCTGTTTATCAAG	Plate 3, G2
Capture Strands	TACCATATCAAAGCAAAGAATTTGTGCCTGTTTATCAAG	Plate 3, G4

Capture Strands	CGTATTCTGAATAATGGAAGGGTTAGAACCTTTTGTGCCTGTTTATCAAG	Plate 3, G6
Capture Strands	TGTGCCTGTTTATCAAGTTTGATGATGAAACAAACATACCTGAATT	Plate 3, G7
Capture Strands	TGTGCCTGTTTATCAAGTTTACAATATTACCGCGCCTGCAA	Plate 3, G8
Capture Strands	CAGTGCCACGCTGAGATTAACACCCAGCCATTGTTTTGTGCCTGTTTATCAAG	Plate 3, G9
Capture Strands	TGTGCCTGTTTATCAAGTTTTTGGCCAGATATATTCGGTCCG	Plate 3, G10
Capture Strands	AACGCGAGAGGATAGTAAATTTTGTGCCTGTTTATCAAG	Plate 3, G11
PAINT docking	CATACCGGGCAAGTGTAGCGTTTTAACATTCC	Plate 1, E7
PAINT docking	AGTAGCCAGCAAGCTGATCACTGCCGGGGTGCTATTAACATTCC	Plate 2, A6
PAINT docking	CAACGTCAAGTGAGCTAACTCTTTTTTAACATTCC	Plate 2, B5
PAINT docking	CTAGGGCGCTGGGTTTCTGGGCCGTTTTACGGTTTTTAACATTCC	Plate 1, B8
PAINT docking	CGTCGGGGTCCGCCGCTGGAAGAAAGCGAAACTGTTTAACATTCC	Plate 1, D1
PAINT docking	GAGAGTTGCAGCAAGCCACCGCCTGGCCCTGATTTTTTAACATTCC	Plate 2, A3

**Table S5.** The list of sequence for staples involved in the sandwich assay.

Name	Sequence (5' to 3' end)
Target	TTCGAATACCACCGTCGAGCCAGAACTGTCTACATTGCCCGAAATGTCCTCATTACCATAA TCGAAAGCATGTAGCATCTTGCTCATACTGCCTCGCCAATTTGGCGGGCAAATTCTTGATA AACAGGCACAACCTGAATATTTTCATCGC
Imager	GCGATGAAATATTCAGT-Alexa Fluor 647
Blocker	ACTTGATAAA
Displacer	TGTGCCTGTTTATCAAGAATTTGCC
Sacrificial DNA	GTGATGTAGGTGGTA

## References

1. Close, C. *et al.* Maximizing the Accessibility in DNA Origami Nanoantenna Plasmonic Hotspots. *Adv Mater Interfaces* **9**, 2200255 (2022).
2. Douglas, S. M. *et al.* Rapid prototyping of 3D DNA-origami shapes with caDNAno. *Nucleic Acids Res* **37**, 5001–5006 (2009).
3. Shetty, R. M., Brady, S. R., Rothemund, P. W. K., Hariadi, R. F. & Gopinath, A. Bench-Top Fabrication of Single-Molecule Nanoarrays by DNA Origami Placement. *ACS Nano* **15**, 11441–11450 (2021).
4. Liu, B. & Liu, J. Freezing Directed Construction of Bio/Nano Interfaces: Reagentless Conjugation, Denser Spherical Nucleic Acids, and Better Nanoflares. *J Am Chem Soc* **139**, 9471–9474 (2017).
5. Jing, X. *et al.* Solidifying framework nucleic acids with silica. *Nat Protoc* **14**, 2416–2436 (2019).



6. Wassermann, L. M., Scheckenbach, M., Baptist, A. V., Glembockyte, V. & Heuer-Jungemann, A. Full Site-Specific Addressability in DNA Origami-Templated Silica Nanostructures. *Advanced Materials* **35**, (2023).
7. Nečas, D. & Klapetek, P. Gwyddion: an open-source software for SPM data analysis. *Open Physics* **10**, 181–188 (2012).
8. Schnitzbauer, J., Strauss, M. T., Schlichthaerle, T., Schueder, F. & Jungmann, R. Super-resolution microscopy with DNA-PAINT. *Nat Protoc* **12**, 1198–1228 (2017).
9. Trofymchuk, K. *et al.* Addressable nanoantennas with cleared hotspots for single-molecule detection on a portable smartphone microscope. *Nat Commun* **12**, 950 (2021).

## 7.2. SUPPORTING INFORMATION FOR P2

Supplementary information

by

Renukka Yaadav, Kateryna Trofymchuk, Feng Gong, Xinghu Ji, Florian Steiner, Philip  
Tinnefeld, and Zhike He

published in

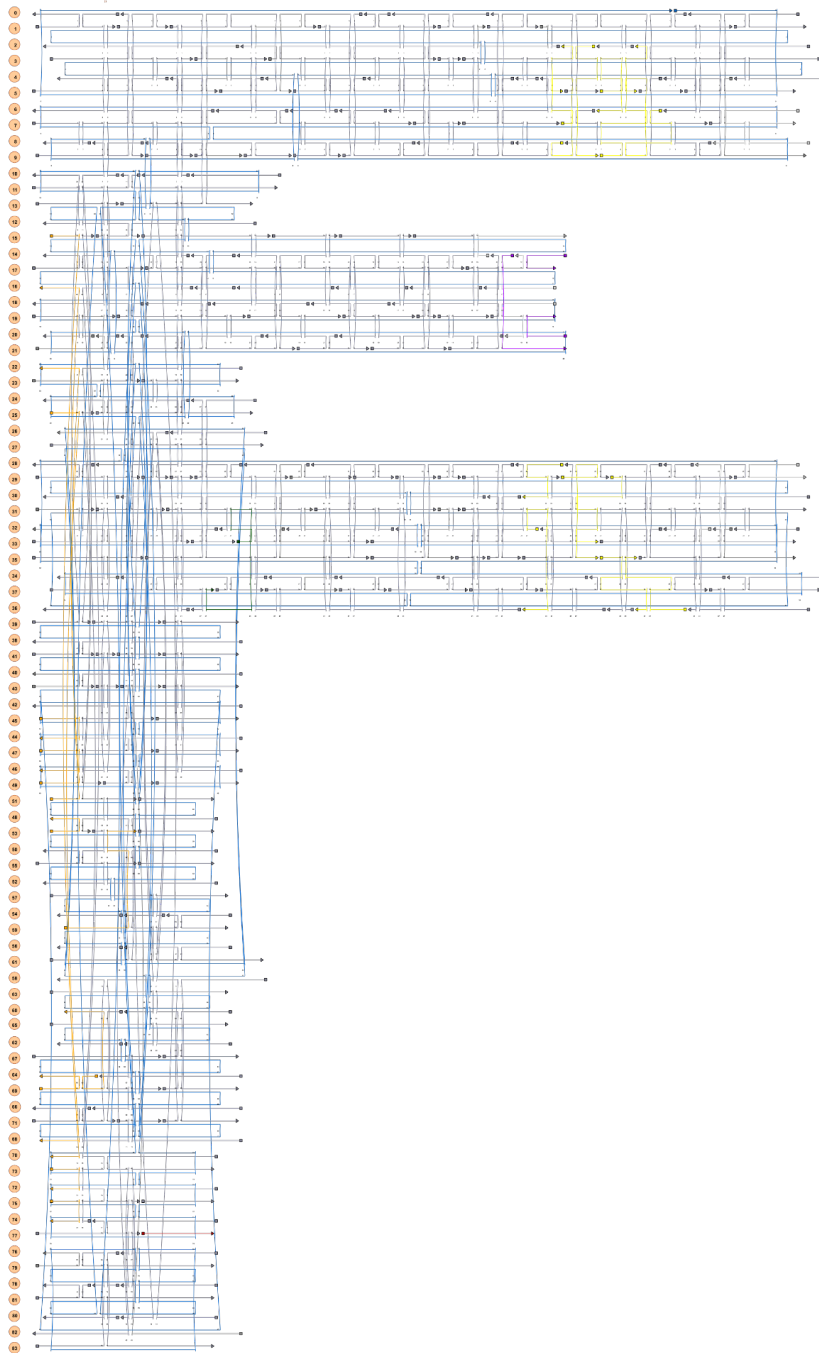
*The Journal of Physical Chemistry C* 2024

as

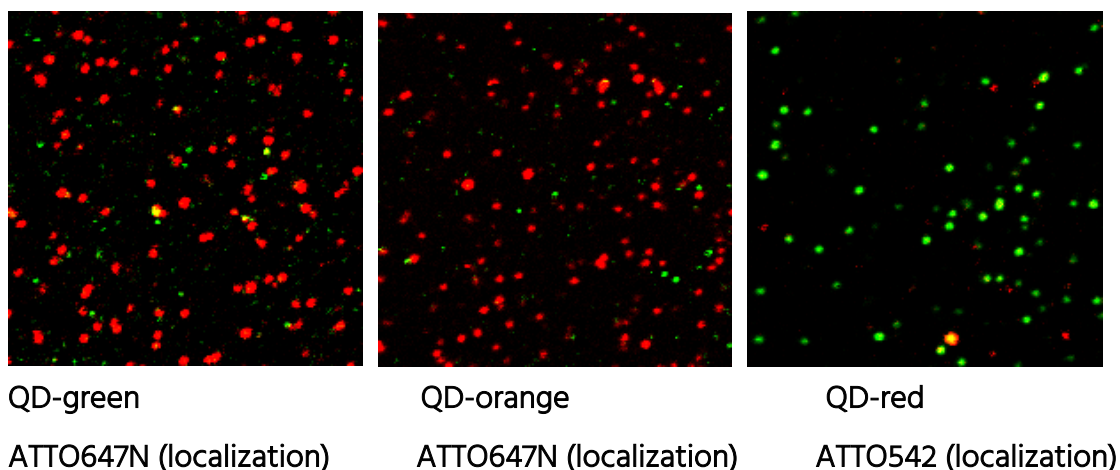
Renukka Yaadav, Kateryna Trofymchuk, Feng Gong, Xinghu Ji, Florian Steiner, Philip  
Tinnefeld, and Zhike He. *The Journal of Physical Chemistry C* 2024 128 (22), 9154-9160.

DOI: 10.1021/acs.jpcc.4c01797

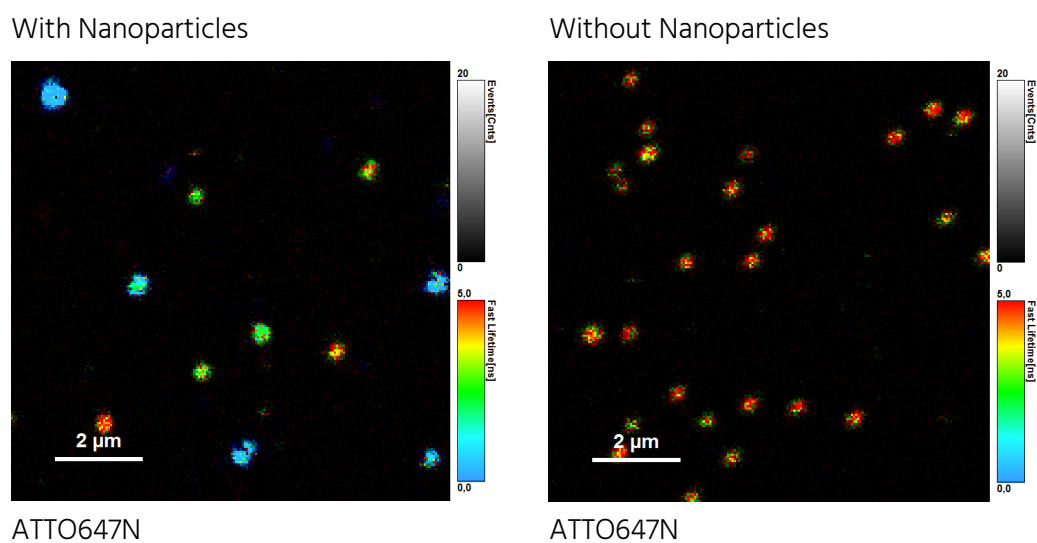
Copyright © 2024, American Chemical Society



**Figure S1.** Staple strand layout of DNA origami Trident in CaDNAno. Yellow: strands for nanoparticle binding, Orange: strands labelled with Biotin, purple: strands for QD capture, Dark green: strand for localization dye-ATTO542 and Red: strand for localization dye-ATTO647N.



**Figure S2.** Representative fluorescence confocal microscopy dual color scans of the DNA origami nanostructure with QD-green on the left, QD-orange in the middle, and QD-red on the right respectively. Due to blinking of the QDs, we first scanned the sample to localize the DNA origami (red spots from ATTO647N for QD-green and QD-orange and green spots from ATTO542 for QD-red) at  $1\mu\text{W}$  excitation for ATTO647N of 640 nm laser or  $1\mu\text{W}$  excitation for ATTO 542 of 532 nm laser with 1 ms integration time per line. Next, we collected time traces for each red or each green spot to record the blinking from the incorporated QDs with 10ms integration time.



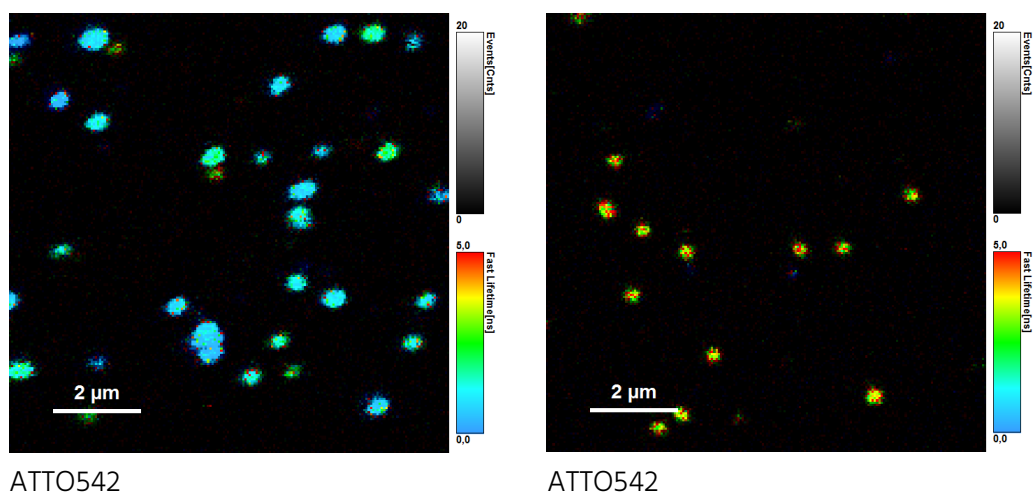


**Figure S3.** Fluorescence Lifetime Imaging Microscopy (FLIM) scans of the localization dye, exhibiting shortened fluorescence lifetime confirmed the successful association of the AgNPs.

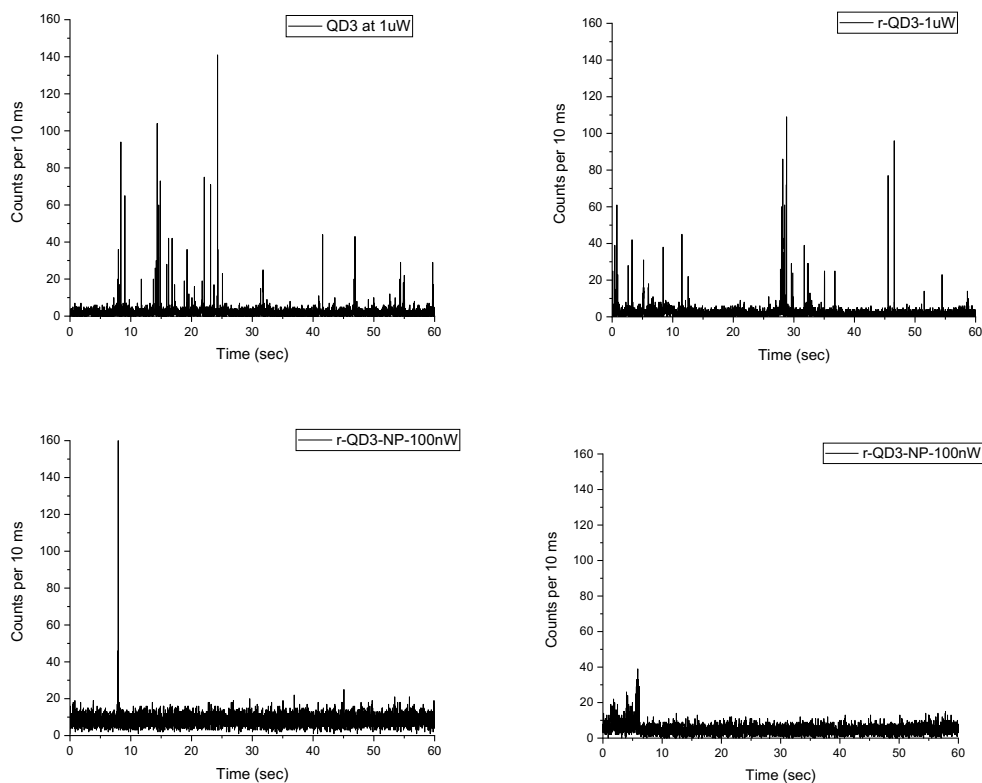


**Figure S4.** Exemplary fluorescent transients in the red channel of the DNA origami containing QD-red in the hotspot region at  $1\mu\text{W}$  of 640 nm laser excitation in the upper panel and at 100nW in the lower panel, showing the characteristic blinking behavior of QDs without (upper panel) and with (lower panel) nanoparticles.

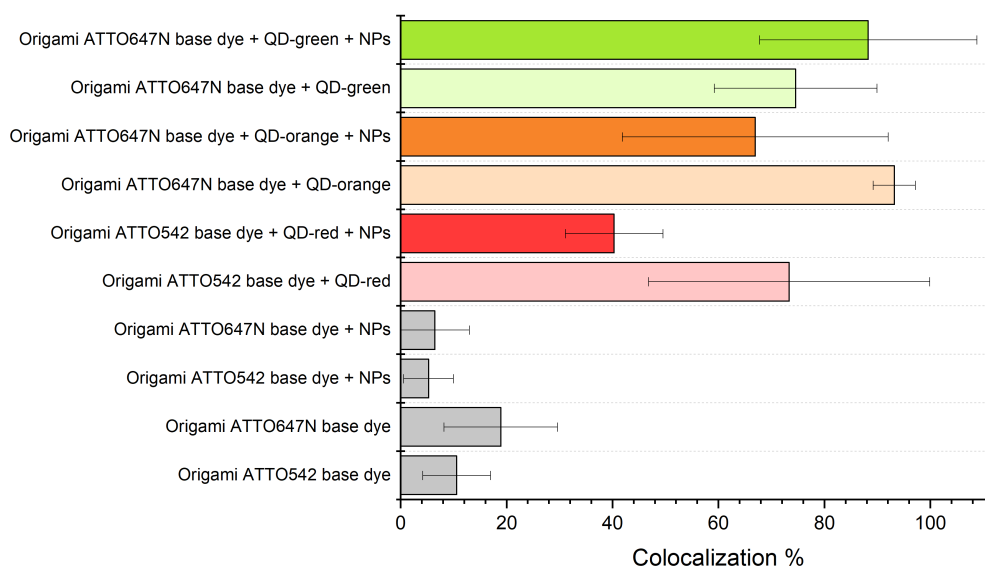


**Figure S5.** Colocalization % plot comparing DNA origami nanostructures with QD incorporation and without, both in the presence of bound nanoparticles and in their absence. Due to the blinking behavior of QDs, we first localized the origami structures with the incorporated base dye and then recorded 60 sec fluorescence transients at each localized spot. In samples with origami nanostructures without the incorporation of QDs showed significantly lower occurrence of transients (shown in grey) compared to those with QDs (color-coded according to the QD used with lighter shades of the color representing absence of NPs and the darker shade represents presence of NPs). The samples without NPs were excited at 1uW and those without NPs were excited at the laser power of 100nW.

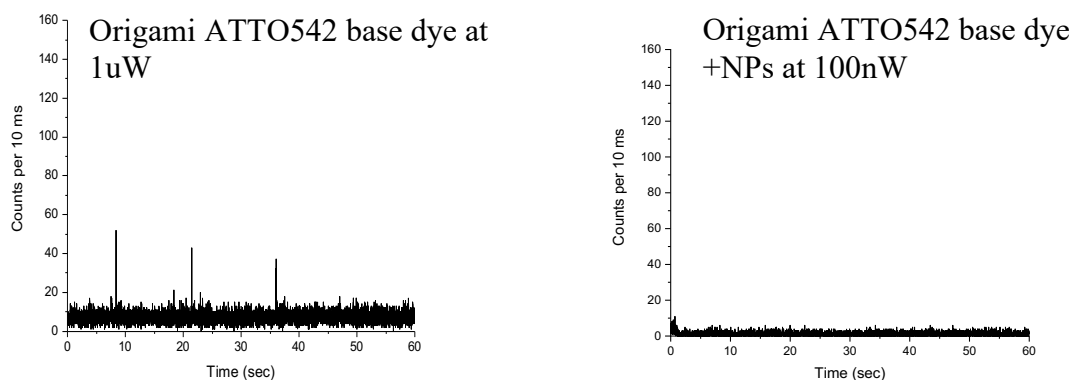


**Figure S6.** Representative fluorescent transients in the red channel in the control measurement of DNA origami labeled with ATTO542 but containing no QD without (left) and with (right)

nanoparticles. The position of DNA origami was determined based on the localization dye, afterward 60 sec fluorescent transients were recorded from the defined location while using a laser for QDs excitation. 6-11 % of the reference sample, **1 $\mu$ W of 640 nm** laser (no NPs, left image) transients demonstrated blinking behavior but of lower intensity, than samples containing QDs. For samples containing NPs (right image) the value of possible false possible localization was at the level 4-6 % at **100 nW excitation power at 640 nm**.

**Table S1:** QD-DNA specification

QD name	Maximum emission wavelength (nm)	Functionalized sequence for QD capture (Indirect labeling)
QD_green	546	TGTCTACATTGCCCGAAAAAAG*G*G*G*G*G*G*G*G*G*G*A
QD_orange	610	(*Indicates the phosphorothioate linkage)
QD_red	657	

**Table S2.** Staple strands used for folding DNA origami Trident. Values in the first and the second columns refer to the helix number in CaDNAo design (height in bp along the axis of the helix in paranthesis). Colored sequences represent sequences that were replaced to add a modification.

Start	End	Sequence
32[192]	28[188]	AACGCGAGAGGATAGTAAA
6[217]	8[193]	CAGTGCCACGCTGAGATTAACACCCAGCCATTG
28[217]	29[219]	TTTGCCAGATATATTCGGTCCG
18[148]	20[134]	AAGCCTCAGAGCATAAGCAAAATGTTTAT
14[129]	15[151]	CGTATTCTGAATAATGGAAGGGTTAGAACC
8[220]	7[216]	ACAATATTACCGCGCCTGCAA
16[148]	14[137]	GATGATGAAACAAACATACCTGAATT
21[1]	20[18]	TGATATTCAACCGTTCCAA
31[115]	35[119]	TTCATACATAAGCTTGAGA
34[24]	28[18]	CCTATAAATCCAGGTTGAAGCCCCCAATAGCGTCA
29[73]	31[79]	AAAACAGGTCTCCAGAGCCACCACCCACCCCTTAC
1[144]	1[128]	CAAAATCGGCCAACGCGCGGGGTGGAA
2[58]	9[59]	CGCCTGTGCAGGTAATGGCATCAGCGGTGGTGCCA
23[0]	26[7]	CAGTATGTTAGCAAACGAAAGCGCATTAGAC
31[1]	32[0]	CTCATTTCAGACGATTGGC
32[198]	35[216]	CGAGTTGGGAAGAAAAATC
32[71]	37[86]	CCTCCAGTAAGCGTCTCAGTGCAGGCGGATAA
79[1]	76[3]	ATTTCTGCTATCGACATA
43[0]	40[0]	AGGGCGATCGGTAAGGGGGATGTG

45[35]	45[58]	TCATAGGTCTGAGAGACTA
82[59]	43[36]	CCGGAAACCAGGCAAAGCGCCATTCGTAAGCTTTC
4[198]	9[219]	CACCTTGCTGGTAATATCCAGA
3[67]	5[73]	CTTGTGTCACCAGTTGAGGATCCCAAGCCGGCTTT
20[17]	53[16]	ATCAAAGGGTGATTAAGACGGAATAGGAAACCAGA
30[24]	19[23]	CAACGGAACAAACAGGGAGCCGTTTTGGCATGAGA
7[192]	1[198]	AGTAGCCAGCAAGCTGATCACTGCCGGGGTGCCTA
9[32]	10[31]	GCCAAACGGCATTAAAAAATCCTTCCGTAATGGGA
1[24]	4[39]	AGCACGCGTGCGGAGCGGCGCCGCGCTTAATGATT
19[24]	10[25]	AAGGAAATGCAAAATTCCTCATAATACGTACAGAG
35[129]	29[121]	TTCATCAACTAGGCATAGTCCCCCTCAAATGCTTG
36[44]	29[45]	AACGTACCGTTTTTCTGAATA
29[91]	33[95]	GAGCCTTGAATGACCCTCC
33[161]	36[163]	TACCAGAAAAGATTACGAAGGGATT
43[18]	42[0]	GCCAACTATATGTAAATGCTGA
37[87]	29[90]	GTGCATAGGTGCCTGTAGCGATCTACCAAAG
34[86]	28[79]	GGGATACATGAGAGCCAGGAACCCGATAAATCAAAA
37[66]	29[72]	TGCTGGAGGTTTACCAGTTCAGAAAAATCTCCA
6[100]	9[87]	AAAGGAATTGTGGCTATGTAATAAAAGGGACTGAG
14[44]	14[58]	GGGCCAGAAGGAGCGGAATTATCATACT
18[31]	23[30]	TTTTCCAGCTATTTTTCAAGCAAATCAGAACTTA
54[56]	59[55]	CGCTAACGAAAATAAACA
15[108]	17[122]	TGATTGTTGGATTATACAAACAGATTAT
43[37]	45[34]	CGGCACCGGCTTAGGTTGGCGCAAAA
21[118]	19[129]	AGACGACGGATAAGTAAGGCAAAGAA
4[143]	8[137]	GCAACGTATTGATCAAACCCTCAATTCGCCATAAT
41[24]	43[17]	AACGACGCCAGCTGGCGAGCGG
53[17]	52[3]	TAGCGAAGCCCATGAAATAGCCCAATAATAAGAG
44[59]	41[58]	GAGAAGAGTCAACGACAGTATCGG
16[57]	18[51]	ATATATGTGCACGGGAGAAACAACAAGGATAAAAA
80[52]	15[30]	TGGCAGCCTCCGGAGTAACCTTTCATCAACAGCATG
72[52]	78[25]	TCAGCTCATTTTTAACTCGATGAACTACCCCGCAG
3[122]	8[109]	ATCATGGTCAGTTGGCAACGAACTGGATTACCAG
32[217]	31[219]	TACGTTAATTAACACTCAT
30[138]	35[138]	GGTAGCTTAAACGACCACATACTTTA
22[59]	16[46]	GCGCCCAATAGCATTGGGTTTAGAACAACGCTAGT
39[17]	41[23]	AAGCATAACCGATCTGACCTAAATTTAGAAAACGGT
6[159]	8[151]	CTGAACGAACCACTTTTGACGCT
36[138]	35[128]	CGAAATTAAGGGAGACGAGAAACACCAAAT
28[187]	32[179]	ATGTTTCCATCGCGCTTTTGGCGGATCCTAAAAACATT
8[192]	0[186]	CAACTATCGGCGCTGGTTCCACTATAAAACCGTCT
68[59]	71[36]	TAGATTTAGTTTGACCATTAGATAACATTTGATT
41[18]	43[24]	TTGTTTTTACGCAAGACAAAGAAGTTATATCTT
81[1]	78[3]	GGGATAGCTCAAACCTAA
12[63]	9[45]	ACAAAGAAACCACCAGATTATCATTAATGCAC



1[129]	4[144]	ATTGTTATCCGAGGTGCCAATCAAAGAATAGTCG
9[74]	6[87]	CTATAATCAGATTCTGGACAATATTTTTGAAAGGA
35[0]	34[7]	CTTGATATTCACAAACAAATTATTCTGAAAC
20[31]	26[39]	TTGGAACATTTTCGCAAATTACCGCACATCGTAAGA
37[192]	29[198]	GCATTACCAAGGCAAAAGAAAGGCCCCACGCATAA
21[96]	19[108]	AAAAGGTAAATAATATCATCCAATAAA
67[0]	64[19]	GGTGAATTATCACCGTCACCGACTGAAATATTGAC
0[217]	1[219]	CAACGTCAAGTGAGCTAACTC
26[66]	33[57]	AATAGCAGCCTTATTTTTATAGTCATCATAATCA
2[149]	5[160]	ATGTTCCACACAACATAAAAATCAATAGGGTT
71[24]	25[17]	TCATGCAAAGACACCACGGCAA
5[0]	4[7]	GTCACGCTGCGCGTAACCAAATCCGCCGGGC
6[51]	3[66]	TAAACTGAAAGCGTAAGAATACGTTTTAGGAGTTT
60[25]	66[17]	CCATTGAGGGAATTTACCAGCGC
34[196]	32[193]	ATTCATTATCAGGACACT
36[220]	34[197]	CTTTGACCCCCAGCGATTAAGGCTGGCCGGAT
4[38]	8[32]	GCAGGTTGCCCGAGCCGTCAATAGACGTATTAGTC
13[25]	73[51]	GAACGTGCTTGCCAGAGAACAATAGGAACGCCATCA
74[52]	76[25]	ATTTTGTTAAAATTCGCTGATAATCACAAATATGGG
10[24]	1[23]	CCGCGACAACCTTAATACATGAGCCGATGCGGCGCC
16[127]	21[117]	AAAACAAAATTAATTAAGGCGAAAATAAAGCTGTCC
76[24]	83[51]	CGGTAAAGCCGCACAGGCGGCTTTAGTGA
20[133]	14[130]	CAACAATAACAATAAGCA
70[52]	80[25]	AAAATAATTCGCGTCTGCTACAAAGGACAAGAGCAC
4[65]	2[59]	GAGATGGTTGCGAACGTGGCGAGACTCCTCATGCG
55[30]	55[51]	TTTGAAGCCTTAAATCA
17[0]	14[3]	AGTATCATATGCTTAATGCCG
30[128]	28[137]	GCTCGAGGTGAATTTTCAT
23[31]	71[23]	TTTTCTCATCGGATTAAGACAGCAGCACCGTAAAT
28[17]	30[3]	GACTATAGAAATTTCAACAGTTTCAGC
1[199]	5[216]	ATGAAGGGCGATAAAGAACGTGGACTC
29[115]	31[121]	CAGCTTTAAACAAAAGGAATTACGAATGCAGATGA
10[70]	10[45]	CGTGGGAACAAACGGCGGAT
47[35]	47[58]	TAGCTTAGATTAAGACGCT
3[115]	7[121]	TAACGATTTAATCACGCAAATTAATTTGGCAATA
63[5]	60[26]	AACGTCACCAATGAAACCATCGATCAGAACCATTA
1[81]	4[66]	TACGACGATCCAGCGCATGCTCGTTTTTACGGCTG
13[1]	49[19]	GTGAGAGATAGACTATACCAGTCCGGCGAATACTAGATAAGAA
38[59]	39[36]	CATCGTAACCGTGATCTGCCAGTAGGGAGGTCAC
8[108]	0[102]	TCACTCTGTCCGACAGGAGAATCAGCTAAAGGGAG
69[37]	63[55]	AACTAAGGATTAGACCGGAAGCAAACCTC
17[32]	13[24]	AGTGAGAATCGCCATGCTTGAGAGCATGTTTAACG
61[5]	51[29]	GGGAGAATTAAGTAACTAACCAGAACCCAAAAGA
35[120]	37[123]	TGGTTTGAACGAGCAGAC
4[224]	3[223]	GAGAGTTGCAGCAAGCCACCGCCTGGCCCTGA

46[59]	39[58]	TTCCCTTAGAATTGTAGATGGGCG
35[139]	37[143]	ATCATTGTTTGGCCCTACCG
18[50]	14[45]	TTGCGCGAGGCTGTCTTTCCTTCTAATTTAAGTA
33[0]	31[17]	CATCGGCATTTTCGGTCATGGCAGGTAGGG
16[106]	21[95]	AACAATTTCAATTTGAACCAAGTTTTTCAGGTCCGAC
8[136]	3[121]	GGATTATTTACCCGTTGTTAGCCGATTAAAGGGGC
34[66]	28[60]	AGTGTTTACCGGCCACCAACCGAATTACCCTGAC
1[1]	0[0]	CATACCGGGGCAAGTGTAGCG
2[170]	5[184]	CCTGAAGCATAAAGTGTCCACTACTTTGGAACAA
37[124]	30[129]	GGTCAATCACCGCGACGTTTCCAAACG
15[87]	18[102]	GGCAATTCATCAATATAAGTAGATTACAAAATTGA
32[178]	37[191]	ATTAGCTCATTATACCAGCCCAAATCAGACCAGGC
43[25]	82[0]	CGCCCATTAGGCTGCGCAACTGTTGGGA
71[0]	66[0]	TTTGTACAATCAGACAAAAGGGC
60[56]	69[58]	CAACAGGTCAAGTACGGTGTC
77[1]	74[17]	AGGAAGATTGTATAAGGAAA
29[103]	35[95]	GTCATAGTTAGCGTAACATTCCACACCCTCGCTTT
52[52]	55[29]	AGATTAGTTGCTATTTTGCACCATAAGCAATAGC
19[130]	16[128]	TTAAGCTAAATTTCAATTCAAG
66[59]	69[36]	TGGAAGTTTCATTCCATATAACAGGGGGAATATGC
16[85]	21[74]	TTTTTTAATGGAAACATTGCCTATATACAGTAAT
1[115]	0[130]	GTTTCGGAACCAGCGGGAGCTAAACAGGAGTAGTA
27[5]	20[25]	AGAATCAAGTTTGCCTTAAAGAACAAATAAAAGAGA
53[30]	53[51]	GGCGTTTTAGCGAACCT
21[75]	19[87]	AAGAGAATACGAGCATTACTAATAGTA
76[52]	77[30]	TGAAGGGTAAAGTTAAATTTTA
9[46]	1[38]	CGTCGGGGTCCGCCGCTGGAAGAAAGCGAAACTGT
54[25]	54[7]	ATATCAGAGAGATAACC
18[101]	20[87]	CCCTGTAATACGCATTAACCCATCCTAAT
57[5]	54[26]	CACAAGAATTGAGTGCTACAATTTTATCCAGAGCC
66[16]	58[7]	CAAAATAGAAATCAGTAGCGAC
28[178]	36[186]	CTGGAAAAACCAAATAGGAACAACGAAAGAGCGC
30[220]	32[199]	CTGAGGCTTGCAAGGAGTTAATACACAAAA
29[1]	28[0]	GGAGTGAGAGTAGCGGTTTT
37[52]	33[44]	GATTAAACAGTTAATGCCATGGAAGCCGCCGCAT
20[65]	15[67]	TCACGAGCCAGTAACAGTCATA
6[72]	9[73]	ATCGGCACAGCCAACAGAGATAGACACGCAACCAG
64[59]	67[36]	AATGCTGTAGCTCAACATGTTTTATATGGCTTAGA
7[0]	8[3]	TAGACTTTACAACGTGGTGCT
56[56]	61[65]	GCCATATTAGTTAACGTCAAAAATGAA
31[38]	34[25]	CCATCGCCACCCTCAGAAGAGACTCTATTTTCGGAA
20[24]	20[32]	CAGTTAATTTAACAACGCCAACATGAATAACCTGT
33[45]	24[45]	CTTTGAAGCAACCGAAAGAACC
58[66]	71[58]	GCGTTTTAATTCGAGCTTCTCTGCGAACGAG
37[101]	34[116]	GTTGATCGGAACGAGGCGTAG

8[16]	39[16]	CAGACAATTCCACGGGAGCC
7[108]	1[114]	TGCATCAACAAGCAAATGCCAGCGGGTCATAGCT
19[115]	15[107]	AGGCCCTGAACAAGAAAAAGTAATTAATTGCTCC
18[78]	20[66]	AGCCTTTATTCAATTCGTAGAAACCAA
26[38]	54[38]	ATAAATTTTTTTTTATCCAGTTACAGCGT
37[5]	30[25]	ATGAAAGTATTAAGAGGCTCCGCCACGCAAGCCAAA
37[144]	29[149]	AACTGACCAACCTGATATACGTAACAGCATCCTT
5[185]	6[179]	GAGTTGCCCCAGGGCAACGCAAATGAAA
19[61]	16[58]	AAGGTGGCATTCAACGTAACGGAGTACATAAATCA
65[5]	62[26]	AGAGCCAGCAAATCACCAGTAGCGAATTTTTGCG
16[45]	11[69]	GAATGAGTAACAACCCGTCGGATTCTC
31[18]	36[3]	ATACCTCAGAGCCACCACC
17[123]	19[114]	TCATCGGTTGTACCAAATAC
78[24]	79[51]	AAACCGCCAGCAGCGATGCTGATTGCCGTT
10[44]	3[45]	TGATGCCCGATAGATTATGCG
9[88]	1[80]	GCCTCCTGAGTATAACGGAGCTTGACGGGGACGGG
9[60]	13[62]	TCCACCCTTCTGACCGTTTTTGCGGA
0[129]	3[114]	AAGCACTAAATCCTGTGTCCGGGTTACCTGCACGT
54[37]	57[55]	CTTTCCTGAATCTTACCAA
55[1]	50[3]	CAAGAAACATTTTTAAGA
15[18]	18[0]	TTTTGATAAAGTTATACATGCCTGAGTAATGTGTAG
31[80]	34[67]	AACGTATCACCGTACTCACAGTACCCTTGAGTAAC
29[39]	35[31]	GCGTATGGGATTTTGCTCAATAGGTGACAGGTCAT
33[96]	29[102]	CTCAGAGCCGCCACCCAGTTCAGAAAACGATAATT
49[20]	41[17]	TAAACACCGTTTGAATTCAGAGGTTTTCCAGTCATAAG
19[0]	20[3]	GTAAAGATTCAACCATCAATA
71[37]	29[38]	CCAATAAAGCGAAGGAAGCAGCGGATAATT
48[52]	29[30]	GTATTCTAAGAACGCGATTAGAAACGCATAAACTA
7[122]	4[137]	GCCCTAAAACACAATATCGAAGAGGCGGTTTGAAT
34[115]	37[100]	TAAATTTGTAAGTGAATAGG
31[122]	31[114]	GGAAGTCTCCATGTTACTTAGCATCCAAGACTTT
4[178]	7[191]	GGCGAGAAGAACTCAAACAGGAAAATGAGGCGGTC
24[44]	25[62]	AAGGGTATCATTCCAAGAA
14[57]	19[60]	TTACATACGGCAGAGGCATTTTATAATCGCTGAA
35[172]	29[163]	CTGCAGGTAGCGACGATATAGCGTCCAATACTTG
20[86]	15[86]	TTATAAAGTATTAACGTGAT
83[1]	78[17]	AAAAAATCCCGTAAAATGTGTACCATTGTCAGCG
5[74]	6[73]	GACGAGCACGAAGTGTTCATAAACTTATCTAAAAT
3[46]	5[52]	GCTCTGTGTGCGGTCGGTGAGCAAGGAAGACAG
78[52]	75[30]	CCGGCAAACGCGGTCGGCGGTA
2[220]	4[199]	ACATTAATTGCGTTGCGCTTGCCTTGCTG
39[0]	10[0]	ACGACGGCCAGTACGGATAACCTC
24[63]	27[65]	CGGGTATTAACCTCAAATATC
9[1]	8[17]	GGTCTGGTCAGCAGCAACGT
0[93]	6[101]	TTATGCTTTCCTGTTAACGGTACTGTGTTGCTTG

19[88]	16[86]	GTATTTGCGTTGAATATTACC
8[31]	0[25]	GGACTTGTAGAACC GAACGCACTCCCACACCGCG
3[5]	6[0]	GCGGTTGCGGTATTTGAGGATTTAGAAGTAT
34[157]	28[151]	GTGAATAAGGCGAATTACTGAGATTTCATAACTCG
0[185]	4[179]	ATCAAAAGCCTCGCTTTCCAGTCGGGTGAGACGCA
34[224]	37[223]	GTAATCTTGACAAGAAGTACCTTCATCAAGA
74[16]	15[17]	AGCTCATATGGGTAATCGGAGCAACTATCAGGCTA
6[86]	0[94]	AGGATCCCTTGCATCACGAGCTCGAATTCGCGAT
29[31]	31[37]	AAGGTGCATCATTATTAGCGTTTGCCAGCATAAC
40[59]	41[36]	CCTCAGGAAGATCGCACTCCAGCCTTCCTTGAGGG
41[37]	47[34]	GACGATAGTGAATTTATCGAAAGCGA
0[101]	4[95]	CCCCTAATCATGTGCCGGTGCCCCACACTGGGCC
29[46]	23[58]	ATATACAGAGGGAATCATTACC
15[68]	18[79]	TTCCTGATTATCAGATCAGATGAGATTGCTGGAGA
62[25]	62[7]	TGAGCCATTTGGAATT
67[37]	65[55]	GCTTAAGAGGTCGTACCTTTAATTGCTC
5[172]	2[160]	CAGGTGAACCATCACCCCGAGCCGGTCGTGCC
15[31]	18[32]	CCTTCCTGTAGCTTAATTATAAAGCCCTCATATA
25[18]	24[3]	CATGCTAGAAAATACATAC
32[52]	37[65]	CAGAGCGCAGTCTCTGAACCCGTATAGCGGGTTT
36[170]	28[179]	GGACACCAACGTCACCCGACAATGACAACAAAGA
28[59]	32[53]	TATTCACGTTGCGTTAGTAAATGAAAACACTGCAC
42[59]	43[58]	CCTTTTTAACCTCCGCTTCTGGTG
28[78]	32[72]	ATAAAGGCTAAGTTTTGTCGTCTTACAAACCAGAG
49[35]	49[58]	TCGTCGCTATTAATTAATT
35[96]	32[103]	TGATGATACAGGAGGGCGCCTCAGA
35[32]	36[45]	TAAAGCCAGACCCTGCCCTCAAGAGAAGGATTCAG
50[52]	56[26]	CCCGACTTGCGGGAGGTTAATTTGCCCAATCCAAA
0[24]	2[3]	CTAGGGCGCTGGGTTTCTGGGCCGTTTTACCGT
51[30]	51[51]	TATAGAAGGCTTATCCG
29[199]	33[216]	CCGAGGGGGTACTTTTGCAAAGAAGT
39[37]	49[34]	GTTGGCCTTGAAAACATTGGGGTAAA
4[94]	7[107]	AGAAACCGAGTAAAAGAGACGACCATAGTCTTTAA
41[0]	38[0]	CTGCAAGGCGATCGACGTTGTAAA
28[136]	32[144]	TGAATAAGAGCAACACTATAG
1[39]	9[31]	TCTGTGCTGCGGCCAGAGGTCCTGCGCTTGAAT
62[56]	67[58]	CTTTTGATAATTGCTGAATAT
19[109]	16[107]	TCAAACATTACGCGCAGCATT
80[24]	81[51]	ATCCAAAAAGAGATTTTTTCGTCTCGTCGC
56[25]	56[7]	ACCCTGAACAAAGTCAG
11[0]	12[3]	ACCGGAAACAATCCGGAATTT
32[102]	34[87]	ACCGCCAGACAGAAGTATAGCCCGACGTCGAGAAGTTTTAACG
36[162]	34[158]	GTATCATCGCTTTGAATCA
5[151]	1[143]	AGAGTTTTTTGGGGTCGCTCA
10[30]	17[31]	TTGGCTTAAATGTGAGCAACCTTGCTTCTAATACC

75[31]	75[51]	TTAAATTTTTGTAAA
29[122]	29[114]	CTTTACAGAGGCTTTGAGGACTACTATCGGTTTAT
5[53]	6[52]	GGCGCGTACTGTGTCCAGGTAAAGGCACTAACAAC
78[16]	80[3]	GATCTCACGGTCTTCTCCGTGGTGAA
4[136]	7[149]	CCCTAGCAATACTTCTTTCGTCTGATAAAAAATACC
33[58]	37[51]	AAATCGAACCACAGTTTCGTAGTACCGCCACCCTAG
36[185]	35[171]	GAAACAAAGTACGGTGTACAACGTAACAAAGCAGAA
29[164]	35[160]	CGCCTCAGCAGCGAAAGATGCCACTCATCAGTCTTATGC
35[161]	36[171]	GATTTTATGCTCATAGAGGACAGATGAACAAC
9[161]	2[171]	TCACTTGACCTACACAGCAGAAGATAAATAAAGCATTACCAGAAA
32[143]	36[139]	GAATGGTAAAAAATTGTGT
28[150]	30[139]	TCATAAATATTTAAACAGGGAACGAG
2[159]	9[160]	AGCTGCGGGTGGTGGTGGTAATAACA
29[150]	33[160]	GATACCGATAGTGCGGAACCTCGTT
6[178]	5[171]	AATCACAGAGGACGCTCATGGAAATCTGAGTAAAATCCGTT
8[150]	5[150]	CAATGATTAGTTCCGAAACCCG
7[150]	2[150]	GAACCTCAAATGGCGCCAATTA
5[161]	6[160]	GAGTGTTTGTGATTTTCTTTCACCTG
69[2]	64[2]	GACATTCAACCGTTATTCATTA
47[2]	46[2]	TTAATTCATCTCCGTGTGATA
73[5]	72[5]	TGAGAGTCTGTAAAATA
25[5]	68[2]	ATAAAGGTGGAATAAGTTTAT
49[2]	16[2]	TAAGGCGTAAAAAAGCCTGTT
15[5]	70[5]	GAGAGGGTAGTCATTGCC
64[18]	60[9]	GGAAAATTGAGGAGCAAGGCCGGA
53[5]	48[5]	AAAGTAAGCGAGGAAACG
51[5]	22[2]	CAATAATAACTCCTTATTACG
59[9]	53[29]	AGGGTAATTGAGCGCTATATCTTACCCGAACAAAG
75[5]	74[5]	GCATGTCAACCCAAAAAC
45[2]	44[2]	TGCAAATCCAATAATATATTTAG
20[151]	19[148]	CAGAACGCGCCTTAAGCAATA
14[151]	17[148]	TACCATATCAAAGCAAAGAA
14[136]	21[151]	ATTTACAACATGTTTACGCTAATG
77[31]	77[51]	AATTGTAAACGTTAAT

**Modifications:**

Localization dye	AAATCGAACCACAGTTTCGTAGTACCGCCACCCTAG [ATTO542]
For Nanoparticle binding	GAAACAAAGTACGGTGTACAACGTAACAAAGCAGAAAAAAAAAAAAAAAAAAAAAAAAAAAA A
For Nanoparticle binding	CGCCTCAGCAGCGAAAGATGCCACTCATCAGTCTTATGCAAAAAAAAAAAAAAAAAAAAA AA
For Nanoparticle binding	GATTTTATGCTCATAGAGGACAGATGAACAACAAAAAAAAAAAAAAAAAAAAAAAAAAAA

For Nanoparticle binding	TCACCTTGACCTACACAGCAGAAGATAAATAAAGCATTACACCAGAAAAAAAAAAAAAAAAAAAAA AAAAAAAAA
For Nanoparticle binding	GAATGGTAAAAAATTGTGTAAAAAAAAAAAAAAAAAAAAAAAAAAAAA
For Nanoparticle binding	TCATAAATATTTAAACAGGGAACGAGAAAAAAAAAAAAAAAAAAAAAAAAAAAAA
For Nanoparticle binding	AGCTGCGGGTGGTTGGTGGTAATAACAAAAAAAAAAAAAAAAAAAAAAAAAAAAA
For Nanoparticle binding	GATACCGATAGTGCAGAACCTCGTTAAAAAAAAAAAAAAAAAAAAAAAAAAAAA
For Nanoparticle binding	AATCACAGAGGACGCTCATGGAAATCCTGAGTAAATCCGTTCAAAAAAAAAAAAAAAAAAAAAA AAAAAA
For Nanoparticle binding	CAATGATTAGTCCGAAACCCGAAAAAAAAAAAAAAAAAAAAAAAAAAAAA
For Nanoparticle binding	GAACCTCAAATGGCGCCAATTAAAAAAAAAAAAAAAAAAAAAAAAAAAAAA
For Nanoparticle binding	GAGTGTGTTGTTGATTTCTTTCACCTTGAAAAAAAAAAAAAAAAAAAAAAAAAAAAA
Biotin modified	GACATTCAACCGTTATTCATTAATA [Biotin]
Biotin modified	TTAATTCATCTCCGTGTGATAATA [Biotin]
Biotin modified	TGAGAGTCTGTAAAACTA [Biotin]
Biotin modified	ATAAAGGTGGAATAAGTTTAT [Biotin]
Biotin modified	TAAGGCGTTAAAAAAGCCTGTTT [Biotin]
Biotin modified	GAGAGGGTAGTCATTGCC [Biotin]
Biotin modified	GGAAAATTGAGGAGCAAGGCCGA [Biotin]
Biotin modified	AAAGTAAGCGAGGAAACG [Biotin]
Biotin modified	CAATAATAACTCCTTATTACG [Biotin]
Biotin modified	AGGGTAATTGAGCGCTATATCTTACCCGAACAAAG [Biotin]
Biotin modified	GCATGTCAACCCAAAAAC [Biotin]
Biotin modified	TGCAAATCCAATAATATATTTAG [Biotin]
For QD capture	TTCGGGCAATGTAGACATTTCCAGAACGCGCCTTAAGCAATA
For QD capture	TTCGGGCAATGTAGACATTTTACCATATCAAAGCAAAAGAA
For QD capture	TTCGGGCAATGTAGACATTTATTACAACATGTTGAGCTAATG
Localization dye	AATTGTAACGTTAAT [ATTO647N]
DNA tagged QD	TGTCTACATTGCCCCGAAAAAAG*G*G*G*G*G*G*G*G*G*G*A (*Indicates the phosphorothioate linkage)

**Table S3.** Annealing ramp for DNA origami folding.

Temperature [°C]	Cooling rate [s/°C]
65	120
64 to 61	180
60 to 59	900
58	1800
57	2700
56	3600
55	4500
54 to 44	5400
43	3600
42	2700
41 to 39	1800
38	900
37 to 30	480
29 to 25	120

Don't give up and be kind to yourself 😊